Flying-V Modeling & Robust Controller Design

Design of a C* Longitudinal Controller within the $\mathcal{H}_\infty$ Signal-Based Mixed Sensitivity Framework

Beatriz Pedroso

TUDelft

Delft
University of
Technology

Challenge the future

Flying-V Modeling & Robust Controller Design

Design of a C^* Longitudinal Controller within the $\mathcal{H}_\infty$ Signal-Based Mixed Sensitivity Framework

by

Beatriz Pedroso

in partial fulfillment of the requirements for the degree of

Master of Science

in Aerospace Engineering

at the Delft University of Technology,
to be defended publicly on Monday 24 March 2025 at 13:00.

TUDelft   Delft
University of
Technology

ABSTRACT

As the aviation industry faces growing environmental and societal pressures, novel concepts such as the Flying-V emerge. Nevertheless, its unconventional configuration poses unique challenges in terms of stability and control, highlighting the pressing need for advanced control systems development. A gap in the literature arises concerning the lack of system robustness in the presence of uncertainties and the absence of robust controllers designed for the aircraft. Hence, the current study aims to increase the maturity of the flight control system of the Flying-V concept by implementing a C^* longitudinal controller, while guaranteeing robustness stability and performance against uncertainty, adequate performance in the presence of disturbances and measurement noise, and compliance with Level 1 handling qualities. The Flying-V model is implemented in MATLAB® and Simulink® which served as the foundation for the controllers synthesis. Three designs are developed, which include a continuous time, a modified continuous time, and a modified continuous time multi-modeling controllers. These are conducted within the standard and signal-based $\mathcal{H}_\infty$ mixed sensitivity frameworks. Extensive analysis of the controllers is performed in terms of stability assessments, linear and nonlinear time domain simulations, and uncertainty sensitivity. Results demonstrate that the feedback of a combined signal demand such as the C^* parameter provides, for a single input multiple-output system, a balanced disturbance rejection at the plant outputs. Conclusions are drawn in terms of the feedback controller structure, highlighting that high gain is necessary at low frequencies for disturbance rejection and roll-off at high frequencies allows control signal reduction and measurement noise attenuation. It is verified that, in the digital formulation, the anti-aliasing filter also contributes to the latter specification. Furthermore, it is concluded that the requirements can be successfully translated into hard constraints imposed on the system, which are shaped across the frequency ranges by imposing a limiting gain, via weighting filters. Moreover, taking into consideration the discretization effects of the flight computer in the design phase improves considerably the stability margins of the controllers. Lastly, it is verified that the proposed controller structures which are designed in the linear domain perform satisfactorily in the nonlinear simulation model and comply with the requirements defined. The multi-modeling controller proved successful in terms of robustness and performance across the flight envelope. Hence, we conclude that implementing this $\mathcal{H}_\infty$ optimization process for the design is a promising and viable method to guarantee robustness against uncertainties, disturbances, and measurement noise, as well as compliance with Level 1 HQ. The present work naturally paves the way for recommendations for future work. Some of these recommendations include the extension to lateral-directional control laws, gain-scheduling to guarantee the requirements across the flight envelope, maturity of the aerodynamic data, and pilot assessments of the handling qualities.

Keywords: Robust control, Flight control, Mixed sensitivity synthesis, $\mathcal{H}_\infty$ optimization, Reduced-order models, Robust stability, Flight Dynamics, Aircraft modeling, Digital control, Sustainable aviation, Flying wings.

ACKNOWLEDGMENTS

This thesis marks the very end of this chapter in Delft, and what great two years and a half these were. I had the chance to live abroad for the first time, move to Munich for a very rewarding internship, travel, learn about the topics I find most interesting, discover new passions and, above all, I had the chance to come across the greatest people. I am proud of what I have accomplished so far in my academic journey, especially with this thesis project, to which I have dedicated myself immensely over the past year. It has pushed me out of my comfort zone multiple times, which is also what makes it so rewarding and fulfilling in the end.

And, as for every great accomplishment, I could not have done it alone. Therefore, I want to thank those who helped me along the way.

To begin with, I want to express my deepest gratitude to my supervisor Dr. Eng. Spilios Theodoulis for the unwavering support and guidance. I want to extend my heartfelt appreciation to my second supervisor, Dr. ir. Tijmen Pollack, for his invaluable insights and dedication. To both of you, thank you for always believing in me, for being so approachable, and for your patience in listening to me during every meeting, regardless of the high number of slides. Your expertise and encouragement have been instrumental for this work.

Moreover, I am deeply grateful to my family. I want to thank my grandparents Aurora and Mário for the endless care. They have taught me by example that good things come with hard work, perseverance, and integrity. I am also forever grateful for my brother, Leonardo, who always pushed me to do better, thank you for always standing by me and for all the care and support. Lastly but definitely not least, I am beyond grateful to my mum, Filomena, who is my role-model. The opportunities that I have had are a direct reflect of her effort, love, and patience.

To my friends in Delft, thank you for making me feel at home in the Netherlands and thank you for inspiring me everyday. To my friends from Técnico, thank you for being a constant reminder of true friendship, even as life has taken us across Europe. I am beyond grateful to always have you by my side. To my friends from Coimbra, thank you for making my return home even sweeter. Lastly, to my rock and partner, Leo, thank you for making every moment so joyful and full of love and for being my biggest supporter. I am forever grateful to have you by my side and to share all my adventures in life with you.

Beatriz Pedroso
Delft, February 2025

NOMENCLATURE

ALS	Automatic Landing System
AoA	Angle of Attack
CA	Control Allocation
CAP	Control Anticipation Parameter
CAS	Control Augmentation System
CFD	Computational Fluid Dynamics
CL	Closed Loop
CoG	Center of Gravity
CoM	Center of Mass
CT	Continuous Time
D/A	Digital-to-Analog
DM	Disk Margin
DoF	Degree of Freedom
DT	Discrete Time
EASA	European Aviation Safety Agency
EoM	Equations of Motion
FAA	Federal Aviation Administration
FCS	Flight Control System
FEP	Flight Envelope Protection
FTE	Flight Test Experiment
GM	Gain Margin
Go6	Gang of Six
GS	Gain Scheduling
HF	High frequencies
HQ	Handling Qualities
ICR	Instantaneous Center of Rotation
IEKF	Iterated Extended Kalman Filter
IMU	Inertial Measurement Unit
INDI	Incremental Nonlinear Dynamic Inversion
L/D	Lift-to-Drag Ratio
LF	Low frequencies
LFT	Linear Fractional Transformation
LMI	Linear Matrix Inequality
LPV	Linear Parameter Varying
LQG	Linear Quadratic Gaussian
LS	Loop Shaping
LTI	Linear Time-Invariant
MIMO	Multi Input Multi Output
MS	Mixed Sensitivity
NASA	National Aeronautics and Space Administration
NDI	Nonlinear Dynamic Inversion
NED	North-East-Down
NMP	Non-Minimum Phase
OEI	One Engine Inoperative

PID	Proportional, Derivative and Integrative
PM	Phase Margin
PS	Pilot Station
RANS	Reynolds-Averaged Navier-Stokes
SAS	Stability Augmentation System
SGT	Small Gain Theorem
SIMO	Single Input Multiple Output
SISO	Single Input Single Output
SP	Short Period
SS	State Space
SV	Singular Values
TD3	Twin-Delayed Deep Deterministic Policy Gradient
TF	Transfer Function
UAV	Unmanned Aerial Vehicle
VLM	Vortex Lattice Method
WC	Worst Case
WF	Weighting Filter
WTE	Wind Tunnel Experiments
ZOH	Zero-Order Hold

CONTENTS

1

INTRODUCTION

The evolution of flight control systems (FCS) originated from challenges in achieving basic stability and control and culminated in today's sophisticated digital systems. This journey, marked by innovation and adaptation, has been pivotal in the advancement of contemporary aviation. The successfully first powered flight in 1903, authored by the Wright brothers, was achieved due to the systematic design approach and the highlight placed on making their aircraft controllable by the pilot rather than inherently stable [Stevens et al., 2015] [Anonymous, 2000]. However, the constant attention from the pilot and high workload spurred the development of automatic flight control systems, aiming to reduce pilot burden and enhance safety [Stevens et al., 2015].

FLY-BY-WIRE SYSTEM

Fly-by-wire (FBW) technology stands at the forefront of modern aviation and it is a demonstration of these advancements. The concept was first explored by the defense sector. While earlier aircraft, such as the NASA-modified F-8 Crusader, had tested digital FBW technology in the early 1970s [Elliott, 1977], the General Dynamics F-16, which entered service in 1978, was the first production aircraft to rely entirely on active stabilization by the FCS design to operate safely [Droste and Walker, 1980]. Its success marked a revolution in FCS design. Due to the enhanced aircraft stability and control as well as pilot workload decrease, the FBW application later spread to the civil aviation. In 1988, the Airbus A320 was the first commercial aircraft that entered service with an electronically managed, or FBW, system [Balas, 2003]. This highlighted the technology's potential to transform civil aviation, with decreased pilot workload, improved safety and handling qualities, and reduction of airline operating and training costs [Pratt, 2000].

The central elements of any FBW system are the control laws, which are algorithms implemented in the flight computer that translate pilot inputs and sensor measurements into precise control actions that induce vehicle motion. The development of control laws follows a rigorous process involving requirement management and, after its design, it undertakes a verification and validation process, ensuring that the system meets airworthiness and performance criteria.

FLYING-V, A STEP TOWARDS SUSTAINABLE AVIATION

As the aviation industry faces growing environmental and societal pressures, the need for innovative aircraft designs that prioritize energy efficiency and sustainability has become paramount. Consequently, novel concepts like the Flying-V, currently researched by TU Delft, represent a bold step toward a more sustainable future for aviation. An asymptote seems to have been reached in the conventional configurations in terms of aerodynamic efficiency gains [Martinez-Val, 2007]. Hence, the Flying-V concept emerges as a promising alternative. The configuration was proposed by Benad [2015] and it is a flying wing with a V-shaped passenger cabin. Preliminary estimations indicated an improved lift over drag ratio of 10% and a 2% reduction of the empty weight [Benad, 2015]. Additionally, in 2022, it was stated that the concept promises a 20% lower fuel burn when compared to a conventional reference aircraft performing the same mission and with the same capacity and wingspan [Benad and Vos, 2022]. However, its unconventional shape and layout pose unique challenges in terms of stability and control, necessitating the development of advanced control systems.

THESIS AIM

This thesis focuses on the development of a robust control system tailored for the Flying-V aircraft that can effectively manage the intricacies of the flying wing model. The proposed solution revolves around guaranteeing robustness stability and performance in the face of uncertainty, adequate performance properties in the presence of disturbances and measurement noise in the model, and compliance with Level 1 Handling Qualities (HQ). The design process for the Flying-V control system involves several key stages. These stem from defining the design requirements based on airworthiness standards, HQ considerations, and specific operational objectives of the Flying-V. The FCS design leverages simulation tools and advanced optimization techniques to iterate and refine the control laws, that allow structured controller designs. The system analysis is conducted in terms of linear and nonlinear simulations, stability assessments, and HQ examinations. This step plays a critical role in the development process, ensuring that the FCS meets all design requirements and performs as intended under real-world conditions, ultimately leading to the verification of robustness and reliability properties. Hence, the proposed controller design aims to increase the maturity of the current FCS of the Flying-V. By addressing the unique challenges posed by this innovative aircraft design, this thesis contributes to the broader effort to redefine the future of air travel, paving the way for a new era of environmentally friendly and economically viable aviation.

THESIS OUTLINE

This thesis is logically organized into several chapters, as detailed in Figure 1.1. To begin with, a comprehensive study of the Flying-V as well as of the state-of-the-art in robust control techniques and other concepts for controller synthesis and implementation is conducted in Chapter 2. From the gaps identified in the literature review, the research proposal is outlined in Chapter 3, where specific objectives and questions are formulated. Moreover, the foundational framework for understanding the key concepts and theories underpinning this research is presented in Chapter 4.

Furthermore, Chapter 5 presents the implementation of the Flying-V simulation model, which is the foundation for the controller synthesis and analysis. The key model subsystems are described, the trimming and linearization procedures are explained, and the bare airframe is analyzed. The FCS design is detailed in Chapter 6, where alternative design choices are presented and discussed, the requirements are formulated, and three controllers are developed: a continuous time (CT), a modified CT, and a multi-modeling modified CT controllers. These are subsequently examined in Chapter 7, in terms of stability margins, handling qualities, linear and nonlinear time domain simulations, and uncertainty analysis.

Finally, Chapter 8 revisits the research questions and answers them using the results of the previous chapters. The recommendations for future work are consequently addressed. As supplementary material, Appendix A presents the detailed tasks and timeline of the project, summarized in a Gantt chart, supporting Chapter 3. Appendix B presents the paper which was submitted to the 11th IFAC Symposium on Robust Control Design (ROCOND'25). It introduces a variation of the designs presented in Chapter 6, with which it is compared.
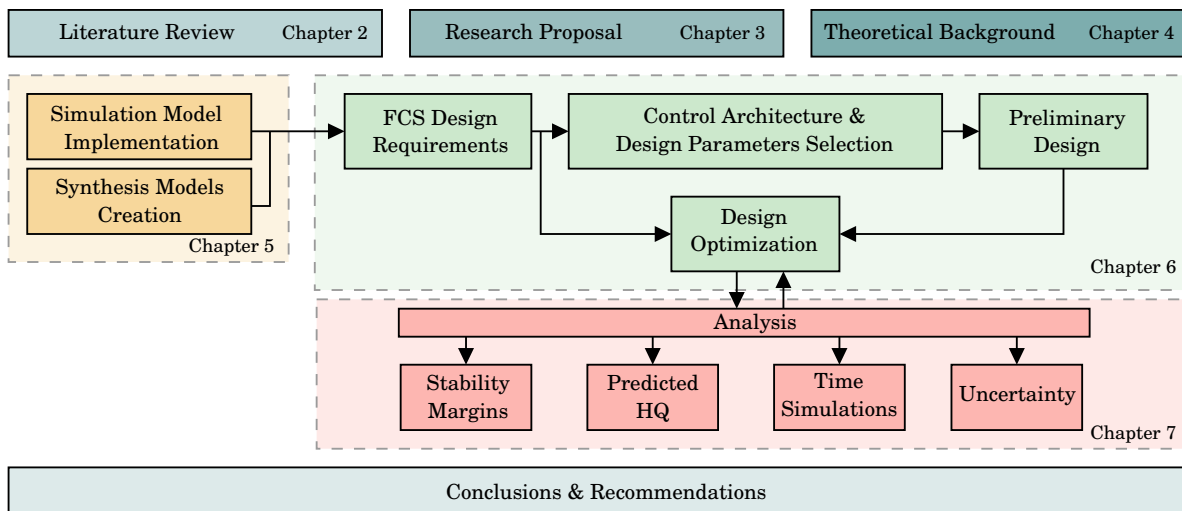
Figure 1.1: Thesis Structure.

2

LITERATURE REVIEW

In the current chapter, a comprehensive study of the Flying-V is performed in order to identify a research gap and progress towards the research objectives and questions. Hence, an examination of the enhancements and innovations implemented in the Flying-V concept is provided in Section 2.1, highlighting the major results in aerodynamics, stability, and control. Moreover, in Section 2.2, the state-of-the-art in robust control techniques for controller synthesis are discussed and, in Section 2.3, the longitudinal control law C^* is introduced and some applications are mentioned. Lastly, the gain-scheduling problem is addressed in Section 2.4. Conclusions are subsequently drawn and discussed in Section 2.5.

2.1. FLYING-V

The aviation industry has experienced a rising demand in recent years. Thus, innovative and sustainable solutions have spurred within the industry to tackle the increasingly negative environmental impact on the planet.

Moreover, an asymptote seems to have been reached in the conventional configurations in terms of aerodynamic efficiency gains. Therefore, for the short-term solution, a possible option is to improve the aircraft airframe design in order to overcome the limits and aim for drag reduction, increased useful load, and diminished environmental impact. [Martinez-Val, 2007]

Flying wings are alternative candidates to the conventional configurations that aim to offer significant aerodynamic and structural benefits [Wood and Bauer, 2001]. Nonetheless, although several studies have been conducted on this configuration, none have reached the commercial aviation market. However, Benad [2015] proposed the novel Flying-V configuration which emerged as a promising prototype. Consequently, given the viable and more energy efficient alternative to conventional designs, since 2016, TU Delft has conducted extensive research on this aircraft model.

The current section is organized as follows. Firstly, in Section 2.1.1, the Flying-V configuration is analyzed, not only by illustrating the concept but also by describing both its promising advantages and limitations. Furthermore, in the current study, major results from the aerodynamic, stability and control areas will be discussed in more detail, respectively, in Section 2.1.2, Section 2.1.4, and Section 2.1.5. Nonetheless, other relevant studies were performed on structural analysis, namely on crashworthiness [Chen et al., 2023] [Koenderink, 2024], structural sizing [Dotman, 2021], unconventional engine mounting structures [Voeten, 2022] [Koenderink, 2024], and on weight estimation [de Ruiter, 2020] [Nanninga, 2023]. Studies were also conducted on landing gear implementation [Bourget, 2020], on engine-airframe [Rubio Pascual, 2018] and on hydrogen fuel tank integration [van Woensel, 2021], on interior and cockpit design [Chung, 2018] [van der Pluijm, 2021], and on climate effects [Reekers, 2021]. The Flying-V aerodynamic simulation model is also explained thoroughly in Section 2.1.3. Lastly, in Section 2.1.6, some of the FCS are discussed and other conclusions are drawn.

2.1.1. Aircraft Configuration

The Flying-V configuration, which is a pure flying wing with a V-shaped passenger cabin, was initially proposed by Benad [2015]. The reference aircraft for the design was the Airbus A350-900, which has the same capacity and cruise speed. The aircraft was, thus, designed to transport 315 passengers over a range of 15.000 km. Moreover, preliminary estimations indicated an improved lift over drag ratio of 10% and a 2% reduction of the empty weight. Additionally, the compactness and simplicity of the design was pointed out as a main benefit, alongside the shielding of the engines from the ground, which results in reduced noise. [Benad, 2015]

Several iterations on the Flying-V design were performed, yielding in the current concept which is portrayed with four different views in Figure 2.1-Figure 2.4 [1]. It can, therefore, be observed that the aircraft contains the engines on top of the wing, close to the center axis. This position allows a low yawing moment in case of engine failure [Benad and Vos, 2022]. Moreover, there are four control surfaces in each wing: three elevons that are located on the trailing edge and one rudder, which are highlighted in Figure 2.1 and Figure 2.4, respectively. The control surface sizing is, nonetheless, currently in the development phase.

Furthermore, this configuration has several advantages over the conventional aircraft. It suggests a 20% lower fuel burn when compared to a conventional reference aircraft performing the same mission and with the same capacity and wingspan [Benad and Vos, 2022], it allows reduced noise levels during take-off and landing [van Ieperen, 2021], and it is a promising ecological solution. Additionally, it was stated that the concept has a 25% higher lift-to-drag ratio when compared to the NASA common research model, and it has a reduced wetted area and frictional drag Moreover, [van Overeem et al., 2022]. Nonetheless, as far as stability is concerned, the Flying-V also has its drawbacks. To begin with, there is low control authority and the dutch roll is unstable [Cappuyns, 2019]. Additionally, pitch break-up tendencies occur for angles of attack (AoA) higher than 20 degrees [Viet, 2019]. However, even though no articles have been published on this matter, it was discovered using both Vortex Lattice Method (VLM) and RANS-based Computational Fluid Dynamics (CFD) simulations that the pitch break-up is happening, for cruise conditions, around 10 degrees of AoA.

It is also important to note that the design of the Flying-V allows for a simple family concept by introducing changes to the highly swept inner wing section. The inboard part of the wing was allowed to stretch given the new parameterization conducted by Hillen [2020]. Oosterom and Vos [2022] worked on a multidisciplinary design optimization which was used to design the three aircraft family members simultaneously. In [Oosterom and Vos, 2022], it was also predicted that, while satisfying 100% commonality with the largest aircraft, there was a reduction in fuel burn of 22% and 20% compared to the A350-900 and A350-100 aircraft, for the same mission range and payload.
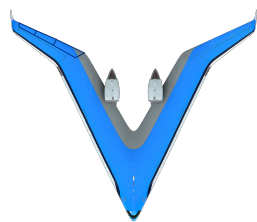
Figure 2.1: Flying-V top view.

Figure 2.2: Flying-V diagonal view.

Figure 2.3: Flying-V front view.

Figure 2.4: Flying-V profile view.

---

[1]https://www.tudelft.nl/en/ae/flying-v (Accessed in March 2024)

2.1.2. AERODYNAMICS RESEARCH OVERVIEW

As mentioned in Section 2.1.1, Benad [2015] introduced a novel configuration, whose research was continued by Faggiano et al. [2017]. Its primary goal was to optimize the design and assess the aerodynamic performance in comparison with the reference conventional configuration during one single condition in cruise (Mach number equal to 0.85, lift coefficient of 0.26, and an altitude of 13.000m). It was proved that the Flying-V was 25% aerodynamically more efficient than the NASA Common Research Model. [Faggiano et al., 2017]

Moreover, research into flight characteristics was needed to conduct sub-scale flight testing. Thus, Viet [2019] conducted wind tunnel campaigns at approach speed and high AoA. Unstable behaviour for AoA higher than 20 degrees was discovered. Additionally, the range of the center of gravity location was determined for trimmed flight and its optimal location was also found, providing a static margin of about 9%. Ruiz Garcia [2019] worked on top of the research conducted by Viet [2019] and obtained an aerodynamic model by using wind tunnel data from a 4.6% scaled model. However, due to limitations of the experiment, only static aerodynamic coefficients were obtained. Additionally, a safe flight envelope for the flight test was defined and the forward and aft limits for the center of gravity were also defined to ensure aircraft controllability. Another aerodynamic model was constructed by Siemonsma [2022], using the two-step approach method: state estimation with an Iterated Extended Kalman Filter, followed by the determination of a polynomial model structure using a stepwise regression algorithm.

Furthermore, several other studies on effects on the aerodynamic performance were conducted. For instance, Ankith John Santosh [2020] evaluated the influence of ground proximity on the lift, drag and pitching moments of the aircraft. Erdinçler [2021] analyzed the effects of ground spoilers on the Flying-V. An experimental investigation was also conducted by Johnson [2021] on the 4.6% scale model, in which the effects of winglet integration, rudder deflection and aileron-rudder interaction effects were quantified. On top of that, the wind tunnel effects were evaluated by Jorge [2023] for several combinations of angle of attack and sideslip angles. It was concluded from this research that the model exhibits resilience against stall up to extreme AoA and the sideslip has a deep effect on the overall flow field.

Moreover, given the drawback of unstable pitch break, van Uitert [2023] came up with three possible solutions with the ultimate goal of eliminating it. Although it does not solve the issue, fence installation on the scaled flight testing model was a recommended measure.

Additionally, various efforts were combined to improve the lift-to-drag (L/D) ratio of the aircraft. To begin with, van Luijk and Vos [2023] evaluated a new design for the outboard wing to maximize the ratio in cruise conditions. From this study, it was concluded that the highest value is of 20.3 when neglecting the control surface integration, while it is 19.4 when the constraints related to the elevon integration are included. Granata [2023] also optimized the wing geometry, aiming to minimize induced drag under specific subsonic conditions. The final design showed a 4.38% increase in L/D ratio compared to the initial one and a 10.5% reduction in induced drag coefficient. Laar et al. [2024] optimized the twist distribution at the wing-winglet junction, resulting in improvements on the ratio and in the decrease of the angle of attack during cruise.

Lastly, Eftekhar [2024] researched the landing performance of the Flying-V by analysing the effects of the integration of high-lift devices, such as split flaps. From this study followed that these successfully allow the reduction of the pitch attitude at landing by 3 degrees. The possibility of reducing the approach speed was also studied, with a decrease of 3 m/s.

2.1.3. SIMULATION MODEL

In order to simulate the behavior of the Flying-V, it is fundamental to have a simulation aerodynamic model. In fact, three sources were used to obtain the stability and control derivatives, namely a VLM, Wind Tunnel Experiments (WTE), and a Flight Test Experiment. Although no references exist yet to corroborate the information, the current aerodynamics model was obtained by RANS-based CFD simulations. Figure 2.5 illustrates the aircraft that were used for both the VLM and WTE experiments.

Firstly, the aerodynamic coefficients for specific Mach numbers can be retrieved using ODILILA, which is a VLM. This model resulted from the work of Cappuyns [2019]. The method is applied on the full-scale aircraft with 2 elevons in the trailing edges and the unstable dutch roll is able to be identified. Nonetheless, given that the resultant model is linear, the pitch break behavior could not be modeled and uncertainties arise if deviations from the linearized points occur. [Cappuyns, 2019]

Secondly, the WTE was conducted by Ruiz Garcia [2019] on a 4.6% scaled half model of the Flying-V, which has 3 elevons and does not have winglets in the configuration. Moreover, during this test, the angle
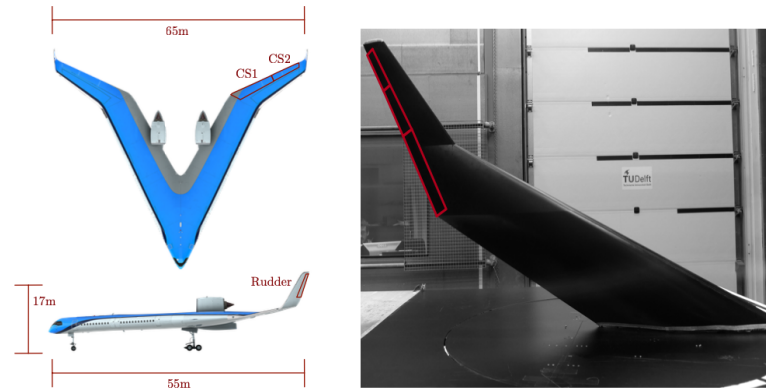
Figure 2.5: Full scale Flying-V used for VLM (landing gear not included for analysis) [van Overeem et al., 2022] and small-scale Flying-V used for WTE [Viet, 2019].

of attack, the wind speed and the elevons deflections were changed over time, so that the aerodynamic coefficients could be obtained. However, it is important to note that the lateral-directional coefficient C_Y could not be estimated due to the high uncertainty associated with it. Only longitudinal (and static) aerodynamic coefficients could be taken into account. Thus, the unstable dutch roll is not present in the model. The pitch break tendencies are, however, captured and the resulting model is nonlinear. [Ruiz Garcia, 2019] [García, 2020]

Lastly, a maiden flight test was performed in July 2020 and, since the aircraft experienced the unstable dutch roll[2], it is expected that this behavior is included in the retrieved model data. Nonetheless, it is expected that the pitch break is not correctly captured due to the small fidelity range. Additionally, there are several uncertainties associated with the FTE model. It is only based on a single flight and the pitching moment model has a low quality given the high noise. [van Overeem et al., 2022]

Therefore, based on this information, van Overeem et al. [2022] proposed a model that combines the models from the VLM and the WTE into a 6 Degree of Freedom (DoF) model, to capture in one model all the main control and stability characteristics, including the unstable dutch roll and the pitch break tendencies. The VLM model is used as a baseline and all the lateral coefficients are obtained from it. Moreover, the longitudinal aerodynamic model curves from VLM and WTE for the approach and cruise phases were analyzed. From these results, which are illustrated in Figure 2.6, it was concluded that the coefficients for the AoA between -5 and 15 degrees should be obtained from the VLM, whereas the ones for the AoA between 15 up to 30 degrees should be retrieved from the WTE. Therefore, Figure 2.7 portrays the model after combining these two data sources. Furthermore, given that the model does not include any zero-lift drag, this coefficient was added and considered equal to the one from Airbus A350-900, which is the reference aircraft for the Flying-V. It is also important to note that a Froude scaling had to be applied since the two models operate in different speed regimes which led to the assumption that the relative moment of inertia was the same for both the sub-scale and the full-scale aircraft. These final two aspects also add uncertainty to the model. Thus, given the benefit of capturing all the relevant behavior, this model proposed by van Overeem et al. [2022] was defined as the baseline for subsequent researches. Nevertheless, in its design, several assumptions were made, which limit the usability and validity of the model. An overview of these assumptions are [van Overeem et al., 2022] [Cappuyns, 2019]:

- Rigid body with a constant mass

- Earth's curvature and angular velocity are neglected

- Zero wind, with perfect atmosphere (atmospheric conditions correspond to the International Standard Atmosphere)

- Resultant thrust lies in the symmetry plane of the aircraft

- Gravity vector is constant

---

[2]https://www.tudelft.nl/en/ae/flying-v/flying-scale-model (Accessed in March 2024)
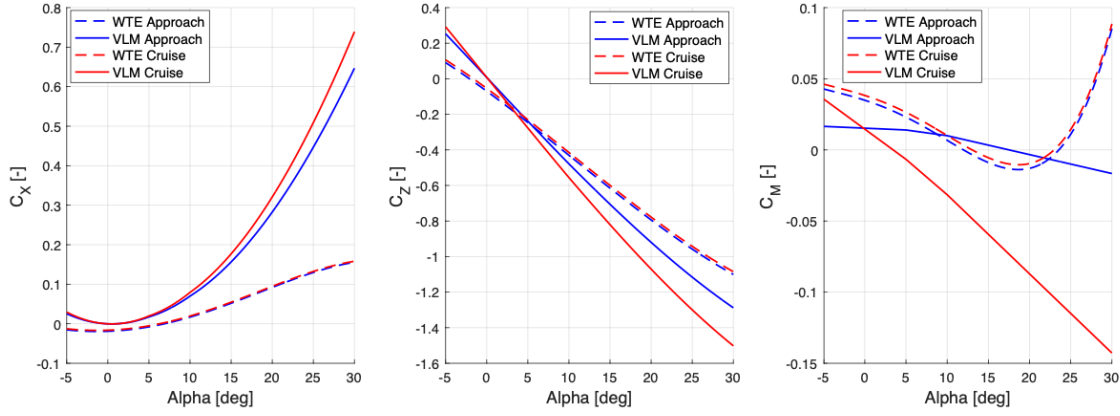
Figure 2.6: Aerodynamic model curves from VLM and WTE for approach and cruise phase. [van Overeem et al., 2022]
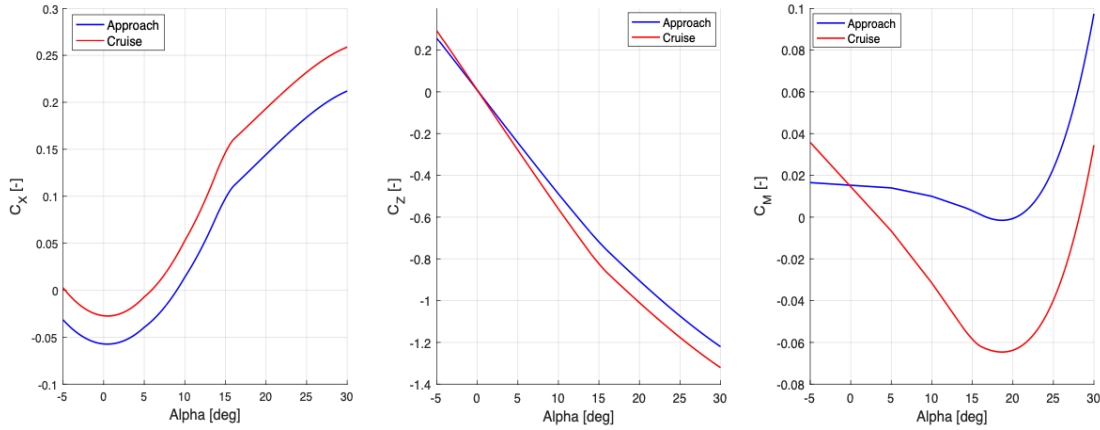
Figure 2.7: Aerodynamic model obtained from combining VLM with WTE. [van Overeem et al., 2022]

2.1.4. STABILITY & HANDLING QUALITIES

From the discussion in Section 2.1.2, it is clear that there are several challenges associated with the flying wing configuration, especially as far as stability is concerned. Thus, the research conducted on this area is considered in the current section, as well as the HQ of the aircraft.

To begin with, the stability and HQ analysis of the Flying-V was first conducted by Cappuyns [2019], which were assessed based on criteria from military standards and on requirements from the European Aviation Safety Agency (EASA). Results presented an unstable dutch roll and rudder control power proved not to be sufficient in case of One Engine Inoperative (OEI) conditions. Moreover, Palermo and Vos [2020] carried out an experimental investigation of the aerodynamic characteristics of the 4.6% geometrically scaled model, by wind tunnel testing. In the experiment, two control surfaces in the outboard wing are deflected to measure their effect in terms of lift, drag, and pitching moment. It was also proved that the deployed control surfaces can trim the aircraft with maximum lift coefficients between 0.6 and 0.7.

Horwitz [2021] determined the outboard wing and winglet geometry parameters that would produce satisfactory lateral-directional stability and control characteristics for the aircraft, addressing its inherent issues. However, it was proved that satisfactory yawing moment due to rudder deflection was not achieved with any design. Additionally, Nolet [2022] also focused on Flying-V surfaces that could result in increased directional control power. The author evaluated the effects of split flaps integration and calculated an adequate split flap design. It was verified that these surfaces on the outboard wing section can effectively contribute to the objective, at the cost of significant drag increase.

Moreover, van Overeem [2022] besides developing a 6 DoF simulation model, which was previously mentioned in Section 2.1.3 and implementing a controller, the author also assessed the stability and HQ performance with respect to military requirements. To begin with, van Overeem et al. [2022] identified

the Flying-V as a Class III aircraft, with prevailing flight phases in Category B and C. Additionally, the nonlinear equations of motion were linearized around the trim conditions, which were computed both for the approach ($M_a = 0.2$) and cruise ($M_a = 0.85$) phases for the aft and forward center of gravity (CoG) ($x_{CoG} = 29.372m$ and $x_{CoG} = 31.714m$ from the nose, respectively). The eigenvalues that were obtained from the state-space system were evaluated for the approach and cruise conditions and for the forward and aft locations of the CoG. Therefore, from the results of the damping ratio and natural frequency of each mode, the flying qualities were examined. A summarized version is portrayed in Table 2.1. Furthermore, the HQ were then analyzed with the Control Anticipation Parameter (CAP). It was verified that moving the CoG aft results in a lower CAP value, which translates into a more sluggish response. It was also verified that the aircraft is at the border of Level 1 HQ at approach condition for the forward CoG and at cruise for the aft CoG, whereas for the other two situations, it has Level 2 HQ. [van Overeem et al., 2022]

Table 2.1: Flying qualities of the Flying-V for the several modes, based on the results presented by [van Overeem et al., 2022].

	CoG Location	Approach		Cruise	
		Aft	Forward	Aft	Forward
	Short Period	Stable, L1	Stable, L1	Stable, L1	Stable, L2
	Phugoid	Unstable	Unstable	Stable, L1	Stable, L1
Mode	Dutch Roll	Unstable	Unstable	Stable, L3	Unstable
	Aperiodic Roll	Stable, L1	Stable, L1	Stable, L2	Stable, L1
	Spiral	Unstable	Unstable	Stable, L1	Stable, L1

Moreover, Torelli et al. [2023] investigated the issues regarding the low speed HQ, the pull-up maneuver and the flight-path-angle response with a pilot in-the-loop experiment. For that purpose, the Cooper-Harper approach was used. In this investigation, the analysis was conducted on the approach speed $M_a \in [0.225, 0.3]$, with maximum deflections of the control surfaces (between 20 and 30 degrees) and with a FCS, which will be further discussed in Section 2.1.5. To begin with, a preliminary HQ analysis was carried out. Three criteria were applied, namely the CAP, the Bandwidth Criteria, and the Gibson Dropback Criteria. Results showed that faster configurations yield better HQ, while slower configurations are notoriously degraded.

Furthermore, another investigation was conducted on the HQ of the Flying-V with a pilot-in-the-loop experiment. The research conducted on Vugts et al. [2023] analyzed the longitudinal HQ in cruise conditions based on the pilot experience in a moving base simulator. Three experiments were conducted: a traditional pitch tracking experiment with the conventional control allocation and a new flight-path-angle tracking experiment, using both the conventional and the flight-path-oriented Control Allocation (CA). Results concluded that the pilots preferred the conventional CA because it has a higher control authority. Overall, the HQ were Level 1 for pitch angle control and Level 2 for flight path angle control. [Vugts et al., 2023]

The lateral-directional HQ were, afterwards, assessed by Joosten et al. [2023]. Firstly, these were quantified only considering the bare-airframe. Results showed that the model was insufficient for compliance with set requirements, due to a lack of pitch, roll, and yaw control authority in low-speed flight conditions, and an insufficiently stable dutch roll. Secondly, both analytically and with a simulator assessment, it was proved that the HQ improved through the implementation of a FCS. However, the control authority was not sufficiently increased for low speed. Thus, if the landing speed is not higher than the baseline, this is still a major challenge in the Flying-V configuration. Recommendations were made on the redesign of the control surfaces.

2.1.5. FLIGHT CONTROL SYSTEMS IMPLEMENTED

In the current section, an overview of the FCS that were designed for the Flying-V aircraft is performed. The techniques previously considered for the concept are highlighted in Figure 2.8[3], bridging to the research gap. To begin with, as mentioned previously, in Torelli et al. [2023] not only a HQ analysis was conducted, but a FCS was also implemented. However, the author's main idea was not to optimize the controller but instead to simply explore the possibility of designing a controller that would comply with the certification requirements. The aircraft was, thus, manipulated through a Control Augmentation System (CAS). The first controller implemented was a direct law, where the side-stick was simply scaled by a linear gain. The second one consisted of a pitch rate command, implemented through a PID and an allocation gain matrix. Additionally, an auto-throttle was also implemented with a proportional controller, which provides constant speed within the physical limits of a realistic engine. After the experiments, it was verified that the CAS proved effective in improving the HQ. The pitch rate command received a better rating over the direct control law, although a main shortcoming of the former controller was clearly identified: a slow pitch rate and, thus, a low control authority. [Torelli et al., 2023]

Secondly, Joosten et al. [2023] implemented an adapted CA and a lateral-directional Stability Augmentation System (SAS). The latter was designed as a combination of sideslip feedback with a reference command, a yaw damper with washout filter, and roll rate feedback with reference command. For longitudinal control, pitch rate feedback was used. As discussed previously in Section 2.1.4, stability improvements were notorious. However, low control authority is a major challenge.

Furthermore, Völker et al. [2023] developed a single loop altitude controller by using the reinforcement learning approach Twin-Delayed Deep Deterministic Policy Gradient (TD3). TD3 is a bio-inspired method that allows offline learning, which mitigates the danger of the system trying unsafe control signals during the learning phase. In fact, the main goals of the research were not only to automate the FCS of the Flying-V but also to construct a controller which is robust to aerodynamic uncertainty, given the poor reliability of the model. The results showed that the TD3 technique learned well the nonlinear simulation model and that it was robust to the uncertainties introduced. However, the controller's performance has not been tested for HQ requirements. [Völker et al., 2023]

Additionally, as it was discussed in Section 2.1.4, van Overeem et al. [2023] implemented a FCS to improve the HQ. Additionally, due to the unfavorable characteristics of the approach phase, this flight condition was the one investigated. To begin with, for the SAS, an Incremental Nonlinear Dynamic Inversion (INDI) controller was designed in the inner loop to control the angular rates and a PID was used to model the airspeed. Regarding the CAS, the roll angle, the flight path angle, and the sideslip were the variables being controlled. Results confirmed that the HQ was satisfactorily improved, resulting in Level 1 flying qualities for all the modes, which is the desired outcome. [van Overeem et al., 2023]

Moreover, in the research of Stougie et al. [2024], a FCS is proposed for the inner loop with a Flight

---

[3]The Adaptive INDI FCS was only recently developed by Atmaca and Kampen [2025] and, thus, it is not discussed in the current section.
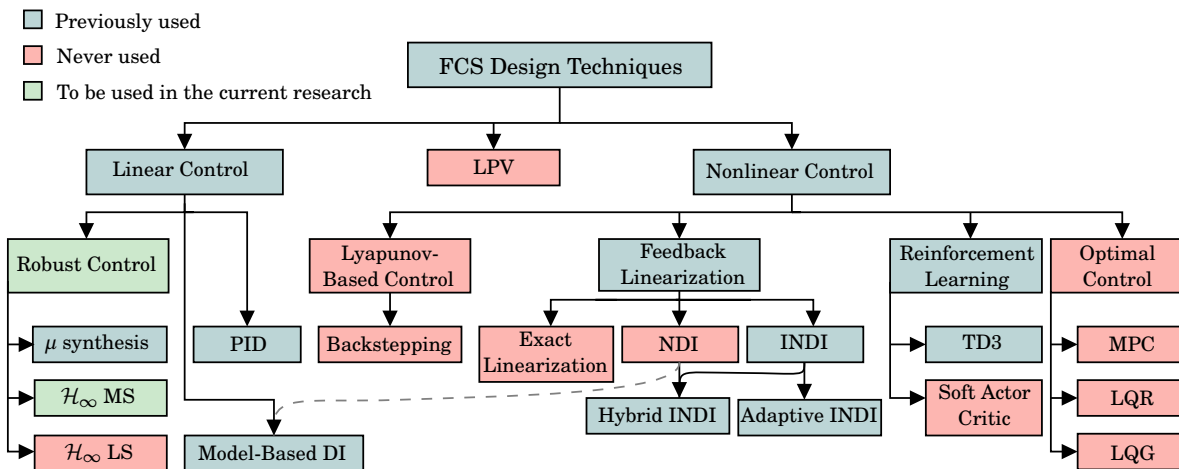
Figure 2.8: Flow chart of the FCS previously designed for the Flying-V and the method to be used in the current research from the possible control design techniques. Inspired by Traas [2024].

Envelope Protection (FEP), which is based on INDI control. Regarding the outer loop, a C* and a Rate Control Attitude Hold (RCAH) control laws were implemented for longitudinal and lateral (for roll angle) control, respectively. The forward CoG was used, which is located 29.4 meters behind the nose. Moreover, three analysis were conducted: one with no sensors included, one with the baseline sensors and the others with the adjusted time delays. It was shown that the aircraft can be tuned within Level 1 HQ if the time delay for the angular rate sensors is no more than 0.04 seconds. It is important to highlight that when the baseline sensor dynamics were added and the controller was made discrete, the gain and phase margin requirements were no longer met. INDI is highly sensitive to sensor measurements, time delays, and unmodeled high frequency (HF) dynamics, which degrades considerably the controller robustness and performance. The C* response was also illustrated and it was verified that a large overshoot occurred for the three models and multiple oscillations were visible for the baseline sensors model. Lastly, a FEP was also implemented and it was verified that AoA higher than 30 degrees were prevented, the load factor did not surpass 2.5, and the roll angle was also limited. Aerodynamic uncertainties were added to the model and it was shown that the controller was robust to these changes.

However, Traas [2024] identified errors in the simulation model used by van Overeem [2022] and Stougie et al. [2024], which may have led to incorrect conclusions. In fact, with the corrected version of the model, some HQ criteria were not satisfied and the FEP structure proved inadequate to more excessive control inputs, causing instability for longitudinal, lateral, and direction control inputs. Thus, this author proposed another FEP structure which performed as desired as well as a different nonlinear controller, known as Hybrid INDI, which combines sensor-based and model-based information. Although improvements were noticed with respect to the sensor-based INDI, some gain stability margins were not satisfied. Additionally, by imposing uncertainty on the system a posteriori, it was evident that the system lacked robustness, as some combinations of uncertainty led to system instability. [Traas, 2024]

Lastly, with the challenges associated with INDI-based control laws identified, especially in terms of sensitivity to time delays, Shahin [2024] proposes a new flight control law. It consists of a multi-loop μ-optimal approach to design a robust inversion-based control system, which was applied to the short period (SP) approximation of the longitudinal dynamics. Thus, robust control techniques are merged with previous design configurations, which shed light on the importance of $\mathcal{H}_\infty$-tools for robust stability and performance. In fact, the HQ tested and the stability margins were in compliance with the requirements for the nominal plant. Nonetheless, when uncertainty is introduced, the worst-case stability margins are below the imposed level. [Shahin, 2024]

2.1.6. FLYING-V REMARKS AND FCS DISCUSSION

The Flying-V configuration emerged as a promising prototype. Some of its advantages include lower fuel burn, reduced noise levels, and higher lift-to-drag ratio. However, there are stability issues, such as an unstable dutch roll, pitch break-up tendencies, and low control authority at low speeds. The aircraft configuration was presented, as well as the main developments in the areas of aerodynamics, stability, and control.

Moreover, in the previous section, an overview of the existing FCS was presented. The ones implemented by Torelli et al. [2023] and Joosten et al. [2023] were mainly to improve the HQ and the research did not have as a main goal the optimization of the controller. Additionally, Völker et al. [2023] developed an altitude controller with a reinforcement learning approach. Although the reference command was satisfactorily followed, the response was slightly oscillatory.

Stougie et al. [2024], van Overeem et al. [2023], and Traas [2024] implemented controllers based on the nonlinear sensor-based and hybrid INDI approaches. Several advantages are pointed out in these methods, namely the guarantee of closed-loop (CL) stability and the fact that it naturally handles nonlinear systems, which aims to alleviate the complex process of gain scheduling. Therefore, it enables a modular approach to desired flying qualities over the flight envelope. Additionally, the sensor-based INDI seeks to address the robustness limitations of the nonincremental counterpart NDI by using direct sensor measurements of the controlled variable derivatives and, thus, circumventing the need for accurate airframe models. Therefore, it is more robust against regular perturbations arising from aerodynamic variations [Pollack and van Kampen, 2023]. However, Pollack and van Kampen [2023] analyzed the robustness properties via the open loop responses of sensor- and model-based linear dynamic inversion schemes with the same control law controller. It was demonstrated that the sensor based inversion schemes result in higher open loop gain at low frequencies but also in higher and often prohibitive crossover frequencies, which penalizes robustness at high frequencies due to insufficient roll-off [Pollack and van Kampen, 2023]. Therefore, a

known challenge for INDI-based control laws involves the high sensitivity to sensor measurement noise, time delays, and unmodeled HF dynamics [Sieberling et al., 2010]. In fact, this is corroborated by the results presented by Stougie et al. [2024], which showed that for angular rate sensors with time delays over 0.04 seconds, gain and phase margins were no longer met. It should also be noted that van Overeem et al. [2023] did not take into account time delays and sensor noise and, thus, the performance degradation cannot be pointed out in that research. Synchronization filters can, however, be applied to attenuate these issues.

Furthermore, contrary to the $\mathcal{H}_\infty$ methods, there are no guarantees of robustness, only of nominal performance in the design phase of dynamic inversion-based controllers [Papageorgiou and Hyde, 2001] [Papageorgiou and Polansky, 2009]. This is highlighted by the research of Traas [2024], where the aircraft becomes unstable sooner than desired for certain combinations of uncertainties, mirroring poor robust stability. Robustness analysis can be conducted after the controller is designed. Nonetheless, in case the requirements are not met, an iterative design is needed which might be time consuming. Additionally, while these inversion-based methods are the result of a time-domain design, robust controller techniques allow to naturally and systematically treat plant model uncertainty [Papageorgiou and Polansky, 2009]. A robust approach to (I)NDI can, nevertheless, set a significant improvement in this regard. This can be achieved via robust outer loop design based on e.g. μ-synthesis against uncertainty sets [Adams and Banda, 1993] [Reiner et al., 1996]. Another approach is to exploit robust synthesis frameworks to perform systematic, robust design of structured controllers [Pollack et al., 2024]. For such designs, this strategy allows the guarantee of important a-priori robustness properties. This does not only concern the outer loop, but the inversion strategy itself as well [Pollack et al., 2024].

Hence, it is verified that the results from Stougie et al. [2024] and, thus, from Traas [2024] could be improved, not only to tackle the drawbacks of INDI already mentioned but also to enhance the longitudinal response of the C*. In fact, it was verified that the C* presented a high overshoot and multiple oscillations, especially with the baseline sensors in the work of Stougie et al. [2024]. Therefore, implementing a C* controller for the Flying-V with a robust control technique is introduced as a research opportunity. Thus, in Section 2.2, the main methods that can be used will be described and their state of the art will be presented.

2.2. ROBUST CONTROL

Moreover, the current section will focus on the $\mathcal{H}_\infty$ robust control. Thus, in Section 2.2.1, the origins and formulation of the $\mathcal{H}_\infty$ problem are considered. Furthermore, in Section 2.2.2 the $\mathcal{H}_\infty$ Mixed Sensitivity design is introduced, followed by a comparison of this method with $\mathcal{H}_\infty$ Loop Shaping, in Section 2.2.3. In Section 2.2.4, μ-synthesis is presented as another powerful method for controller synthesis.

2.2.1. $\mathcal{H}_\infty$ CONTROL

Prior to the rise of robust control theory in the early 1980's, a significant focus on classical and optimal (modern) control theory was present. Nonetheless, the fundamental problem of these time-domain methods was that system uncertainty was not taken into consideration. Thus, the apparently "optimal" controllers were prone to poor performance, or even instability, in real scenarios. [Bates and Postlethwaite, 2002]

Therefore, robust control rose as a reaction to the flaws and loss of transparency of time-domain methods and to the shortcoming of LQG control when Zames [1981] formally proposed the concept of $\mathcal{H}_\infty$. Plant uncertainty was emphasized and the gain from disturbance inputs to error output signals in the controlled system could be specified. In the 1980's and 1990's, three solutions to the problem were found. It was proved in Doyle et al. [1988] that the $\mathcal{H}_\infty$ problem requires the solution of two Algebraic Ricatti Equations. The process to reach the previous milestone is discussed in Doyle [1996], where a solution to the problem that emerged in 1984 is also mentioned. Lastly, Gahinet and Apkarian [1994] also solved the problem by reducing it to a Linear Matrix Inequality (LMI). Nevertheless, there was a common shortcoming to the three solutions which was that the resulting controllers were all unstructured i.e. full-order. Moreover, computing a reduced fixed-order controller is of high complexity given that the objective is non-convex, non-smooth, and there are stability issues in the CL [Apkarian and Noll, 2017]. Nonetheless, Apkarian and Noll [2006a] solved the $\mathcal{H}_\infty$ problem again, using non-smooth optimization techniques, which allows the imposition of the controller structure. Additionally, extensions to the previous solution were created recently, namely on multi-model design, controller-plant optimization, multi-objective design, parametric robust control, and anti-windup. Furthermore, several methods emerged from the $\mathcal{H}_\infty$ control.

These involve, for instance, mixed $\mathcal{H}_2/\mathcal{H}_\infty$ control [Doyle et al., 1989], $\mathcal{H}_\infty$ Loop-Shaping (LS) [McFarlane and Glover, 1990] [McFarlane and Glover, 1992]. Additionally, early examples of Mixed Sensitivity (MS) control can be found, for instance, in Safonov et al. [1991].

The foundation of this method is the $\mathcal{H}_\infty$ norm, which corresponds to the peak value over frequency of the largest singular value of its frequency response. In fact, the minimization of the norm corresponds to minimizing the energy of the worst case output signal vector. Thus, it allows manipulation of open and closed loop transfer functions (TF) in order to achieve certain robustness and performance specifications. [Bates and Postlethwaite, 2002] [Skogestad and Postlethwaite, 2005]

2.2.2. $\mathcal{H}_\infty$ MIXED SENSITIVITY

$\mathcal{H}_\infty$ Mixed Sensitivity design consists of shaping certain closed loop transfer functions, which depend on the design specifications required. In fact, given that a control system has to satisfy several design objectives and not all of them can be met simultaneously, feedback design is a trade-off over frequency of conflicting objectives. However, it is also true that the frequency ranges over which the goals are important can be quite different, which simplifies the compromise. The singular values of those TF are shaped through the implementation of the weighting filters (WF). Some methods and recent literature in which these were applied are further discussed in this section. [Skogestad and Postlethwaite, 2005]

S/KS METHOD

To begin with, S/KS allows output disturbances attenuation, control effort reduction, and robustness to additive uncertainty. This method was applied in Huang et al. [2010] and potential problems were highlighted. On the one hand, the desired shape for all TF is not achieved. In this particular scenario, the TF SG gain was very high at low frequencies, which amplifies the effect of input disturbances on the output when the plant is poorly damped. This issue motivates the four-block method, which will also be discussed. On the other hand, this approach is prone to pole-zero cancellations and may affect the CL stability. The relation between the cancellations and the weighting functions was studied in Tsai et al. [1990]. In this paper, a particular construction for the weights is given that not only prevents the cancellations but also acts as a mechanism for (partial) pole placement. An alternative approach to S/KS was proposed by Kwakernaak [1993] and further researched by Cao and Hori [1997], which tackles the previous issue. This method consists of adding a rational matrix $V = D^{-1}M$ (assuming the plant representation $P = D^{-1}N$), where the roots of M can be assigned as the dominant poles of the CL system. Nonetheless, Huang et al. [2010] points out that the weighting function selection is a very time consuming task and that it also decreases the freedom of tuning. Recent literature includes Javed et al. [2021] where the S/KS method was applied and achieved both robust stability and performance in the presence of modeling inaccuracies and external disturbance.

S/T & S/KS METHODS

Moreover, the complementary sensitivity T also plays a fundamental role in the $\mathcal{H}_\infty$ MS framework, given that it allows robustness to multiplicative uncertainty and attenuation of measurement noise at the output. Therefore, the use of S/T or $S/KS/T$ is motivated. Recent literature where the latter method is applied include Zhang et al. [2021], where a quantum genetic algorithm was used to optimize the selection of the weight function matrices. In Pirat et al. [2020] the approach was applied to a nanosatellite and compared to the μ-synthesis approach via Monte Carlo simulations. A dual loop controller was implemented for a helicopter in Ji and Wu [2011], where the outer loop was designed with MS, while the internal loop was designed with $\mathcal{H}_\infty$ LS. Other relevant papers are Saripudin et al. [2019] and Zhao et al. [2019]. Additionally, for the S/T approach, in Oloomi and Shafai [2003] the selection of appropriate weighting functions is addressed.

FOUR-BLOCK METHOD

As previously mentioned, if the TF SG is ignored, the input disturbances are not constrained and, thus, these can have an amplifying effect on the system. Additionally, the TF also imposes a large controller gain at low frequencies, which provides the necessary integral action. Hence, the four-block method emerges as the solution by shaping the TF S, KS, SG, and KSG with the respective weighting functions. Moreover, Huang et al. [2010] points out the low complexity associated with the construction of the weighting filters as well as the fact that the principles to select these are well established. An example of a variant of the four-block method is present in Chapter 12 of Skogestad and Postlethwaite [2005], where a disturbance

rejection design was implemented and integrated with signal-based control. Signal-based $\mathcal{H}_\infty$ control focuses on the minimization of the energy in certain error signals given a set of exogenous input signals [Skogestad and Postlethwaite, 2005]. Recently literature on this method is, for instance, [Biertümpfel et al., 2024], where it was applied to a space launcher and mixed with a linear time varying synthesis approach. In Kim and Whang [2018] the four-block method was implemented in a highly unstable missile system. Additionally, in [Theis et al., 2016], the standard four-block formulation is extended to target specific dynamic modes and to add damping.

MODEL FOLLOWING

Lastly, it is important that the Flying-V complies with the HQ, as described in Anonymous [1997] and in Mitchell et al. [1994]. Thus, the model matching sensitivity M can be added so that the controller robustly meets performance requirements. One approach that can be followed is to add a second order target closed loop system after the reference. The difference between the output of the reference model and the output of the model is constrained by another weighting function. In Sève et al. [2014], an S/KS approach is integrated with a model matching problem and a similar approach was conducted in Sève et al. [2017], where an $M/S/KS/T$ approach was introduced. Both were performed as a first step to the $\mathcal{H}_\infty$ loop shaping design procedure.

2.2.3. $\mathcal{H}_\infty$ LOOP SHAPING VS. $\mathcal{H}_\infty$ MIXED SENSITIVITY

The $\mathcal{H}_\infty$ MS framework was discussed in detail. Nonetheless, there are other approaches for the synthesis of a controller, namely the $\mathcal{H}_\infty$ LS. Whereas the former shapes the closed-loop performance, the latter first shapes the open loop of the system to meet certain requirements and only afterwards the controller is designed.

Moreover, Bates and Postlethwaite [2002] points out several advantages of the LS over the MS. Firstly, no γ-iterations are needed, given that the robustness margin is imposed a priori by the designer in a single step. The controller matrices are, thus, synthesized to achieve and optimize that sub-optimal robustness specification. Additionally, robustness to NCF uncertainty can be achieved while in MS only additive and multiplicative uncertainty can be taken into account. Additionally, there are no pole-zero cancellations as opposed to the S/KS method in MS. Although in MS this can be avoided, complex weighting schemes would be necessary. Additionally, balanced robustness and performance properties at the plant input and output are provided and there is a clear management of conflicting specifications around crossover. [Bates and Postlethwaite, 2002]

Nevertheless, the $\mathcal{H}_\infty$ LS also offers some shortcomings. Generally, it is more difficult to obtain the optimal parameters for the shaped plant filters, especially in the case of Multi Input Multi Output (MIMO) systems. Shaping the open-loop is challenging due to the need of ensuring stability of the resulting closed-loop system [McFarlane and Glover, 1992]. This requires the consideration of the plant phase properties, whose stability requirements might limit the open loop shape [McFarlane and Glover, 1992]. Furthermore, "badly aligned" plants in terms of singular values need to be pre-conditioned. Moreover, if the MS technique is well mastered by the designer, equally good results can be achieved. In fact, in Huang et al. [2010] four different methods were applied: S/KS, four-block, LS, and a variation of S/KS. Firstly, in terms of performance, all the $\mathcal{H}_\infty$ methods fulfilled the objectives and no conclusive statement could be drawn with respect to the superiority or inferiority of a certain method. Secondly, in terms of implementation, the four-block approach of the MS was considered the most promising one, not only because of the low complexity of weighting filters construction but also because the effects of pole-zero cancellations are easily manipulated and provides the most direct and explicit access to enhance closed loop performance. Additionally, LS design also does not offer detailed parameters for adjustment and has no direct control over KS, SG, and KSG. This procedure specifies, instead, closed loop objectives in terms of requirements on the open loop singular values of the compensated system [McFarlane and Glover, 1992]. However, while these are only restricted to frequencies of low and high loop gain, the MS approach considers all frequencies [McFarlane and Glover, 1992].

2.2.4. μ-SYNTHESIS

The structured singular value, μ, is a powerful tool for the analysis of robustness performance with a certain controller. Nevertheless, μ-synthesis can also be used for controller synthesis. For example, the DK-iteration is a sub-optimal method that combines $\mathcal{H}_\infty$ and μ-analysis. However, a fundamental problem with this approach is that joint convexity (for both K-step and D-step) is not guaranteed [Skogestad and Postlethwaite, 2005]. Thus, the iterations may converge to a local optimum. Additionally, one should be careful about combining synthesis and analysis into one single step. Furthermore, in Bennani and Looye [1998], the robust performance indicator μ was optimized for a FCS for a civil aircraft via DK-iteration. The μ-synthesis approach was also combined with a feedback linearization-based controller in Hamza et al. [2022] and applied to a quadrotor UAV.

2.3. C* Longitudinal Control Law

In the 1960's, the C^* parameter was first introduced by Boeing as a normalized linear sum of pitch rate and normal acceleration [Malcom and Tobie, 1965] [Field, 1993]. Even though its validity was disputed by Neal and Smith [1970] on the ground of not being able to control the two variables independently, this type of control law is now the standard in the commercial aviation industry, with both Boeing and Airbus flying variations of it [Favre, 1994].

Furthermore, a C^* controller is founded on the idea that the main control cues at low and high velocities are, respectively, pitch rate and load factor (i.e. n_z) dominated [Niedermeier and Lambregts, 2012] [Field, 1993]. Moreover, a large number of literature exist where this topic is applied, namely Lombaerts et al. [2017] where an adaptive safe FEP algorithm is implemented with a C^* longitudinal control law in the outer loop combined with an NDI approach in the inner loop. Also, in Vigano et al. [2017] it was also applied to the "airplane mode" of a tiltrotor in combination with a flight path angle hold for the longitudinal control. Moreover, Marcos [2017] designed a C^* control law with a classical (root locus) and an advanced (structured $\mathcal{H}_\infty$) approach for a large commercial aircraft. Additionally, in Field [1993], a simple proportional C^* controller was applied to a Boeing 747-100 in landing configuration and it was assessed against the C^* criterion. Moreover, Niedermeier and Lambregts [2012] and Nieto-Wire and Sobel [2011] both feedback the C^* parameter as well as the pitch rate signal for a SAS. The second author also opts to use the AoA measurement signal, where a proportional gain is applied. Furthermore, other C^*-like approaches exist in literature. For instance, Guilhem and Jean-Marc [2013] and Delannoy and Oudin [2013] feedback the pitch rate and the load factor to match the commanded signal of the n_z parameter.

Nonetheless, a drawback of this configuration is the loss of airspeed stability, which can be tackled by the variant of the algorithm: C^*U. This method consists of adding an airspeed feedback loop to the controller integrator, artificially restoring the stability and, thus, causes the aircraft to return to the commanded trim speed [Niedermeier and Lambregts, 2012]. In fact, this C^* version is applied both to the B777 and B787 [Field, 1993] [Arent and Falatko, 1992].

2.4. Gain Scheduling and Multi-Modeling

Furthermore, as previously stated, one of the key benefits of INDI is the avoidance of the complex process of gain scheduling (GS). However, so that the linear $\mathcal{H}_\infty$ synthesis is able to control nonlinear systems, this process needs to be applied. Although there are more advanced methods in control theory, the conventional, simple, and intuitive GS is still a widespread technique [Lhachemi et al., 2016].

To begin with, a flight envelope is defined using scheduling parameters and on each of these equilibria points, the system is linearized, creating a family of Linear Time-Invariant (LTI) systems, where, for each, a controller is also synthesized. A posteriori, the gains are interpolated with respect to the scheduled parameters creating a nonlinear representation. The gains are usually computed in real time, based on the measurements of the scheduling variables. Lastly, the controller should be assessed both in the linear and nonlinear domains. Nevertheless, global stability and performance guarantees are not offered a priori, only local stability is guaranteed. [Rugh, 1990] [Shamma et al., 1988] [Simões and Cavalcanti, 2023]

Moreover, GS has its drawbacks, namely hidden coupling terms [Rugh and Shamma, 2000] [Lawrence and Rugh, 1995], inability to capture the time-varying properties of the nonlinear system in the linearization process [Wu, 1974], and trim point uncertainty introduced by Jacobian linearization. Additionally, Jacobian linearization can be avoided by a quasi-Linear Parameter-Varying (LPV) scheduling approach, in which the plant dynamics are rewritten to disguise nonlinearities as time-varying (scheduling) parameters [Rugh and Shamma, 2000].

State of the art papers on the subject include Theodoulis and Proff [2021], where the gain-scheduled controller was conducted following two methods: a posteriori (point by point) and a priori (for all design points simultaneously) and Theodoulis et al. [2020] where a gain-scheduled 4-loop highly agile missile autopilot was designed. A new synthesis technique was introduced in Simões and Cavalcanti [2023], where a LPV/Linear Fractional Transformation (LFT) gain-scheduled controller of fixed structure was implemented.

Another method of implementing linear controllers in a nonlinear setting is the multi-model approach. A controller is usually designed for a single plant. Nonetheless, with this approach, a single controller is synthesized for several plants simultaneously, allowing the designer to consider uncertain dynamical systems and systems with changing parameters. This approach is followed in Lhachemi et al. [2014], where the gains are self-scheduled, and in Goz and Theodoulis [2025].

2.5. CONCLUSION AND DISCUSSION

The current chapter allowed an in-depth analysis of the state-of-the-art enhancements in the Flying-V as well as in the $\mathcal{H}_\infty$ robust control techniques. Thus, the important information is discussed in order to identify the research gap, which is presented in Chapter 3.

To begin with, it was highlighted that the advantages of the Flying-V come at the expense of stability issues, unstable dutch roll, pitch break-up tendencies, and low control authority at low speeds. Hence, besides the redesign of some structures in the configuration, it is necessary to mature the flight control systems so that the Flying-V can make it to the civil aviation market.

The main FCS that were implemented consist of the nonlinear control approach INDI and these showed interesting results. The complexities and nonlinearities of the system are effectively handled with this method and, when compared to classical techniques, it alleviates the time-consuming process of gain scheduling. Nevertheless, INDI is highly sensitive to sensor measurement noise, time delays, and unmodeled HF dynamics, which is a known challenge for INDI-based control laws. Additionally, this sensor-based method is the result of a time-domain design and there are no guarantees of robustness during this design process. As discussed, a robust approach to I(NDI) can set a significant improvement in this regard. Taking everything into consideration, although this control approach has several advantages, there are issues associated with it, especially in terms of robustness, that can be ultimately solved through the design of the FCS based on $\mathcal{H}_\infty$ robust control techniques.

In fact, robust control emerged as a reaction to the flaws and loss of transparency of time domain methods. Moreover, it allows the treatment of system uncertainties naturally and systematically during the design process and it is a powerful method to balance between performance and robustness, given the possibility to shape closed loop and open loop transfer functions. Thus, some of the $\mathcal{H}_\infty$ methods were analyzed. The $\mathcal{H}_\infty$ Mixed Sensitivity is widely applied, allows the treatment of additive and multiplicative uncertainty, and shapes the closed loop transfer functions given the required design objectives. $\mathcal{H}_\infty$ Loop Shaping first shapes the open loop and it is also an effective method for controller synthesis, which takes into account NCF uncertainty. It clearly manages conflicts around crossover frequency and there are no pole-zero cancellations, as opposed to the S/KS method in the MS approach. Thus, although it has some benefits over MS, some of the drawbacks include the complexity of obtaining optimal parameters in MIMO systems, some plants need to be pre-conditioned and there is no direct control over certain requirements. μ-synthesis was also discussed. Nonetheless, although it may result in a less conservative controller, combining the synthesis and analysis into one single step needs caution. Additionally, it is important to highlight that these methods can use classical control tools, such as bode plots, root locus, and Nyquist plots, which provide a higher level of design transparency and intuition.

Furthermore, the C^* longitudinal control law was discussed given that this configuration was also implemented with the INDI approach in the Flying-V. Moreover, it was also concluded that loss of airspeed stability is a drawback of the configuration. Hence, the variation C^*U arises to tackle the issue by adding an airspeed feedback loop that allows the aircraft to return to the trim speed in the long term response.

Lastly, the gain-scheduling problem is addressed, highlighting the working principle as well as the main drawbacks. Alternative approaches to the conventional one are presented, namely LPV and multi-model.

Taking everything into consideration, the research gap, objectives, and questions can now be formulated, which will be presented in the following chapter. A gap in the research exists when it comes to robust control techniques applied to the Flying-V. Moreover, the lack of robustness to model uncertainties is also an aspect that needs further consideration.

3

RESEARCH PROPOSAL

This research proposal aims to identify and highlight the knowledge gaps derived from the literature review, in Section 3.1, and bridge them to a well-structured, coherent research timeline (see Section 3.2.1). The outlined research objectives in Section 3.2 are designed to be both achievable and scientifically significant, aligning with the goals established within the Flying-V project framework.

3.1. RESEARCH GAP & RELEVANCE

In the previous chapter, a detailed literature review was conducted, which allowed the identification of potential problems that should be addressed as well as research opportunities.

To begin with, as it was discussed in Chapter 2, three main categories of FCS approaches were implemented in the Flying-V, namely classical PIDs, a reinforcement learning method, and nonlinear approaches. Its inherent issues were highlighted. The PIDs were only optimized for stability improvement, while the second method was not tested against HQ requirements. Lastly, the sensor-based INDI control laws are highly sensitive to sensor measurement noise, time delays, and unmodeled HF dynamics. Additionally, these are the result of a time-domain design, with no guarantees of robustness during this process, although a robust approach to I(NDI) can set a significant improvement in this regard. This lack of robustness guarantees a priori is corroborated by the instability that arises earlier than expected in systems employing these control methods, given the applied uncertainties [Traas, 2024]. Thus, an identified research gap arises from the absence of $\mathcal{H}_\infty$ robust controllers designed for the aircraft, which would address issues related to sensor measurements time delays, take into consideration performance and robustness specifications, and would treat uncertainties in the design process. Furthermore, discretization effects were considered in the works of Stougie et al. [2024] and Traas [2024], which, in the former, caused problems in terms of stability margins specifications. Thus, it is important to also consider this aspect and make sure that, with the robust controller such a result is not obtained. Furthermore, the longitudinal control law C^* was developed in both studies. Thus, to follow their work and given that this parameter is applied in commercial aviation controllers, it is decided to also control this signal.

Moreover, from the preceding chapter, several robust controller methods were described. From the information presented, it is decided to implement the controller in the Mixed Sensitivity framework, more specifically, with the signal-based MS $\mathcal{H}_\infty$ approach. This more general method is appealing for systems of higher complexity as it shifts the focus towards the size of the signals and allows specific signal paths to be targeted for more detailed control. In fact, equally good results can be achieved with Mixed Sensitivity and with Loop Shaping. However, MS offers a more intuitive design given the explicit access to closed loop TF and it avoids the complexity of obtaining optimal parameters for the shaped plant filters. Additionally, pole-zero cancellations, which are one of the major drawbacks of the MS design, can be easily manipulated with other methods besides the S/KS.

From what was introduced, it was verified that an Automatic Landing System (ALS) was never implemented and, therefore, also posed as valuable research to be conducted. Nonetheless, recent breakthroughs occurred in the aerodynamic knowledge on the Flying-V, regarding pitch break-up tendencies for low angles of attack. Thus, this factor in combination with the low control authority for low speed, was identified as a main issue that needs to be tackled by redesigning surfaces or by adding some structures to the aircraft

configuration. Some iterations are still needed in the Flying-V design, which will primarily affect the low speed phase. Therefore, at the current stage, the constructed ALS system would probably not have enough validity.

Additionally, it should be highlighted that, at the beginning of the project, trimming and linearization problems existed in the simulation model provided, as well as some errors in the equations of motion of the Flying-V model, which yielded unexpected and undesirable behavior. Some problems were later addressed by Traas [2024]. Nonetheless, given the poor validity of the model at the beginning of the research project, especially for designs highly dependent on linear approximations, the need to redesign the model was pressing. Thus, an ameliorated version of the simulation model should also be conducted in the current research.

Lastly, a new version of the aerodynamic data became available during the development of the current research, which is used in this study. Thus, although interesting, it is not possible to directly compare results with the ones obtained from previous research, as none used this data.

These identified knowledge gaps form the basis for the research objectives and questions, which are outlined in Section 3.2. The detailed research plan, designed to systematically address these gaps, is provided in Section 3.2.1.

3.2. Research Formulation

From the identified research gaps, the outlined research objective is defined. To achieve this objective, the research is organized around three central questions, each addressing a main part of the FCS development, namely the Flying-V model simulation development, the controller synthesis, and analysis.

> **The research objective is to increase the maturity of the FCS of the Flying-V by implementing a C^* controller within the Signal-Based Mixed Sensitivity $\mathcal{H}_\infty$ framework, while guaranteeing robustness stability and performance against uncertainty, adequate performance in the presence of disturbances and measurement noise, and compliance with Level 1 HQ.**

Research Question 1

How can the challenges and limitations of Flying-V's current nonlinear model be addressed, thereby facilitating the development of a robust and effective FCS design?

1.1. What are the main challenges of the previous modeling approach, and how can these limitations be improved?

1.2. How does the trimming and linearization of the Flying-V model facilitate the development of robust control systems, and what are the key considerations in this process?

1.3. What main aspects should be considered to ensure a successful implementation when translating the nonlinear model insights into a linear system?

Research Question 2

How can the maturity of the Flying-V FCS be enhanced through the implementation of a signal-based $\mathcal{H}_\infty$ Mixed Sensitivity C^* controller?

2.1. What are the critical design alternatives for the longitudinal FCS, and how do these affect the systems' robustness and performance?

2.2. How are the design requirements translated into the constraints imposed on the system?

2.3. To what extent does the structure of the controller influence the robustness of the system and how can it be determined?

2.4. To what extent is the system influenced by the discretization effects of the flight computer and how can this potential challenge be addressed?

Research Question 3

To what extent does the signal-based Mixed Sensitivity $\mathcal{H}_\infty$ C* controller meet the specified performance and robustness requirements across a range of flight conditions?

3.1. To what extent does the linear control system comply with the requirements imposed a priori?

3.2. How does the linear control system design behave in the nonlinear 6 DoF model?

3.3. How can the robustness and performance specifications be guaranteed across the flight envelope and to what extent are these met with the proposed design?

3.2.1. RESEARCH PLAN

The research plan is divided into four different phases. The first encompasses the elaboration of the literature study and definition of research goals and objectives. The second phase focuses on the redesign of the Flying-V model and on the synthesis and analysis of preliminary controllers with $\mathcal{H}_\infty$ MS. The following research phase includes the exploration of alternative designs for the FCS configuration, the transition to digital design, and the multi-modeling approach. The research culminates in the Dissemination, in which the report is submitted and the defense is prepared.

The detailed Gantt Chart of the project is presented in Appendix A.

4

THEORETICAL BACKGROUND

The current theoretical background chapter sets the foundational framework for understanding the key concepts and theories underpinning this research. Thus, segments of the robust framework are discussed in Section 4.1, followed by a discussion on stability margins, in Section 4.2. Moreover, the formulation of the C* control law is detailed in Section 4.3 and lastly, Section 4.4 focuses on the handling qualities.

4.1. ROBUST CONTROL

Robust control plays a pivotal role in ensuring system stability and performance in the presence of uncertainties and disturbances. Therefore, the following terms should be highlighted [Skogestad and Postlethwaite, 2005]:

- **Nominal stability**: The system is stable with no model uncertainty.

- **Nominal performance**: The system satisfies the performance specifications with no model uncertainty.

- **Robust stability**: The system is stable for all perturbed plants about the nominal model up to the worst-case model uncertainty.

- **Robust performance**: The system satisfies the performance specifications for all perturbed plants about the nominal model up to the worst-case model uncertainty.

The robust control framework is understood over the generalized interconnection structure presented in Figure 4.1, which will be intrinsically discussed. Hence, the current section provides a comprehensive summary of the most fundamental aspects, namely regarding singular values in Section 4.1.1, system norms in Section 4.1.2, the formal statement of the $\mathcal{H}_\infty$ control problem in Section 4.1.3, and uncertainty
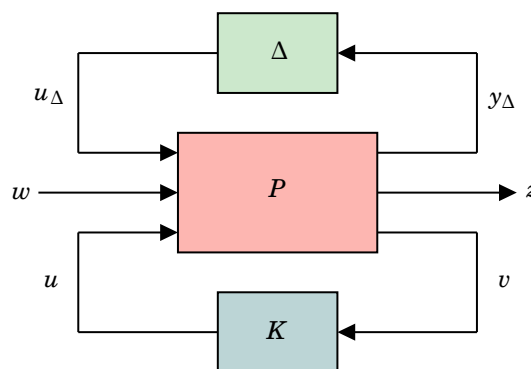
Figure 4.1: General control configuration for controller synthesis.

representations in Section 4.1.4. Additionally, the frequency design specifications and trade-offs are explored in Section 4.1.5 and the $\mathcal{H}_\infty$ MS and signal-based $\mathcal{H}_\infty$ MS frameworks are discussed in Section 4.1.6 and in Section 4.1.7, respectively. Lastly, model order reduction techniques are presented in Section 4.1.8, whereas in Section 4.1.9 a discussion on controller structures and optimizations tools is conducted.

4.1.1. SINGULAR VALUES

Singular Values (SV) are used to generalize the gain from Single Input Single Output (SISO) systems to MIMO systems. In fact, the eigenvalues magnitude of a matrix does not accurately indicate its gain, since these only measure the gain for the special case where the vector inputs and outputs are in the same direction. The SV decomposition is, thus, used to examine the effect of the inputs in all directions of the outputs. [Bates and Postlethwaite, 2002]

For a given G matrix, the SV are computed as the positive square roots of the eigenvalues of $G^H G$, where G^H is the complex conjugate transpose of G, i.e.

$$\sigma_i(G) = \sqrt{\lambda_i(G^H G)} \tag{4.1}$$

Therefore, the singular value decomposition of the matrix G is described as:

$$G = U \Sigma V^H, \tag{4.2}$$

where U and V are matrices whose columns are the output singular vectors of u_i and the input singular vectors of v_i, respectively. Σ is a diagonal matrix, with the SV distributed along it. [Bates and Postlethwaite, 2002]

4.1.2. SYSTEM NORMS

$\|\cdot\|_A$ SYSTEM NORM

Several norms can be used to measure the size of multivariate systems. The $\|\cdot\|_A$ systems norm is one of the alternatives. Assuming that $z(t) = g(t)w(t)$, where $g(t)$ is the impulse response matrix of a stable LTI system, then

$$\left\| g(t) \right\|_A = \sup_{w \neq 0} \frac{\|z(t)\|_\infty}{\|w(t)\|_\infty} \tag{4.3}$$

Nonetheless, it is used in $\mathcal{L}_1$ control [Dahleh and Díaz-Bobillo, 1995] which is a purely time domain theory. Additionally, the mathematical tools that are used to compute these optimal controllers are not as developed and user-friendly than those required for the $\mathcal{H}_2$ and $\mathcal{H}_\infty$ theories [Bates and Postlethwaite, 2002].

$\mathcal{H}_2$ SYSTEM NORM

Alternatively, the $\mathcal{H}_2$ norm is usually used in stochastic optimal control problems. For a stable and strictly proper system, $G(s)$, it can be computed as:

$$\left\| G(s) \right\|_2 = \sqrt{\frac{1}{2\pi} \int_{-\infty}^{+\infty} \mathrm{trace}\Big(G(j\omega)^H G(j\omega)\Big) d\omega}, \tag{4.4}$$

Nonetheless, this system norm cannot be interpreted as an induced norm, which poses as a disadvantage in the setting of robust stability using the Small Gain Theorem (SGT) [Bates and Postlethwaite, 2002].

$\mathcal{H}_\infty$ SYSTEM NORM

For a stable multivariate LTI system, $G(s)$, the $\mathcal{H}_\infty$ norm corresponds to the peak value over frequency of the largest singular value of its frequency response. Therefore, given that the $\mathcal{H}_\infty$ system norm is induced by the $\mathcal{L}_2$ signal norm, it can be defined as in Equation (4.5).

$$\left\| G(s) \right\|_\infty = \max_w \bar{\sigma}\Big(G(jw)\Big) = \sup_{w \neq 0} \frac{\left\| z(t) \right\|_2}{\left\| w(t) \right\|_2}, \tag{4.5}$$

where w and z are the input and output of the system, respectively. From this expression, it is possible to conclude that the minimization of the norm corresponds to minimizing the energy of the worst case output signal vector. [Bates and Postlethwaite, 2002]

Moreover, some advantages of the $\mathcal{H}_\infty$ norm include that it is a natural extension of many of the concepts from classical control methods to multivariate systems. For signal and system uncertainty, it is an intuitive formulation. Additionally, it also allows the development of powerful tools for stability and performance robustness analysis. [Bates and Postlethwaite, 2002]

4.1.3. $\mathcal{H}_\infty$ OPTIMAL CONTROL FORMULATION

The $\mathcal{H}_\infty$ optimization problem has the main goal of minimizing the effect of the exogenous inputs, w, on the outputs, z [Skogestad and Postlethwaite, 2005]. Given the real rational plant $P(s)$ and the controller space $\mathcal{K}$ of real rational transfer functions $K(s)$, the optimal solution $K^*(s) \in \mathcal{K}$ is the solution of the following optimization:

$$
\begin{aligned}
\text{minimize} \quad & \|T_{w \to z}(P,K)\|_\infty \\
\text{subject to} \quad & K \text{ stabilizes } P \text{ internally} \\
& K \in \mathcal{K}
\end{aligned}
\tag{4.6}
$$

The transfer function $T_{w \to z}(P,K)$ can be represented as the lower Linear LFT of P and K (i.e. $F_l(P,K)$). Assuming the uncertainty block to be null, the transfer function of the generalized plant $P(s)$ relates the input vectors w and u to the output vectors z and y as it is shown in Figure 4.2 and in Equation (4.7).

$$
\begin{bmatrix} z \\ v \end{bmatrix} = \begin{bmatrix} P_{11} & P_{12} \\ P_{21} & P_{22} \end{bmatrix} \begin{bmatrix} w \\ u \end{bmatrix}
\tag{4.7}
$$

The state space representation of the plant $P(s)$ has the form:

$$
P : \begin{cases} \dot{x} = Ax + B_1 w + B_2 u \\ z = C_1 x + D_{11} w + D_{12} u \\ y = C_2 x + D_{21} w + D_{22} u \end{cases}
\qquad
P(s) : \left[\begin{array}{c|cc} A & B_1 & B_2 \\ \hline C_1 & D_{11} & D_{12} \\ C_2 & D_{21} & D_{22} \end{array} \right]
\tag{4.8}
$$

where $x \in \mathbb{R}^{n_x}$ is the state, $u \in \mathbb{R}^{n_u}$ the control, $y \in \mathbb{R}^{n_y}$ the measured output, $w \in \mathbb{R}^{n_w}$ the exogenous input, and $z \in \mathbb{R}^{n_z}$ the regulated output.

As previously discussed in Section 2.2.1, the $\mathcal{H}_\infty$ problem is computed through the solution of two Algebraic Riccati Equations [Doyle et al., 1988] or through LMIs [Gahinet and Apkarian, 1994]. However, these convex optimization solutions are all obtained within the space $\mathcal{K}_{full} \in \mathbb{R}^N$ of full-order controllers, where $N \triangleq n_x^2 + n_x(n_y + n_u) + n_y n_u$.

Additionally, in industry applications, low order controllers are preferred due to the transparency and clear functionality, reduced hardware and software requirements, and cheaper, smaller, and lighter implementations [Bates and Postlethwaite, 2002]. To achieve that, three approaches can be followed. These consist of reducing the controller after its synthesis, reducing the order of the plant prior to the controller design, or directly designing a controller with a certain dimension and complexity. Thus, model reduction techniques and structured and unstructured controllers will be further discussed in Section 4.1.8 and in Section 4.1.9, respectively.

Furthermore, obtaining the sub-optimal problem is usually sufficient and it is beneficial in terms of computation and theoretical complexity. Thus, assuming γ_{min} as the minimum value of $\|F_l(P,K)\|_\infty$ over all stabilizing controllers K, the sub-optimal control problem is: given a $\gamma > \gamma_{min}$, find all stabilizing controllers K such that Equation (4.9) is verified. It is clear that iteratively reducing the value of γ an optimal solution is approached.

$$
\|F_l(P,K)\|_\infty < \gamma
\tag{4.9}
$$
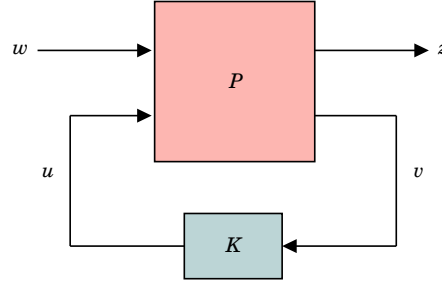
Figure 4.2: General configuration for the $\mathcal{H}_\infty$ controller design without uncertainty.

4.1.4. Uncertainty Representations

Realistically, the bare airframe deviates from the computed nominal behavior due to several factors, which yields in uncertainty in the plant model. Thus, the synthesis process entails finding a controller K which minimizes the effect w on z, which is limited by several factors. These include the unavailability of some variables in the measurements, the fact that the plant is not exactly known and the possibility of w containing uncertain disturbance signals. [Skogestad and Postlethwaite, 2005]

Moreover, the general configuration for the $\mathcal{H}_\infty$ controller design presented in Figure 4.2 can be reformulated in $N - \Delta$ and $M - \Delta$ structures, as represented in Figure 4.3 and in Figure 4.4, respectively. One the one hand, $N - \Delta$ is used for robust performance analysis, where the block Δ represents the system uncertainty and N corresponds to the known part of the system (i.e. plant and controller). The uncertain closed-loop transfer function from w to z ($z = F(\Delta)w$) is related to N and Δ by the upper LFT [Skogestad and Postlethwaite, 2005]:

$$F = F_u(N, \Delta) = N_{22} + N_{21}\Delta(I - N_{11})^{-1}N_{12} \tag{4.10}$$

While nominal performance is ensured by $\bar{\sigma}(N_{22}(j\omega)) < 1, \forall \omega$, the robust performance requirement is that [Bates and Postlethwaite, 2002]:

$$\bar{\sigma}\left(F_u(N, \Delta)\right) = \bar{\sigma}\left(N_{22} + N_{21}\Delta(I - N_{11})^{-1}N_{12}\right) < 1, \forall \omega \tag{4.11}$$

On the other hand, the $M - \Delta$ structure is constructed for robust stability analysis. Here, $M = N_{11}$ is the transfer function from the output to the input of perturbations. Hence, assuming that the nominal closed-loop in Figure 4.4 is asymptotically stable and that Δ is a complex unstructured uncertainty block, the SGT states that the closed loop system is stable if and only if [Bates and Postlethwaite, 2002]:

$$\bar{\sigma}(\Delta(j\omega)) < \frac{1}{\bar{\sigma}(M(j\omega))}, \forall \omega \tag{4.12}$$

Thus, Equation (4.12) sets a robust stability measure for a closed loop system that is subject to unstructured uncertainty in terms of the maximum SV of the matrix M and, consequently, N_{11}.

Moreover, it is important to differentiate two main representations of uncertainty. These entail unstructured and structured uncertainty and will be further detailed.
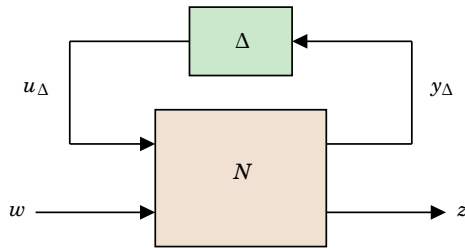
Figure 4.3: N-Δ structure for robust performance analysis.
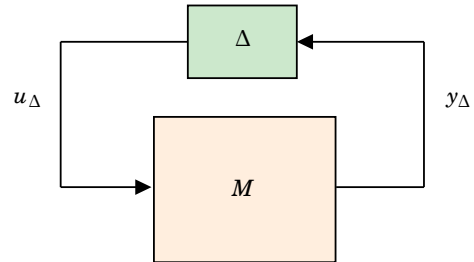
Figure 4.4: M-Δ structure for robust stability analysis.

Unstructured Uncertainty

Unstructured uncertainty assumes unknown yet bounded uncertainty models. Neglected and unmodeled dynamics are usually modeled with this type of uncertainty, which may add additional state variables. These are particularly present at HF where the fidelity of the airframe and actuator models diminishes. Models used in flight control typically match the aircraft behavior below 10 to 20 rad/s [Honeywell Technology Center, Lockheed Martin Skunk Works and Lockheed Martin Tactical Aircraft Systems, 1996]. Key sources of this non-parametric uncertainty include the effects of airframe flexibility and the inertial nature of aerodynamic flows, as well as high-frequency uncertainties related to actuation systems. Hence, this representation is usually used to get simpler descriptions. For an unstructured uncertain block $\Delta(s)$ that satisfies $\|\Delta(s)\|_\infty \leq 1$, the uncertain model $G_P(s)$ can be modeled as [Skogestad and Postlethwaite, 2005]:

- Additive uncertainty: $G_P = G_0 + w_A \Delta_A$

- Multiplicative input uncertainty: $G_P = G_0(I + w_I \Delta_I)$

- Multiplicative output uncertainty: $G_P = (I + w_O \Delta_O)G_0$

- Inverse additive uncertainty: $G_P = G_0(I - w_{iA} \Delta_{iA})^{-1}$

- Inverse multiplicative input uncertainty: $G_P = G_0(I - w_{iI} \Delta_{iI})^{-1}$

- Inverse multiplicative output uncertainty: $G_P = (I - w_{iO} \Delta_{iO})^{-1} G_0$

Moreover, via the SGT, the necessary and sufficient condition for robust stability can be obtained as $\|W_1 M_0 W_2\|_\infty < 1$ [Bates and Postlethwaite, 2002]. These six formulations are intimately related to closed loop transfer functions of the Go6, as described below [Skogestad and Postlethwaite, 2005]:

- Additive uncertainty: $M_0 = K(I + GK)^{-1} = KS_O$

- Multiplicative input uncertainty: $M_0 = K(I + GK)^{-1}G = T_I$

- Multiplicative output uncertainty: $M_0 = GK(I + GK)^{-1} = T_O$

- Inverse additive uncertainty: $M_0 = (I + GK)^{-1}G = S_O G$

- Inverse multiplicative input uncertainty: $M_0 = (I + KG)^{-1} = S_I$

- Inverse multiplicative output uncertainty: $M_0 = (I + GK)^{-1} = S_O$

Hence, by optimizing the controller such that $\|M_0(s)\|_\infty$ is small, robust stability is guaranteed for unstructured uncertainty.

Structured Uncertainty

On the contrary, structured uncertainty is characterized and quantified using mathematical models. Frequently, uncertainties are related to specific parameters such as mass and inertia, as well as aerodynamic stability coefficients and measurement device imperfections that can further influence system performance. These are usually referred to as parametric uncertainties. It is assumed that the structure (order) of the model is known and only some of the parameters are unknown. These uncertainties may arise from deliberately neglecting known variations within the model, which, while known, complicate the design of control laws by increasing their complexity. [Skogestad and Postlethwaite, 2005] [Pollack, 2024]

Parametric uncertainty is quantified by considering that each uncertain parameter is within the region $[\alpha_{min}, \alpha_{max}]$. Therefore, the parameter sets are of the form [Skogestad and Postlethwaite, 2005]:

$$\alpha_p = \bar{\alpha}(a + r_\alpha \Delta), \tag{4.13}$$

where $\bar{\alpha}$ represents value of the parameter mean, $r_\alpha = (\alpha_{max} - \alpha_{min})/(\alpha_{max} + \alpha_{min})$ is the relative uncertainty in the parameter, and Δ is a real scalar that verifies $|\Delta| \leq 1$.

STRUCTURED SINGULAR VALUE ROBUSTNESS MEASURE μ

In case the uncertainty affecting the system is known and can be translated into a matrix Δ with a diagonal or block diagonal structure, i.e.

$$\Delta(j\omega) = \text{diag}\Big(\Delta_1(j\omega), ..., \Delta_n(j\omega)\Big), \bar{\sigma}(\Delta_i(j\omega)) \leq l, \forall \omega, \tag{4.14}$$

the structured singular value μ can be used to decrease the level of conservationism. To compute the maximum value of k for which the closed loop system remain stable, the SGT could also be applied. Nonetheless, since the structure is not take into consideration, the robustness measure will be pessimistic [Bates and Postlethwaite, 2002]. Hence, Doyle et al. [1982] introduced the non-conservative solution:

$$\mu(N) \triangleq \frac{1}{min\Big(k \text{ subject to } \det(I - kN_{11}\Delta = 0)\Big)} \tag{4.15}$$

It should be noted that lower μ values are desired since large μ values translate into the fact that smaller perturbations makes $I - N\Delta$ singular [Skogestad and Postlethwaite, 2005].

4.1.5. FREQUENCY DOMAIN DESIGN SPECIFICATIONS AND TRADE-OFFS

The configuration presented in Figure 4.2 was extended, yielding in the representation of Figure 4.5. The input and output vectors, w and z, respectively, were therefore also augmented. The inputs (generalized disturbances) consist of the reference signal, r, the input and output disturbances, d_i and d_o, and the measurement noise n. Moreover, the outputs (performance signals) consist of the plant output, y, the input of the actuators, which can also be referred to as the plant input, u_p, the controller output, u, and the tracking error ($e = r - y$).
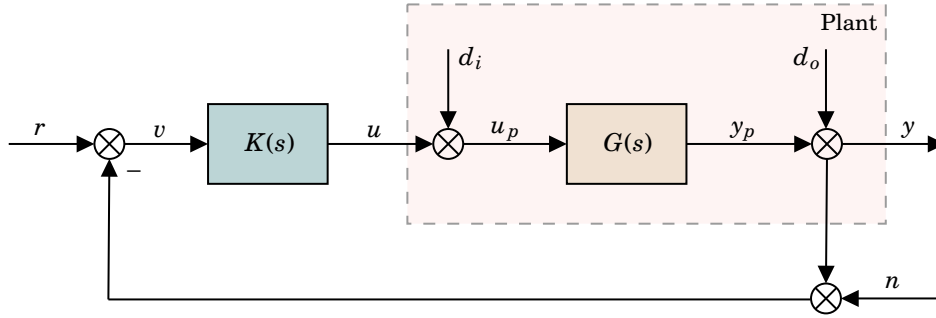
Figure 4.5: General feedback configuration of a control system.

Besides closed loop nominal stability, other requirements are also usually imposed, namely disturbance rejection, reference tracking, noise attenuation, and control signal reduction. These closed loop nominal performance requirements can be fulfilled by taking into consideration the properties of the "Gang of Six" (Go6), namely the sensitivity functions in the input and output, S_i and S_o, the complementary sensitivity functions in the input and output, T_i and T_o, as well as S_oG and KS_o. In fact, these are the TFs that describe the relationships from the disturbance signals to the performance signals, as it is described in Equation (4.16).

$$\begin{bmatrix} y \\ u_p \\ u \\ e \end{bmatrix} = \begin{bmatrix} S_oG & S_o & -T_o & T_o \\ S_i & -KS_o & -KS_o & KS_o \\ -T_i & -KS_o & -KS_o & KS_o \\ -S_oG & -S_o & T_o & S_o \end{bmatrix} \begin{bmatrix} d_i \\ d_o \\ n \\ r \end{bmatrix} \tag{4.16}$$

Moreover, the necessary and sufficient condition for robust stability can be obtained, via the SGT as $\|W_1M_0W_2\|_\infty < 1$, where, for each type of unstructured uncertainty, M_0 corresponds to one of the terms of the Go6 [Bates and Postlethwaite, 2002], as explained in Section 4.1.4. Hence, by imposing low gain on the Go6 TFs, both nominal performance and robust stability are improved. However, this is not possible to be done simultaneously across all frequency ranges. Thus, given that a control system has to satisfy several design objectives, feedback design is a trade-off over frequency of conflicting objectives. Nonetheless, it is

also true that the frequency ranges over which the goals are important can be quite different, allowing for an easier practical approach.

On the one hand, at Low Frequencies (LF), it is desired to reject disturbances, have a satisfactory reference tracking, and reduce control signal effort. For the first two goals, the sensitivity functions should be small in this frequency range, which translates necessarily into large gains in the open loop, $L_i = KG, L_o = GK$, given that $S_i = (I + L_i)^{-1}$ and $S_o = (I + L_o)^{-1}$. For disturbance rejection, the TFs SoG and KS_o are also crucial. Assuming K and G invertible:

$$\bar{\sigma}(S_o G) \approx \frac{1}{\underline{\sigma}(K)} \qquad \bar{\sigma}(KS_o) \approx \frac{1}{\underline{\sigma}(G)} \qquad (4.17)$$

Thus, in order to reject input disturbances, large control gains are a must. Nonetheless, although $\bar{\sigma}(KS_o) << 1$ would be desired, it is solely dependent on having a large plant gain. Furthermore, for control signal attenuation, T_i and KS_o are relevant. Nonetheless, $\bar{\sigma}(T_i) \approx 1$. Therefore, to avoid control saturation, sufficient plant (control) authority is needed ($\bar{\sigma}(G) >> 1$). All in all, at LF control saturation is independent to the control engineer and if saturation occurs, plant redesign should be followed. For controller authority both large open loop and control gains are necessary.

On the other hand, at HF both noise attenuation and control signal reduction are important. The former requirement is dependent on $\bar{\sigma}(T_o) << 1$, which is translated into low gains of L_o, and $\bar{\sigma}(KS_o) << 1$. Given that at HF, $S_o \approx 1$, then $\bar{\sigma}(KS_o) \leq \bar{\sigma}(K)$. Therefore, the controller gains also need to be small. For control signal attenuation T_i and KS_o should be small. The former is satisfied by having low open loop gains and the latter was already taken into account and said achieved in case the controller gains are reduced. These requirements are, therefore, clearly translated into open loop requirements as described in Figure 4.6.
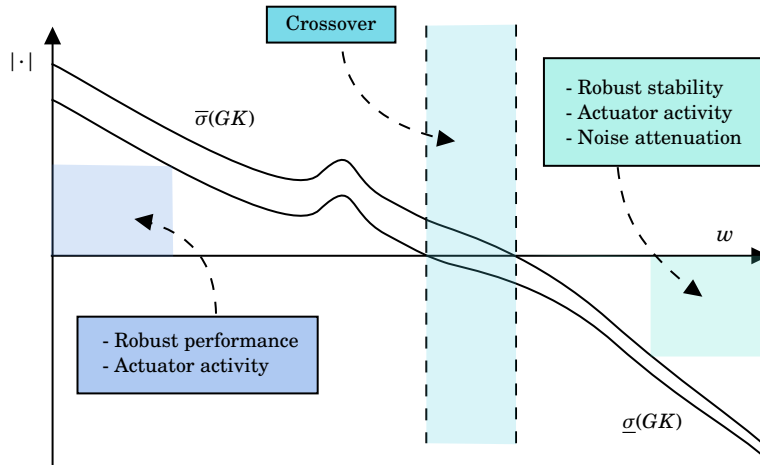
Figure 4.6: Design specifications of the open loop singular values. Based on [Pollack, 2024] and [Bates and Postlethwaite, 2002].

Thus, the basis of the $\mathcal{H}_\infty$ MS design is explained. It constitutes a powerful technique that enables controller synthesis, by optimally satisfying the various design objectives described above. Further discussions on it will be conducted in Section 4.1.6

4.1.6. STANDARD MIXED-SENSITIVITY $\mathcal{H}_\infty$

WEIGHTING FILTERS

$\mathcal{H}_\infty$ MS design involves shaping specific closed-loop TF based on the given design requirements. This is accomplished by shaping the singular values of those TF over the frequency range, which is conducted through the implementation of the main tuning knobs: weighting filters.

For a certain tunable SISO constraint, $H_i = H_i(j\omega, K)$, simple stable and proper low-pass and high-pass filters are usually sufficient to achieve the desired frequency-dependent shaping. Considering the desired shape $H_{i_{ref}} = H_{i_{ref}}(j\omega)$ for H_i to satisfy in terms of gain, then the design is satisfactory in case

$$|H_i(j\omega)| < |H_{i_{ref}}(j\omega)|, \forall \omega \qquad (4.18)$$

If $H_{i_{ref}}(j\omega)$ is defined as $(W_{H_i}(j\omega))^{-1}$, where $W_{H_i}(j\omega)$ is the WF set by the designer, then Equation (4.18) becomes:

$$|W_{H_i}(j\omega)H_i(j\omega)| < 1, \forall \omega \iff \|W_{H_i}H_i\|_\infty < 1 \tag{4.19}$$

As discussed in Section 4.1.2 and shown in Equation (4.9), the $\mathcal{H}_\infty$ optimization is set up so that Equation (4.20) is achieved. Thus, if the WF reflects the desired shape, the aim is to obtain a performance level, γ, close to 1.

$$|W_{H_i}H_i| < \gamma, \gamma > 0 \tag{4.20}$$

STACKED REQUIREMENTS

To combine the MS objectives, a stacking procedure is usually used. For illustration purposes and assuming that demands are requested on the TF H_1 and H_2, the following formulation is specified, where W_{H_1} and W_{H_1} are the respective WF:

$$\left\|N\right\|_\infty = \max_w \bar{\sigma}\left(N(jw)\right) < 1, \text{where } N = \begin{bmatrix} W_{H_1}H_1 \\ W_{H_2}H_2 \end{bmatrix} \tag{4.21}$$

To measure the size of the matrix N at each frequency, the maximum singular value $\bar{\sigma}(N(jw))$ is used. For SISO systems, it corresponds to the Euclidean vector norm:

$$\bar{\sigma}\left(N\right) = \sqrt{|W_{H_1}H_1|^2 + |W_{H_2}H_2|^2} \tag{4.22}$$

However, this stacking procedure does not allow to exactly specify the bounds on the individual TF and the higher the number of stacked requirements, the higher is the resulting error. For n specifications, the possible error in each is at most $\sqrt{n}$ [Skogestad and Postlethwaite, 2005]. In fact, although it is desired to achieve $|W_{H_1}H_1| < 1$ and $|W_{H_2}H_2| < 1$, getting Equation (4.22) to be lower than 1 is similar but not exactly the same.

CONTROL PROBLEM FORMULATIONS

Based on design objectives which are set a priori, it is possible to synthesize a controller that is robust to multiplicative and additive uncertainty, rejects disturbances, attenuates measurement noise, while also allowing reference model following and control energy reduction. Section 4.1.5 discussed in the detail how such specifications can be managed through the closed loop TF. Hence, several methods can be used, including 2-, 3-, and 4-Block formulations. Each of these formulations can also have several variations, which will differ from each other by the performance and disturbance signals defined. Hence, some of the possible control formulations will be further explored.

2-Block Problems

A simple 2-Block formulation is the output disturbance rejection control problem (see Figure 4.7) in which it is desired to maintain the plant output $y(t) = 0$, despite the presence of an output disturbance $d_o(t) \neq 0$. Considering the remarks highlighted in Section 4.1, the augmented plant is defined as:

$$\begin{bmatrix} \begin{pmatrix} z_1 = y \\ z_2 = u \end{pmatrix} \\ v \end{bmatrix} = \begin{bmatrix} \begin{pmatrix} I \\ 0 \end{pmatrix} & \begin{pmatrix} G \\ I \end{pmatrix} \\ -I & -G \end{bmatrix} \begin{bmatrix} w = d_o \\ u \end{bmatrix} = \begin{bmatrix} P_{11} & P_{12} \\ P_{21} & P_{22} \end{bmatrix} \begin{bmatrix} d_o \\ u \end{bmatrix} \tag{4.23}$$

Applying the rule for LFT's, Equation (4.24) is obtained. Therefore, minimizing the effect of the d_o on the plant output y and on the control input u is accomplished by minimizing the bundled TF $T_{wz}(s)$.

$$\begin{aligned} T_{wz} = \mathcal{F}_l(P,K) &= P_{11} + P_{12}K(I - P_{22}K)^{-1}P_{21} \\ &= \begin{pmatrix} I \\ 0 \end{pmatrix} - \begin{pmatrix} G \\ I \end{pmatrix} K(I + GK)^{-1}I = \begin{pmatrix} S_o \\ -KS_o \end{pmatrix} \end{aligned} \tag{4.24}$$

Furthermore, a similar S/KS problem that is used for output reference tracking is shown in Figure 4.8, where $w = r$ and $z = [e\ u]^T$. Another output disturbance rejection formulation is a S/T problem (see Figure 4.9), where $T_{wz}(s) = [S_o\ T_o]^T$, with $w = r$ and $z = [e\ y]^T$.
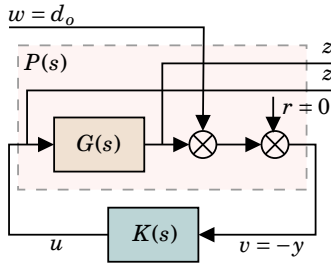
Figure 4.7: d_o rejection S/KS configuration.
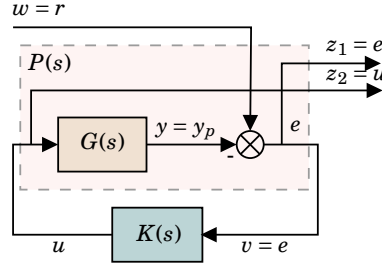
Figure 4.8: Output reference tracking S/KS configuration.
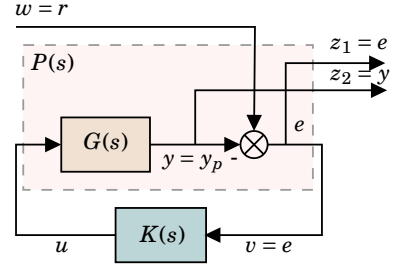
Figure 4.9: d_o rejection S/T configuration.

3-Block Problems

As previously stated, reducing the controller gain at HF is necessary for control signal attenuation, which is achieved by the KS_o constraint. Hence, a third performance signal may be added, resulting in a 3-Block problem and in a $S_o/T_o/KS_o$ scheme. A configuration in terms of the reference signal r and of the output disturbance d_o can be considered. These are represented in Figure 4.10 and Figure 4.11, respectively. For the latter configuration, the augmented plant is the following:

$$\begin{bmatrix} \begin{pmatrix} z_1 = y \\ z_2 = y_p \\ z_3 = u \end{pmatrix} \\ v \end{bmatrix} = \begin{bmatrix} \begin{pmatrix} I \\ 0 \\ 0 \end{pmatrix} & \begin{pmatrix} G \\ G \\ I \end{pmatrix} \\ -I & -G \end{bmatrix} \begin{bmatrix} w = d_o \\ u \end{bmatrix} \tag{4.25}$$

$$T_{wz} = \begin{pmatrix} I \\ 0 \\ 0 \end{pmatrix} - \begin{pmatrix} G \\ G \\ I \end{pmatrix} K(I+GK)^{-1}I = \begin{pmatrix} S_o \\ -T_o \\ -KS_o \end{pmatrix} \tag{4.26}$$
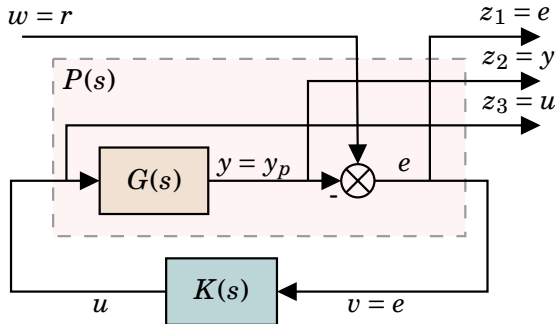
Figure 4.10: $S_o/T_o/KS_o$ control setup (reference).
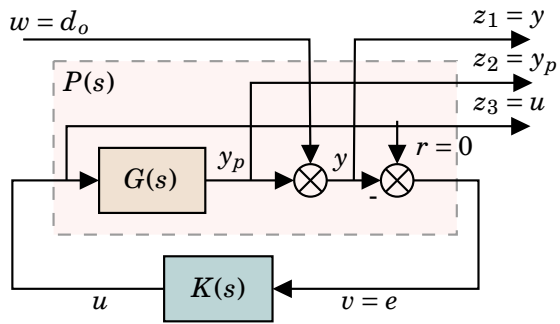
Figure 4.11: $S_o/T_o/KS_o$ control setup (disturbance).

4-Block Problem

The 4-Block problem offers the main advantage of also considering the TF S_oG and, thus, allowing to constrain the input disturbances as well, besides d_o. Minimizing this TF is also translated into integral action at LF. Its configuration is presented in Figure 4.12. The augmented plant and, therefore, the closed loop is obtained as:

$$\begin{bmatrix} \begin{pmatrix} z_1 = y \\ z_2 = u \end{pmatrix} \\ v \end{bmatrix} = \begin{bmatrix} \begin{pmatrix} I \\ 0 \end{pmatrix} & \begin{pmatrix} G \\ I \end{pmatrix} \\ -I & -G \end{bmatrix} \begin{bmatrix} \begin{pmatrix} w_1 = d_o \\ w_2 = d_i \end{pmatrix} \\ u \end{bmatrix} \tag{4.27}$$

$$T_{wz} = \begin{pmatrix} I & G \\ 0 & 0 \end{pmatrix} + \begin{pmatrix} G \\ I \end{pmatrix} K(I + GK)^{-1} \begin{pmatrix} -I & -G \end{pmatrix} = \begin{pmatrix} S_o & S_o G \\ -KS_o & -T_i \end{pmatrix} \qquad (4.28)$$
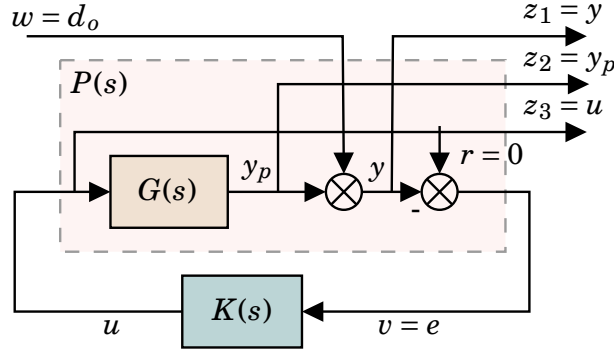
Figure 4.12: 4-Block control problem setup.

Reference Model Following

Furthermore, the Flying-V must meet certain HQ, as described in [Anonymous, 1997], which will also be further discussed in Section 4.4. Thus, a controller that robustly meets performance requirements based on an ideal response model should also be discussed within the $\mathcal{H}_\infty$ Mixed Sensitivity framework. Therefore, besides the reference tracking that was previously discussed, it is also possible to add a model matching constraint, M. One approach that can be followed is to minimize the error between the output of a reference model when excited by the reference and the plant output. Another weighting function is, therefore, added. For that purpose, the implementation of a feed-forward controller in filtering or injection form is beneficial for this reference model tracking, whereas the feedback controller guarantees system robustness.

4.1.7. SIGNAL-BASED MIXED-SENSITIVITY $\mathcal{H}_\infty$

Although the MS approach is a good option for controller design, it might become limiting as the complexity of the system and requirements increase. For systems that are more intricate, there may be information regarding exogenous signals in addition to a variety of signals to be minimized. Therefore, the lack of generality of the MS approach leads to the usage of more flexible and advanced techniques, such as the signal-based approach. [Skogestad and Postlethwaite, 2005]

Hence, the generality of the signal-based approach is appealing for multivariable problems in which several objectives must be considered simultaneously. In this method, the focus lies on the size of the signals since the plant and potentially model uncertainty, the class of external signals, as well as the norm of the error signals that are desired to keep small can be defined. Weighting filters continue as a central element to describe the desired frequency behavior of the signals and, as in the MS $\mathcal{H}_\infty$ control, these need to be stable and proper. Thus, the signal-based MS approach derives from the standard MS method with a more flexible essence. [Skogestad and Postlethwaite, 2005]

For exemplification purposes, Figure 4.13 portrays a diagram of a signal-based $\mathcal{H}_\infty$ problem. Here, G and G_d represent the nominal plant and disturbance models, K is the controller to be synthesized, the weights W_d, W_r, and W_n can be used to define the desired frequency content of the associated signals and/or of its relative importance. Additionally, the weight W_{ref} is a desired closed loop transfer function between the weighted r_s signal and the output y. W_e and W_u portray the desired frequency behavior of the error and control signals, respectively. Thus, the problem can be formulated as an $\mathcal{H}_\infty$ optimization problem (see Figure 4.2) where

$$w = \begin{bmatrix} d \\ r \\ n \end{bmatrix} \qquad z = \begin{bmatrix} z_1 \\ z_2 \end{bmatrix} \qquad v = \begin{bmatrix} r \\ y_m \end{bmatrix} \qquad u = u \qquad (4.29)$$
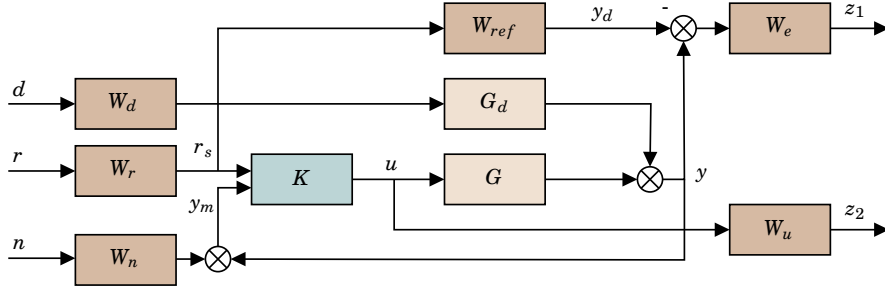
Figure 4.13: A signal-based $\mathcal{H}_\infty$ control problem. Adapted from Skogestad and Postlethwaite [2005].

4.1.8. MODEL & CONTROLLER ORDER REDUCTION TECHNIQUES

Controller synthesis methods such as $\mathcal{H}_\infty$ generate controllers of order at least equal to that of the plant and, possibly, higher due to the addition of weights. Thus, as low order controllers are preferred due to the increased transparency, reduced hardware and software requirements, and lighter implementations, model reduction techniques should be addressed. Therefore, the central problem is to find a low-order approximation such that the the difference $\|G - G_a\|$ is small, where G is a high order stable model and G_a is the reduced order system.

Hence, three main methods will be addressed, namely balanced truncation, balanced residualization, and optimal Hankle norm approximation. Nevertheless, the truncation and residualization techniques will be detailed at first.

TRUNCATION & RESIDUALIZATION

Consider the stable system $G(s)$ and its minimal realization (A, B, C, D), where the state vector x of dimension n is partitioned into $[x_1 \ x_2]^T$. x_2 is the vector of $n - k$ states that are desired to be removed. With adequate transformations, the state space representation becomes:

$$\begin{aligned}
\dot{x}_1 &= A_{11}x_1 + A_{12}x_2 + B_1 u \\
\dot{x}_2 &= A_{21}x_2 + A_{22}x_2 + B_2 u \\
y &= C_1 x_1 + C_2 x_2 + Du
\end{aligned} \tag{4.30}$$

Truncation

The truncation method aims to discard the dynamics associated with x_2. Hence, the kth order truncation of the system is defined as $G_a = (A_{11}, B_1, C_1, D)$. At infinite frequency, $G(\infty) = G_a(\infty)$. Nonetheless, no other guarantees are detailed for the remaining frequencies. To tackle this issue, $G(s)$ can be converted into the Jordan form so that x_2 correspond to the HF modes. Therefore,

$$A = \begin{bmatrix} \lambda_1 & 0 & \cdots & 0 \\ 0 & \lambda_2 & \cdots & 0 \\ \vdots & \vdots & \ddots & \vdots \\ 0 & 0 & \cdots & \lambda_n \end{bmatrix} \qquad B = \begin{bmatrix} b_1^T \\ b_2^T \\ \vdots \\ b_n^T \end{bmatrix} \qquad B = \begin{bmatrix} c_1 & c_2 & \cdots & c_n \end{bmatrix} \tag{4.31}$$

By ordering the λ_i so that $|\lambda_1| < |\lambda_2| < \cdots$, the fastest modes are removed from the model and the mismatch between G and G_a is given by:

$$\|G - G_a\|_\infty \leq \sum_{i=k+1}^{n} \frac{\bar{\sigma}(c_i b_i^T)}{|Re(\lambda_i)|} \tag{4.32}$$

One advantage of the model truncation method is that the poles of the resulting model are a subset of the original model poles. Hence, its physical interpretation remains.

Residualization

Contrarily to the truncation method, the residualization involves setting $\dot{x}_2 = 0$ in the state space representation of Equation (4.33) and solving for x_2 in terms of x_1 and u, followed by its substitution in the equations. Assuming A_{22} invertible, the following result is obtained:

$$\dot{x}_1 = \underbrace{(A_{11} - A_{12}A_{22}^{-1}A_{21})}_{A_r}x_1 + \underbrace{(B_1 - A_{12}A_{22}^{-1}B_2)}_{B_r}u$$

$$y = \underbrace{(C_1 - C_2A_{22}^{-1}A_{21})}_{C_r}x_1 + \underbrace{(D - C_2A_{22}^{-1}B_2)}_{D_r}u \qquad (4.33)$$

Therefore, the residualization of $G(s)$ is the reduced order model $G(a) = (A_r, B_r, C_r, D_r)$. Preferably, $G(s)$ is also put into the Jordan form. One imprtant characteristic of this method is that it preserves the steady-state gain of the system, posing itself as a beneficial approach for LF modeling.

BALANCED REALIZATIONS

Considering the (A, B, C, D) as the minimal realization of the stable system $G(s)$, then (A, B, C, D) is referred to as balanced if the solutions to the Lyapunov equations

$$AP + PA^T + BB^T = 0$$
$$A^T Q + QA + C^T C = 0 \qquad (4.34)$$

are $P = Q = diag(\sigma_1, \sigma_2, ..., \sigma_n) \triangleq \sum$, where $\sigma_1 \geq \sigma_2 \geq ... \geq \sigma_n \geq 0$. σ_i are the Hankel SV of $G(s)$. P and Q are the controllability and observability Gramians that are also defined as

$$P \triangleq \int_0^\infty e^{At}BB^T e^{A^T t}dt$$
$$Q \triangleq \int_0^\infty e^{A^T t}C^T C e^{At}dt \qquad (4.35)$$

The benefit of balanced realizations for model order reduction emerge from each state x_i being as controllable as it is observable. Therefore, each σ_i associated with each x_i provides a balanced contribution measure of each state to the system's overall input-output behavior. The states with the lower Hankel SV are truncated and/or residualized to obtain the reduced model.

The error bound for the balanced truncation model reduction was first presented by Enns [1984]. Glover [1984] subsequently gave an independent proof. Therefore, it is stated that given the balanced truncation of $G(s)$ to the first states $(r_1 + r_2 + ... + r_k)$, where each σ_i has multiplicity r_i, then Equation (4.36) is verified. Moreover, Anderson and Liu [1989] showed that this error bound is also applies for the balanced residualization model reduction.

$$\|G(s) - G_a^k(s)\|_\infty \leq 2(\sigma_{k+1} + \sigma_{k+2} + ... + \sigma_N) \qquad (4.36)$$

OPTIMAL HANKEL NORM APPROXIMATION

Given the stable model $G(s)$ of order n, the Hankel norm approximation aims to find the reduced model $G_h^k(s)$ of order k for which the Hankel norm of the approximation error, $\|G(s) - G_h^k(s)\|_H$, is minimized. The Hankel norm of any stable transfer function is defined as

$$\|E(s)\|_H \triangleq \sqrt{\rho(PQ)}, \qquad (4.37)$$

where P and Q are the controllability and observability Gramians of $E(s)$ and ρ is the spectral radius (maximum eigenvalue). Thus, the optimizations stands on finding an error which is in some sense the closest to being unobservable and uncontrollable. The interested reader is invited to read Glover [1984], where a complete treatment of the problem is conducted.

4.1.9. CONTROLLER STRUCTURES & OPTIMIZATION TOOLS

UNSTRUCTURED CONTROLLERS

The $\mathcal{H}_\infty$ control problem solutions obtained via Algebraic Riccati Equations [Doyle et al., 1988] and LMIs [Gahinet and Apkarian, 1994] are of full-order, i.e. unstructured. To compute such controllers, the optimization MATLAB® function `hinfsyn` can be used. It allows to synthesize the controllers based on one of these approaches by considering the augmented system (plant plus weighting filters). The function uses a γ-iteration technique, which is a bisection algorithm, to determine the optimal value of the performance level γ and optimal $\mathcal{H}_\infty$ control design.

Nevertheless, as simple controller architectures are preferred by practitioners, not allowing the specification of controller structures a priori poses as a major disadvantage. This motivated the investigation of structured $\mathcal{H}_\infty$-synthesis. However, the difficulty in the $\mathcal{H}_\infty$ control problems stands on the fact that the objective detailed in Equation (4.6) is non-convex and non-smooth and that there are also stability issues in the closed-loop. Therefore, developments on new optimization methods emerged to allow additional structural constraints in the controllers, which started with Apkarian and Noll [2006a].

NON-CONVEX NON-SMOOTH OPTIMIZATION FOR STRUCTURED CONTROLLERS

Considering that $K(\kappa)$ is structured, where $\kappa \in \mathbb{R}^n$, and assuming that $D_{22} = 0$ in Equation (4.7), the closed loop transfer function from $w \to z$ (see Figure 4.2) is defined as:

$$T_{w \to z}(P, K(\kappa)) : \left[\begin{array}{c|c} A(K(\kappa)) & B(K(\kappa)) \\ \hline C(K(\kappa)) & D(K(\kappa)) \end{array} \right] \tag{4.38}$$

Then, the objective described in Equation (4.6), becomes:

$$\begin{aligned}
\min_\kappa f(\kappa) &\triangleq \min_\kappa \| T_{w \to z}(P, K(\kappa)) \|_\infty \\
&= \min_\kappa \max_{w \in \mathbb{R}} \bar{\sigma}\left(C(K(\kappa))(j\omega I - A(K(\kappa)))^{-1} B(K(\kappa)) + D(K(\kappa)) \right)
\end{aligned} \tag{4.39}$$

which is a non-smooth, non-convex function. It's defined in the domain $D_f = \{ \kappa \in \mathbb{R}^n : f(\kappa) < \infty \}$ that contains the internally stabilizing set

$$D_s = \{ \kappa \in \mathbb{R}^n : K(\kappa) \text{ stabilizes } P \text{ internally} \} = \{ \kappa \in \mathbb{R}^n : A(K(\kappa)) \text{ stable } \} \tag{4.40}$$

Tools for structured $\mathcal{H}_\infty$ synthesis were, thus, developed, leveraging the investigations conducted on non-smooth optimizers [Apkarian and Noll, 2006a] [Burke et al., 2006] to directly tune any single or multiple loop control architecture. The MATLAB® function hinfstruct became available to the general public in 2010 [Gahinet and Apkarian, 2011], allowing the structured controllers, such as PIDs, to be optimized instead of tuned [Apkarian and Noll, 2017].

Furthermore, multiple extensions were developed and incorporated into MATLAB® function systune [Apkarian and Noll, 2017]. Some include the synthesis in the multiband frequency domain [Apkarian and Noll, 2007], multi-objective $\mathcal{H}_2/\mathcal{H}_\infty$ synthesis [Apkarian et al., 2008], multidisk $\mathcal{H}_\infty$ synthesis [Apkarian and Noll, 2006b], systematic tuning of gain scheduled control systems [Gahinet and Apkarian, 2013], and parametric robust $\mathcal{H}_\infty$ control [Apkarian et al., 2015].

Hence, systune that is publicly available since 2012, elevates itself as a strong alternative to hinfstruct. Moreover, while the latter optimizes the tuning goals simultaneously, leading to a single performance level γ, the former individually optimizes the tuning objectives, enabling more design flexibility. One pivotal feature of systune is also the multi-model, multi-objective synthesis. This approach is depicted in Figure 4.14, where the structured controller synthesis is conducted given a family of requirements and models [Apkarian et al., 2014]. Moreover, given the hard requirements $f(\kappa)$ and soft requirements $g(\kappa)$, the design problem across multiple models can be formalized as
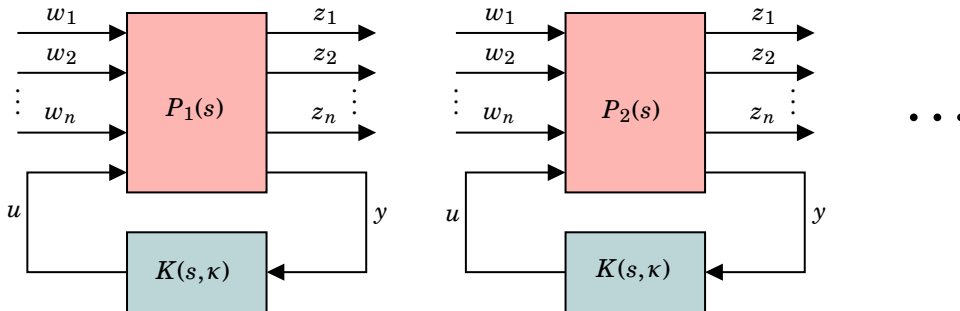
Figure 4.14: Synthesis against multiple requirements and models.

$$\underset{\kappa}{\text{minimize}} \ \underset{i=1,\dots,n_f}{\max} \ f_i(\kappa)$$

$$\text{subject to} \ \underset{j=1,\dots,n_g}{\max} \ g_j(\kappa) \le 1 \tag{4.41}$$

which can be defined in terms of the closed loop transfer function from $w \to z$:

$$\underset{\kappa}{\text{minimize}} \ \underset{i,p}{\max} \left\{ \| T^{(p)}_{w_i \to z_i}(K(s,\kappa)) \| \right\}$$

$$\text{subject to} \ \underset{j,p}{\max} \left\{ \| T^{(p)}_{w_j \to z_j}(K(s,\kappa)) \| \right\} \le 1 \tag{4.42}$$

where κ denotes the vector of tunable parameters, $T^{(p)}_{w \to z}$ is the closed loop map from the signal w to signal z for the pth plant model, and $\|\cdot\|$ is either the $\mathcal{H}_2$ or the $\mathcal{H}_\infty$ norm.

4.2. STABILITY MARGINS

A key requirement for the certification process lays on the proof of the aircraft closed-loop stability, which is addressed by computing the stability margins for the linearized models around several operating points over the flight envelope. In fact, real systems are not accurately defined by their mathematical models and vary both in magnitude and phase, especially in high frequencies where uncertainty increases [Seiler et al., 2020]. Thus, stability margins account for this mismatch by introducing gain and phase perturbations in the feedback. Hence, these are measures of how high the perturbations can be before the system becomes unstable. Minimum specifications of 6 dB and 45° of gain and phase margins, respectively, are prescribed for military standards and are used as guidelines[Dobos-Bubno and Hartsook, 1977] [Seiler et al., 2020] [Anonymous, 2000]. These values correspond to the classical gain and phase margins and, if met, are also within limits of the civil requirements [Cook, 2013].

CLASSICAL GAIN AND PHASE MARGINS

Classical stability margins are SISO robustness measures which are defined in terms of broken-loops. These margins consider independent uncertainty in the plant gain and phase. Thus, the Gain Margin (GM) specifies the factor by which the loop gain may be increased before the CL system becomes unstable, whereas the Phase Margin (PM) considers the amount of plant phase variation before the CL becomes unstable. Phase variations arise due to time delays in the feedback loop or deviations in the plant dynamics. In fact, time delays are intimately related to the phase margin as $\theta_{max} = PM/\omega_c$. However, GM and PM can be misleading by themselves when simultaneous perturbations are induced in the system. In fact, small plant perturbations may cause robustness issues even if the system has large gain and phase margins. Moreover, a typical extension of the classical margins to MIMO systems involve a repeated analysis by assessing gain and phase perturbations for each input and output channel. Nonetheless, this "loop-at-a-time" analysis fails to capture the simultaneous effects. [Bates and Postlethwaite, 2002] [Seiler et al., 2020]

DISK GAIN AND PHASE MARGINS

Furthermore, Disk Margins (DM) arise naturally as the solution to some of the limitations of the classical margins. These account for simultaneous perturbations and also provide additional information regarding the influence of model uncertainty over the frequency range. Firstly, the set $D(\alpha_{max}, \sigma)$ represents the stable region for gain and phase variations, where σ represents the skew and α_{max} represents the smallest of all the frequency-dependent DM. Moreover, the disk margin is defined as in Equation (4.43). [Seiler et al., 2020]

$$\alpha_{max} = \frac{1}{\left\| S + \frac{\sigma-1}{2} \right\|_\infty} \tag{4.43}$$

In fact, $\sigma = 0$ corresponds to the balanced case ($S - T$ based) and it means that the gain can increase or decrease by the same amount. A positive or negative skew is translated into a bias on the logarithmic/decibel scale, towards gain increase or decrease. The skew values are, thus, highly related to the sensitivity functions, as defined in Equation (4.44). For $\sigma = 1$, the so-called *modulus* margins is obtained. Additionally, DM are also used for multiple-loop analysis of MIMO systems, which provide a more accurate

robustness assessment. This analysis provide an introduction to more general robustness frameworks such as structured singular-value μ. [Seiler et al., 2020]

$$\sigma = 0 \Rightarrow \alpha_{max} = \frac{1}{\left\|\frac{S-T}{2}\right\|_\infty}, \qquad \sigma = +1 \Rightarrow \alpha_{max} = \frac{1}{\left\|S\right\|_\infty}, \qquad \sigma = -1 \Rightarrow \alpha_{max} = \frac{1}{\left\|T\right\|_\infty} \qquad (4.44)$$

4.3. C* LONGITUDINAL CONTROL LAW

In the 1960's, the C* parameter was first introduced by Boeing as a normalized linear sum of pitch rate and normal acceleration [Malcom and Tobie, 1965] [Field, 1993]. Although not completely successful [Gibson, 1999], the parameter led to the creation of the C* response, which is now frequently used in commercial aviation industry as a flight control law, with both Boeing and Airbus flying variations of it [Favre, 1994]. Furthermore, although not the pure C*, several fighter aircraft, like the Lockheed Martin's F-16 and F-18 [Field, 1993], also claim to use this law. In fact, C* controllers sometimes cover any combination of n_z and q.

The C* signal is originally defined as a normalized sum of the pitch rate and normal acceleration at the pilot station. It is asserted that the pilots respond to a combination of these two signals, whose ratio varies according to the natural variations of the aircraft response [Field, 1993]. The normal acceleration cues are intensified at higher velocities (where slight pitching produces large n_z changes), whereas the pitch rate cues are more predominant in lower velocities. Thus, a constant ratio was defined, where the relative contributions of n_z and q would automatically change based on the velocity, as a consequence of the inherent characteristics of their transfer function. Therefore, C* was described as:

$$C^* = n_z + \frac{V_{CO}}{g}q, \qquad (4.45)$$

where g corresponds to the standard gravity and V_{CO} corresponds to the crossover velocity, where both cues would translate into equal pilot sensation. This velocity was defined to be 400 feet per second (≈ 122 m/s). Therefore, the ratio is equal to 12.4. This control law is followed in several publications, including Lombaerts et al. [2017]. Additionally, Niedermeier and Lambregts [2012] also feedbacks this parameter as well as a proportional pitch rate, which increases the damping of the SP. Nieto-Wire and Sobel [2011] also implements a proportional gain in the angle of attack signal, in addition to the ones used in the previous formulation.

Moreover, there are several other configurations, as it was also previously mentioned, that are "C*-like" approaches. A first configuration is represented in Equation (4.46), which is followed by Guilhem and Jean-Marc [2013], Marcos [2017], as well as in Airbus flight control algorithms [Favre, 1994] [Delannoy and Oudin, 2013].

$$u = K_q q + K_{n_z} n_z + K_{int} \int (n_{z_c} - n_z) + K_{n_{z_c}} n_{z_c}, \qquad (4.46)$$

where the load factor and pitch rate signals are fed back to match the commanded load factor n_{z_c}, delivered by the pilot. Another approach, followed by De Paula and Paglione [2007], is to feedback the load factor signal and include a proportional controller in the pitch rate.

Additionally, it is often claimed that the C* approach guarantees flight path stability [Niedermeier and Lambregts, 2012]. It is true that this algorithm has a close relation with γ in straight and level flight, since the small n_z perturbations are equivalent to $V_0 \delta\gamma$, where V_0 is the trimmed airspeed [Vigano et al., 2017]. In fact, the controller tends to stabilize the aircraft at a constant vertical speed or flight path angle, for a constant airspeed. Nevertheless, since there is no integral action applied to the flight path angle signal, the controller cannot reject external disturbances on it, yielding in flight path deviations. Moreover, any pilot input changes the reference and it results in the airspeed to drift away, unless the thrust is re-trimmed. Therefore, the C* disrupts the natural speed stability of the aircraft.

Moreover, a turn coordination term is frequently added to the C* formulation. Nonetheless, given that only the longitudinal control is within the scope of the thesis, no further considerations on this term will be drawn.

4.4. Handling Qualities

Handling Qualities of an aircraft correspond to the properties that dictate the ease and precision with which the vehicle responds to the pilot commands, while executing a certain flight task [Cook, 2013]. Additionally, this assessment can be approached as defined by the civil certification authorities, such as EASA or Federal Aviation Administration (FAA). Nonetheless, these requirements are not very specific and are, thus, difficult to use during the design and certification of the aircraft, as shown by van Overeem [2022]. On the contrary, the military HQ standards are thoroughly defined and, generally, far more demanding [Cook, 2013] [Luckner, 2002]. These are also extensively used in the development of FCS for civil aircraft [Luckner, 2002]. In fact, designing an aircraft that meets the military requirements ensures the civil ones are also met [Cook, 2013]. For that reason, MIL-STD-1797 [Anonymous, 1997] represents a significant reference for HQ guidelines for the Flying-V, as well as WL-TR-94-3162 [Mitchell et al., 1994]).

Furthermore, the standards in MIL-STD-1797A are a function of the aircraft classification and flight phases. The Flying-V is a class III aircraft (large, heavy, low to medium maneuverability) and the relevant flight phase for the current research consists of Category B (gradual maneuvering, less precise tracking and accurate flight path control). Additionally, the handling characteristics are specified in terms of qualitative degrees of suitability and Levels, which are briefly described as [Anonymous, 1997]:

Satisfactory (Level-I) - "[...] clearly adequate for the mission Flight Phase."
Acceptable (Level-II) - "[...] adequate to accomplish the mission Flight Phase, but some increase in pilot workload or degradation in mission effectiveness, or both, exists."
Controllable (Level-III) - "[...] the aircraft can be controlled in the context of the mission Flight Phase, even though pilot workload is excessive or mission effectiveness is inadequate, or both."

Moreover, it is important to highlight that these levels can be distinguished into predicted and assigned levels. The former is based on the set of quantitative parameters that, together, are expected to accurately reflect HQ, whereas the latter is based on piloted assessments during flight test maneuvers [Mitchell et al., 1994]. However, there may be conflicts between the two provided that the predicted levels may not capture accurately the characteristics experienced by the pilot. Thus, for an accurate assessment of the HQ levels, the two tests must be conducted. Nevertheless, the current research is confined to the use of simulations which makes all of the HQ described hereafter belong to the group of Predicted Levels.

Additionally, although MIL-STD-1797A provide alternative requirements, no guidance is given on how to use each assessment metric. On the contrary, Mitchell et al. [1994] provides an extensive discussion on this, describing the road-map for the use of the short-term pitch response criteria.

Based on Mitchell et al. [1994], the best specification and desired criteria entail the attitude and flight path bandwidth requirement in combination with the dropback, which yields in the most effective in specifying flying qualities than any other criteria. Additionally, it is also versatile, given that it is the only criteria applicable to all response-types. Hence, these will be further discussed in Section 7.3.

5

FLYING-V MODEL

A solid simulation model of the Flying-V is pivotal for the controller design. Thus, in the current chapter, the modeling of the aircraft, which was developed in MATLAB® and Simulink® is discussed. To begin with, the most important subsystems of the model are described in Section 5.1, namely the actuator dynamics, aerodynamics, equations of motion (EoM), and sensors. Secondly, the trimming and linearization procedures are introduced in Section 5.2, where the methodology is explained and the main results are presented. Lastly, in Section 5.3, the analysis of the bare airframe is conducted, in terms of eigenmotions and validity of the approximation models.

5.1. NONLINEAR MODELING

The Flying-V model is implemented in MATLAB® and Simulink® using a tensor-based formulation. Thus, to begin with, the tensors formulation is briefly introduced in Section 5.1.1. Each of the main subsystems that integrate the full model is discussed in the upcoming subsections. The main flow of the model is depicted in Figure 5.1. Therefore, the actuator dynamics are briefly described in Section 5.1.2. The airframe is subdivided into Aerodynamics and EoM, which are addressed in Section 5.1.3 and Section 5.1.4, respectively. Lastly, some important aspects related to the sensors are addressed in Section 5.1.5. However, it is important to note that an F-16 Simulink® model, which was used in Naäman [2024], was provided and served as a foundation to design the Flying-V model.
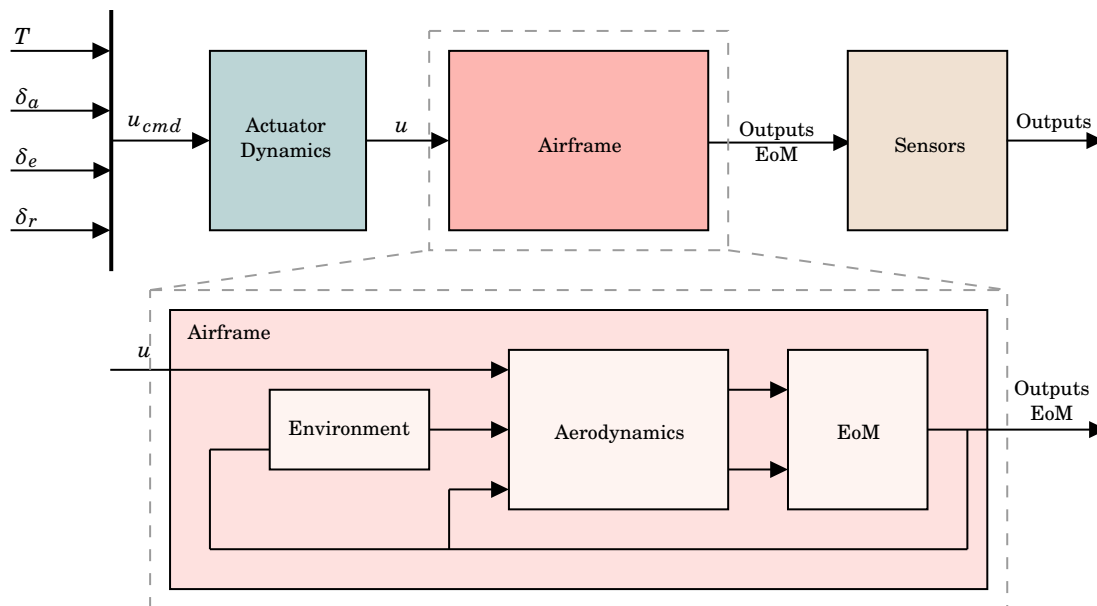
Figure 5.1: Overview of *Simulink*'s Flying-V model.

The notation used in the current section is based on Zipfel [2007] nomenclature, where scalars (zeroth-order tensors) are represented by lower-case characters, vectors (first-order tensors) are represented by bold lower-case characters, and tensors (second-order tensors) by bold upper-case characters.

5.1.1. INTRODUCTION TO TENSORS

An integral aspect of the modeling lays in the tensors' mathematical formulation. Thus, this concept is briefly introduced. To begin with, Zipfel [2007] states that, from a physical point of view:

> "Tensors describe properties of intrinsic geometrical or physical objects, i.e., objects that do not depend on the form of presentation (coordinate system)."

In fact, with or without coordinates, physical quantities exist a priori. The coordinate systems are simply introduced for numerical evaluation and for the interpretation of results. Thus, tensors hold the physical characteristics and remain unaffected by the choice of a coordinate system. This is highly advantageous to generalize the EoM, allowing for subsequent projection into any coordinate system. Moreover, Zipfel [2007] also presents the mathematical perspective:

> "... tensors are the total aggregate of all ordered n-tuples, they are defined in all coordinate systems and thus are not tied to any particular one."

For illustration purposes, a first-order tensor $\boldsymbol{x}$ (respectively second-order tensor $\boldsymbol{X}$) is the aggregate of ordered triples (respectively, 9-tuples), any two of which satisfy the transformation law represented in Equation (5.1) (respectively Equation (5.2)):

$$[\boldsymbol{x}]^B = [T]^{BA}[\boldsymbol{x}]^A, \tag{5.1}$$

$$[\boldsymbol{X}]^B = [T]^{BA}[\boldsymbol{X}]^A[\bar{T}]^{BA}, \tag{5.2}$$

where $]^A$ and $]^B$ are any allowable coordinate system. It is clear that the tensors themselves, represented by $\boldsymbol{x}$ and $\boldsymbol{X}$, are invariant across coordinate systems. It is only after projection on a coordinate system that a transformation matrix is required to establish equivalence between the expressions. [Zipfel, 2007]

Moreover, one important formulation that is used across the model is the rotational derivative, which is also invariant to the coordinate system. For example, considering the displacement vector s_{BA} between point B and any arbitrary reference point associated with frame A, the linear velocity of point B with respect to (wrt) frame A can be defined as:

$$\boldsymbol{v}_B^A = D^A \boldsymbol{s}_{BA} \tag{5.3}$$

The linear acceleration can, hence, be simply determined as the rotational derivative of the velocity:

$$\boldsymbol{a}_B^A = D_A \boldsymbol{v}_B^A = D^A D^A \boldsymbol{s}_{BA} \tag{5.4}$$

Additionally, the Euler transformation is another fundamental definition, which involves the transformation of the rotational time derivative between two reference frames. It is defined, for any vector $\boldsymbol{x}$ as in Equation (5.5), where Ω^{BA} corresponds to the velocity matrix between frame B and A. [Zipfel, 2007]

$$D^A \boldsymbol{x} = D^B \boldsymbol{x} + \boldsymbol{\Omega}^{BA} \boldsymbol{x}, \tag{5.5}$$

5.1.2. ACTUATOR DYNAMICS

Regarding the control surfaces, the Flying-V will possess several elevons on the trailing edges, which is particularly important for redundancy. Nonetheless, since this subdivision is still in development phase, the aerodynamic data used in the simulation only accounts for one control surface on each side, that functions both as elevator and aileron. Additionally, there is also a rudder located on each side of the wing's back. In terms of aerodynamic data, the contributions of both rudders are presented as a single one.

Furthermore, these control surfaces are modeled by a first-order linear system with a time constant of 0.07 seconds and complemented with position and rate saturation. The actuators' characteristics are summarized in Table 5.1, whose values are retrieved from a commercial aircraft, as described in Bérard et al. [2012]. Lastly, the engine is modeled with a first-order system with a time constant of 0.2 seconds.

Table 5.1: Control surfaces characteristics.

	δ_a	δ_e	δ_r
Minimum Deflection Position (deg)	-25	-25	-30
Maximum Deflection Position (deg)	+14	+14	+30
Maximum Deflection Rates (deg/s)	± 60	± 60	± 60

5.1.3. Aerodynamic Model

To compute the forces and moments acting on the aircraft, which are consequently used in the EoM, aerodynamic data is needed. This data was generated by the aerodynamics team by using RANS-based CFD simulations. The global values for the coefficients are given as a function of other variables, which include the angle of attack, α, the angle of sideslip, β, the dimensionless angular accelerations, $\hat{p}, \hat{q}, \hat{r}$, the control surface deflections, $\delta_a, \delta_e, \delta_r$, and the CoG location. Each of these coefficients were also provided for a total of sixteen flight conditions, which are dependent on the Mach number, M_a, and altitude.

Therefore, the Air Data Computer outputs, namely V, α, β, the dynamic pressure, and Mach number, have to be computed. For that purpose, the velocity of the aircraft with respect to the air around it ($[v_B^A]^L$) is used, since it is what is measured by the air data sensor. The velocity is defined in the local-level coordinate system, which is a special case of the geographic coordinate system. It is used when the particular location on the globe is not relevant. Therefore, any local tangent plane can serve as a geographic coordinate system, independent of the longitude and latitude designations [Zipfel, 2007]. It maintains a fixed, level orientation and it is sometimes also referred to as the North-East-Down (NED) coordinate system. Additional computations needed involve the transformation of the coordinate system from the local-level to the body coordinate system, yielding in $[v_B^A]^B$, which is consequently used to compute the aerodynamic angles and airspeed velocity, as expressed in Equation (5.6).

$$V = \left\| [v_B^A]^B \right\|_2, \quad \alpha = \arctan\left(\frac{w_A}{u_A}\right), \quad \beta = \arcsin\left(\frac{u_A}{V}\right), \quad \text{where} \quad [v_B^A]^B = \begin{bmatrix} u_A \\ v_A \\ w_A \end{bmatrix} \tag{5.6}$$

Furthermore, with these values, it is possible to interpolate the global coefficients, which were originally provided. Hence, since all the parameter are known, the expressions to obtain the aerodynamic forces and moments coefficients, which are expressed in Equation (5.7), can be implemented.

$$\begin{aligned}
C_x &= C_{x_\alpha}(M_a, h, \alpha) + C_{x_{\delta_e}}(M_a, h, \delta_e) \\
C_y &= C_{y_\beta}(M_a, h, \beta) + C_{y_r}(M_a, h, r, CoG) + C_{y_{\delta_a}}(M_a, h, \delta_a) + C_{y_{\delta_r}}(M_a, h, \delta_r) \\
C_z &= C_{z_\alpha}(M_a, h, \alpha) + C_{z_q}(M_a, h, q) + C_{z_{\delta_e}}(M_a, h, \delta_e) \\
C_l &= C_{l_\beta}(M_a, h, \beta) + C_{l_p}(M_a, h, p) + C_{l_r}(M_a, h, r, CoG) + C_{l_{\delta_a}} + C_{l_{\delta_r}}(M_a, h, \delta_r) \\
C_m &= C_{m_\alpha}(M_a, h, \alpha, CoG) + C_{m_q}(M_a, h, q, CoG) + C_{m_{\delta_e}}(M_a, h, \delta_e, CoG) \\
C_n &= C_{n_\beta}(M_a, h, \beta, CoG) + C_{n_p}(M_a, h, p, CoG) + C_{n_r}(M_a, h, r, CoG) + \\
&\quad + C_{n_{\delta_a}}(M_a, h, \delta_a, CoG) + C_{n_{\delta_r}}(M_a, h, \delta_r, CoG)
\end{aligned} \tag{5.7}$$

The total aerodynamic forces and moments are calculated as:

$$\begin{aligned}
F_{x_a} &= \bar{q} S C_x & M_{x_a} &= \bar{q} S b C_l \\
F_{y_a} &= \bar{q} S C_y & M_{y_a} &= \bar{q} S c C_m \\
F_{z_a} &= \bar{q} S C_z & M_{z_a} &= \bar{q} S b C_n
\end{aligned} \tag{5.8}$$

where $\bar{q} = 1/2\rho V^2$ is the dynamic pressure, S is the wing area, b is the wingspan, and c is chord length. Moreover, the propulsion and gravity forces are added to get the overall force acting on the aircraft. Additionally, the thrust contribution to the moments is also considered, given that the motors have displacements of 8.028m, $\pm$ 5.7m, and 0.8m in the x-, y-, and z-axis, respectively [Rubio Pascual, 2018]. The displacement in the x-axis does not have any considerable effect since it is aligned with the thrust force. On the y-axis there is also no significant contribution because the two motors balance each other. Hence, only the distance in the z-axis matters, which is multiplied by the propulsive force in the x-axis.
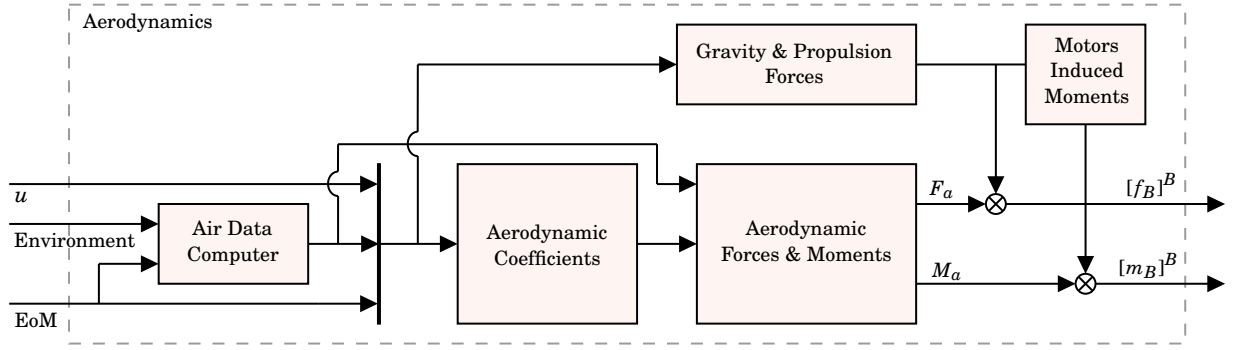
Figure 5.2: Overview of the aerodynamic Block of the Flying-V model, implemented in Simulink®.

Therefore, only the moment around the y-axis is affected. For further comprehension, the aerodynamics system is portrayed in Figure 5.2.

5.1.4. EQUATIONS OF MOTION

The 6 DoF simulation, which is implemented assuming a flat Earth model, allows to fully model the three translational and angular accelerations, velocities, and positions from the forces and moments acting on the system. Moreover, given that the simulation supposes in-atmosphere, near-Earth flight, Earth frame E is considered to be the inertial frame [Zipfel, 2007]. The EoM are implemented and can be sub-categorized into four main parts (see Figure 5.3): attitude and translational dynamics and attitude and translational kinematics. While kinematics deal with bodies' motion without any reference to force or mass, the dynamics equations do reference these and apply Newton's and Euler's laws. The previously mentioned four main parts are briefly explained in the current subsection.
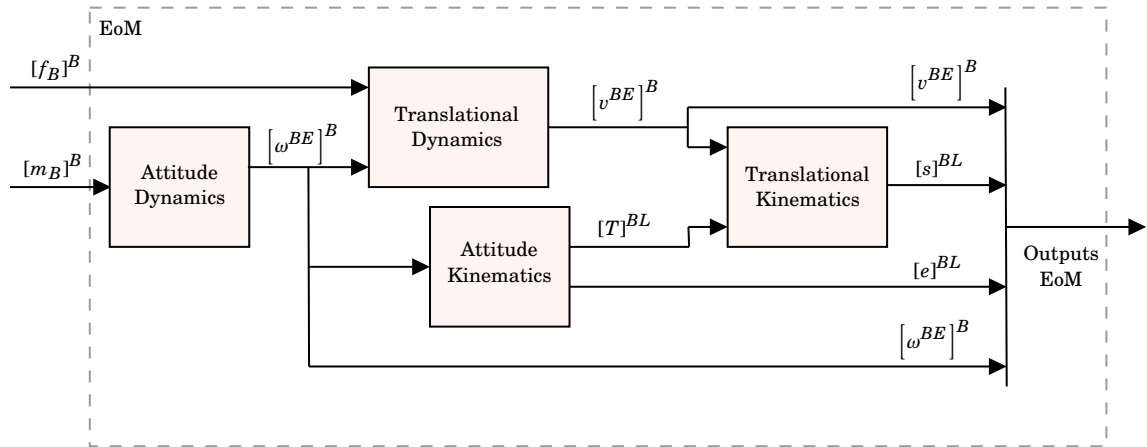
Figure 5.3: EoM System of Flying-V model, implemented in Simulink®.

ATTITUDE DYNAMICS

Attitude dynamics formulate the attitude equations, which are governed by Euler's law. As depicted in Equation (5.9), the law states that the time rate of change of angular momentum is equal to the moments applied externally, $\boldsymbol{m}_B$. [Zipfel, 2007]

$$D^E\left(\boldsymbol{I}_B^B \boldsymbol{\omega}^{BE}\right) = \boldsymbol{m}_B, \tag{5.9}$$

where $\boldsymbol{I}_B^B$ is the moment of inertia of the aircraft body frame B referred to the CoM and $\boldsymbol{\omega}^{BE}$ are the angular rates of body frame B with respect to frame E.

Moreover, Euler's transformation (see Equation (5.5)) is applied, in order to express the rotational derivative in the body frame. Expanding it with the chain rule, yields Equation (5.10).

$$\underbrace{D^B \boldsymbol{I}_B^B}_{= \, 0 \text{ for a rigid body}} \boldsymbol{\omega}^{BE} + \boldsymbol{I}_B^B D^B \boldsymbol{\omega}^{BE} + \boldsymbol{\Omega}^{BE} \boldsymbol{I}_B^B \boldsymbol{\omega}^{BE} = \boldsymbol{m}_B, \tag{5.10}$$

The body coordinate system was chosen given that it expresses the moment of inertia tensor in constant form, it results in the ordinary time derivative of the body rates and represents the aerodynamic moments in their preferred format [Zipfel, 2007]. Thus,

$$\left[I_B^B\right]^B \left[\frac{d\omega^{BE}}{dt}\right]^B + \left[\Omega^{BE}\right]^B \left[I_B^B\right]^B \left[\omega^{BE}\right]^B = \left[m_B\right]^B$$

$$\iff \left[\frac{d\omega^{BE}}{dt}\right]^B = \left(\left[I_B^B\right]^B\right)^{-1} \left(-\left[\Omega^{BE}\right]^B \left[I_B^B\right]^B \left[\omega^{BE}\right]^B + \left[m_B\right]^B\right), \tag{5.11}$$

where

$$\left[\omega^{BE}\right]^B = \begin{bmatrix} p \\ q \\ r \end{bmatrix} \quad \text{and} \quad \left[\Omega^{BE}\right]^B = \begin{bmatrix} 0 & -r & q \\ r & 0 & -p \\ -q & p & 0 \end{bmatrix}. \tag{5.12}$$

TRANSLATIONAL DYNAMICS

Moreover, the translational dynamics are derived from Newton's second law wrt the inertial frame which, for the flat-Earth assumption, leads to Zipfel [2007]:

$$mD^I \boldsymbol{v}_B^I = \boldsymbol{f}_{a,p} + m\boldsymbol{g} \iff mD^E \boldsymbol{v}_B^E = \boldsymbol{f}_{a,p} + m\boldsymbol{g}, \tag{5.13}$$

where m is the aircraft mass, D^E is the rotational time derivative, $\boldsymbol{v}_B^I$ (= $\boldsymbol{v}_B^E$) is the velocity of the vehicle center of mass (CoM) in frame B wrt the inertial frame I (which is assumed to be earth frame E), $\boldsymbol{f}_{a,p}$ are the subjected aerodynamic and propulsion forces, and $\boldsymbol{g}$ is the gravity term.

By applying the Euler transformation (see Equation (5.5)), the rotational time derivative can be shifted to the body reference frame. Equation (5.14) is valid in any coordinate system.

$$m(D^E \boldsymbol{v}_B^E + \boldsymbol{\Omega}^{BE} \boldsymbol{v}_B^E) = \boldsymbol{f}_{a,p} + m\boldsymbol{g}, \tag{5.14}$$

Although in Zipfel [2007] the body frame was the chosen coordinate system, the wind frame and coordinate system are the most adequate since the relevant states (V and α) can be directly used in the linearization without recurring to any approximations. This derivation in the wind framework was conducted in Naäman [2024]. The most important steps are, thus, described. Equation (5.14) was transformed to the wind frame W:

$$m\left(D^W \boldsymbol{v}_B^E + \boldsymbol{\Omega}^{WB} \boldsymbol{v}_B^E\right) + m\boldsymbol{\Omega}^{BE} \boldsymbol{v}_B^E = \boldsymbol{f}_{a,p} + m\boldsymbol{g}, \tag{5.15}$$

All terms are expressed in the coordinate system $]^W$ and the unknown body rates and forces in the Wind coordinate system are transformed into known representations, as represented in the under-brace descriptions:

$$m\left[\frac{dv_B^E}{dt}\right]^W + m\left[\Omega^{WB}\right]^W \left[v_B^E\right]^W + m\underbrace{\left[\Omega^{BE}\right]^W}_{[T]^{WB}\left[\Omega^{BE}\right]^B[\bar{T}]^{WB}} \left[v_B^E\right]^W = \underbrace{\left[f_{a,p}\right]^W}_{[T]^{WB}\left[f_{a,p}\right]^B} + m\underbrace{\left[g\right]^W}_{[T]^{BL}[g]^L}, \tag{5.16}$$

It should be noted that zero wind conditions are assumed. The term $\left[D^W v_B^E\right]^W$ corresponds to the change in velocity of the aircraft body wrt the Earth, in the wind axis. Additionally, it is also important to express the angular rates of the wind to the body frames, in the wind coordinate system, $\left[\Omega^{WB}\right]^W$. The skew-symmetric tensor can be obtained from the angular rates from the Earth to the body reference frames in $]^W$ ($\left[\Omega^{WB}\right]^W = \left[\omega^{WB}\right]^W \times I$). The latter is dictated by the derivatives of $\dot{\alpha}$ and $\dot{\beta}$, as it can be verified in Figure 5.4. Thus, the expression was solved for $\dot{V}, \dot{\alpha},$ and $\dot{\beta}$, concluding the derivation of the most important steps of the translational dynamics.
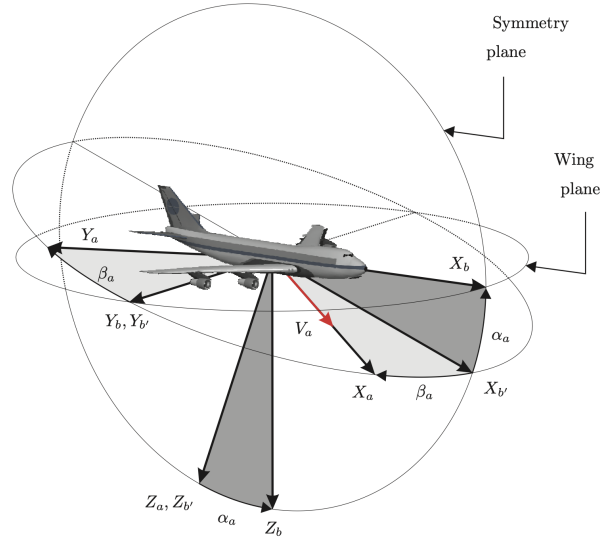
Figure 5.4: Transformation from the body-fixed reference frame (F_b) to the wind reference frame (F_a). Subscript $_a$ corresponds to the wind/aerodynamic reference frame, whereas $_b$ corresponds to the body frame. [Mulder et al., 2013]

ATTITUDE KINEMATICS

Furthermore, the body attitudes can be retrieved from the body rates using three different approaches: Euler angle, quaternion, or direction cosine matrix [Zipfel, 2007].

The differential Euler angle equations are computed by using the transformation matrix between the Euler angles and the body frame, as derived in [Zipfel, 2007]:

$$\begin{bmatrix} \dot{\phi} \\ \dot{\theta} \\ \dot{\psi} \end{bmatrix} = \begin{bmatrix} 1 & \sin(\phi)\tan(\theta) & \cos(\phi)\tan(\theta)) \\ 0 & \cos(\phi) & -\sin(\phi) \\ 0 & \sin(\phi)\cos(\theta) & \cos(\phi)/\cos(\theta)) \end{bmatrix} \begin{bmatrix} p \\ q \\ r \end{bmatrix} \tag{5.17}$$

Although the Euler angles are directly calculated, which poses as an advantage of this method, singularities occur at $\theta = \pm\pi/2$.

TRANSLATIONAL KINEMATICS

Moreover, the location of the aircraft's CoM in frame B wrt an Earth reference point E is obtained by integrating twice the differential equations of the velocity vector [Zipfel, 2007] (output of the Translational Dynamics subsystem), which are described in Equation (5.18).

$$\dot{u} = \cos(\alpha)\cos(\beta)\dot{V} - \cos(\beta)\sin(\alpha)V\dot{\alpha} - \cos(\alpha)\sin(\beta)V\dot{\beta}$$
$$\dot{v} = \sin(\beta)\dot{V} + \cos(\beta)V\dot{\beta} \tag{5.18}$$
$$\dot{w} = \cos(\beta)\sin(\alpha)\dot{V} + \cos(\alpha)\cos(\beta)V\dot{\alpha} - \sin(\alpha)\sin(\beta)V\dot{\beta}$$

Hence,

$$\begin{bmatrix} D^E s_{BE} \end{bmatrix} = \begin{bmatrix} v_B^E \end{bmatrix} \tag{5.19}$$

The integration was carried out in the local-level coordinate system, as expressed in Equation (5.20).

$$\begin{bmatrix} \frac{ds_{BE}}{dt} \end{bmatrix}^L = \begin{bmatrix} \bar{T} \end{bmatrix}^{BL} \begin{bmatrix} v_B^E \end{bmatrix}^B \tag{5.20}$$

The six first-order differential equations that are fundamental to the motion of the aircraft with the Earth as the inertial reference frame are, now, completely obtained.

5.1.5. SENSORS

For some measurements, including the normal acceleration, an extra device is needed. In this case an accelerometer / Inertial Measurement Unit (IMU) is used. However, in case the IMU is displaced from the CoM, additional corrections need to be taken into consideration. This transformation was addressed by Grubin and, thus, it carries his name [Zipfel, 2007]. To begin with, as described in Equation (5.21) and in Figure 5.5, the position vector of a point in the body B with respect to an inertial frame point I is equal to the sum of the position vectors from the sensor B_r to the CoM and from the inertial point to the reference sensor Zipfel [2007].

$$s_{BI} = s_{BB_r} + s_{B_rI} \tag{5.21}$$
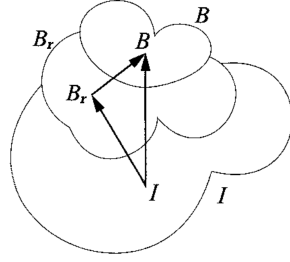
Figure 5.5: Reference frame B_r. Adapted from Zipfel [2007].

By performing the second derivative of the vector triangle in Equation (5.21) and by substituting the expression in Newton's Second Law, the result is the following:

$$m^B D^I D^I s_{BB_r} + m^B D^I D^I s_{B_rI} = f \tag{5.22}$$

Additionally, with successive Euler transformations applied to the first term and by assuming that the position of the sensor with respect to the body is fixed, the Grubin's form of Newton's second law is obtained:

$$m^B D^I v^I_{B_r} = f - m^B \Big(\underbrace{D^I \Omega^{BI} s_{BB_r}}_{\text{angular acceleration}} + \underbrace{\Omega^{BI} \Omega^{BI} s_{BB_r}}_{\text{centrifugal acceleration}} \Big)$$
$$\Longleftrightarrow a^I_{B_r} = a^I_B - \Big(D^I \Omega^{BI} s_{BB_r} + \Omega^{BI} \Omega^{BI} s_{BB_r} \Big) \tag{5.23}$$

Hence, Equation (5.23) describes the relation between the sensor acceleration and the acceleration of the body in the CoM. Nonetheless, it is important to note that the accelerometer is a specific force measuring device [Stevens et al., 2015]. Therefore, the magnitude of the true force acting on the accelerometer is equal to the accelerometer weight and has a negative direction to the gravity vector derived from the reaction of the surface where it is applied [Stevens et al., 2015]. Hence, it reads -1 g-unit, given that the (North-East-Down) NED reference frame is used. Nevertheless, as described in Section 5.1.3, in the airframe model the gravity was compensated by being added to the forces acting on the body. Thus, if no other compensation was reintroduced, the measured acceleration and, consequently, load factor would be null.

Moreover, conventionally, the load factor should have the opposite sign of the normal acceleration and, in the steady wings-level condition, it should measure +1 g-unit. Thus, the standard gravity compensation factor ($[T]^{BL}[g]^L$) is subtracted from the acceleration value and multiplied by $-1/g_0$. In case the gravity force was not added in the Airframe calculations, this factor would not be necessary.

Furthermore, given that a C^* control law will be designed, the value of n_z also needs to be captured in the Pilot Station (PS) or near the Instantaneous Center of Rotation (ICR), as it will be further discussed in the following chapters. Hence, Grubin's transformation can be applied analogously, where B_r and B correspond to the accelerometer and the PS/ICR positions, respectively.

IMU LOCATION

To begin with, the choice of sensors location plays an integral role in the aircraft design. In fact, the IMU detects not only the rigid-body motion but also higher frequency oscillation which are aggravated by the resonance or flexible mode of the structure. Hence, these undesired effects may be passed through the FCS, which may possibly create unstable structural coupling characteristics. [Kim et al., 2024]

Although no aero-elasticity effects are considered within the model, the location of the sensor has to be decided. It is widely known that the sensor should be positioned at a location where structural coupling with the lowest-frequency modes is the smallest. However, different approaches are followed for several configurations of aircraft [Kim et al., 2024]. For instance, in the Experimental Aircraft Program, where tests were conducted on the forerunner of Eurofighter, the sensors were located where cooling air could be more easily supplied to, to tackle electronics overheating. Nevertheless, the fuselage bending mode largely excited the pitch angular rate response [Caldwell et al., 2000]. Additionally, in the F-22 Raptor, the accelerometers were placed at the cockpit [Jr, 1999]. Lastly, in the AFTI/F-16 fighter, it was located forward to the CoG and as close as possible to the center of percussion [Kim et al., 2024].

A more in-depth investigation should be conducted specifically for the Flying-V. Nonetheless, as a preliminary position, it was assumed the sensor should be placed slightly in front of the most forward ICR position. This location is assumed to have reduced sensitivity to structural and other HF sources. This point was computed for all the available data points of the flight envelope based on the SP approximation, by applying the formula [McRuer et al., 1973]:

$$l_{x_{ICR}} = \frac{Z_{\delta_e}}{M_{\delta_e}} \tag{5.24}$$

The values to be applied in Equation (5.24) are obtained directly from the B matrix of the SP state space and from the trimmed airspeed velocity V_0, given that

$$\dot{x} = Ax + Bu, \text{ where } B = \begin{bmatrix} \frac{Z_{\delta_e}}{V_0} \\ M_{\delta_e} \end{bmatrix} \tag{5.25}$$

The ICR locations obtained for each flight condition, which is dependent on Mach number and altitude, are displayed in Table 5.2.

Table 5.2: ICR distance from the CoG (towards the nose) for several flight conditions.

Flight Condition	ICR location (m)
Ma = 0.6, h = 3250 m	6.9805
Ma = 0.6, h = 5450 m	6.9778
Ma = 0.6, h = 7650 m	6.9686
Ma = 0.5, h = 3250 m	7.0526
Ma = 0.5, h = 5450 m	7.0410
Ma = 0.5, h = 7650 m	7.0147
Ma = 0.4, h = 3250 m	7.0873
Ma = 0.4, h = 5450 m	7.0503

Hence, the location for the sensor was defined to be at a distance of 7.2 meters from the CoG, towards the nose. Moreover, it is known that any point of the aircraft located aft of the ICR experiences a non-minimum phase (NMP) behavior. Thus, for instance, in a pitching up movement, that point experiences, at first, a sinking movement. This phenomenon can be clearly verified by examining Figure 5.6 and Figure 5.7, where the commanded elevator deflection to normal acceleration TF poles and zeros are shown. On the left side, in Figure 5.6, the load factor is being measured in the CoG, whereas on the right, in Figure 5.7, the variable is being measured in the IMU location, slightly forward to the ICR. As expected, from the CoG to the IMU, the NMP zeros frequency starts increasing until it reaches the point where the zeros migrate to the left hand plane (LHP). This transition occurs in the ICR location. Furthermore, it is important to note that the forward value for the CoG of 29.372 meters was taken from van Overeem [2022], given that it was the point where the response of the Flying-V was considered to be more sluggish.
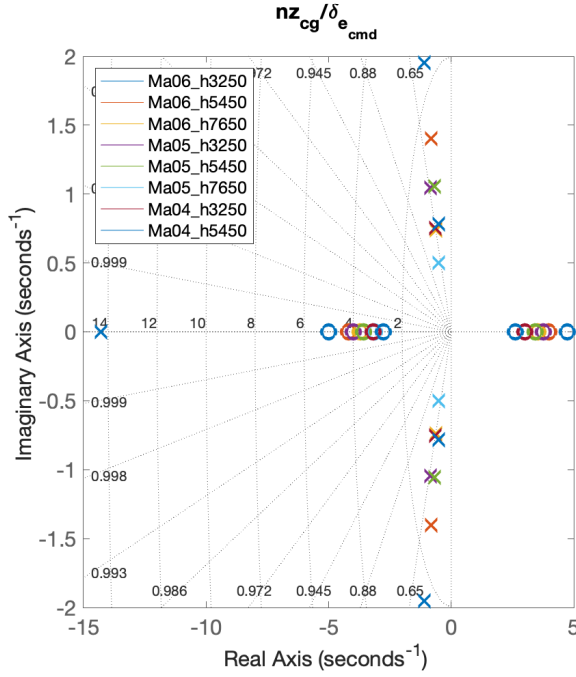
Figure 5.6: Pzmap of the TF from the elevator deflection command to the normal acceleration at the CoG, for several flight conditions.
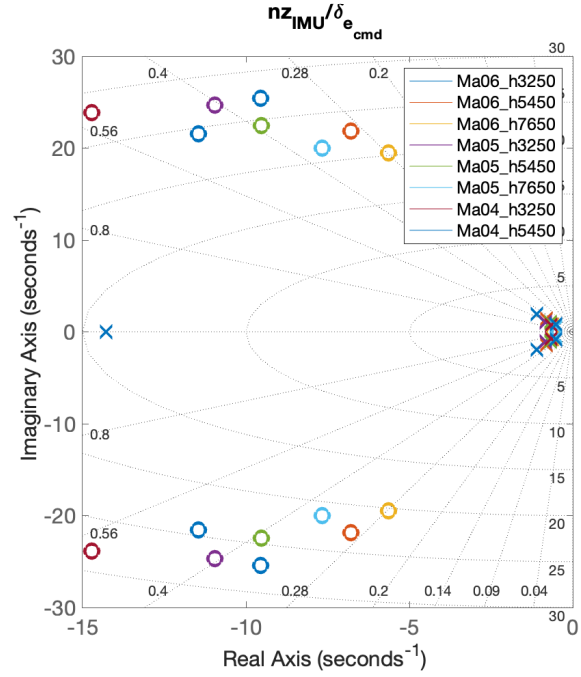
Figure 5.7: Pzmap of the TF from the elevator deflection command to the normal acceleration at the IMU, for several flight conditions.

5.2. Trimming & Linearization

Steady-state flight provides an initial condition for flight simulation, ensuring stability and maintaining the desired flight condition. In fact, equilibrium point computation is the first step towards the linearization of the nonlinear dynamics. Hence, the complex dynamics are approximated around the operating points, which allows efficient analysis, control system design, and stability assessment.

Thus, the trimming methodology will be further discussed in Section 5.2.1, followed by the results that validate the accuracy of the trimming procedure, in Section 5.2.2. Lastly, in Section 5.2.3, the linearization process is discussed more in depth.

5.2.1. Trimming Methodology

To begin with, the accuracy of the linearized model is intimately dependent on the accuracy of the trimming, provided that the linear approximations describe small perturbations around a certain trim condition. Thus, it is crucial that this foundation is computed based on accurate assumptions.

The trimming procedure involves the calculation of the equilibrium points around an imposed condition $\boldsymbol{\rho}(t) = \bar{\boldsymbol{\rho}} = [\bar{M}_a \ \bar{h}]^T$ so as to zero out the forces and moments contribution of the body and control surfaces. The EoM can be represented in a general parameter-dependent form as:

$$\begin{cases} \dot{\mathbf{x}}(t) = \mathbf{f}_x[\mathbf{x}(t), \mathbf{u}(t), \boldsymbol{\rho}(t)], \ \ t \in \mathfrak{R}_+ \\ \mathbf{y}(t) = \mathbf{f}_y[\mathbf{x}(t), \mathbf{u}(t), \boldsymbol{\rho}(t)] \end{cases} \tag{5.26}$$

where $\mathbf{x} = [p \ q \ r \ \phi \ \theta \ \psi \ V \ \alpha \ \beta \ x_L \ y_L \ z_L]^T$ represents the state vector, $\mathbf{u} = [T \ \delta_a \ \delta_e \ \delta_r]^T$ is the control input vector, and $\mathbf{y} = [n_x \ n_y \ n_z \ p \ q \ r]^T$ is the output vector. The aircraft is in equilibrium if $\dot{\mathbf{x}}(t) \overset{\Delta}{=} 0$. Solving this condition assumes that there are as many algebraic equations as unknown variables, which is not the case.

Thus, it is fundamental to address which variables can be chosen independently and what constraints exist on the remaining state and control variables. Firstly, the control variables, which consist of the thrust (T) and control surface deflections (aileron, elevator, and rudder) must be adjusted by the trimming algorithm. Secondly, the NED altitude can be predefined, given that the flight conditions around which the trimming procedure is conducted are dependent on this state and the Mach number. However, the

other two position states are not relevant. Additionally, for steady wings-level flight, we can consider that the roll angle, ϕ, and the angular rates, p, q, r, are all null. The yaw angle, ψ, can be specified freely. Nonetheless, the sideslip angle, β, must be adjusted by the algorithm, in case a side force has to be counteracted. Hence, only the states V, α, and θ remain to be considered. However, the first two states are interrelated because of the lift through the dynamic pressure and the lift coefficient. Thus, V is signaled as known and α as not known. Therefore, the unknown variables are: $\theta, \alpha, \beta, \delta_a, \delta_e, \delta_r$, and the thrust, which accounts for 7 variables. However, from the forces and moments equations, only six unknown variables can be found. Hence, an output constraint is imposed on the flight path angle, γ, for it to be zero. Thus, given that $\gamma = \theta - \alpha$, the number of variables to be trimmed by the procedure is adequate. This information is summarized in Table 5.3. [Stevens et al., 2015]

Table 5.3: Trimming object specifications.

States	Steady State	Known	Inputs	Known	Outputs	Known
p	✓	✓	T	✗	γ	✓
q	✓	✓	δ_a	✗		
r	✓	✓	δ_e	✗		
ϕ	✓	✓	δ_r	✗		
θ	✓	✗				
ψ	✓	✓				
V	✓	✓				
α	✓	✗				
β	✓	✗				
x_L	✗	✓				
y_L	✓	✓				
z_L	✓	✓				

The trimming can be conducted either with an analytical or numerical method. The former involves solving the moment and forces equations, which is complex and time-consuming. The latter, on the other hand, iteratively adjusts the independent variables until the requirements are met, which can be tightened as desired. The numerical approach is followed [1]. Several options for the algorithm were outlined, which are summarized in Table 5.4.

To begin with, the optimizer type chosen was *lsqnonlin*. While the *graddescent-elim* is the function default option [2], it is a very strict optimizer, where equality constraints are imposed to force the states time derivatives to zero and output signals to be equal to their specified known values. Consequently, the optimizer fixes the state and inputs that are marked as *Known* and optimizes the remaining variables. Nevertheless, *lsqnonlin* provides a more flexible approach, which can be tightened as much as needed by the number of function evaluations, iterations, and tolerance values. As observed in Table 5.4, these variables were exploited to great extent, in order to achieve the best results possible. Thus, the working principle of this optimizer consists of first fixing the states and inputs marked as *Known* and optimizing the remaining variables. Then, the algorithm tries to minimize both the error in the time derivatives of the states and the error between the outputs and their specified known values. Given that the system is highly nonlinear, imposing equality constraints make it more challenging to converge to a feasible solution. Hence, *lsqnonlin* balances multiple errors rather than enforcing hard constraints. Moreover, the *trust-region-reflective* was chosen, as it is a large-scale algorithm.

---

[1] `findop()` MATLAB® function is used. Its arguments are the Simulink® model, the operating point object of the system states, inputs and outputs, and the options object of the numerical algorithm, which uses the function `findopOptions()` of the Simulink Control Design toolset.

[2] https://www.mathworks.com/help/slcontrol/ug/findopoptions.html (Accessed in February 2025)

Table 5.4: Set of options for finding the operating point from specifications.

findop() & Optimization Options	Chosen Option
Optimizer type	*lsqnonlin*
Maximum number of function evaluations	2^9
Maximum number of iterations	2^9
Termination tolerance on function value	1^{-10}
Termination tolerance on x, the current point	1^{-10}
Algorithm	*trust-region-reflective*
Jacobian	*on*
Tolerance on the constraint violation	1^{-10}

5.2.2. TRIMMING RESULTS & DISCUSSION

Hence, with the procedure described in the previous section, the equilibrium points for each of the flight conditions are computed. The trimmed values for the control surfaces and motor's thrust are shown in Table 5.5. The thrust values include the contribution of both motors.

Moreover, it should be noted that, although sixteen aerodynamic data points were provided, only eight were considered for trimming and linearization, and subsequent controller design and analysis. This decision was driven by the low maturity of both the aerodynamic data and the aircraft's development. To begin with, it should be highlighted that the author of the thesis requested ten of these sixteen data points as supplementary information for this research, meaning the flight conditions were not specified by a member of the flight performance group. Moreover, the low velocity conditions until approximately $M_a = 0.3$ could not be trimmed due to thrust limitations. Furthermore, for these conditions, the values obtained for the trimmed AoA (if no limitations were imposed on the thrust), were extremely high. This highlights the need for further refinement of the Flying-V aerodynamic model. Furthermore, the conditions with the highest velocity, corresponding to $M_a = 0.7$, also portrayed undesired behavior. By observing the tendency of the pitching moment, it was verified that the aircraft would become unstable after 2.5° of AoA. Hence, given these challenges, only the central aerodynamic data points were deemed suitable to be used. All in all, the flight envelope is not fully determined yet and further iterations on the concept design may be necessary to improve the aircraft flight dynamics.

Table 5.5: Inputs trimmed values for each flight condition.

	Flight Condition							
	Ma = 0.6			Ma = 0.5			Ma = 0.4	
Variables	h = 3250 m	h = 5450 m	h = 7650 m	h = 3250 m	h = 5450 m	h = 7650 m	h = 3250 m	h = 5450 m
T (N)	113940	100540	116350	114770	114420	132300	96221	142440
δ_a (deg)	0	0	0	0	0	0	0	0
δ_e (deg)	-0.69	-1.57	-2.31	-1.22	-1.75	-2.92	-3.45	-3.63
δ_r (deg)	0	0	0	0	0	0	0	0

As expected, given that there is no wind modeled and that the aircraft is symmetrical, the lateral inputs have null values. Moreover, two main tendencies can be observed in the elevator deflection angles. Firstly, for a fixed velocity, increasing the altitude yields higher magnitudes. Secondly, for a fixed altitude, decreasing velocities also results in higher control deflection angles. Both behaviors are partly concerned with the dynamic pressure, $\bar{q}$, which decreases in lower velocities and higher altitudes since the air density, ρ, is also lower. Hence, the control effectiveness in these conditions is reduced, motivating larger deflections to generate the same forces and moments, which explains the first tendency. Additionally, to maintain the same lift, when the speed is reduced, the lift coefficient needs to be higher, which is why the second tendency is observed. This relation can be better understood by examining Equation (5.27). Higher deflection angles increase the angle of attack, which also rises the lift coefficient. Furthermore, it can also be seen that at Ma = 0.6, the aircraft is still on the backside of the power curve, since the thrust values, for a fixed altitude, are lower than for lower velocity conditions.

$$L = C_L \underbrace{\frac{1}{2}\rho V^2}_{\bar{q}} S \tag{5.27}$$

Figure 5.8 to Figure 5.11 portray the evolution of the aircraft states over a period of 50 seconds when the states and inputs are initialized with the values that were obtained from the trimming procedure. These simulations were run in the nonlinear Simulink® model.

The first three states are the angular velocities and their time series can be observed in Figure 5.8. It is verified that the trimmed values are all null by paying attention to the values for t = 0 seconds. Some oscillations in the pitch rate are visible. Nonetheless, the magnitude is in the order of 10^{-6} degrees and, therefore, it is not significant.

Figure 5.9 portrays the Euler angles evolution. The lateral angles remain at zero, as expected, whereas the values for the pitch angle are distributed over a large range. By comparing these results with the ones in Figure 5.10, which shows the airspeed velocity and the aerodynamic angles, it is possible to verify that the values for the angle of attack are equal to the angles of the pitch angle. This is the result of the additional constraint applied in the flight path angle. All of the states remain in the trimming condition, as it is observed by the completely stable values, validating the procedure. Additionally, the trimmed values for α corroborate the reasoning made on the elevator deflection magnitudes tendency. In fact, for a fixed altitude, when the velocity decreases, α rises. This occurs in order to augment the lift coefficient and maintain the same lift force applied on the aircraft. Moreover, for a fixed speed and higher altitudes, α is also higher. This effect is due to the air density being lower and, thus, the lift coefficient needs to be compensated.

Lastly, Figure 5.11 shows the the position values in the local-level coordinate system. The position in the x-axis is increasing, given that the aircraft is moving forward. There is no change in the y-axis position, given that no sideforce is applied in the aircraft. It is evident that the altitude remains stable in all conditions. The negative value in the z-axis is due to the frame used, NED.
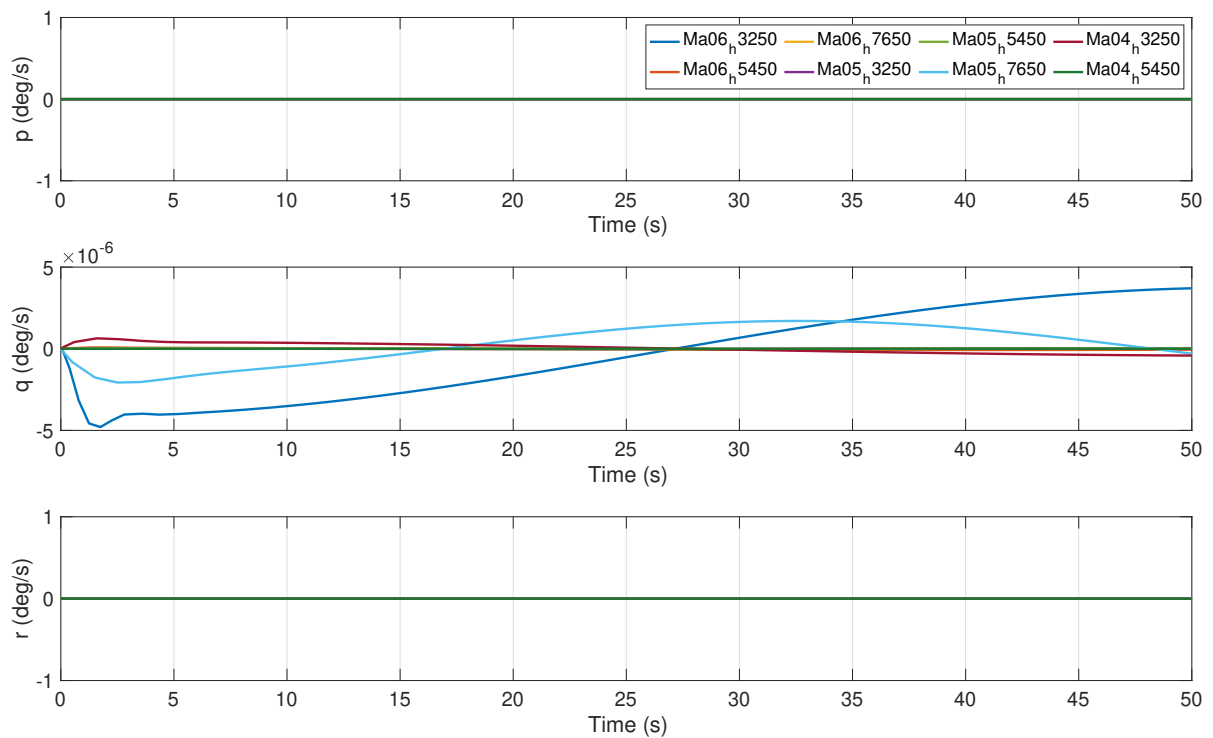
Figure 5.8: Nonlinear time simulations over 50 seconds of the angular velocities, when initializing the inputs and states with the trimmed values.
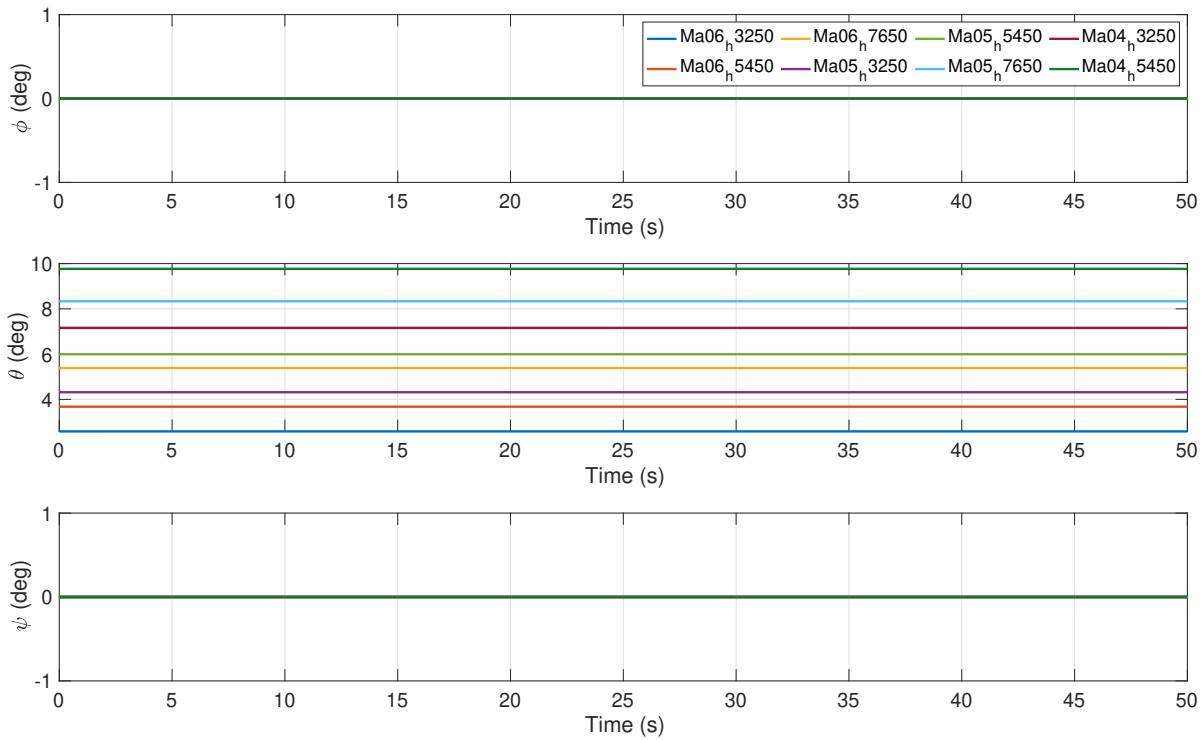
Figure 5.9: Nonlinear time simulations over 50 seconds of the euler angles, when initializing the inputs and states with the trimmed values.
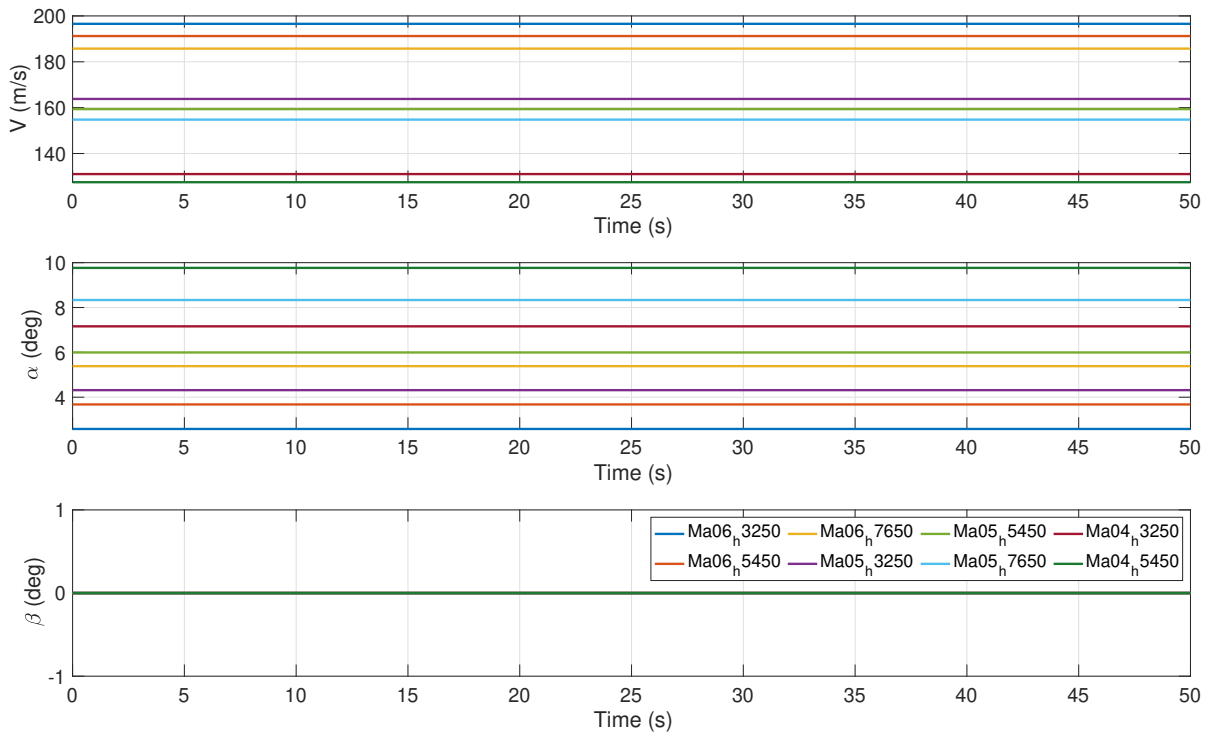
Figure 5.10: Nonlinear time simulations over 50 seconds of the airspeed and the aerodynamic angles, when initializing the inputs and states with the trimmed values.
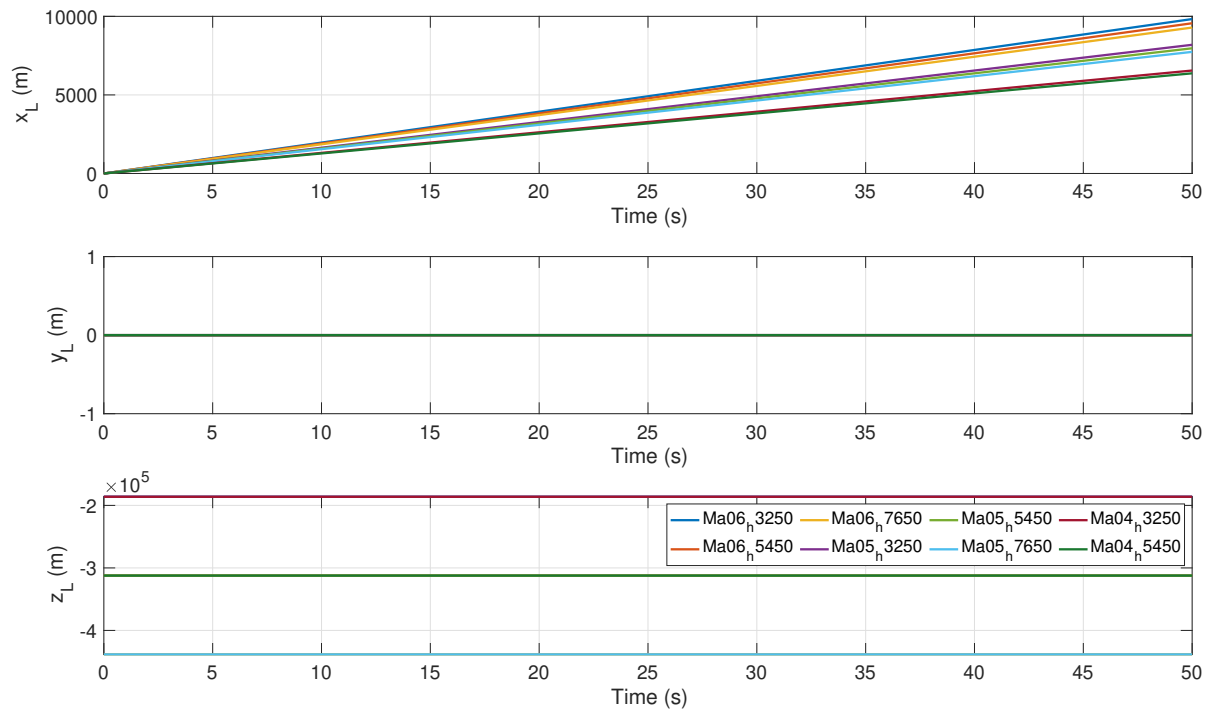
Figure 5.11: Nonlinear time simulations over 50 seconds of the aircraft position, when initializing the inputs and states with the trimmed values.

5.2.3. LINEARIZATION

The linearization procedure involves the approximation of the nonlinear dynamics, which were extensively discussed in Section 5.1, around the trim points. Thus, for each flight condition, there is a State Space (SS) representation of the form:

$$
\begin{aligned}
\dot{x}_\delta(t) &\approx A x_\delta(t) + B_u u_\delta(t) \\
y_\delta(t) &\approx C_y x_\delta(t) + D_{yu} u_\delta(t),
\end{aligned}
\tag{5.28}
$$

where the quantities $x_\delta(t) \approx x(t) - \bar{x}$ and $u_\delta(t) \approx u(t) - \bar{u}$ approximate deviations from the operating point. Here, the higher order terms are assumed to be zero. It is important to note that, by abuse of notation, the δ will be omitted in the notation when referring to the SS models.

The linearized SS model involves all of the longitudinal and lateral states and inputs. However, for controller design, approximations of this model that excite the necessary states can be used. In fact, for the longitudinal motion, the SP and Phugoid modes can be used separately by only considering either the α and q states or the V and θ states. These SS models can be easily obtained by selecting the appropriate rows and columns of the complete SS dynamics. These considerations are further discussed in Section 5.3. Furthermore, similarly to the trimming procedure, the linearization can also be computed analytically or numerically. The numerical approach is followed [3].

5.3. BARE AIRFRAME ANALYSIS

In the previous section, the linearization process was introduced and, by applying it, it is possible to obtain the approximate dynamics of the aircraft around a certain trim condition. Moreover, for the Flight Control System (FCS) design, which is conducted in Chapter 6, a single flight condition is used. As previously discussed, there are eight flight conditions from which this flight condition could be chosen from. It was decided to consider the operating point which is located in the middle, in terms of altitude and Mach number, of the not fully determined flight envelope. This corresponds to a Mach number of 0.5 and an altitude of 5450 meters.

---

[3]`linearize()` MATLAB® function is used. Its arguments consist of the nonlinear Simulink® model, the inputs and outputs of the system, the operating point retrieved from the`findop()` function, the state order which specifies the order of the states in the SS model, and the linearization options.

Thus, for this specific condition, a Linear-Time-Invariant (LTI) system is obtained as the SS model, which is examined in the current section. Furthermore, given that the lateral dynamics are not relevant to the research goal, only the longitudinal states are selected, which yields in the system depicted in Equation (5.29). The outputs are defined to be the load factor in the CoG and the pitch rate.

$$
\begin{bmatrix} \dot{V} \\ \dot{\theta} \\ \dot{\alpha} \\ \dot{q} \end{bmatrix} = \underbrace{\begin{bmatrix} -6.654 \cdot 10^{-3} & -9.807 & 5.846 & -0.432 \\ 0 & 0 & 0 & 1 \\ -7.933 \cdot 10^{-4} & 1.659 \cdot 10^{-11} & -0.601 & 0.974 \\ 2.238 \cdot 10^{-4} & -9.173 \cdot 10^{-11} & -1.154 & -0.748 \end{bmatrix}}_{A} \begin{bmatrix} V \\ \theta \\ \alpha \\ q \end{bmatrix} + \underbrace{\begin{bmatrix} 4.144 \cdot 10^{-6} & -1.601 \\ 0 & 0 \\ -2.731 \cdot 10^{-9} & -0.141 \\ -2.897 \cdot 10^{-8} & -3.198 \end{bmatrix}}_{B} \begin{bmatrix} T \\ \delta_e \end{bmatrix}
$$

$$
\begin{bmatrix} n_z \\ q \end{bmatrix} = \underbrace{\begin{bmatrix} 0.01289 & -2.802 \cdot 10^{-10} & 9.655 & 0.4222 \\ 0 & 0 & 0 & 1 \end{bmatrix}}_{C} \begin{bmatrix} V \\ \theta \\ \alpha \\ q \end{bmatrix} + \underbrace{\begin{bmatrix} 0 & 2.3 \\ 0 & 0 \end{bmatrix}}_{D} \begin{bmatrix} T \\ \delta_e \end{bmatrix}
$$

(5.29)

The LTI systems can also be represented with transfer functions, using the Laplace operator s, as:

$$
H(s) = C(sI - A)^{-1}B + D, \tag{5.30}
$$

For the purpose of investigating the eigenmotions, the states were temporarily defined as the outputs Thus, C and D were defined, respectively, as the identity and a zeros matrix. Hence, the following set of TFs from the elevator input to the states are retrieved:

$$
\begin{aligned}
\frac{V}{\delta_e} &= \frac{-1.6006(s - 2.792)(s^2 + 3.794s + 3.861)}{(s^2 + 0.004114s + 0.006535)(s^2 + 1.352s + 1.575)} \\
\frac{\theta}{\delta_e} &= \frac{-3.1978(s + 0.5406)(s + 0.01643)}{(s^2 + 0.004114s + 0.006535)(s^2 + 1.352s + 1.575)} \\
\frac{\alpha}{\delta_e} &= \frac{-0.14129(s + 22.79)(s^2 + 0.006472s + 0.007823)}{(s^2 + 0.004114s + 0.006535)(s^2 + 1.352s + 1.575)} \\
\frac{q}{\delta_e} &= \frac{-3.1978s(s + 0.5406)(s + 0.01643)}{(s^2 + 0.004114s + 0.006535)(s^2 + 1.352s + 1.575)}
\end{aligned}
$$

(5.31)

From these equations, the dynamic behavior of the Flying-V can be examined. For completion, the pole-zero map of these equations is shown in Figure 5.12 and in the zoomed in Figure 5.13.
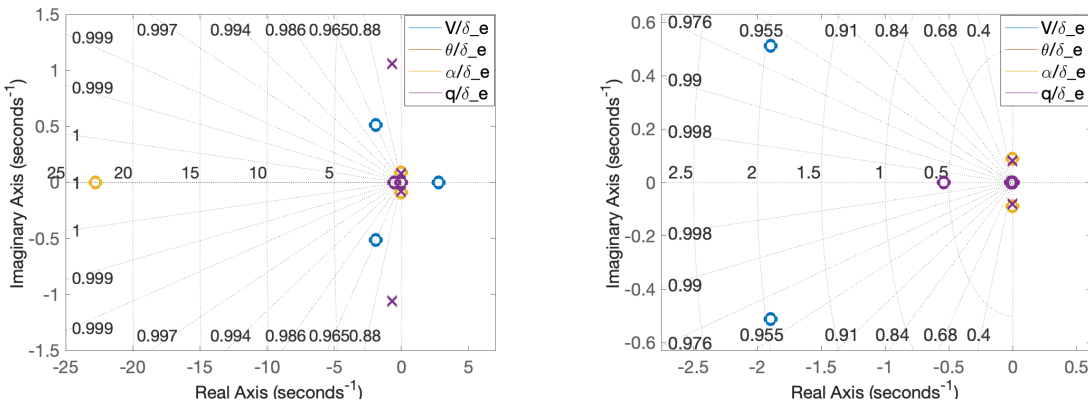
Figure 5.12: Pzmap of the elevator to states TFs. **Figure 5.13:** Zoomed in portion of Figure 5.12.

To begin with, it is observed that all of the denominators are the same, whereas the numerators are unique. The denominator, which corresponds to the characteristic polynomial, represents the dynamics of the two longitudinal modes: SP and phugoid. The pair of poles that define each motion can be clearly

identified in Figure 5.12, where the phugoid ones are closer to the origin. The main characteristics of both motions are represented in Table 5.6. The phugoid mode is very lightly damped. Given its long period, the pilot would have no difficulty in damping out the phugoid excitation [Stevens et al., 2015], although certain damping requirements still must be met for this motion. By observing Figure 5.13, it is verified that the poles are all in the LHP and, thus, the aircraft is longitudinally stable for the Ma = 0.5, h = 5450m flight condition. This affirmation is further corroborated by the Routh-Hurwitz criterion, given that the coefficients of the second order characteristic polynomials are all positive (see Equation (5.31)).

Table 5.6: Longitudinal characteristics of the SP and phugoid modes.

	Modes	
Characteristics	Short Period	Phugoid
Natural Frequency w_n (rad/s)	1.25	0.0808
Damping ratio ζ (-)	0.539	0.0254

Moreover, the contribution of each state to these modes is easily identified by investigating the frequency of the poles and zeros of each transfer function. For instance, in the α/δ_e TF (see Equation (5.31)), it is verified that the conjugated zeros cancel the phugoid eigenmotion. The SP approximation is directly reduced to the description in Equation (5.32). Additionally, in the q/δ_e TF (see Equation (5.31)), if the zero at the origin and the zero at $(s + 0.01643)$ cancel the phugoid poles, the SP approximation for the pitch rate results in the description in Equation (5.33). Conversely, although less straightforward, the zeros of the V/δ_e TF cancel partly the SP motion, given their higher frequency characteristics, as well as one of the zeros of the θ/δ_e TF.

$$\frac{\alpha}{\delta_e} = \frac{-0.14129(s + 22.79)}{(s^2 + 1.352s + 1.575)} \tag{5.32}$$

$$\frac{q}{\delta_e} = \frac{-3.1978(s + 0.5406)}{(s^2 + 1.352s + 1.575)} \tag{5.33}$$

Moreover, Figure 5.14 portrays the step response to one degree of elevator deflection of the complete longitudinal dynamics. The SP transient response can be fully observed in the α and q states in the first 5 seconds, which is not visible in the other two states, provided the extremely LF. This corroborates the results drawn in the frequency domain.
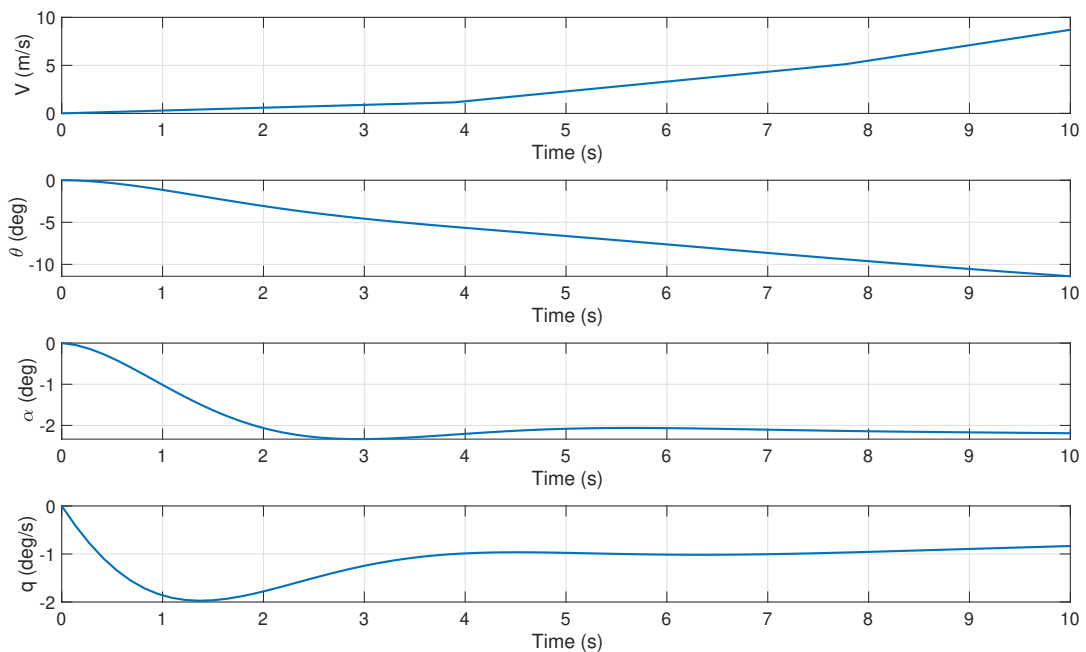
Figure 5.14: Step response of the states to 1 degree of input deflection over 10 seconds.

As previously mentioned, since the frequency of the phugoid motion is so low, the human pilot easily handles it. On the contrary, the frequency of the SP motion is much closer to that of the pilot. Thus, to achieve satisfactory HQ, the SP is a key eigenmotion for the controller design. Additionally, as it is widely accepted, the reduced model of the short period approximation will be used throughout the thesis as the foundation for controller design in the linear domain. This SS model will be introduced and its validity will be verified. From the full order longitudinal dynamics presented in Equation (5.29), the columns and rows that are solely dependent on the α and q states, which are the ones that are most dominant in the SP, and on the elevator deflection input are selected. Consequently, the SP SS model results in:

$$
\begin{bmatrix} \dot{\alpha} \\ \dot{q} \end{bmatrix} = \underbrace{\begin{bmatrix} -0.601 & 0.974 \\ -1.154 & -0.748 \end{bmatrix}}_{A_{SP}} \begin{bmatrix} \alpha \\ q \end{bmatrix} + \underbrace{\begin{bmatrix} -0.141 \\ -3.198 \end{bmatrix}}_{B_{SP}} \delta_e
$$

$$
\begin{bmatrix} n_z \\ q \end{bmatrix} = \underbrace{\begin{bmatrix} 9.655 & 0.4222 \\ 0 & 1 \end{bmatrix}}_{C_{SP}} \begin{bmatrix} \alpha \\ q \end{bmatrix} + \underbrace{\begin{bmatrix} 2.3 \\ 0 \end{bmatrix}}_{D_{SP}} \delta_e
$$

(5.34)

In order to verify the validity of this approximation, the frequency gain and phase plots of the elevator to load factor and of the elevator to pitch rate TFs of the complete longitudinal dynamics were compared to the SP ones. This analysis is presented in Figure 5.15-Figure 5.18. Regarding Figure 5.15 and Figure 5.16, the magnitude plots of the elevator to n_z and q, respectively show a similar tendency. In both plots, a large peak is observed at a frequency close to the natural frequency of the lightly damped phugoid mode ($w_n = 0.0808$ rad/s). The noticeable but smaller peak is due to the more heavily damped SP mode. From the phase and magnitude plots, it is concluded that the approximation closely matches the full dynamics for frequencies higher than around 0.02 Hz.
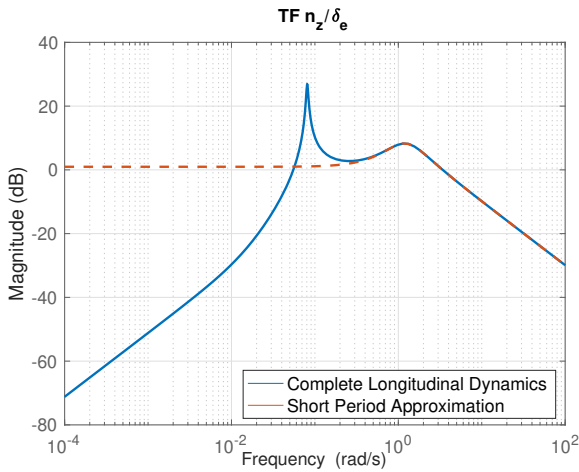
Figure 5.15: Bode gain plot of the elevator to load factor transfer function.
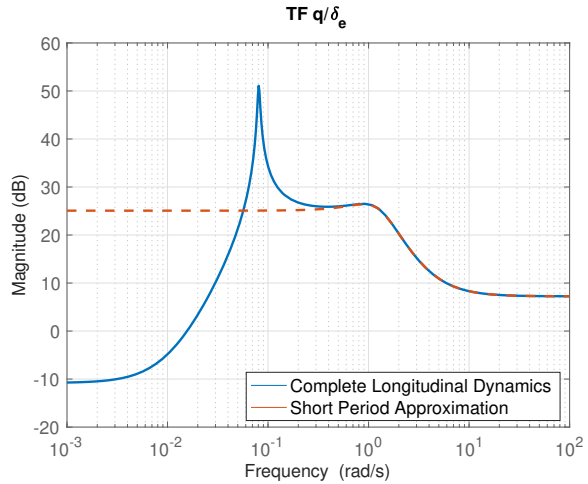
Figure 5.16: Bode gain plot of the elevator to pitch rate transfer function.
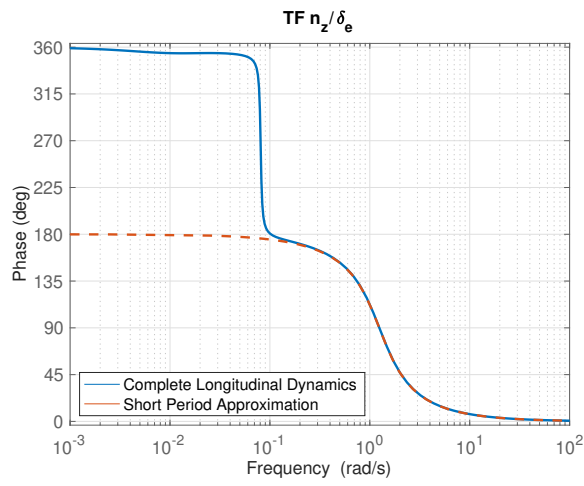
Figure 5.17: Bode phase plot of the elevator to load factor transfer function.
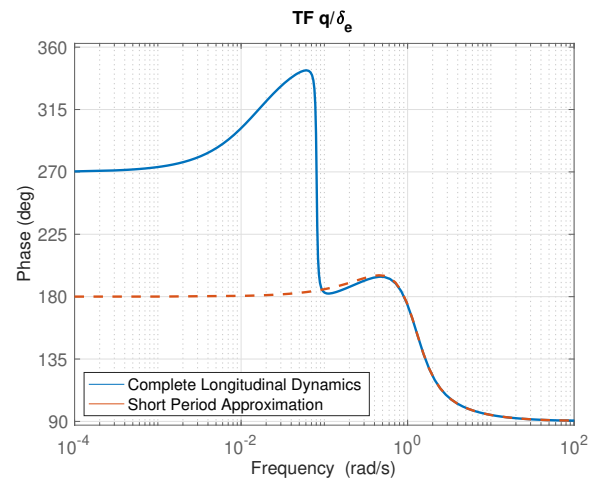
Figure 5.18: Bode phase plot of the elevator to pitch rate transfer function.

6

FLIGHT CONTROL SYSTEM SYNTHESIS

The current chapter focuses on the development and synthesis of the C^* longitudinal controller. To achieve that, several design alternatives are evaluated in Section 6.1 and the requirements to impose on the design are specified in Section 6.2. The final design decided from the first section is, consequently, synthesized in a CT formulation in Section 6.3 and in a modified CT formulation to implement as a digital controller, in Section 6.4. Lastly, the digital controller design is expanded to a region of the flight envelope and a multi-modeling modified CT controller design is conducted in Section 6.5.

6.1. FLIGHT CONTROL SYSTEM DESIGN OPTIONS

From Section 4.3 regarding the C^* longitudinal law, it is clear that there are several formulations that can be followed. In order to justify the final approach, three main design characteristics are discussed. The first design alternative, further analyzed in Section 6.1.1, is concerned with the decision of which signals should be used in the feedback. Secondly, the locations where the performance and feedback signals are measured are also of interest and will be further examined in Section 6.1.2. Lastly, the output disturbance modeling is also investigated for two different alternatives, in Section 6.1.3.

To evaluate the different design alternatives, several controllers were synthesized. However, the main purpose of the current section is to motivate the designs presented in Section 6.3, Section 6.4, and Section 6.5. Therefore, in the current section, only the final results and conclusions of the different setup configurations will be analyzed. For further details on the design and procedure to obtain such controllers, please refer to Section 6.3.2.

6.1.1. FEEDBACK SIGNALS

As it was previously mentioned in Section 4.3, there are several configurations for the FCS, by using the C^* or C^*-like approaches. In fact, besides the proportional controllers, the integral action can be applied in the n_z signal, in q, or in C^*. Hence, this choice needs to be further examined. The SP effects will be the main focus, as it is the approximation used for the linear controller synthesis procedure.

To begin with, the pitch rate feedback provides excellent attitude disturbance rejection, even in turbulent conditions, at the expense of possible heave motions. This occurs because the conventional aircraft gust alleviation response, that consists of pitching into gusts, is prevented. Nevertheless, the pilot may feel more in control given that the attitude is not being randomly disturbed and, thus, it can be an acceptable compromise. [Gibson, 1999]

Secondly, the normal acceleration command controls directly the flight path. In turbulence conditions, γ is less affected because α is continuously changed in order to maintain a constant vertical acceleration. Therefore, attitude disturbances are more prone to occur and the pilot is "closing the loop" to suppress the attitude excursion, introducing increased workload. [Gibson, 1999]

Moreover, combined demand systems are also a strong possibility, since none of the basic maneuver demand systems have all the favorable qualities on their own. This is where the C^* parameter comes into play. This signal is in line with the cues perceived by the pilots, which in low velocities are dominated by attitude control (q is the predominant signal), whereas in high velocities, the control priority shifts naturally to load factor, where structural limitations are also a priority. [Gibson, 1999]

From this discussion, the combined demand approach is considered as the most promising procedure. Nonetheless, given that in literature several FCS designs implement n_z as the feedback signal, this approach and the pure C* are both designed for further examination. Considering that the output disturbance is applied on the signal that is in the feedback path, a controller is synthesized using signal-based MS $\mathcal{H}_\infty$ for both methods, n_z and C*. For brevity reasons, only the open loops are evaluated. The open loops are retrieved by opening the system in several locations, namely at the plant input, L_i, and at the plant output at n_z in the CoG and q, respectively Lo_{n_z} and Lo_q, and at the virtual output C*$_{IMU}$, $Lo_{C*_{IMU}}$. The results are shown in Figure 6.1.

By observing Figure 6.1, it is verified that at HF, the open loops have similar magnitudes, which are low, as desired. On the contrary, at LF, it is verified that the signal that is fed back in each case can easily reject disturbances since it has a high magnitude. The other output signals have low magnitudes at LF, so these are affected by disturbances considerably.

Regarding the top plot in Figure 6.1, the C* has satisfactory disturbance rejection as previously stated, given the integral action applied on it, whereas the n_z and q signals have lower values. However, by looking at the plot at the bottom where the integral action is applied on n_z, it is verified that the disturbance rejection is excellent on this signal at the expense of lowering the rejection capabilities in the q channel even more.

Thus, it is concluded that to have a balanced disturbance rejection at LF in the signals q and n_z, the pure C* configuration should be followed, which also yields good disturbance rejection in this signal. Therefore, this conclusion is an additional reason to follow the combined demand approach.

It should be noted that, although the signals are measured at the PS in the results shown, these feedback configurations were also tested with the signals measured at the IMU location. The results obtained also follow the same tendency and, thus, are not depicted.
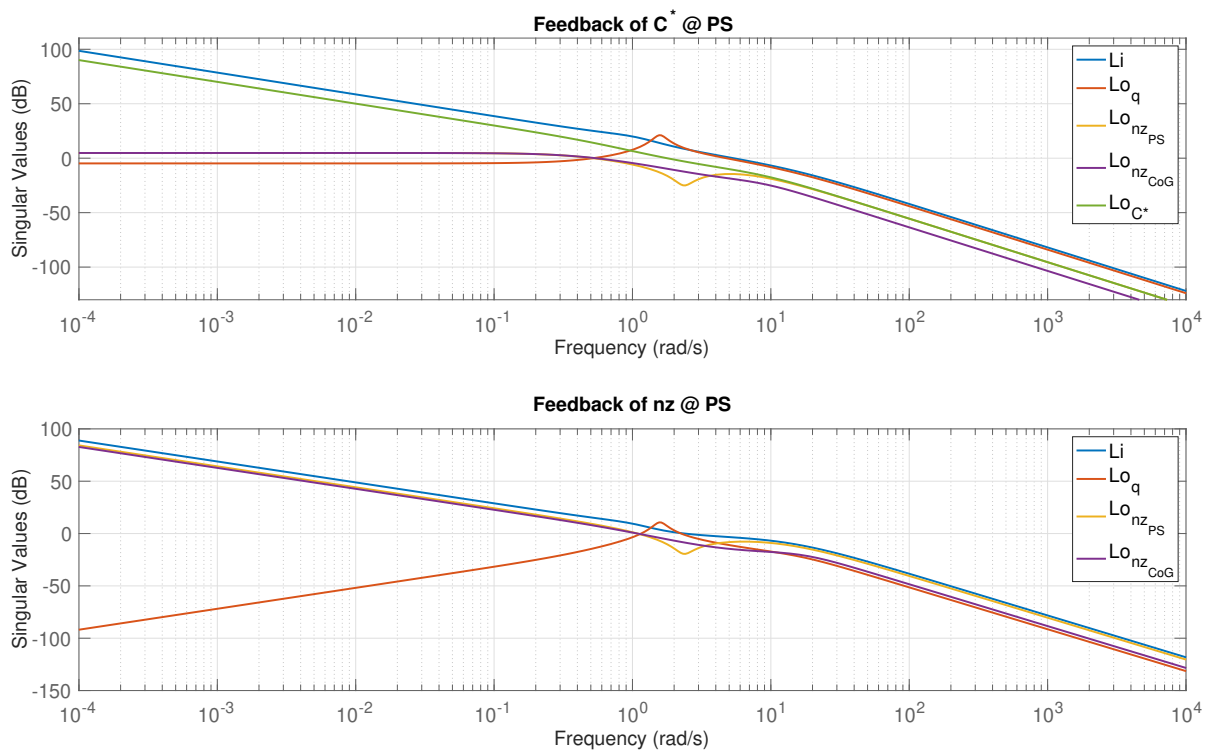
Figure 6.1: Input (Li) and Output (Lo) Open Loops for the controller synthesized with C* and n_z signals in the feedback, respectively portrayed at the top and bottom.

6.1.2. C* SIGNALS MEASUREMENT LOCATION

In the previous subsection, it was concluded that the feedback signal should be C*. Although many procedures compute the C* parameter with n_z at the PS because this signal is a reflection of how the pilot experiences the aircraft's dynamic response, this should also be more closely examined.

The performance signal is the one that is used to track a certain reference model so that the aircraft follows the correct trajectory. This signal was defined to be the C* parameter at the PS since it is intimately related to the motions the pilots feel and, therefore, the pilot stick inputs are more easily commanded.

However, the feedback signal, which is fundamental to providing the system robustness properties, can be a different one. In fact, it needs to be considered that:

$$n_{z_{PS}} = n_{z_{IMU}} + \frac{\dot{q}(x_{IMU \to CoG} + x_a)}{g_0}, \tag{6.1}$$

where $n_{z_{PS}}$ and $n_{z_{IMU}}$ are the load factors measured at the CoG and at the IMU, respectively. The term $x_{IMU \to CoG}$ = -7.2 meters corresponds to the distance from the IMU to the CoG location and x_a is equal to the distance between the CoG and the PS. This value was retrieved based on the information provided in van der Pluijm [2021], where the nose x-location was defined at x_{nose} = 1.5 meters and the cockpit end location at x_{PS} = 6.7 meters. Thus,

$$x_a = x_{CoG} - x_{nose \to PS} = x_{CoG} - x_{PS} + x_{nose} \iff x_a = 24.1720 \text{ meters.} \tag{6.2}$$

Therefore, two FCS are synthesized with the feedback signal C*. The first measures the signal at the PS, whereas the second measures it at the IMU. The open loops for both situations are presented in Figure 6.2.

To begin with, $\dot{q}$ dynamics have a relatively low contribution at LF. However, the opposite occurs at HF, yielding the second term on the right side of Equation (6.1) to significantly rise. This tendency is further amplified by being multiplied by the distance from the IMU to the PS. These behaviors can be verified by examining Figure 6.2, where at LF the open loop singular values of C* and n_z are very similar (so, low contribution of $\dot{q}$ dynamics) and at HF the signals measured at the PS have higher magnitudes.
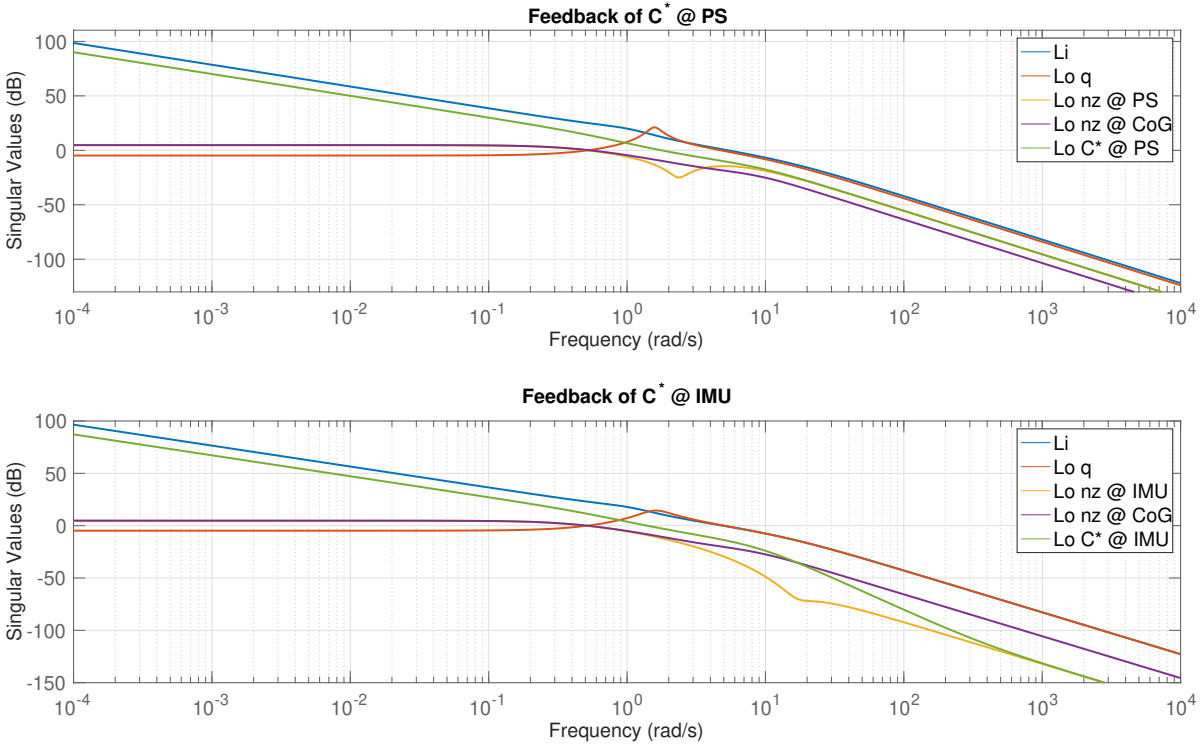
Figure 6.2: Open Loops of the FCS at several locations, using the C* signal for the feedback at the PS (top) and at the IMU (bottom).

Physically, it also makes sense that the gain at HF is higher in the PS than in the ICR, which is very close to the location of the IMU. While at the ICR the load factor is only dependent on the translational dynamics, at the PS there is an additional and high contribution of the angular accelerations.

It is decided to feedback the signal measured at the IMU. The reasoning behind this stands on the fact that open loop roll-off is desired at HF. This can be successfully achieved by not having a large derivative term in the n_z measurements which arises due to $\dot{q}$. As discussed in Section 5.1.5, there are several considerations to be carefully taken into account in terms of where the IMU should be located. However, in the current research, it was assumed that the IMU was placed slightly in front of the ICRs computed for the flight envelope. For further details on this topic, please refer back to Section 5.1.5. Therefore, in this location, since the angular accelerations are almost null, HF roll-off can be accomplished. Secondly, less control action is required to stabilize the aircraft given that in this location, there is not a big bump at the beginning of the step response of the elevator to load factor transfer function that needs to be compensated for.

All in all, the feedback signal is C^* measured at the IMU to provide robustness since it is less affected by sensitivity to structural and other sources of HF dynamics. On the contrary, the commanded signal to be tracked is C^* at the PS, since it better aligns with the pilot-perceived HQ requirements.

6.1.3. OUTPUT DISTURBANCE MODELING ANALYSIS

The $\mathcal{H}_\infty$ signal-based MS involves shaping the closed loop TFs to attenuate the disturbances, be robust against uncertainties, and maintain the desired performance specifications, as previously discussed in Section 4.1.6 and Section 4.1.7. Moreover, one of the most critical aspects is how to address the output disturbance, which affects the output of the system and can lead to tracking inaccuracies, degraded performance, and potential instability. Therefore, the output disturbance needs to be introduced in the design phase, to shape S_o and KS_o as desired.

Therefore, two synthesis approaches were considered. Case I entails considering directly the output disturbance which is added to the plant output, whereas, in Case II, the output disturbance is modeled. The two controllers were designed in a similar manner to the process detailed in Section 6.3.2. Thus, for a more detailed understanding of the mechanisms behind the design, the reader is invited to refer to that section. Overall, the main purpose of this section is to examine if modeling the output disturbance would bring benefits worth the extra complexity in the design phase. Therefore, this section is presented here to motivate the final design choice, which is going to be completely detailed in the following sections.

Furthermore, it should be noted that the integral action in the controllers designed is only applied in the feedback signal, C^*. Thus, it is not expected that the pitch rate and the load factor, which are the actual plant outputs, are ameliorated.

CASE I - NO OUTPUT DISTURBANCE MODELED

For simplification purposes, the disturbance is sometimes introduced directly at the plant output or feedback signal and it is not properly modeled as a physical characteristic of the system, as depicted in Figure 6.3, where K_q corresponds to the constant ratio V_{CO}/g, described in the C^* formulation (see Equation (4.45)).
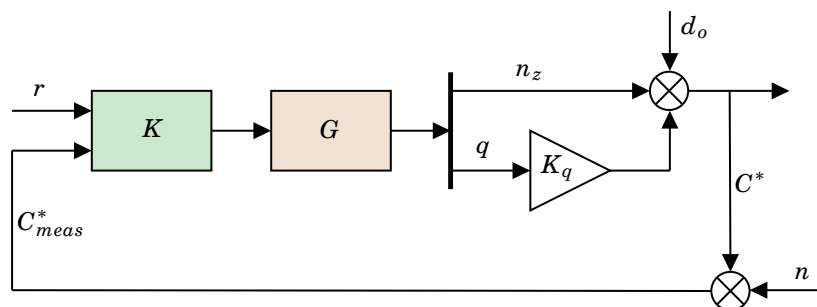
Figure 6.3: System setup with the output disturbance, d_o, applied on the C^* feedback signal.

Case II - Output Disturbance Modeled

Moreover, disturbances are LF signals that act on the plants. These can be, for instance, atmospheric disturbances, which can enter the system through α gusts (i.e. α_g). Therefore, it may be important to take this into the design procedure. Furthermore, to be precise, the linear model in terms of deviation variables is computed as:

$$y = Gu + G_d d, \tag{6.3}$$

where G, the plant model, is used to represent the effect of the inputs, u, on the outputs, y, whereas G_d, the disturbance model, represents the effect of disturbances, d, on the outputs. The G model is represented by the SP SS model, as described in Equation (5.34). To obtain G_d, the input matrix of the G model was expanded as shown in Equation (6.4), where it is assumed that α_g has the same aerodynamic effect as the variable α.

$$\begin{bmatrix} \dot{\alpha} \\ \dot{q} \end{bmatrix} = \begin{bmatrix} Z_\alpha(h, Ma) & Z_q(h, Ma) \\ M_\alpha(h, Ma) & M_q(h, Ma) \end{bmatrix} \begin{bmatrix} \alpha \\ q \end{bmatrix} + \begin{bmatrix} Z_{\delta_e}(h, Ma) \\ M_{\delta_e}(h, Ma) \end{bmatrix} \delta_e - \begin{bmatrix} Z_\alpha(h, Ma) \\ M_\alpha(h, Ma) \end{bmatrix} \alpha_g \tag{6.4}$$

Hence, G_d is obtained by considering the TFs from α_g to n_z and q. The FCS synthesis is also performed by modeling the gust, which is conducted as depicted in Figure 6.4
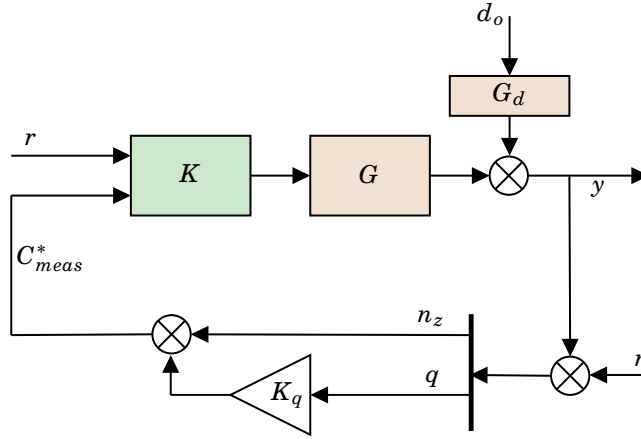
Figure 6.4: System setup with the output disturbance, d_o, modeled as an α gust.

Analysis & Discussion

The controllers are implemented and several variables are analyzed in the time domain. To begin with, the C^* and the α state time series in the presence of a gust are shown in Figure 6.5. For clearer results, the C^* commanded signal is null. Moreover, a 1-cos(α_g) with amplitude of 5 degrees and a period of 6 seconds, was introduced at the time instant $t = 6$ seconds. Both controllers are tested in the same condition with the angle of attack gust modeled in G_d provided that it is the most realistic one.

The disturbance rejection is extremely improved on the C^* channel with the second approach. Although it takes more time to stabilize, the response is smoother and, in terms of magnitude, its response is reduced by approximately 41%, in comparison with the first approach. The benefits of modeling the gust and using it in the controller synthesis are clearly noticeable. Thus, case II is the approach followed for the controllers design in the following sections.

Moreover, in Figure 6.6, the q and n_z outputs are also shown. As expected, the response for both controllers is similar, with a slight although not significant improvement for the second controller.
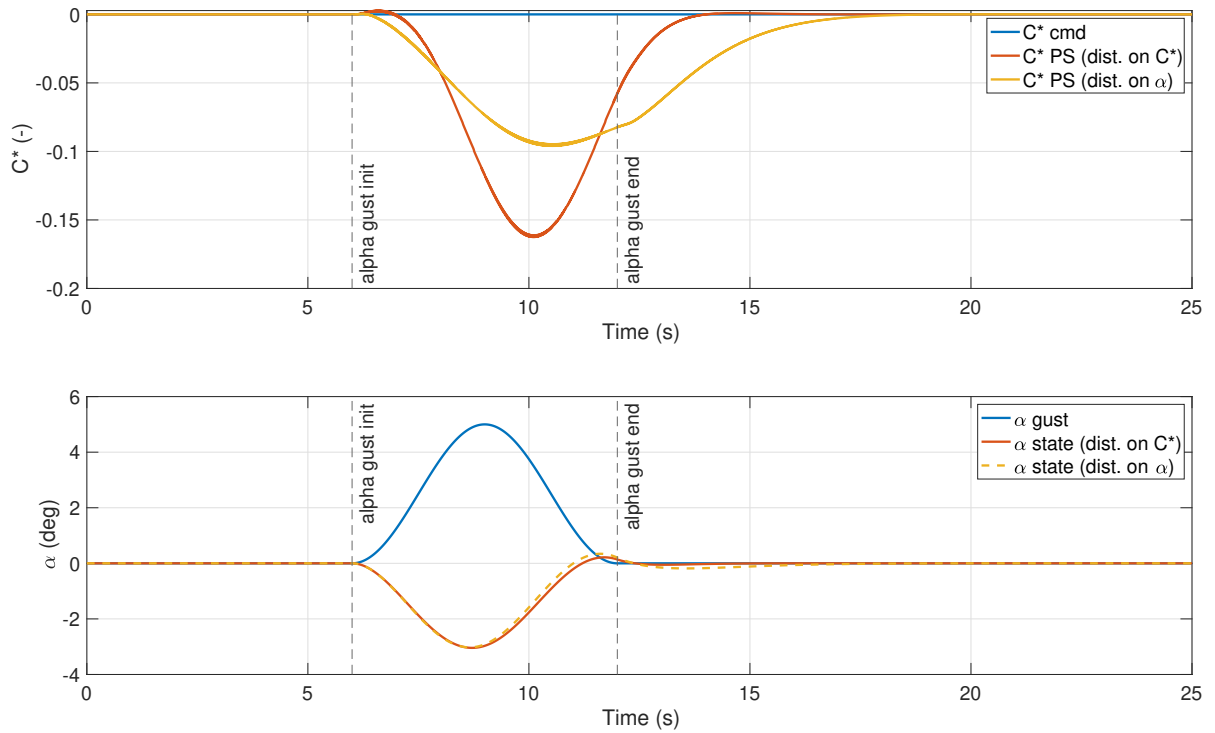
Figure 6.5: Tracking response of C* at the PS in the presence of an α gust, for two controller designs.
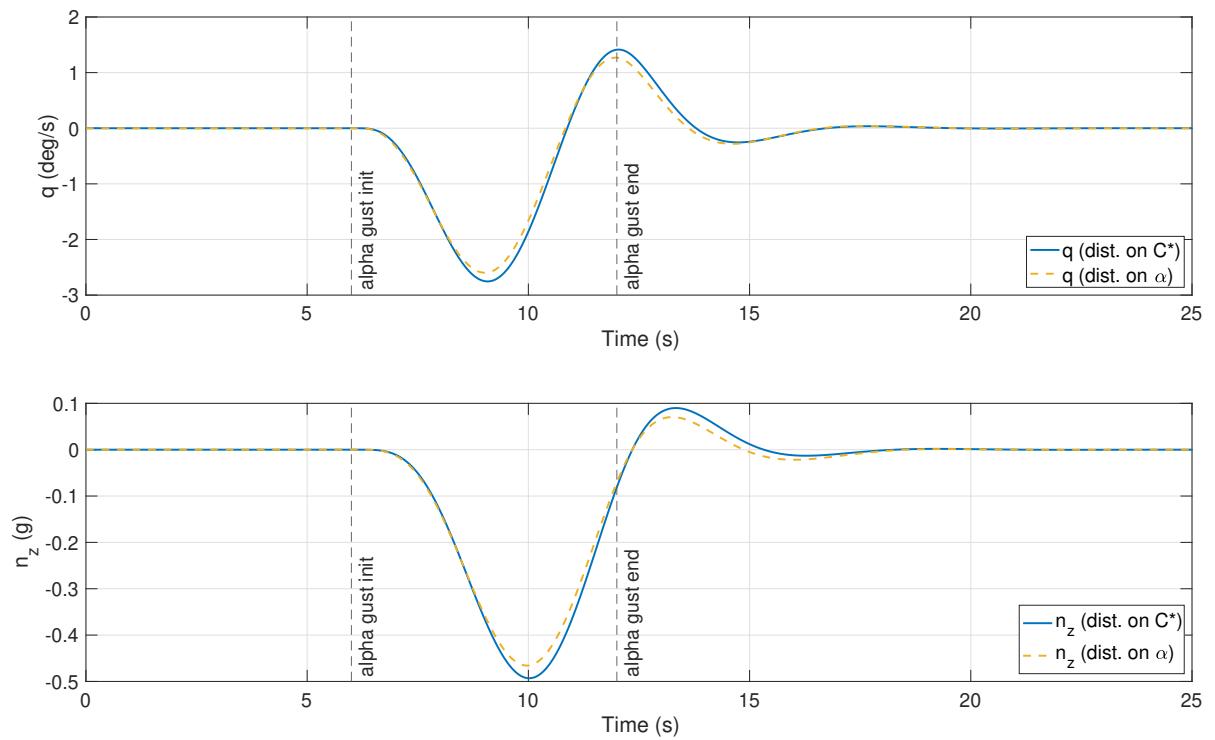
Figure 6.6: q and n_z responses in the presence of an α gust, for two controller designs.

6.2. DESIGN REQUIREMENTS

Before proceeding to the synthesis of the controller, it is fundamental to outline the goals to adequately define its design. These ensure safety and reliability of the aircraft operation by encompassing a range of critical considerations. The following specifications are considered:

(R1) Disturbance rejection at the plant input and output.

(R2) Sensor noise attenuation at the plant input and output.

(R3) Control effort reduction. As described in Table 5.1, the elevator deflection position and rates should also be in the range [-25º, 14º] and ± 60º, respectively.

(R4) Ideal minimum allowable limit for the classical stability GM and PM of 6 dB and 45°, respectively, for all broken loops in the plant input and output (soft constraint).

(R5) Robustness guarantees in terms of disturbance rejection and sensor noise and control effort attenuation in the presence of independent parametric uncertainties in the aerodynamic coefficients, varied across the range of ±30%. Stability margins shall not degrade by more than 50% of the requirements imposed in R4 in the presence of said uncertainty.

(R6) Predicted HQ within Level 1.

To fulfill these requirements, a feedback controller must be designed taking into account the fundamental trade-offs across all frequencies which were detailed in Section 4.1.5. The controller structure is the result of a balance between complexity and effectiveness, where a low order controller is preferred in a real implementation scenario.

Moreover, as discussed in Section 4.4, the stability margins (SM) requirement R4 is defined as for military standards, which, consequently, ensures that the civil ones are also met Cook [2013]. These requirements are highlighted in [Dobos-Bubno and Hartsook, 1977], [Seiler et al., 2020], and [Anonymous, 2000]. Therefore, given that the Flying-V is a civil aircraft concept, requirement R4 is a soft constraint where SM values close to 6 dB and 45° should be obtained, although it is not strictly necessary to have these lower bounds.

A fundamental control law design objective, as highlighted in requirement R6, is to achieve desirable and consistent flying qualities over the flight envelope, even in the presence of disturbances and uncertainties. The final objective is to achieve Level 1 in the Cooper-Harper Rating Scale when the controller is implemented and simulated by test pilots. For that, predicted HQ are examined. To achieve this requirement, a suitable response model is necessary. As previously stated in Section 6.1.1, the signal that will be tracked is C^* at the PS. An initial reference model was proposed, which was iteratively tuned to achieve the desired dynamics for the short-term pitch response specifications. Since the C^* parameter is not directly related to any main and frequently used HQ criterion as, for example, the pitch rate is, the reference model was gradually changed until a suitable model was achieved. This iterate process was conducted by testing the system against three main criteria that follow from the recommendations in Mitchell et al. [1994], namely the new Gibson's dropback criteria (pitch rate overshoot and pitch attitude dropback) in combination with the attitude and flight path bandwidth criteria. For the system to be properly tested, a preliminary controller had to be implemented. Nonetheless, given the adequate first approximation of the reference model, it revealed itself as a smooth process. The final reference model is of second order and it is described in Equation (6.5). For this specification, a feedforward controller can further enhance reference tracking capabilities.

$$T_{ref}(s) = \frac{C^*_{ref}(s)}{r(s)} = \frac{K_{num}(s + z_{ref})}{s^2 + 2\xi_{ref}\omega_{ref}s + \omega^2_{ref}} \tag{6.5}$$

Here, r corresponds to the pilot stick input signal. Taking into consideration the requirements for Class III aircraft (large, heavy, low-to-medium maneuverability aircraft) and Category B flight phase (non-terminal, cruise), adequate values were selected for the short-period frequency, damping, and numerator time constant [Anonymous, 1997]. Thus, to minimize control surface activity [Favre, 1994], the desired natural frequency was set to ω_{ref} = 1.4 rad/s, which is similar to the nominal bare airframe value (ω_{SP} = 1.25 rad/s) in the condition that will be evaluated (Ma = 0.5, h = 5450 meters). Additionally, defining the
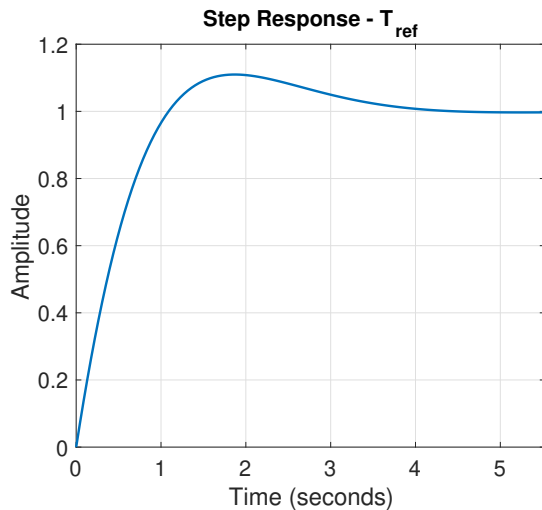
Figure 6.7: Step response of T_{ref}.
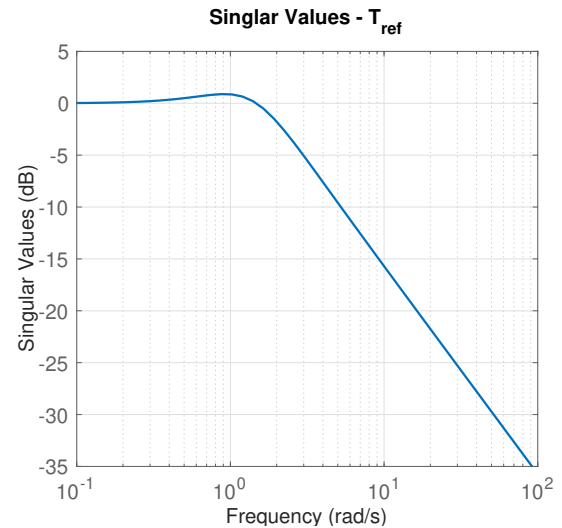
Figure 6.8: Frequency response of T_{ref}.

desired damping ratio as $\xi = 0.75$ and the numerator $z_{ref} = 1.2$, yields Level 1 performance in the selected HQ criteria. So that T_{ref} has unitary static gain, $K_{num} = 1.6333$ was selected. The step response and singular values of the reference model are shown in Figure 6.7 and Figure 6.8, respectively.

6.3. FLIGHT CONTROL SYSTEM - CONTINUOUS TIME DESIGN

From the requirements outlined in Section 6.2 and the considerations regarding the performance and feedback signals as well as output modeling, which were discussed in Section 6.1, the CT controller design is conducted. As it was previously discussed, the feedback controller C_{FB} provides robustness, while the feedforward controller C_{FF} improves the tracking performance. Moreover, given that the SP damping

Figure 6.9: General CT configuration of the system for FCS design.

ratio for the defined flight condition is around $\xi_{SP} = 0.54$ (see Table 5.6), a SAS is implemented with a feedback gain on the pitch rate channel, C_q. Therefore, from this information, the general configuration for the controller design is established, which is depicted in Figure 6.9. As seen previously, the gain K_q has the value 12.4 and corresponds to V_{CO}/g, as previously described in Equation (4.45).

Furthermore, to synthesize a structured controller in the signal-based MS $\mathcal{H}_\infty$ framework, the structure of the three controllers must be established beforehand. For that reason, a full-order feedback controller is designed as a preliminary result in Section 6.3.1, which is consequently reduced to determine the most adequate order. Hence, this result is imposed in the structured synthesis which is discussed in Section 6.3.2. In this second section, the need for a feedforward controller is also analyzed.

6.3.1. Preliminary Unstructured Feedback Controller Continuous Time Synthesis

To determine the optimal structure for the feedback controller, a full-order feedback controller is initially designed. It is subsequently reduced using balanced truncation. For more details on the model reduction method, please refer to Section 4.1.8. It should be noted that this is a preliminary step and is only used to provide a foundation to the final CT controller synthesis, performed in Section 6.3.2.

Moreover, several combinations of performance and disturbance signals could have been used for this standard $\mathcal{H}_\infty$ MS design, as described in Section 2.2.2. The often used $S/KS/T$ methods and variations of it in 2- and 3-Block problems could be implemented in several configurations to reject output disturbance rejection, improve output reference tracking, and decrease control effort. Nevertheless, the standard $\mathcal{H}_\infty$ MS four-block method design is used, since it effectively addresses both input and output disturbance rejection [Huang et al., 2010]. Thus, the plant output, y, and the controller output, u, were chosen as the output signals whereas the input and output disturbances, d_o and d_i, were chosen as the input signals, as shown in Figure 6.10. Therefore, the weighted closed loop matrix transfer function $T_{wz}(s)$ is described as in Equation (6.6).

$$\begin{bmatrix} y \\ u \end{bmatrix} = \begin{bmatrix} S_o & S_oG \\ -KS_o & -T_i \end{bmatrix} \begin{bmatrix} d_o \\ d_i \end{bmatrix} \implies T_{zw} = \begin{bmatrix} W_1S_o & W_1S_oGW_3 \\ -W_2KS_o & -W_2T_iW_3 \end{bmatrix} \tag{6.6}$$

Here, W_1, W_2, and W_3 are the filters used to shape the CL TFs. Although W_1 and W_2 would allow a satisfactory design, the low-pass W_3 is a complement that allows a tighter shaping at S_oG Medium Frequencies (MF) and of T_i roll-off at HF. The $\mathcal{H}_\infty$ optimal controller is obtained by solving:

$$\min_K \|T_{wz}\|_\infty, \tag{6.7}$$

where K is a full order stabilizing controller. Assuming that the optimal $\mathcal{H}_\infty$ norm is $\gamma = \min_K \|T_{wz}\|_\infty$, the resulting TFs from a solution to Equation (6.7) are close to γ times the bounds selected by the designer via the WF. Nevertheless, the unstructured controller is computed as a result of the optimization of a stacking procedure, which is selected for mathematical convenience and does not enable individual bound specifications. The four goals are optimized in combined form, resulting in a single performance level γ.

Figure 6.10: Unstructured CT controller design configuration.

Thus, for each, there is a possible resulting error of at most $\sqrt{n}$, where $n = 4$ corresponds to the number of stacked requirements. [Skogestad and Postlethwaite, 2005]

The WF are tuning knobs of the optimization and are defined as the inverse of the desired frequency responses. Given that $\|T_{wz}\|_\infty < \gamma$, then the conditions shown in Equation (6.8) are verified [Bérard et al., 2012], although with the inherent error (i.e. $\sqrt{n}$) associated with them.

$$
\begin{aligned}
\|W_1(s)S_o(s)\|_\infty < \gamma &\iff \forall \omega \in \Re, |S_o(j\omega)| < \frac{\gamma}{|W_1(j\omega)|} \\
\|W_1(s)S_o(s)G(s)W_3(s)\|_\infty < \gamma &\iff \forall \omega \in \Re, |S_o(j\omega)G(j\omega)| < \frac{\gamma}{|W_1(j\omega)W_3(j\omega)|} \\
\|W_2(s)K(s)S_o(s)\|_\infty < \gamma &\iff \forall \omega \in \Re, |K(j\omega)S_o(j\omega)| < \frac{\gamma}{|W_2(j\omega)|} \\
\|W_2(s)T_i(s)W_3(s)\|_\infty < \gamma &\iff \forall \omega \in \Re, |T_i(j\omega)| < \frac{\gamma}{|W_2(j\omega)W_3(j\omega)|}
\end{aligned}
\tag{6.8}
$$

Firstly, the sensitivity function should behave as a high-pass filter provided that disturbances are LF signals. Thus, S_o should be an increasing function up to its frequency $\omega_{S_o max}$ starting form a very small gain in LF, which ensures small steady state error in the disturbance rejection. At MF, an overshoot cannot be avoided [Stein, 2003], which translates into the amplification of disturbances. Therefore, the feedback only remains effective up to around the bandwidth frequency. This peak is also closely related to the minimum GM and PM, for SISO systems, and to the minimum modulus margins, for MIMO systems, as described in Section 4.2 (see Equation (4.43)).

On the contrary, the control sensitivity KS_o is similar to a low pass filter. At LF, the gain of the singular value is approximately the inverse of the plant gain. At HF, in order to avoid actuator saturation and provide robustness to additive uncertainties, KS_o must have a small gain. At MF, a value can be chosen to impose roll off or to choose an attenuation level at the system's actuator frequency.

Thus, the inverse of the filters W_1 and W_2 must impose the gain limits described for S_o and KS_o, respectively. These are defined as first-order high pass and low pass filters, as represented in Equation (6.9a) and Equation (6.9b). Additionally, S_oG is shaped with W_1 and W_3, while T_i is dependent on W_2 and W_3. W_3 can be a constant filter. However, if made dynamic, both the mid frequencies of S_oG and the roll off of T_i at HF can be shaped. Thus, W_3 was defined as a high-pass filter (see Equation (6.9c)), and its magnitude was increased iteratively until T_i was performing as desired.

$$
W_1^{-1}(s) = \frac{s + \underline{k}_{W_1}\overline{k}_{W_1}}{\overline{k}_{W_1}^{-1}s + \overline{k}_{W_1}}
\tag{6.9a}
$$

$$
W_2^{-1}(s) = \frac{\overline{k}_{W_2}s + \overline{k}_{W_2}}{s + \overline{k}_{W_2}\underline{k}_{W_2}^{-1}}
\tag{6.9b}
$$

$$
W_3(s) = \frac{k_0(s + z_3)}{s + p_3}
\tag{6.9c}
$$

where $\underline{k}$ and $\overline{k}$ are, respectively, the desired low and high frequency attenuation, and $\overline{\omega}$ is the desired gain at a certain frequency $\overline{\omega}$. The $W_1^{-1}(s)$ and $W_2^{-1}(s)$ filters characteristics are summarized in Table 6.1[1], while, for $W_3(s)$, $k_0 = 170$, $z_3 = 10$ rad/s, and $p_3 = 10^4$ rad/s.

Table 6.1: $W_1^{-1}(s)$ and $W_2^{-1}(s)$ filters characteristics for the unstructured CT design.

	W_1^{-1}	W_2^{-1}
$\underline{k}$	-50 dB	50 dB
$\overline{\omega}$	1.3 rad/s	14.3 rad/s
$\overline{k}$	0 dB	0.3 dB
$\overline{\overline{k}}$	6.19 dB	-50 dB

---

[1] `makeweight()` MATLAB® function from the Robust Control Toolbox is used to create the WF. This function produces a N-th order TF with poles and zeros in a Butterworth pattern. The higher the order N is, the steeper the transition from low to high gain is.
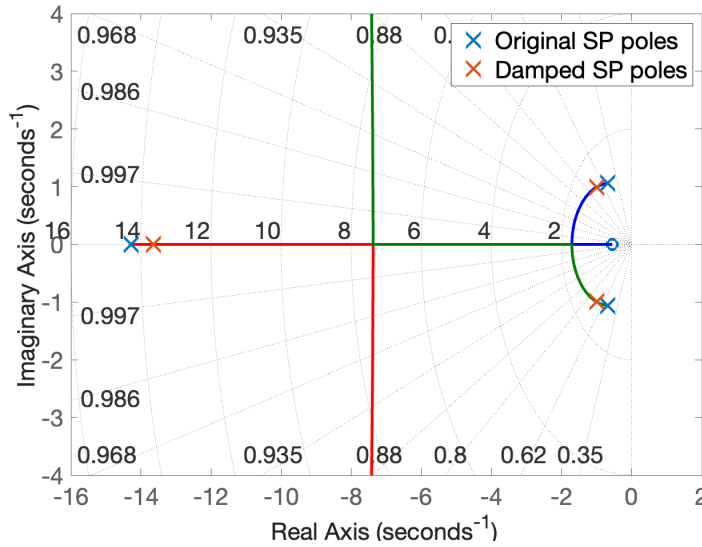
Figure 6.11: Root Locus superimposed with original and damped SP poles.

Only the feedback controller applied on the C* signal is synthesized with this procedure. Nevertheless, as portrayed in Figure 6.10, the controller C_q is also present, which has not been yet defined. In fact, this gain is applied on the pitch rate channel using negative feedback in order to increase the damping of the SP. Using root locus techniques, the appropriate gain of C_q = -0.182 was chosen so that the typical value of ξ = 0.707 for closed loop damping is achieved. Figure 6.11 shows the root locus plot which was superimposed with the original and damped SP poles.

In Figure 6.10, the signals u_{FB} and v represent the controller output signal and the controller input measurement signal. Besides these signals, the $\mathcal{H}_\infty$ synthesis is conducted by considering the linearized plant from the inputs $\omega = [\omega_1\ \omega_2]$ to the outputs $z = [z_1\ z_2]$ [2]. The performance level obtained is $\gamma = 0.9895$. The resulting unstructured controller obtained is represented in Equation (6.10).

$$C_{FB_{FO}}(s) = \frac{-27538(s+9975)(s+4646)(s+13.5800)(s+1.9360)(s+0.9906)}{(s+1.3940e\,05)(s+7396)(s+1875)(s+32.5)(s+1.2350)(s+0.0035)} \tag{6.10}$$

Model order reduction was applied to the FO controller[3] to define the most adequate structure. From the FO TF (see Equation (6.10)), it is evident that the zeros s = -9975 rad/s, s = -4646 rad/s and the poles s = -1.394 · 10^5 rad/s, s = -7396 rad/s, and s = -1875 rad/s are very HF and, hence, can be discarded. The pole s = -1.2350 rad/s and the zero s = -0.9906 rad/s have similar frequencies and, therefore, can be reduced. Thus, only the integrator-like pole (s ≈ -0.0035 rad/s), the zeros s = -13.5800 rad/s and s = -1.9360 rad/s, and the pole s = -32.5 rad/s remain.

Choosing the controller structure balances complexity and effectiveness, with a low-order controller preferred for real implementation. The frequency responses of the FO and of three reduced order controllers are shown in Figure 6.12. An adequate trade-off is achieved with the second order controller (i.e. PI + low pass filter) in terms of complexity and satisfactory frequency matching. Nonetheless, it is clear that the low pass filter in this controller is only contributing to the behavior of the system around 10^4 rad/s. This frequency is not significant for the Flying-V FCS. Thus, a simple PI should be sufficient. Hence, the structure which will be imposed in the structured design is defined. The reduced order controller obtained from the algorithm that still contains the HF low pass pole is the following is represented in Equation (6.11).

---

[2] hinfsyn() MATLAB® from the Robust Control Toolbox is used by providing the linearized plant, the number of measurements and controls, which are both equal to one, and by increasing the relative tolerance to 10^{-6} in the optimization options.

[3] getrom() MATLAB® function is used to obtain the reduced-order models using balanced truncation. Consider Section 4.1.8 for further details on the technique. The frequency range of $[10^{-2}, 10^2]$ rad/s is highlighted as the most critical. The lower bound is due to the integrator-like pole, whose frequency is close to 10^{-2}. Given that the actuator frequency is 14.3 rad/s, 10^2 is defined as the upper critical bound.
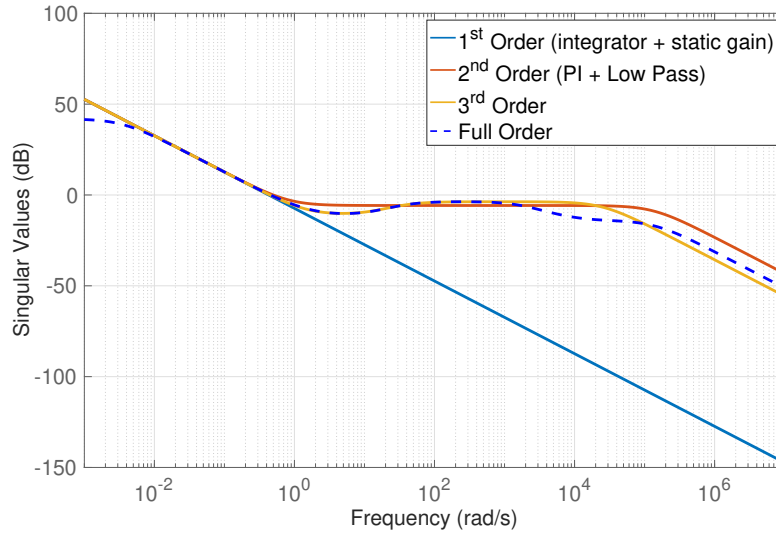
Figure 6.12: Unstructured and reduced controllers obtained in the CT MS $\mathcal{H}_\infty$ design.

$$C_{FB_{O2red}}(s) = \frac{-68584(s + 0.8346)}{s(s + 1.336e05)} \tag{6.11}$$

The full-order controller is implemented in the closed loop configuration, from which "Gang of Six" (Go6) is computed. The frequency responses of these TF are shown in Figure 6.14.

It is evident that the CL TFs follow the desired shape as these are all below the gain limits (i.e. the WF inverse). It is important to highlight that the sensitivity functions are not completely standard. These should have a HF gain of 0 dB, given the duality $S + T = 1$. Nonetheless, one can observe that depending on the signals selected to define the individual TFs, the sensitivities behavior is changed. On the one hand, the TFs S_o and S_i, which are defined from the inputs r and d_i to the performance signals e and u_p, respectively, behave as expected. On the other hand, the one that is closely related to the output disturbance signal rejection in the output of the system (from d_o to y), has a significant decreasing gain and it is displaced around 20 dB from the other sensitivity functions. This is due to the output disturbance model which is being applied on the d_o input. The disturbance model, G_d, scales the TF and adds these dynamics in HF. This can be clearly witnessed from its singular value frequency response, which is shown in Figure 6.13.
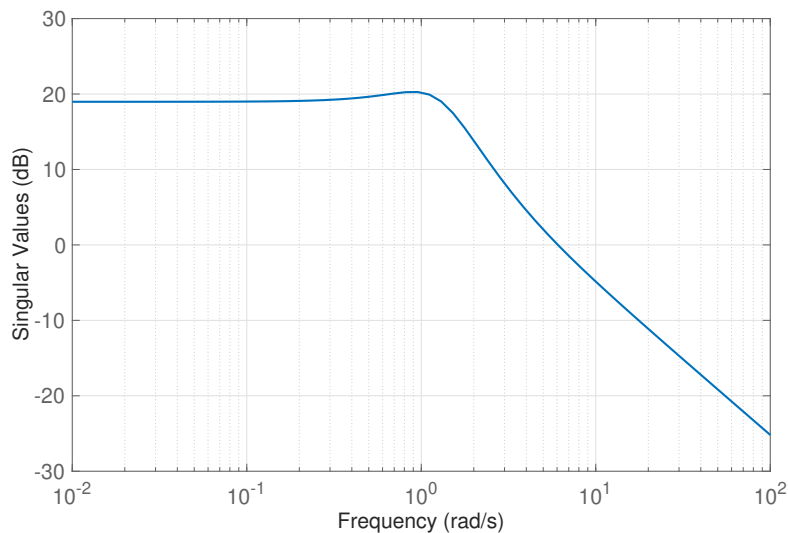
Figure 6.13: Frequency response of the output disturbance model of the alpha gust, G_d.

(a) Individual S_o and S_i frequency responses.

(b) Individual T_o and T_i frequency responses.

(c) Individual KS_o frequency response.

(d) Individual S_oG frequency response.
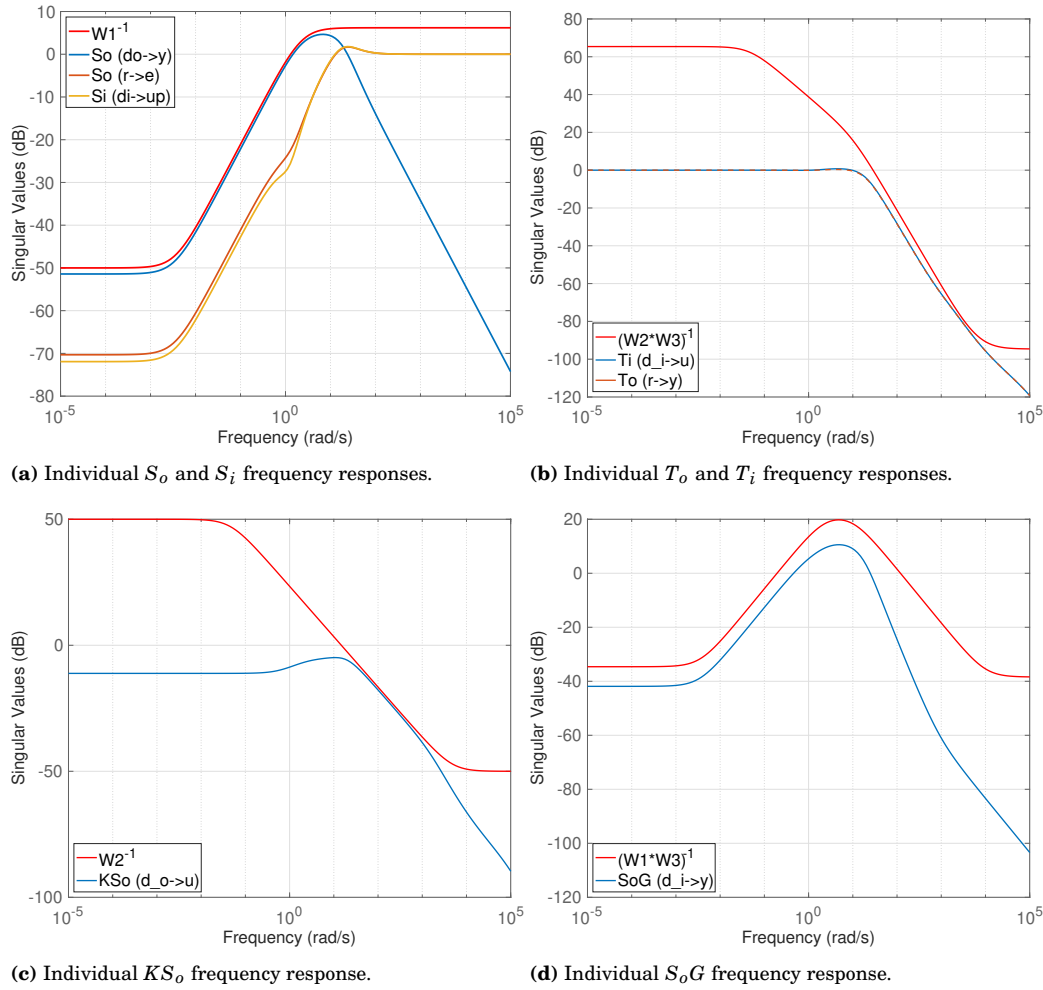
Figure 6.14: Go6 of the CL TFs obtained in the CT unstructured MS $\mathcal{H}_\infty$ design.

6.3.2. SIGNAL-BASED MS $\mathcal{H}_\infty$ CONTINUOUS TIME FCS SYNTHESIS

Provided that the controller structure is already known for the C_q and C_{FB} controllers, the structured controller synthesis procedure can begin. The methodology consists of designing, at first, C_q and C_{FB}, based on the robustness requirements and by shaping the TFs of the Go6. Consequently, the ideal feedforward controller is computed based on T_{ref} and on the closed loop TF, already with the feedback controllers implemented (ideal $C_{FF} = T_{ref} \cdot T_o^{-1}$). From this, an adequate order for the controller is found, which corresponds to one zero and two poles. For brevity reasons, this analysis is not shown here. Nonetheless, an a posteriori analysis of the order of the feedforward controller is given in order to justify why the structure is adequate. Furthermore, with this information, the three controllers are re-tuned iteratively by finely tuning the WF accordingly. Only the final results are shown and described in the current section.

SYNTHESIS FCS SET UP

Additionally, the system set up that is used to design the controllers is shown in Figure 6.15. As previously discussed, the plant is constituted by the actuator dynamics, the SP model and the output disturbance model, which mimics an α gust. The FCS was extensively described, where three controllers need to be tuned. The sensors introduce noise at the plant output signals n_z and q. The reference tracking subsystem allows to verify the satisfaction of the model following, where the C* signals are computed without any noise, which corresponds to the actual behavior of the Flying-V. It should be noted again that the C* measured at the IMU is used for the feedback whereas this parameter is measured at the PS for reference tracking purposes. This was discussed in Section 6.1.1.

The input and output signals are represented in Figure 6.15, which are used to define the TFs that are consequently shaped via the WF. The performance signals correspond to $u, u_{weighted}, u_p, y_{IMU}, y_{PS}, e_{ref}$,
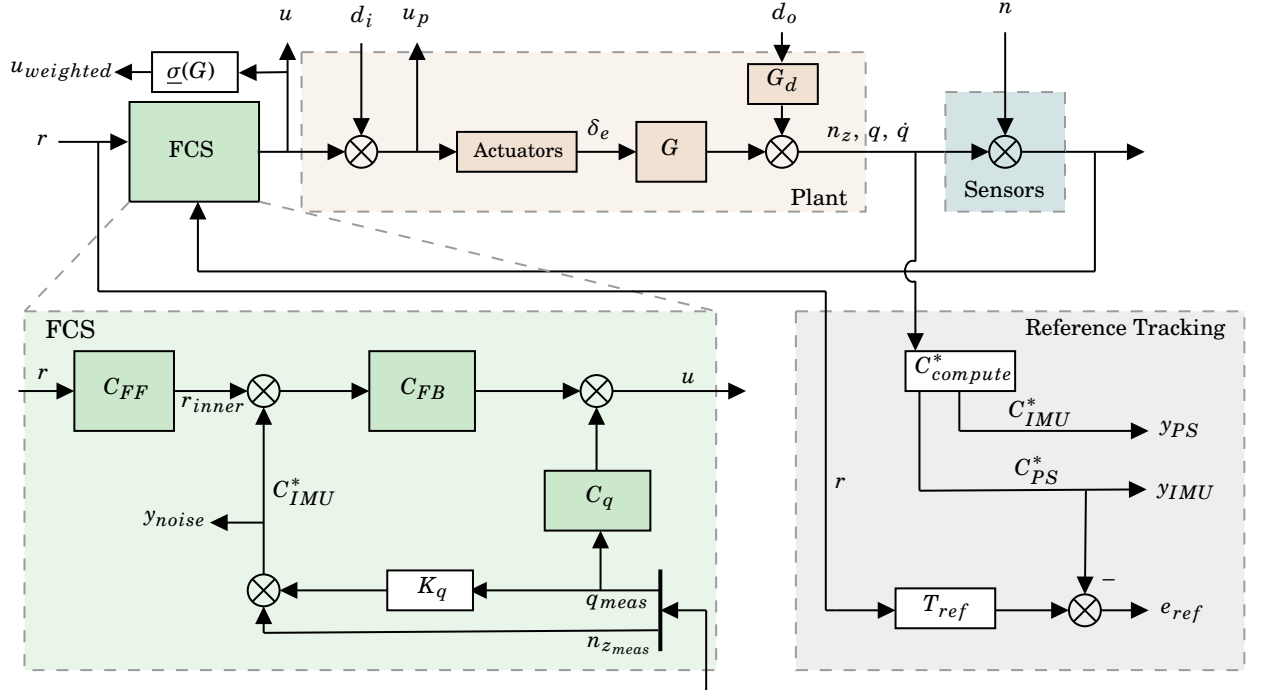
Figure 6.15: FCS set up for the structured CT controller design.

and y_{noise}. The input signals involve d_i, d_o, n, r, and r_{inner}. Furthermore, it should be noted that the plant was augmented to also output $\dot{q}$. This signal is fundamental to compute the C* parameter because of the load factor. Although this signal is measured in the IMU location, it must also be computed at the PS for the reference tracking of the C$_{PS}^*$ parameter. This transformation is obtained via Equation (6.1).

Constraints & Weighting Filters Selection

Moreover, as outlined in Section 4.1.5, shaping the Go6 TFs, ensures that the system remains robust against disturbances and uncertainties. Other requirements are also achieved, namely noise attenuation, control signal reduction, and satisfactory reference tracking. Hence, it is fundamental to define the tuning knobs of the optimization, the WF, which also allow to write the specific constraints. Some of the WF, especially the ones related to S_o and KS_o were already discussed in Section 6.3.1. Nonetheless, the main features that must be imposed are discussed for all of the TFs in the current subsection.

S_o Constraint

To begin with, the first constraint, S_o, involves the rejection of the output disturbance d_o at the system output y_{IMU}. This constraint involves the output sensitivity $S_o = (1 + L_o)^{-1}$. The LF gain must be reduced to improve the disturbance rejection and ensure small steady state error. Using the appropriate WF W_{S_o}, the hard constraint is written as $\|W_{S_o}S_o(s)\|_\infty$. The TF S_o is an increasing function until it reaches its peak, which is closely linked to the degradation of the effectiveness of the attenuation and, thus, it is related to the minimum GM and PM. The peak cannot be avoided [Stein, 2003] at MF and it is related to the closest distance to the critical point -1 in the complex plane. Its magnitude can be translated into SM values as described by the DM expression below, which was already mentioned in Section 4.2 [Seiler et al., 2020]:

$$\alpha_{max} = \frac{1}{\left\| S + \frac{\sigma - 1}{2} \right\|_\infty} \tag{6.12}$$

The WF inverse is selected as a high pass filter, as represented in Figure 6.16. Its LF and HF gains were, respectively, selected as $\underline{k}_{S_o}$ = -50 dB and $\overline{k}_{W_{S_o}}$ = 6.84 dB (magnitude of 2.2). The latter value was chosen as the lowest possible to increase the SM. This relatively high value is due to the output disturbance modeling, which allows for a more realistic scenario but also introduces degrading factors. The values obtained with Equation (6.12) correspond to the worst case and maximum degradation that
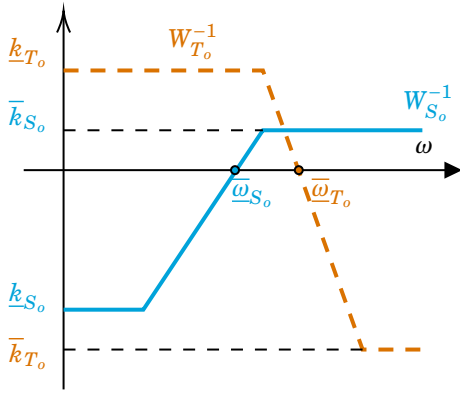
Figure 6.16: Singular value shape for the desired S_o (blue) and T_o (orange) functions.
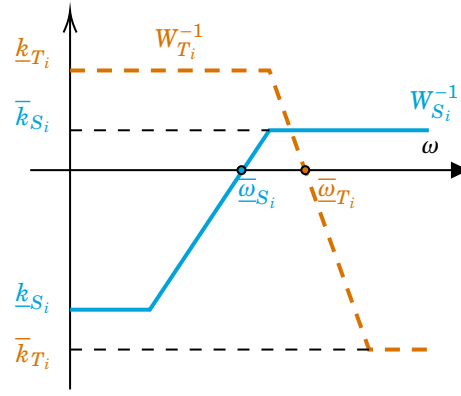
Figure 6.17: Singular value shape for the desired S_i (blue) and T_i (orange) functions.

might be achieved. Nevertheless, system robustness is analyzed a posteriori with classical and disk SM and these are the values that correspond to the actual robustness of the system. Furthermore, $\overline{k}_{S_o}$ = 0 dB at $\overline{\omega}_{S_o}$ = 0.95 rad/s. The higher this frequency value is, the higher is the range of effectiveness of the disturbance rejection and, hence, the robustness of the system when faced with output disturbances also improves.

Furthermore, to verify that these values are worsened because of the output disturbance modeling, in Appendix B, a paper submitted to the 11th IFAC Symposium on Robust Control Design, is presented. It proposes the same control law as in the current section but without the G_d modeling. It is observed that $\overline{k}_{W_{S_o}}$ = 5.58 dB (magnitude of 1.9), and that the crossover frequency increased to $\overline{\omega}_{S_o}$ = 1.7 rad/s which is almost double of what can be achieved in the current design.

S_i Constraint

Secondly, the constraint, S_i, involves the rejection of the input disturbance d_i at the plant input u_p. This constraint involves the input sensitivity $S_i = (1 + L_i)^{-1}$. It should follow a similar tendency to S_o, with reduced LF gain, as portrayed in Figure 6.17. Using the appropriate WF W_{S_i}, the hard constraint is written as $\|W_{S_i} S_i(s)\|_\infty$. Thus, $\underline{k}_{S_i}$ = -50 dB. Contrarily to the output disturbances, d_i is not modeled. This translates into the possibility to design a tighter filter for S_i than for S_o, resulting in $\overline{k}_{S_i}$ = 6.02 dB (magnitude of 2), $\overline{k}_{S_i}$ = 0 dB, and $\overline{\omega}_{S_i}$ = 5.8 rad/s.

T_i & T_o Constraints

The constraints associated with the complementary sensitivity functions at the input and output, T_i and T_o, follow a similar tendency. These are defined as the TFs from d_i to the controller output u and from r_{inner} to the system output y_{IMU}, respectively. The latter allows good reference tracking (at LF), where its gain is unitary, given the duality with the sensitivity functions. At HF, T_o contributes to noise attenuation and T_i to control signal attenuation by their low gain, which also imposes roll off in the open loops in this frequency range. Using the appropriate WF W_{T_i} and W_{T_o} as presented in Figure 6.17 and Figure 6.16, respectively, the hard constraints are written as $\|W_{T_i} T_i(s)\|_\infty$ and $\|W_{T_o} T_o(s)\|_\infty$. Hence, the desired low and high gain are selected equally for both TFs with $\underline{k}_T$ = 12.04 dB and $\overline{k}_T$ = 12.04 dB, respectively. Although a peak usually appears at MF, the peaks of the sensitivity functions are usually higher. Since the sensitivity TFs are already constrained in this range, the peaks of T are not limited tightly. Furthermore, the crossover frequencies are selected as the lowest possible which correspond to values of $\overline{\omega}_{T_i}$ = 15.8 rad/s and $\overline{\omega}_{T_o}$ = 13 rad/s. In order to improve the roll off of the open loop, a steeper slope is induced by increasing the order of the filter to two.

KS_o Constraint

The TF from d_o to u and allows to impose control signal attenuation. At LF, the TF is approximately equal to the inverse of the plant, and it is not dependent on the controller designer. To interpret better the attenuation level requested at MF and HF, a scaling is used for the LF by multiplying KS_o with the dcgain of the plant. Thus, the additional input to the system $u_{weighted}$ is created (see Figure 6.15) to shape the TF KS_o. Using the appropriate WF W_{KS_o} as represented in Figure 6.18, the hard constraint is written as $\|W_{KS_o} KS_o(s)\|_\infty$. Thus, $\underline{k}_{KS_o}$ = 50 dB is selected as a high value because the TF should not be constrained
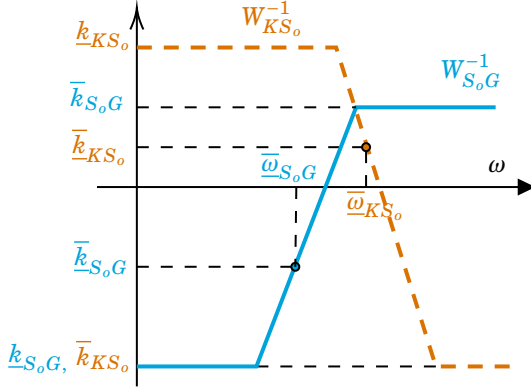
Figure 6.18: Singular value shape for the desired S_oG (blue) and KS_o (orange) functions.
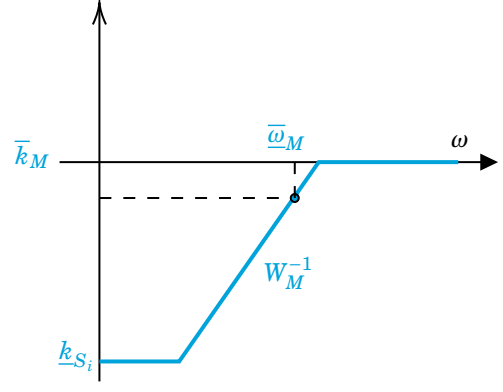
Figure 6.19: Singular value shape for the desired M function.

at LF. At HF gain must be reduced to impose noise attenuation and control signal attenuation. For that reason, $\overline{k}_{KS_o}$ = -50 dB. At MF, the attenuation level is defined at the actuator frequency (i.e. $\overline{\omega}_{KS_o} \approx 14.3$ rad/s). Although not negative, the minimum value possible is defined, which is $\underline{\overline{k}}_{KS_o} \approx 8$ dB.

S_oG Constraint

The TF S_oG is selected from d_i to y_{IMU} and it is crucial to provide input disturbance rejection at the system output. It involves the plant times output sensitivity function. Once again, since disturbances are LF signals, the LF gain must be reduced. The hard constraint is written as $\|W_{S_oG}S_oG(s)\|_\infty$. From the desired SV shape of S_oG represented in Figure 6.18, $\underline{k}_{S_oG}$ = -50 dB and $\overline{k}_{S_oG}$ = 30 dB were defined. The latter value is not significant because at HF the gain of S_oG is not relevant, provided that it is approximately equal to the plant singular values. At $\overline{\omega}_{S_oG}$ = 10^{-2} rad/s, it is imposed $\underline{\overline{k}}_{S_oG}$ = -36.2 dB.

M Constraint

Reference tracking is also a key requirement. To fulfill it, a model matching constraint is defined (i.e. $\|W_M M(s)\|_\infty$), which imposes low gain at MF and MF. Moreover, the lower the gain at LF, the lower is the steady state error in the response. The higher the bandwidth is, the better is the matching of the response with the ideal one imposed. However, it is a trade-off between robustness and performance. If this characteristics are improved, the parameters for the previously mentioned filters have to be worsened to avoid filters violation. These trade-offs are especially noticeable in terms of sensitivity functions and control sensitivity. A balance was achieved when considering $\underline{k}_M$ = -45 dB, $\overline{k}_M$ = 0 dB, $\underline{\overline{k}}_M$ = -3.01 dB, and $\overline{\omega}_M$ = 5.3 rad/s, considering the desired shape of M depicted in Figure 6.19.

WF Conclusions & Optimization

During the design procedure, the WF were finely tuned, by consecutive iterations in order to account for a balanced solution and ensure all of the constraints are verified. The final characteristics were already mentioned and are summarized in Table 6.2 [1]. Moreover, contrarily to the unstructured design, the $\mathcal{H}_\infty$ optimization is conducted for each TF constraint individually, yielding seven performance levels. More information on this optimization algorithm can be found in Section 4.1.9. The expressions in Equation (6.13) are verified, which concludes that defining the WF as the inverse of the desired shapes for each TF and having a γ lower or equal to unity results in the satisfaction of the gain limitations imposed.

Table 6.2: WF characteristics for the structured CT controller design.

	$W_{S_o}^{-1}$	$W_{S_i}^{-1}$	$W_{T_i}^{-1}$	$W_{T_o}^{-1}$	$W_{KS_o}^{-1}$	$W_{S_oG}^{-1}$	W_M^{-1}
$\underline{k}$ (dB)	-50	-50	12.04	12.04	50	-50	-45
$\overline{\omega}$ (rad/s)	0.95	5.80	15.80	13	14.29	10^{-2}	5.30
$\underline{\overline{k}}$ (dB)	0	0	0	0	7.98	-36.20	-3.01
$\overline{k}$ (dB)	6.84	6.02	-80	-80	-50	30	0
Order	1	1	2	2	1	1	1

$$\|W_{S_o}(s)S_o(s)\|_\infty < \gamma_{S_o} \iff \forall \omega \in \Re, |S_o(j\omega)| < \frac{\gamma_{S_o}}{|W_{S_o}(j\omega)|}$$

$$\|W_{S_i}(s)S_i(s)\|_\infty < \gamma_{S_i} \iff \forall \omega \in \Re, |S_i(j\omega)| < \frac{\gamma_{S_i}}{|W_{S_i}(j\omega)|}$$

$$\|W_{T_i}(s)T_i(s)\|_\infty < \gamma_{T_i} \iff \forall \omega \in \Re, |T_i(j\omega)| < \frac{\gamma_{T_i}}{|W_{T_i}(j\omega)|}$$

$$\|W_{T_o}(s)T_o(s)\|_\infty < \gamma_{T_o} \iff \forall \omega \in \Re, |T_o(j\omega)| < \frac{\gamma_{T_o}}{|W_{T_o}(j\omega)|} \tag{6.13}$$

$$\|W_{KS_o}(s)K(s)S_o(s)\|_\infty < \gamma_{KS_o} \iff \forall \omega \in \Re, |K(j\omega)S_o(j\omega)| < \frac{\gamma_{KS_o}}{|W_{KS_o}(j\omega)|}$$

$$\|W_{S_oG}(s)S_o(s)G(s)\|_\infty < \gamma_{S_oG} \iff \forall \omega \in \Re, |S_o(j\omega)G(j\omega)| < \frac{\gamma_{S_oG}}{|W_{S_oG}(j\omega)|}$$

$$\|W_M(s)M(s)\|_\infty < \gamma_M \iff \forall \omega \in \Re, |M(j\omega)| < \frac{\gamma_M}{|W_M(j\omega)|}$$

IMPLEMENTATION PROCEDURE

The design specifications of Section 6.2 are defined via `sltuner()` that interfaces a Simulink file mimicking Figure 6.15. The analysis points and tunable blocks are defined, originating the object CL0 that corresponds to the control system to be tuned. The structure of the blocks C_{FF}, C_{FB}, and C_q is defined by using pre-defined structures such as "tunableTF" and "tunableGain", where the number of zeros and poles are chosen. Moreover, the `systune()` function is called as:

$$[\text{CL, fSoft, gHard, info}] = \text{systune(CL0, SoftGoals, HardGoals, opt)}~[4]$$

where the tuning goals are defined as hard requirements (HardGoals), which correspond to the shaping of the Go6 TFs and the Model Matching (M) constraints. These were all defined as hard objectives since these are all related to the hard requirements described in Section 6.2, which must be necessarily met. Therefore, there are no SoftGoals for the current design. For the seven constraints, the inputs and outputs are defined as well as the maximum gain as a function of frequency (via the WF). Options for the optimization can also be selected. The number of additional optimizations starting from random values were chosen as 100 and parallel computing was enabled.

Regarding the output arguments, CL corresponds to the tuned control system, fSoft and gHard correspond, respectively, to the best achieved soft and hard performance level values. If all of the values returned are below unity, then all of the constraints imposed are satisfied. Lastly, info contains detailed information about each optimization run.

RESULTS & DISCUSSION

Moreover, with the final values for the filters, the performance levels for each of the constraints are obtained and are summarized in Table 6.3.

Table 6.3: Performance levels, γ, for each hard tuning goal retrieved from `systune` in the CT controller design.

	S_o	S_i	T_i	T_o	KS_o	S_oG	M
γ	0.9993	0.9568	0.9739	0.9847	0.9997	0.9899	0.9910

The controllers obtained from the optimization are represented in Equation (6.14). The controllers singular value frequency responses are shown in Figure 6.20.

$$C_{FF} = \frac{1.6734 \cdot (s + 1.223)}{(s^2 + 2.032s + 2.059)} \qquad C_{FB} = \frac{-0.22178 \cdot (s + 3.003)}{s} \qquad C_q = -1.6442 \tag{6.14}$$

---

[4]Please refer to Section 4.1.9 for information regarding the function as well as the mechanisms behind it.
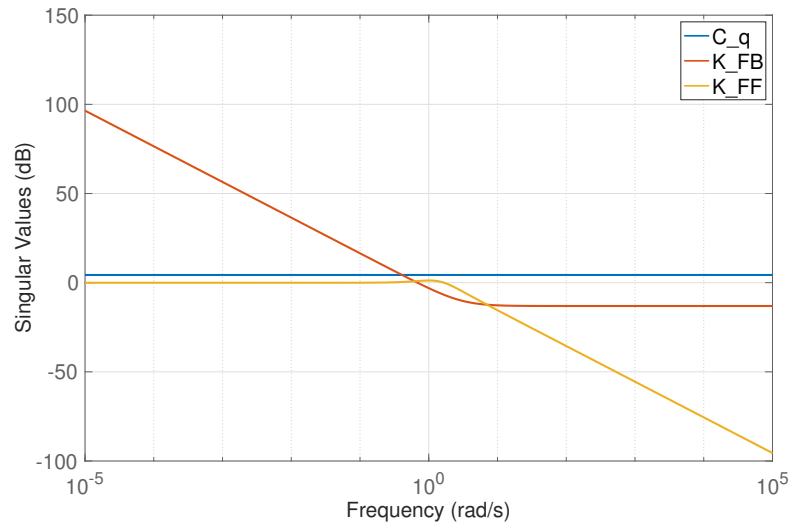
Figure 6.20: Frequency response of the controllers obtained in the structured CT FCS design.
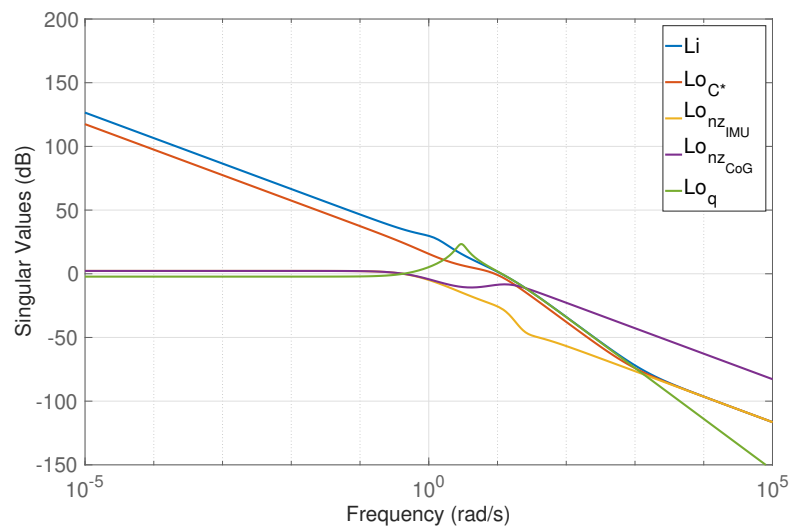
Figure 6.21: Open Loops of the FCS system, with the CT controller design.

Furthermore, the controllers are implemented in the closed loop system and the open loops are computed in several locations. These include the plant input, L_i, and the plant outputs n_z measured at the IMU and q, respectively $L_{o_{nz}}$ and L_{o_q}. However, in order to better analyze the system, an open loop was also computed at the virtual plant output C^*, $L_{o_{C^*}}$, and at the load factor measured at the CoG, $L_{o_{nz_{CoG}}}$. All of these are shown in Figure 6.21.

At LF, the open loop gains are high for L_i and $L_{o_{C^*}}$, which enables disturbance rejection, as described in Section 4.1.5. As previously discussed in Section 6.1.1, disturbance rejection is not possible on n_z and q signals when it is directly applied on them. This occurs because no integral action is applied in these signals. From that discussion, it was preferred to guarantee disturbance rejection in the balanced parameter C^*. It is evident that the HF gain is low, as desired for noise attenuation and control signal attenuation. Moreover, it is also verified that the zero of the feedback controller around 3 rad/s also contributes to decrease the slope around crossover of the $L_{o_{C^*}}$ which improves stability margins.

Additionally, the closed loops TFs that were shaped in order to impose system robustness are also shown in Figure 6.22, as well as the inverse of the WF. From the performance levels, which were all below one, and from observing that all of the TFs are below the WFs inverse, it is verified that all of the filters are respected.
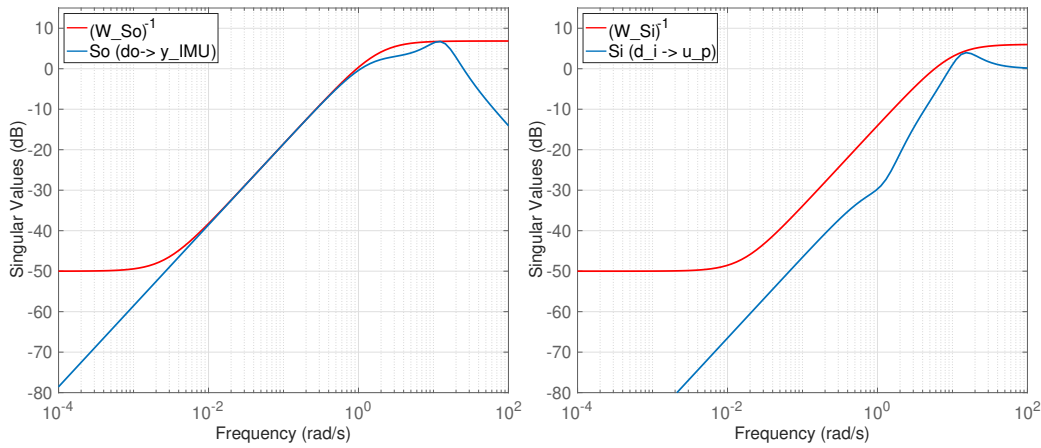
(a) Sensitivity S_o, and its filter inverse, W_{So}^{-1}.
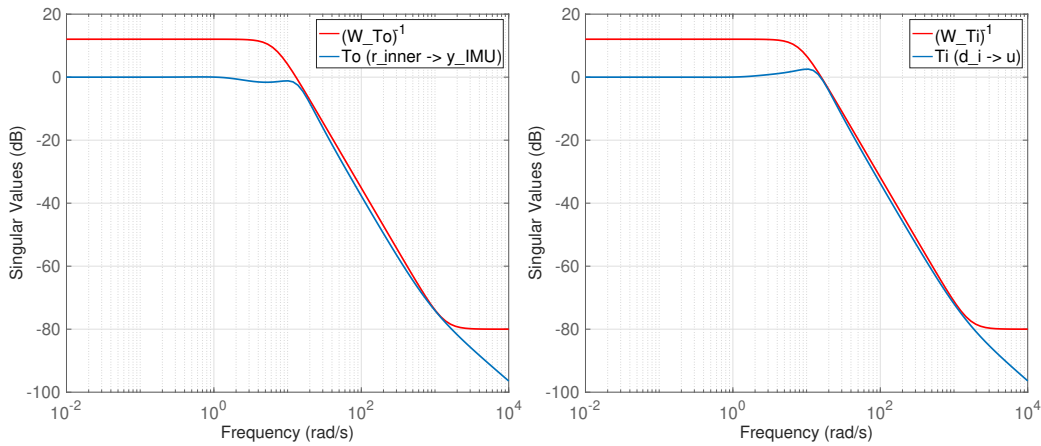
(b) Sensitivity S_i, and its filter inverse, W_{Si}^{-1}.

(c) Complementary sensitivity T_o, and its filter inverse, W_{To}^{-1}.

(d) Complementary sensitivity T_i, and its filter inverse, W_{Ti}^{-1}.

(e) Control sensitivity KS_o, KS_o scaled with $\underline{\sigma}(G)$ at LF, and its filter inverse, W_{KSo}^{-1}.
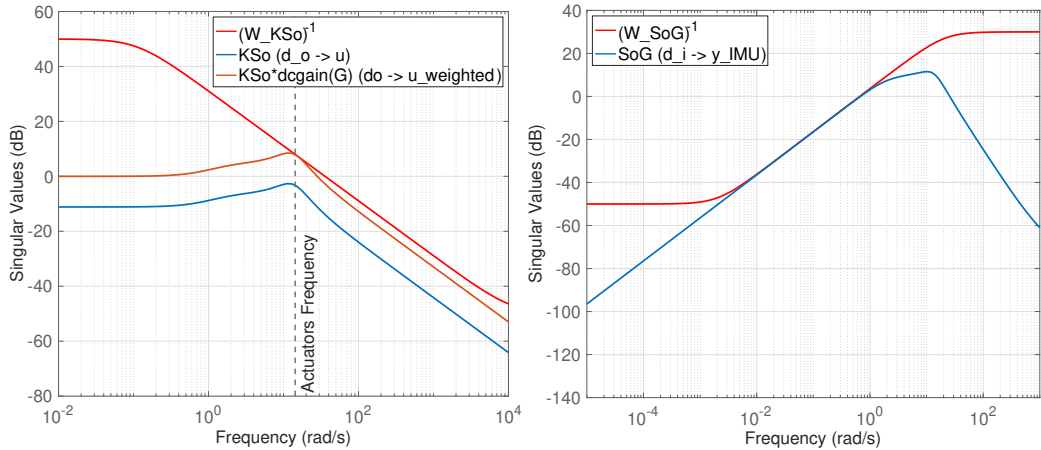
(f) S_oG, and its filter inverse.

Figure 6.22: Singular Values of the Go6 closed loop TFs, namely of S_o (6.22a), S_i (6.22b), T_o (6.22c), T_i (6.22d), KS_o (6.22e), and S_oG (6.22f), with the associated WF' inverse.

Attention should be paid to Figure 6.22a, where the HF gain starts decreasing, although from the duality with T_o it would be expected that this stabilized at 0 dB in this frequency range. However, as already mentioned, the output disturbance model behaves as a low pass filter and, at HF, its SV has low gain, as it can be observed in Figure 6.13. Thus, its contribution is visible at HF in S_o because it is scaled with G_d. From the paper presented in Appendix B, the output sensitivity function, S_o, stabilizes in 0 dB at HF, as expected for the synthesis procedure without output disturbance modeling. Moreover, the same aspect is present in the KS_o function, shown in Figure 6.22e since it is also defined from the input d_o and, thus, affected by the G_d model. Therefore, although not perceptible at first, KS_o does not behave as desired, given that it does not have low gain at HF. Instead, the KS_o which is not scaled by the disturbance model is shown in Figure 6.23.

The necessary roll off is guaranteed by low gain of the feedback controller at HF. However, as observed in Figure 6.20, the controller does not have any roll off at HF. This aspect was hidden through the unstructured design procedure given the G_d was scaling all of the TFs from d_o. Nonetheless, this issue can be easily tackled by adding a low pass filter to the feedback controller, which will behave similarly to G_d and, thus, achieve the desired requirements, as shown in Figure 6.22e. By adding an additional pole to the feedback structure imposed previously and by selecting the KS_o function from n to u instead of from d_o to u, the problem can be easily fixed. However, given that the CT design is an intermediate step to the digital design, which will be discussed in Section 6.4, the controller was not redesigned in the current section. Instead, it serves as a good analysis of the intricacies of the control design. Additionally, this problem becomes automatically fixed in the digital design because of the anti-alias low pass filter, although roll off in the feedback controller should also be imposed at HF.

On the other hand, from the S_oG SV shown in Figure 6.22f, it is seen that at LF the gain is small. In this frequency range, the TF is approximately the inverse of the controller singular value. In fact, that is corroborated by the large control feedback gains of the feedback controller, introduced via the integrator.

Additional TFs that are not shown in Figure 6.22, are depicted in Figure 6.24a. These consist of $S_o(r \rightarrow e)$, $S_oG(d_i \rightarrow e)$, and $KS_o(r \rightarrow u)$. Hence, all in all, it is verified that, at LF in terms of robustness and singular values, the output disturbances are attenuated at the plant output, via S_o, the steady state tracking error is reduced, $S_o(r \rightarrow e)$, input disturbances are attenuated at the system output, via S_oG, at the tracking error $S_oG(d_i \rightarrow e)$, as well as at the plant input, $S_i(d_i) \rightarrow u_p$, and control signals are attenuated from r to u.

Moreover, additional TFs are portrayed in Figure 6.24b, in order to verify that, at HF, there is noise attenuation in the plant outputs and virtual plant output by its low gain. Therefore, at HF in terms of robustness and singular values, noise is attenuated at the plant output (T_o) and control signal is attenuated from the input disturbances (T_i). Nonetheless, as previously discussed, a low pass must be added to C_{FB} to provide noise attenuation at the plant input and control signal attenuation from the output disturbances.
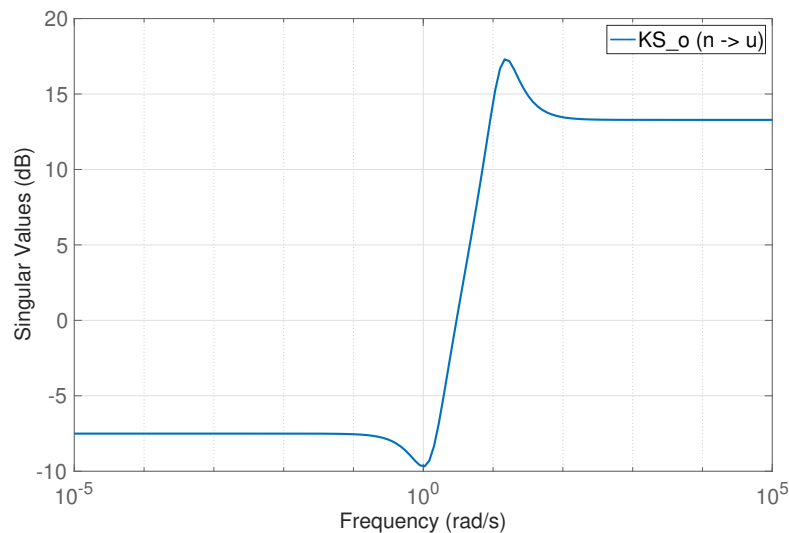
Figure 6.23: Control Sensitivity function, which is not scaled by the disturbance model, G_d.
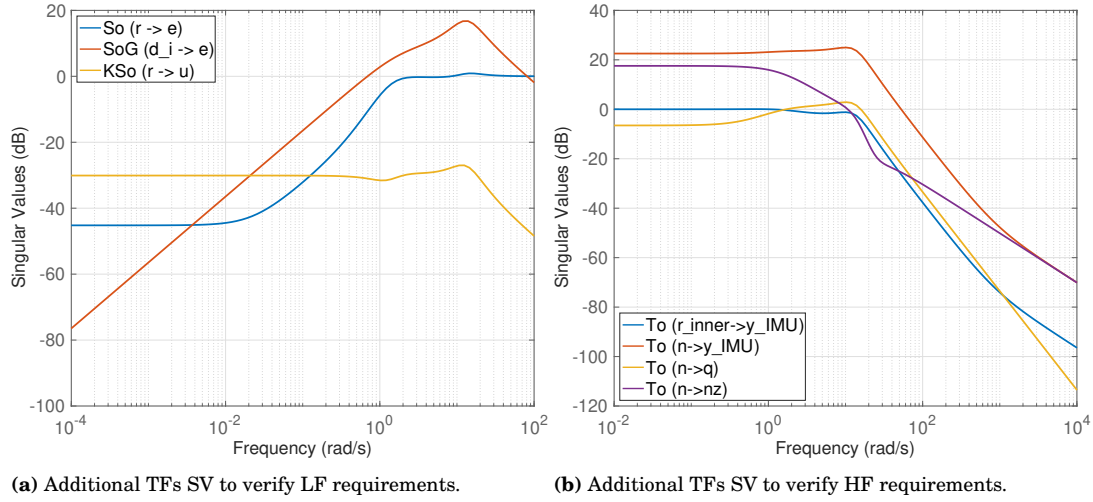
(a) Additional TFs SV to verify LF requirements.

(b) Additional TFs SV to verify HF requirements.

Figure 6.24: Additional closed loops TFs SV to verify additional requirements at LF (6.24a) and at HF (6.24b).
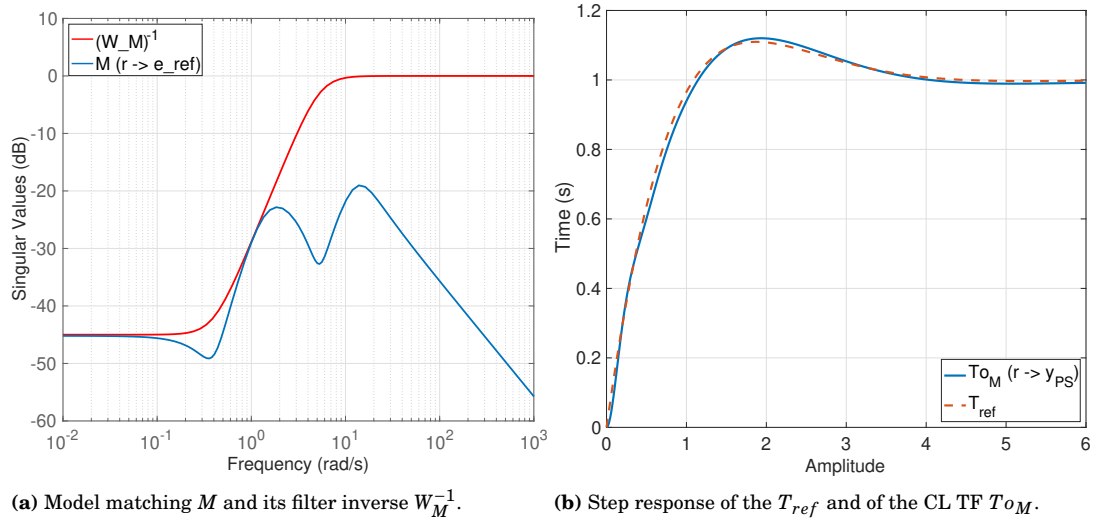
(a) Model matching M and its filter inverse W_M^{-1}.

(b) Step response of the T_{ref} and of the CL TF T_{oM}.

Figure 6.25: Performance of the reference tracking, in terms of model matching frequency 6.25a and time 6.25b responses.

Furthermore, the performance requirements in terms of reference tracking is also a fundamental aspect to analyze. The model matching constraint is imposed from the reference to the error, which corresponds to the subtraction between C* at the PS and the output of the reference model excited by the reference signal r. The corresponding transfer function, M, and the filter inverse used, W_M^{-1} is shown in Figure 6.25a. It is clear that the filter is not violated, which goes hand in hand with the performance level shown in Table 6.3. Additionally, a time step response from the reference to the output to be tracked (C* at the PS) is also shown in Figure 6.25b. The reference model for the ideal response, T_{ref} is superimposed. As expected from the frequency domain, the time domain corroborates that the model matching constraint is functioning satisfactorily.

Moreover, the structure of the feedforward controller was defined to have two poles and one zero. Now, it is important to verify why that structure is accurate. To begin with, the ideal feedforward controller can be obtained by Equation (6.15), where $T_{oM_{inner}}$ is the TF from r_{inner} to C_{PS}^* (i.e. y_{PS}).

$$C_{FF_{ideal}} = T_{ref} \cdot T_{oM_{inner}}^{-1} \tag{6.15}$$

(a) Pzmap of $T_{o_{M_{inner}}}^{-1}$ and of T_{ref}.

(b) Pzmap of $T_{o_{M_{inner}}}^{-1}$ and of T_{ref} zoomed in C_{FF}.
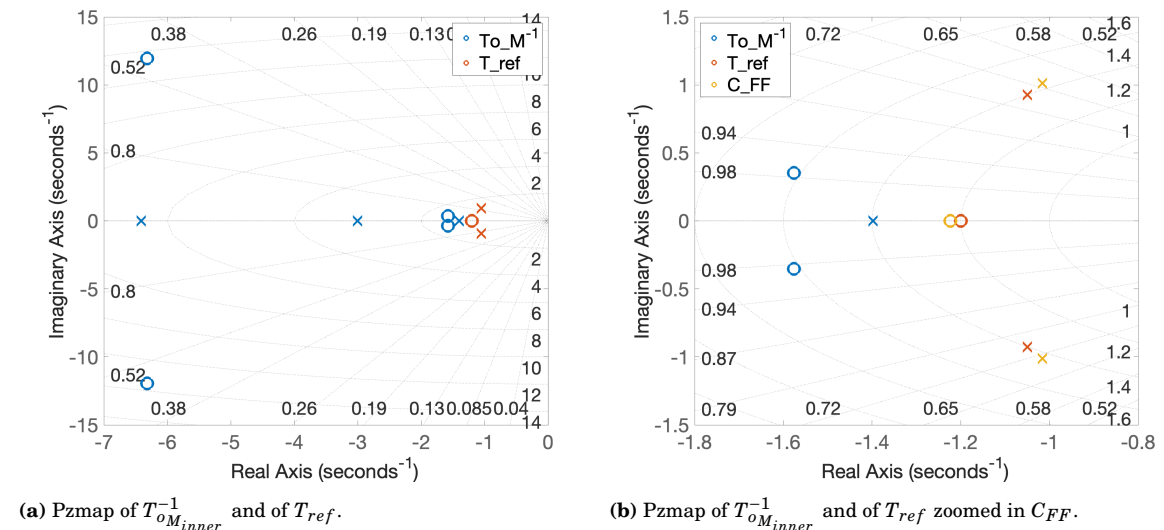
Figure 6.26: Pole zero map of the inner CL TF inverse $T_{o_{M_{inner}}}^{-1}$ and of T_{ref}, zoomed out in 6.26a and zoomed in with C_{FF} superimposed in 6.26b.

Thus, for a comprehensive analysis, the pole-zero map of T_{ref} and of $T_{o_{M_{inner}}}^{-1}$ is shown in Figure 6.26a. It is clear that the ideal feedforward is, therefore, all of the poles and zeros shown in the figure. Nonetheless, its complexity should be as low as possible since low order controllers are preferred due to the transparency and clear functionality, reduced hardware and software requirements, and cheaper, smaller, and lighter implementations. Therefore, it is more fundamental to look at the LF poles and zeros, which are the most dominant. Therefore, Figure 6.26a was zoomed in, yielding Figure 6.26b. On this figure, the C_{FF} controller synthesized is also superimposed. Moreover, it is verified that a simple approach was to choose two poles and one zero, which correspond to the most dominant dynamics. However, if the performance obtained was not as good as desired, an extra pole, or a pole and 2 zeros could be added to the structure. Overall, the idea is to focus on the lower frequency signals and add extra dynamics until a balanced performance is obtained. Further analysis on this CT controller design will be conducted in Chapter 7, in terms of stability margins, handling qualities, and time domain analysis in the linear and 6 DoF models.

6.4. DIGITAL FLIGHT CONTROL SYSTEM - MODIFIED CT DESIGN

Furthermore, since digital controllers are implemented in current aircraft, the design developed in the previous section will be expanded to take additional considerations with respect to this implementation. Thus, in Section 6.4.1, the digital design is introduced and motivated. Additionally, an unstructured preliminary controller is developed in Section 6.4.2, leading to the structured and final design in Section 6.4.3, which is conducted via the signal-based method.

6.4.1. DIGITAL DESIGN - INTRODUCTION & MOTIVATION

In Section 6.3, a CT controller was designed. Nevertheless, control laws are implemented with digital FBW in modern aircraft. In fact, there are several ways to approach digital control design. One option is to discretize the CT controller using, for instance, the bilinear transformation or the matched pole zero technique. Its advantage is that the sample period does not have to be selected a priori to the controller design. Nonetheless, as a consequence, to ensure the digital controller performs similarly to the CT version, the sampling time, T_s, must be small, giving worse results as it increases. Further details on how the system robustness is affected by not taking the discretization effects a priori are discussed in the analysis chapter, in Section 7.2.2. Secondly, the controllers can be directly designed in the z-domain. Lastly, another option is to design a CT controller, which already takes into consideration some properties of the sampling process and computation delays in the synthesis. The discrete time (DT) version of this controller yields a digital control system with improved performance, in comparison with the first approach, and allows the use of larger sample periods. This procedure is more suitable and, thus, it will be followed. It is known as
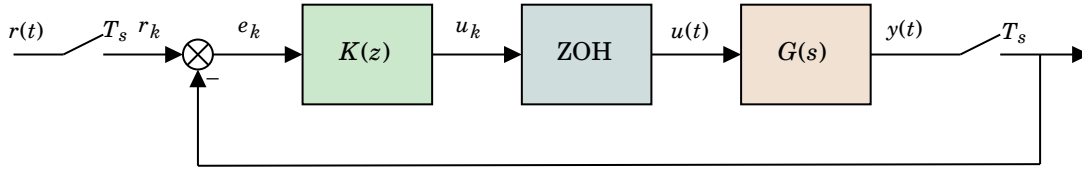
Figure 6.27: General configuration of a digital controller. Based on Stevens et al. [2015].

modified CT controller design for discretization. [Stevens et al., 2015]

The general configuration of the digital control scheme is represented in Figure 6.27. The plant $G(s)$ is continuous and $K(z)$ is a digital controller, where s and z correspond, respectively, to the Laplace and Z-transform variables. Additionally, the hold device corresponds to a Digital-to-Analog (D/A) converter, whose main purpose is to convert u_k, the digital control samples, into a CT signal $u(t)$. This signal $u(t)$ is updated at times kT_s. Moreover, the samplers have sampling time T_s and are Analog-to-Digital (A/D) converters. These take the samples $y_k = y(kT_s)$ and $r_k = r(kT_s)$ of the output $y(t)$ and $r(t)$, respectively, which are fed into the controller $K(z)$. [Stevens et al., 2015]

Furthermore, given that in the design of the CT controller, effects of the sampling and aliasing, computational delays and hold devices need to be considered, a more in-depth examination of these and how their implementation is performed will be conducted.

SAMPLING AND ALIASING

To begin with, it is important to define the Nyquist frequency $\omega_N = \omega_s/2$, where the sampling frequency is defined as $\omega_s = 2\pi/T_s$. In order to make sure aliasing does not occur, ω_s should be greater than twice the highest frequency appearing in the CT signal. In fact, aliasing yields in poor signal reconstruction, which might result in HF signals being misinterpreted as LF signals. [Stevens et al., 2015]

By following the condition for ω_s, the effects of aliasing are small. Nonetheless, the measurement noise also appears in the closed-loop system and may not be band-limited. Hence, HF measurement noise may be aliased down to lower frequencies that are within the plant bandwidth, contributing negatively to the system performance. Thus, in order to avoid this effect, a low-pass anti-aliasing filter is implemented after the measuring devices and before the samplers. [Stevens et al., 2015]

Moreover, it is assumed that the flight control computer runs at a sampling rate, f_s, of 80 Hz, which is adopted in existing design studies [Muir, 1997]. Therefore, the sampling time, T_s, sampling frequency, ω_s, and Nyquist frequency, ω_N, are described in Equation (6.16).

$$T_s = \frac{1}{f_s} = 0.0125 (s) \qquad \omega_s = 2\pi f_s = 502.65 (rad/s) \qquad \omega_N = \frac{\omega_s}{2} = 251.33 (rad/s) \qquad (6.16)$$

Furthermore, the cutoff frequency of the anti-aliasing filter, ω_a, should be selected as a value lower than ω_N, in order to guarantee good attenuation beyond this frequency [Stevens et al., 2015]. Thus, it was defined as in Equation (6.17).

$$G_a(s) = \frac{\omega_a}{s + \omega_a}, \quad \text{where} \quad \omega_a = 150 \text{ (rad/s)} \qquad (6.17)$$

COMPUTATIONAL DELAY

Additionally, it might happen that the microprocessor is so fast that the computational delay is negligible. Nevertheless, in case it is significant, the closed-loop response may be largely affected by it and, thus, it should be taken into consideration in the design. This entails special consideration if the signals are delayed by an entire sample period. [Stevens et al., 2015]

In fact, this delay occurs given that the A/D and D/A conversions and the FCS computations take time. Two different ways exist to address this. The first case consists of measuring the variables read at t_k which are used to compute the control signal applied at time t_{k+1}. The other approach is to measure the variable at time t_k and the D/A conversions are changed as soon as possible. Thus, the control signals are commanded to the plant as soon as these are computed. The first procedure is the worst case scenario, where the control actions are delayed by a full cycle, T_s. In the second procedure, the delay might be variable. Thus, an average value for the simulation might be considered. Taking this into account, the first method is followed, given that it represents the worst case possible and, therefore, it for sure works even if the delay is more reduced in the real situation. [Åström and Wittenmark, 1997]

Furthermore, the computational delay of a T_s has the following transfer function:

$$G_{comp}(s) = e^{-sT_s}, \tag{6.18}$$

where the magnitude is unitary and the phase is equal to $-\omega T_s$ radians. Nonetheless, given that the TF is not rational, Padé approximations of the exponential term are used to match the first few terms of the Taylor series expansion. An approximation of suitable order was chosen and it is represented in Equation (6.19). This approximation was chosen based on frequency and time domain results, in which the digital Simulink® block was compared with the discrete formulations of several Padé approximations. These were compared to verify the structure that captured the fundamental dynamics, while not being of a very complex structure. For brevity reasons, this is not depicted in the current report. This process was conducted not only for the computational delay approximation but also for the ZOH.

$$G_{comp}(s) = e^{-sT_s} \approx \frac{(1 - s \cdot T_s/4)}{(1 + 3 \cdot s \cdot T_s/4 + (s \cdot T_s)^2/4 + (s \cdot T_s)^3/24)} \tag{6.19}$$

ZERO-ORDER HOLD

Lastly, the D/A hold device reconstructs the plant control input $u(t)$ from the samples u_k. For that a Zero-Order Hold (ZOH) is used, which has the following working principle:

$$u(t) = u(kTs) = u_k, \quad kT_s \leq t \leq (k+1)T_s. \tag{6.20}$$

The ZOH is represented by the TF represented in Equation (6.21). The Padé approximant used is also shown.

$$G_0(s) = \frac{1 - e^{-sT_s}}{sT_s} \approx \frac{(1 - s \cdot T_s/14 + 23 \cdot (s \cdot T_s)^2/840 - (s \cdot T_s)^3/840)}{(1 + 3 \cdot s * T_s/7 + (s \cdot T_s)^2/14 + (s \cdot T_s)^3/120)} \tag{6.21}$$

DIGITAL CONFIGURATION

Moreover, given the previous properties, the configuration of the system used for the CT FCS design can be transformed to take into account the effects of aliasing, computational delays and hold devices. Figure 6.28 portrays how these previously mentioned terms are added to the design.
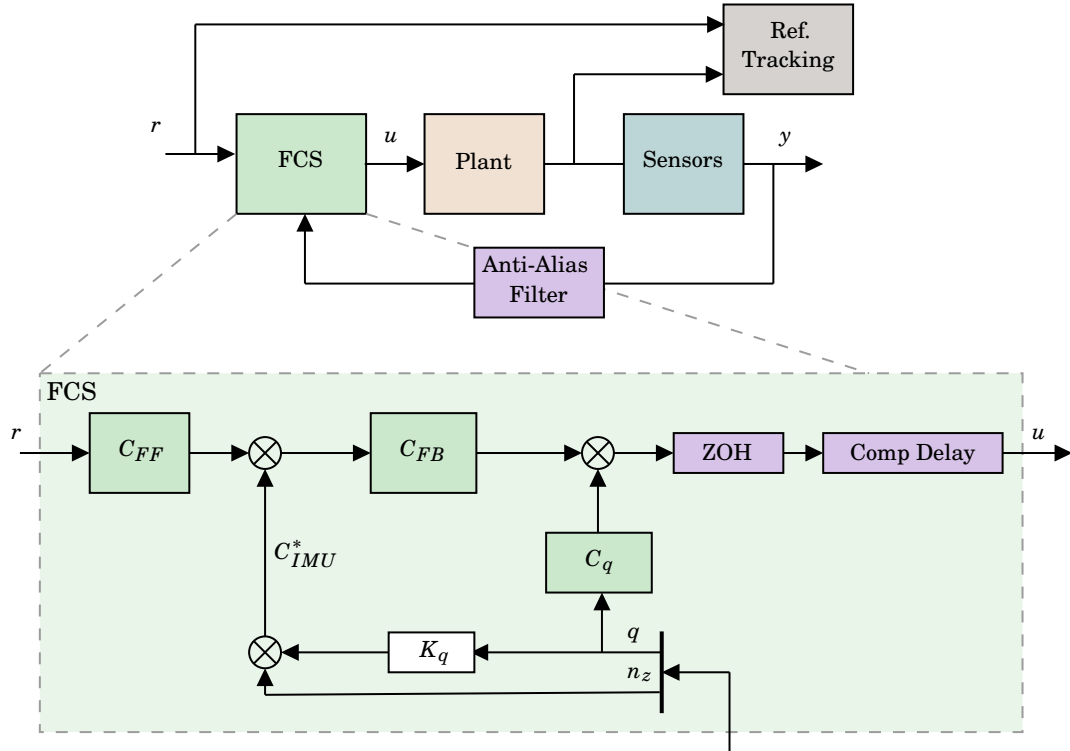
Figure 6.28: General configuration of the system for FCS design considering discretization effects.

6.4.2. Preliminary Unstructured Feedback Controller Modified CT Synthesis

Similarly to the procedure for the CT design, the optimal structure for the feedback controller is determined by synthesizing a full-order controller which is consequently reduced. The same procedure was followed, using the 4-Block method (see Equation (6.6)). The control setup is shown in Figure 6.29.
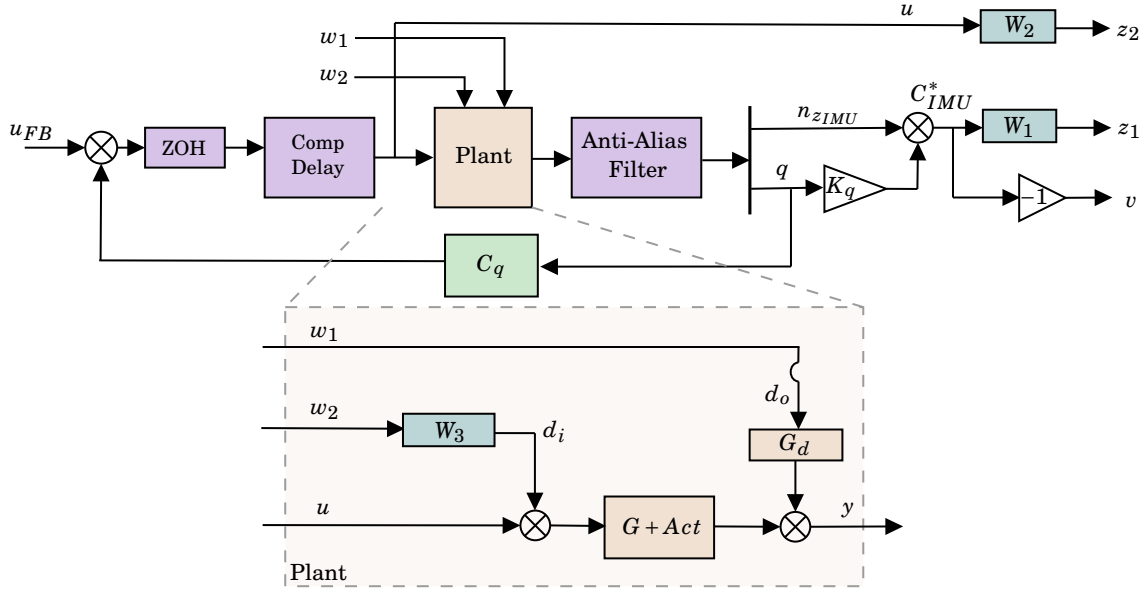
Figure 6.29: Control setup used for the unstructured modified CT design.

Thus, the filters W_1, W_2, and W_3 are designed accordingly as the inverse of the desired shape of the TFs, which was extensively described in Section 6.3.1. W_1^{-1} and W_2^{-1} are defined as high pass and low pass filters, respectively [1]. The correspondent characteristics are summarized in Table 6.4. W_3 is defined as a high pass filter and it is described as follows:

$$W_3(s) = \frac{160(s + 10)}{s + 10^4} \tag{6.22}$$

Table 6.4: WF characteristics for the MS unstructured modified CT design.

	W_1^{-1}	W_2^{-1}
$\underline{k}$	-50 dB	50 dB
$\overline{\omega}$	1.2 rad/s	14.3 rad/s
$\underline{\overline{k}}$	0 dB	1 dB
$\overline{k}$	6.02 dB	-50 dB

Moreover, as an approximation, the SAS, which is implemented as a gain on the pitch rate channel, C_q, was defined equally to the one computed for the CT design. The unstructured controller was obtained and the resulting performance level was $\gamma = 1.0055$ [2]. Given the value proximity to unity, the design objectives are very close to being met. The unstructured controller obtained is represented in Equation (6.23).

$$C_{FB_{FO}}(s) = \frac{\splitfrac{-5.5022e12(s + 1e04)(s + 5074)(s+287)(s + 204.6)(s + 200.6)(s + 13.44)(s + 1.745)}{(s + 1.007)(s^2 + 274.9s + 5.922e04)(s^2 + 399.4s + 2.144e05)}}{\splitfrac{(s + 1.003e04)(s + 1964)(s + 1755)(s + 316.4)(s + 37.56)(s + 1.235)(s + 0.003286)}{(s^2 + 79.56s + 2.441e05)(s^2 + 6.377e04s + 1.985e09)(s^2 + 1.449e05s + 1.049e10)}} \tag{6.23}$$

It is evident that several very HF poles and zeros exist, which can be discarded. Additionally, there is also the integrator-like pole (i.e. s ≈ -0.003 rad/s). However, several terms remain. The controller was, therefore, reduced into three different controllers in order to determine the most suitable structure [3]. These are shown in Figure 6.30. It is clear that the first order controller is only a good approximation until around 10^0 rad/s. Therefore, the final choice is between the second or third order controllers. It is observed that the third order would generate better results. Nevertheless, given that the second order controller is not largely mismatched up until 10^2 rad/s, this structure is highlighted as the most adequate one. In case satisfactory results are not achieved, the order should be augmented.

Moreover, from Equation (6.24) which represents the reduced second order controller obtained from the algorithm, and from Figure 6.30, it is observed that the low pass pole only influences the system around 10^8 rad/s. In normal circumstances, this additional pole could be discarded. Nonetheless, as discussed in Section 6.3, it is crucial to have roll off at HF in the feedback controller, although this requirement is masked through G_d. Thus, it is decided to impose the feedback structure as a PI plus a low-pass filter, where the low-pass is expected to be tuned as a pole within the dominant frequency range, contrary to the HF pole observed in this controller reduction. It is predicted that the zero and pole of the controller structure will be tuned to reduce the open loop crossover frequency slope and behave as a lead-lag compensator. All in all, control signal reduction and noise attenuation are, therefore, expected to behave as desired, contrary to the results obtained in the CT design.

$$C_{FB_{O2red}}(s) = \frac{-4.4655e07(s + 2.281)}{s(s + 2.149 \cdot 10^8)} \tag{6.24}$$

Additionally, the Go6 is computed by introducing the unstructured controller in the closed loop simulation and the frequency responses are shown in Figure 6.31. From observing the figure, it is clear that all of the CL TFs follow the desired shape.

Furthermore, it should be noted that the same tendency that occurred in the CT design is also observed in these results, in terms of the scaling introduced by the G_d model. This is the reason why the sensitivity function at HF has a decreasing gain. Besides the disturbance model, the anti-aliasing filter which is introduced at the plant output also contributes to this tendency provided that it is a low-pass filter. This is the reason why, at HF, several Go6 TFs obtained in the modified CT design have a lower gain when compared to the ones obtained in the CT design (see Figure 6.14).
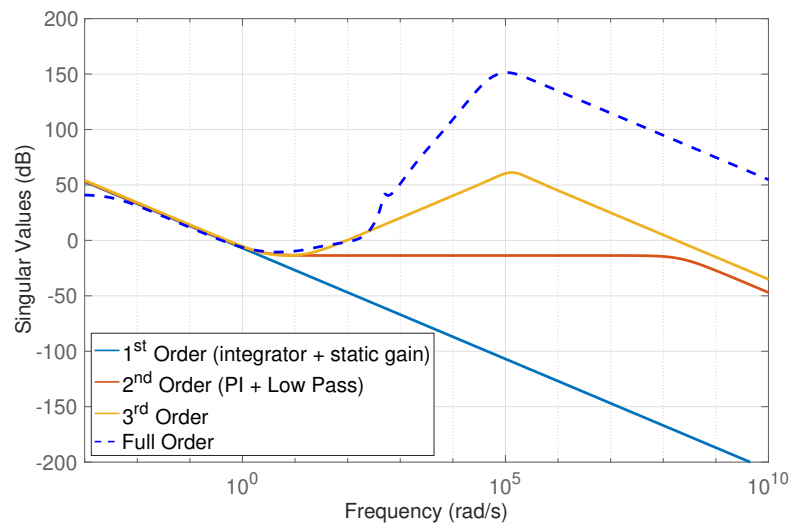
Figure 6.30: Unstructured and reduced controllers for the modified CT design with unstructured $\mathcal{H}_\infty$ MS design.

(a) S_o and S_i singular values.

(b) T_o and T_i singular values.

(c) KS_o singular values.

(d) S_oG singular values.
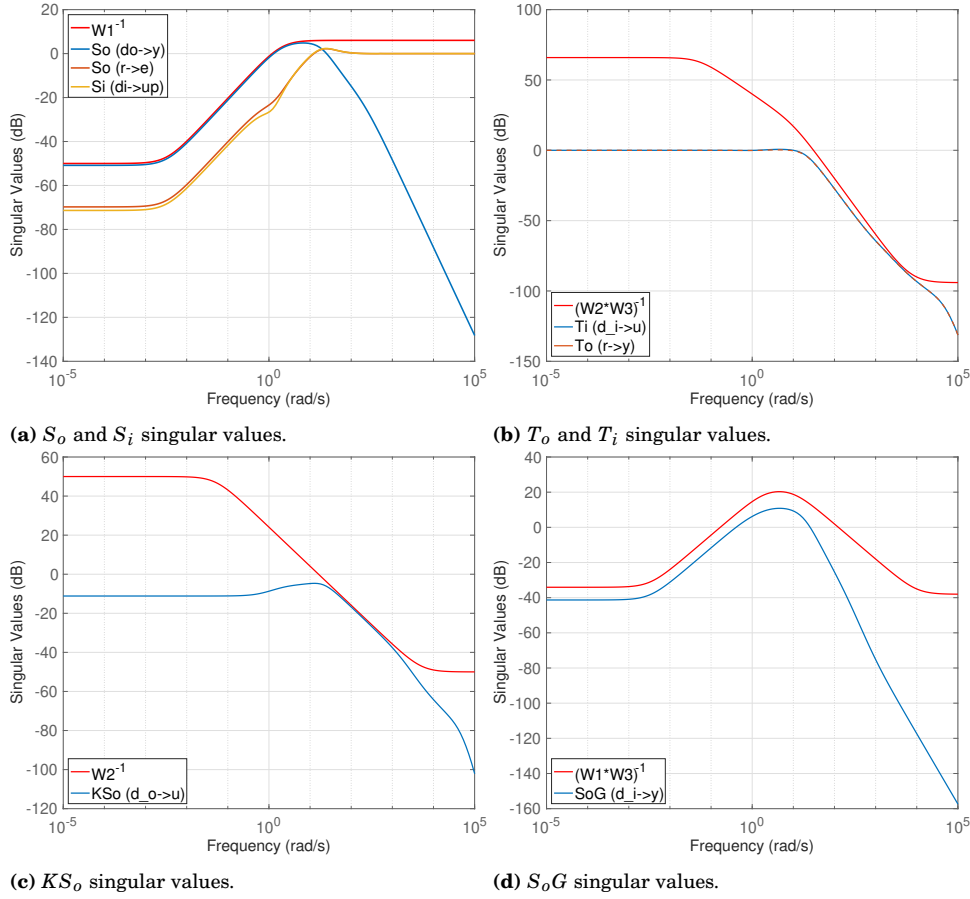
Figure 6.31: Go6 of the CL TFs obtained in the unstructured modified CT MS $\mathcal{H}_\infty$ design.

6.4.3. SIGNAL-BASED MS $\mathcal{H}_\infty$ MODIFIED CT FCS SYNTHESIS

The modified CT controller synthesis is conducted similarly to the CT procedure, detailed in Section 6.3.2, with the additional consideration of the discretization effects of the flight computer. To begin with, provided that the structures for C_q and C_{FB} are already pre-defined (see Section 6.4.2), the design requirements are imposed via limiting gains on the Go6 TFs as hard constraints to obtain the tuned C_q and C_{FB}. From these controllers, a study is performed to define an adequate structure for the feedforward controller. Consequently, by adding the model matching constraint as an additional hard constraint, the C_q, C_{FB}, and C_{FF} controllers are tuned simultaneously. In this final part of the procedure, some iterations are necessary in terms of WF adjustments to achieve a good balance between requirements. Therefore, the final results are shown in the current section and further analysis of the controller in terms of stability margins, handling qualities, and time domain simulations will be conducted in Chapter 7.

SYNTHESIS FCS SET UP

The implementation hardware effects, which were described in Section 6.4.1, are taken into consideration in the modified CT controller design. Therefore, the setup that is used as the controller synthesis foundation is shown in Figure 6.32. Additionally, the plant and reference tracking subsystems are expanded and portrayed in Figure 6.33.

CONSTRAINTS & WEIGHTING FILTERS SELECTION

Furthermore, it is fundamental to define the WF for the seven hard constraints. Given that the DT effects of the hardware are considered, namely the computational delay and the ZOH, it is expected that the filters need to be less tight when compared to the ones of the CT design (see Table 6.2). All of the filters follow the same tendency as before so that the requirements described in Section 6.2 are fulfilled. The filters inverse characteristics are presented in Table 6.5.

Table 6.5: WF characteristics for the structured modified CT controller design.

	$W_{S_o}^{-1}$	$W_{S_i}^{-1}$	$W_{T_i}^{-1}$	$W_{T_o}^{-1}$	$W_{KS_o}^{-1}$	$W_{S_oG}^{-1}$	W_M^{-1}
$\underline{k}$ (dB)	-50	-50	12.04	12.04	20	-50	-50
$\overline{\omega}$ (rad/s)	0.2	5.15	23.4	6.4	10^2	10^{-2}	3.05
$\overline{\overline{k}}$ (dB)	0	0	0	0	-13	-30.5	-23
$\overline{k}$ (dB)	11.6	9.69	-80	-80	-100	30	-4
Order	1	1	3	3	1	1	1
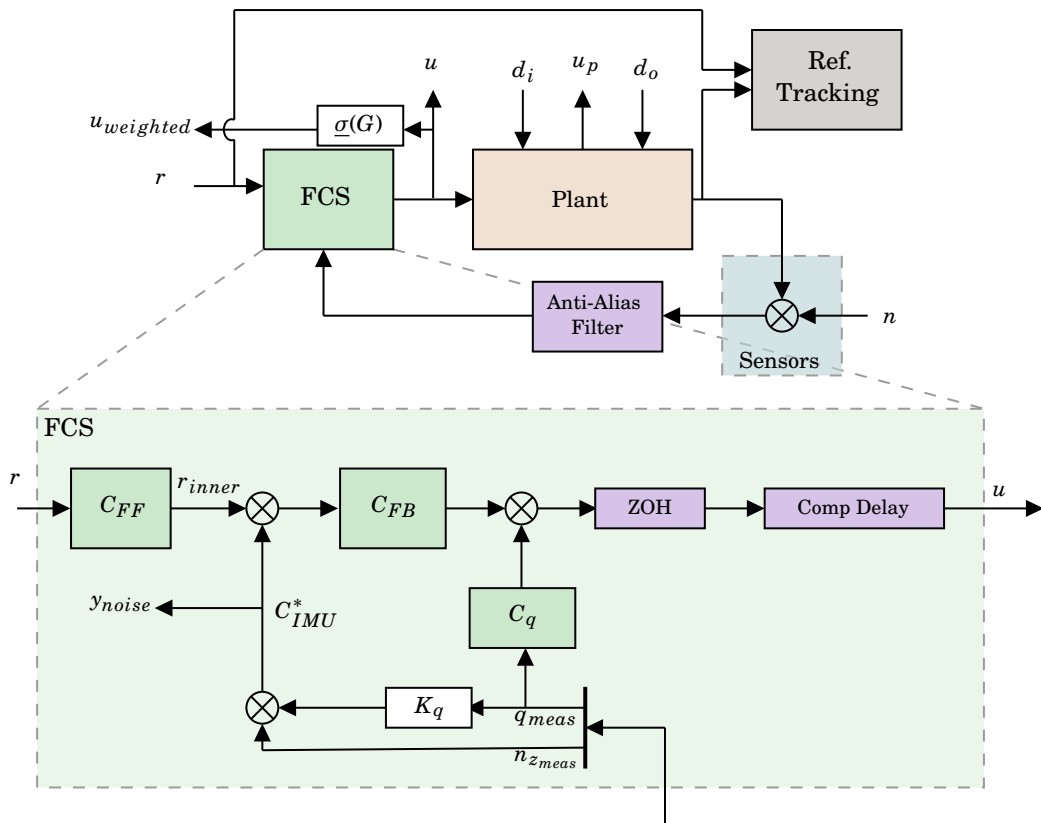
Figure 6.32: FCS set up for the structured modified CT controller design.
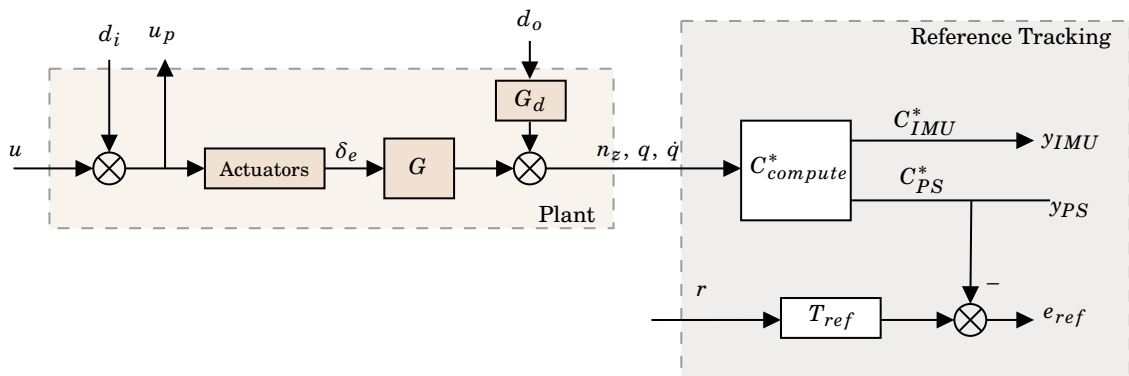
Figure 6.33: Plant and reference tracking subsystems, which are expanded from Figure 6.32.

Moreover, with the final values for the filters, the performance levels for each of the constraints are obtained and summarized in Table 6.6.

Table 6.6: Performance levels for each constraint for the structured modified CT controller design.

	S_o	S_i	T_i	T_o	KS_o	S_oG	M
γ	0.9981	0.9946	0.9915	0.9998	0.9900	0.9998	0.9998

During this process, it was noticed that the structure of the feedback controller, previously decided to be a PI plus a low pass, could be further reduced. In general, high gain at LF and roll off at HF is needed for the feedback controller. Additionally, a lead-lag compensator is usually beneficial to reduce the slope around crossover. Nevertheless, the results showed that the pole and zero of this representation were too close in terms of frequency and, thus, the contribution of this compensator would be insignificant. Furthermore, the optimization also tuned the zero to have a slightly higher frequency than the pole, contributing to the opposite effect as desired. Moreover, from the optimization procedure, the zero of this structure was tuned to have a frequency higher than the crossover frequency, which corroborated the fact that the pole and zero could be disregarded. Given the filters defined in Table 6.5, the tuned controller with the previously defined structure, is the following:

$$C_{FB}(s) = \frac{-0.33958(s+21.66)}{s(s+20)} \tag{6.25}$$

Although the preliminary study conducted in Section 6.4.2 provides insightful results and a strong basis for the controller design, it is important to re-examine the initial considerations. Therefore, given the resulting controller shown in Equation (6.25), the controller structure imposed for the feedback controller became a simple integrator multiplied by a static gain. From the optimization, the controllers retrieved are represented in Equation (6.26), while the corresponding frequency response is shown in Figure 6.34. Moreover, although the zero and pole of the feedforward controller are also very close in terms of frequency, it was decided to maintain the structure. The reasoning stands on the noticeable improvements in terms of the reference tracking response. This situation will be further discussed in the current section by analyzing Figure 6.39 to Figure 6.44.

$$C_{FF}(s) = \frac{1.0674(s+0.496)}{s+0.5307} \qquad C_{FB}(s) = \frac{-0.36499}{s} \qquad C_q(s) = -3.2555 \tag{6.26}$$

Moreover, for the actual implementation, the CT blocks that represent the discretization flight computer effects are substituted in Simulink® by delay blocks and ZOH blocks. Thus, the controllers also need to be discretized given that the FCS runs with a fixed sampling rate. The A/D and D/A converters allow to bridge this sampling rate with the remaining CT system. The digital implementation will be discussed in more detail in Section 7.1. Various methods can be used to convert controllers from CT to DT. The Tustin
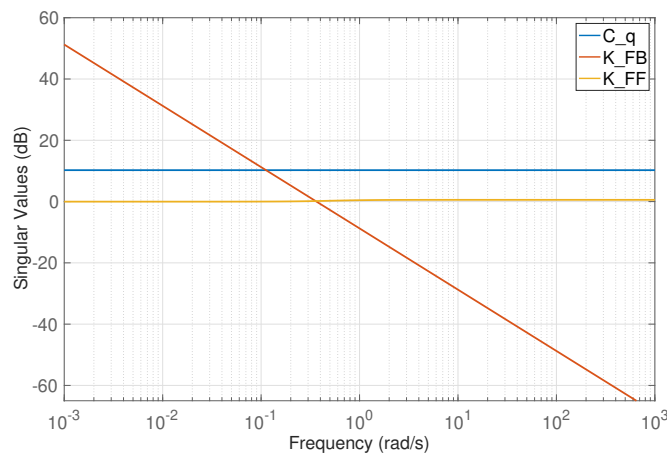
Figure 6.34: Singular Values of the controllers obtained for the modified CT FCS design.

method was selected for this purpose. While zero-order hold and first-order hold methods can also be employed, providing an exact discretization in the time domain for staircase and piecewise linear inputs respectively, the Tustin method focuses on the frequency domain. It ensures good frequency matching between the CT and DT models. The DT controllers obtained with sampling time $T_s = 0.0125$ seconds are shown in Equation (6.27).

$$C_{FF}(z) = \frac{1.067 - 1.061z^{-1}}{1 - 0.9934z^{-1}} \qquad C_{FB}(z) = \frac{-0.0022812 - 0.0022812z^{-1}}{1 - z^{-1}} \qquad C_q = -3.2555 \qquad (6.27)$$

The open loops were computed with the digital implementation, whose results are shown in Figure 6.35. The digital simulation with the DT controllers and DT blocks are the reason why a vertical line appears in the Nyquist frequency and no data is observed beyond that frequency. This occurs because the sampling process introduces limitations on the range of frequencies that can be accurately represented. As previously discussed in Section 6.4.1, this limit corresponds to half of ω_s. Frequencies beyond ω_N would introduce aliasing and, hence, corrupt the accuracy of the data. Moreover, the open loops represented include the plant input, L_i, and the plant outputs n_z measured at the IMU and q, respectively $L_{o_{nz}}$ and L_{o_q}. An open loop was also computed at the virtual plant output C^*, $L_{o_{C^*}}$, and at the load factor measured at the CoG, $L_{o_{nz_{CoG}}}$.

Figure 6.35 shows that, at LF, there is disturbance rejection on the loops opened at the plant input (L_i) and virtual plant output ($L_{o_{C^*}}$). On the contrary, this is not noticeable for the open loops of q and n_z given that no integral action is applied directly on these signals. At HF all of the loops decrease its gain considerably, as desired for noise attenuation and control signal reduction. It is verified that the $L_{o_{nz_{CoG}}}$ HF gain is considerably higher when compared to $L_{o_{nz_{IMU}}}$. As it was discussed in Section 6.1.2, this makes sense because, while at the IMU location (placed close to the ICR), the load factor is only dependent on the translational dynamics, at any other location there are additional contributions from the angular accelerations.

Additionally, the Go6 closed loops TFs that were shaped in order to impose system robustness are shown in Figure 6.36. The WFs inverse are also depicted. From the performance levels, which are all below unity (see Table 6.6), and from observing that all of the TFs are below the WF inverse, it is verified that no filter was violated. It should be noted that the Go6 was computed in the simulations with the modified CT setup, as shown in Figure 6.32.

Regarding the CL TFs, with d_o as the input, it is clear that these are under the influence of G_d. Nevertheless, contrarily to the CT design, KS_o behaves as desired because of the feedback controller roll off at HF (see Equation (6.26)) and because of the anti-aliasing filter. The control sensitivity function obtained from n to the control output, u, is shown in Figure 6.37. Thus, it is verified that at HF, there is roll off in this TF and noise attenuation and control signal reduction are guaranteed. Additionally, all of the other TFs were already extensively discussed previously and these are all shaped in the frequency domain as expected and desired.
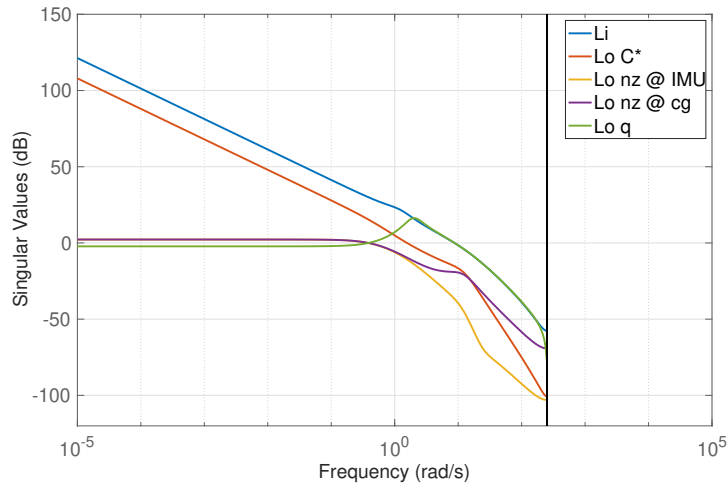
Figure 6.35: Open Loops of the FCS system, with the modified CT controller design.
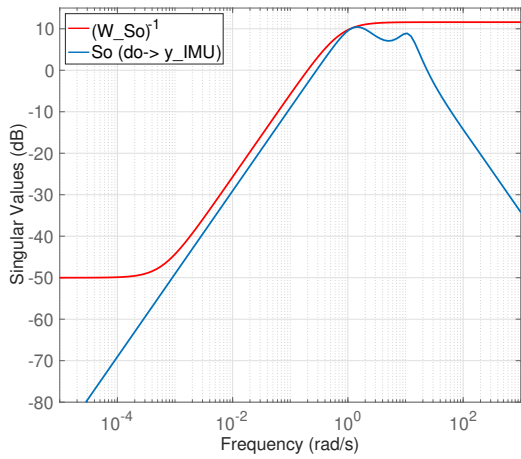
(a) Sensitivity S_o, and its filter inverse, W_{So}^{-1}.
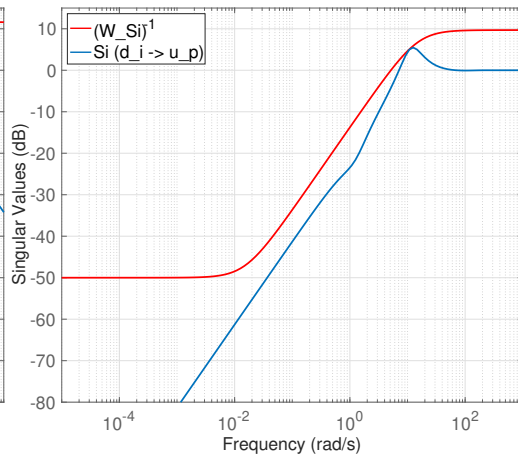
(b) Sensitivity S_i, and its filter inverse, W_{Si}^{-1}.

(c) Complementary sensitivity T_o, and its filter inverse, W_{To}^{-1}.
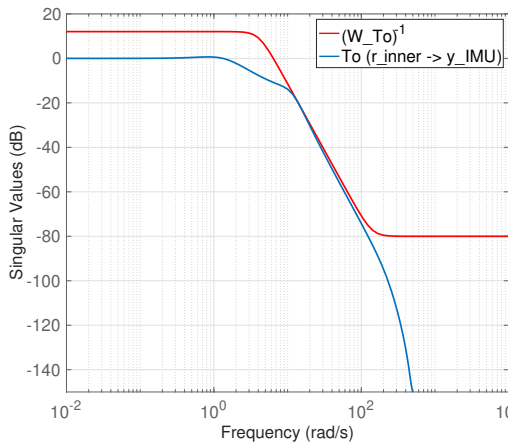
(d) Complementary sensitivity T_i, and its filter inverse, W_{Ti}^{-1}.
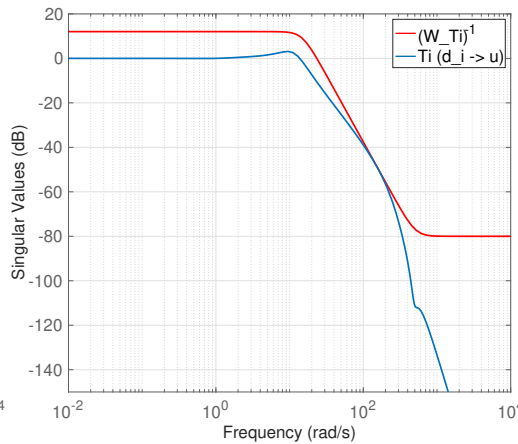
(e) Control sensitivity KS_o, KS_o scaled with $\underline{\sigma}(G)$ at LF, and its filter inverse, W_{KSo}^{-1}.
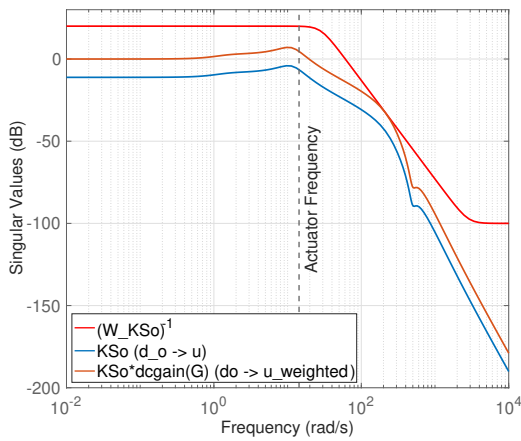
(f) S_oG, and its filter inverse.
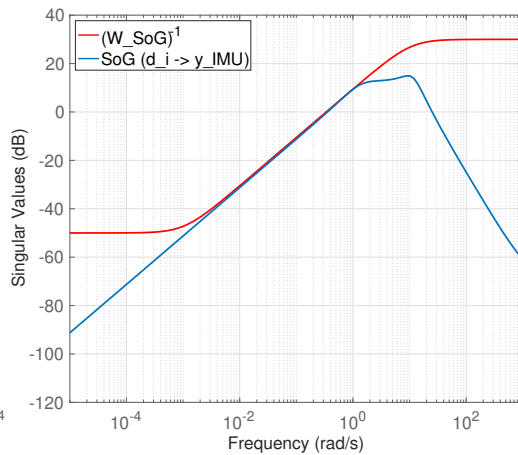
Figure 6.36: Singular Values of the Go6 closed loop TFs, namely of S_o (6.36a), S_i (6.36b), T_o (6.36c), T_i (6.36d), KS_o (6.36e), and S_oG (6.36f), with the associated WF inverse. Obtained from the structured modified CT design.
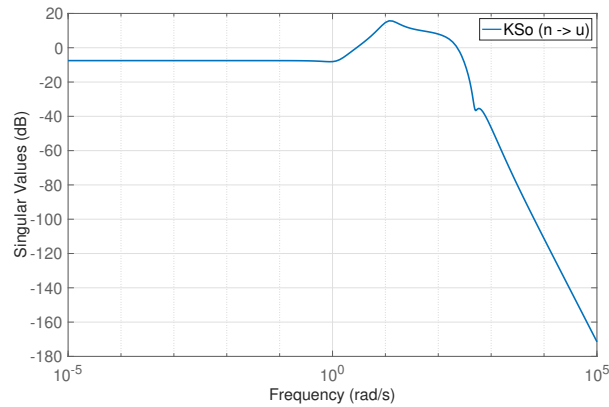
Figure 6.37: Control Sensitivity function, which is not scaled by the disturbance model, G_d, obtained in the structured modified CT controller design.
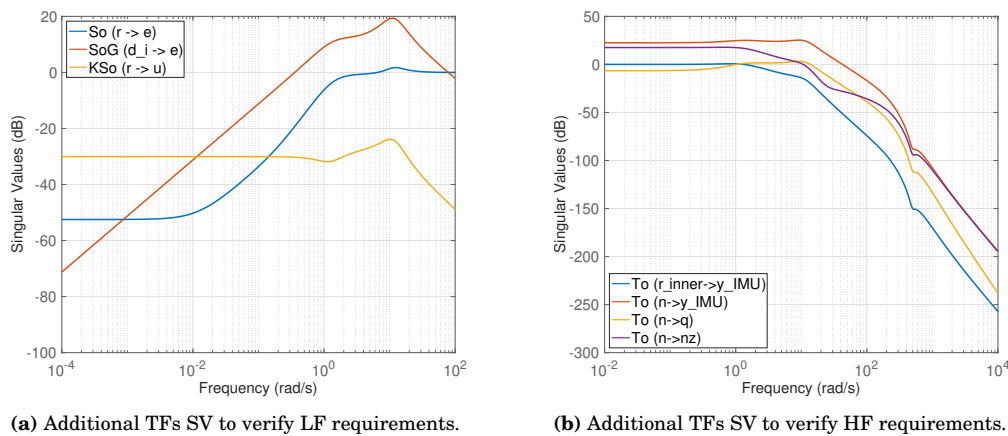
(a) Additional TFs SV to verify LF requirements.

(b) Additional TFs SV to verify HF requirements.

Figure 6.38: Additional closed loops TFs SV to verify additional requirements at LF (6.38a) and at HF (6.38b), obtained with the structured modified CT controller design.

Additional TFs relevant at LF that were not shown in Figure 6.36, are depicted in Figure 6.38a. These consist of $S_o(r \to e)$, $S_o G(d_i \to e)$, and $KS_o(r \to u)$. Hence, all in all, it is verified that, at LF in terms of robustness and singular values, the output disturbances are attenuated at the plant output, via S_o, the steady state tracking error is reduced, $S_o(r \to e)$, input disturbances are attenuated at the system output, via $S_o G$, at the tracking error $S_o G(d_i \to e)$, as well as at the plant input, $S_i(d_i \to u_p)$, and control signals are attenuated from r to u. This figure can be compared with Figure 6.24a, which are the same transfer functions from the CT design and it is observed that no major differences are noticeable.

Additional TFs are portrayed in Figure 6.38b, in order to verify that, at HF, there is noise attenuation in the plant outputs and virtual plant output by its low gain. At HF, in terms of robustness and singular values, noise is attenuated at the plant output ($T_o(r_{inner} \to y_{IMU})$) and control signal is attenuated from the input disturbances ($T_i(d_i \to u)$). Additionally, noise attenuation at the plant input and control signal attenuation from the output disturbances are now guaranteed given the low pass pole and the anti-aliasing low pass filter. Their contribution is clear in terms of HF roll off since it is significantly higher when compared to the CT design (see Figure 6.24b).

Furthermore, the model matching constraint and the corresponding TF are shown in Figure 6.39, while Figure 6.40 portrays the step response of the signal to be tracked superimposed with the ideal reference model. Thus, it is verified that the performance requirements imposed in terms of reference tracking are achieved. Additionally, in the step response, in the initial transient, a slight bump can be observed. This is due to the response that also occurs in the $n_{z_{PS}}$ signal itself, given that it is measured in the PS, which is forward of the ICR. Moreover, it was discussed that the zero and pole that constitute the feedforward controller (see Equation (6.26)) are very close in terms of frequency. Therefore, these could cancel each other and C_{FF} would be deemed redundant. To evaluate if the feedforward controller was beneficial, the

reference tracking step response was generated by assuming $C_{FF} = 1$. By comparing Figure 6.39-6.40 and Figure 6.41-6.42, it was decided to maintain the feedforward controller since it results in a noticeable improvement in terms of model matching with the reference model. Nonetheless, it is recognized that not implementing C_{FF} would also result in a satisfactory outcome. As an additional analysis, the pzmap of the ideal $C_{FF} = T_{ref} \cdot T_{o_{M_{inner}}}^{-1}$ is represented in Figure 6.43, which is zoomed in yielding Figure 6.44. The feedforward obtained from the optimization corresponds exactly to the lowest frequency pole and zero, which are the most dominant.
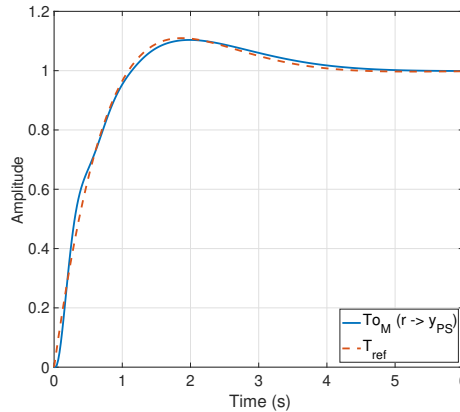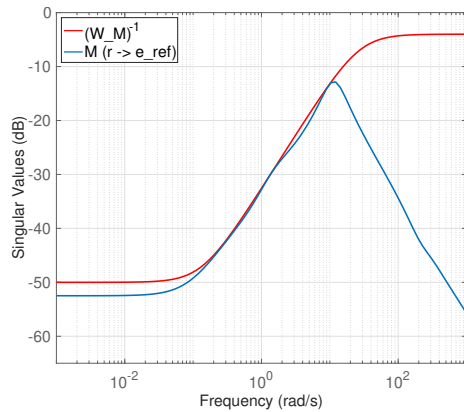
Figure 6.39: Model matching M and its filter inverse W_M^{-1}, obtained from the structured modified CT design.

Figure 6.40: Step response of the T_{ref} and of the CL TF T_{oM}, obtained from the structured modified CT design.
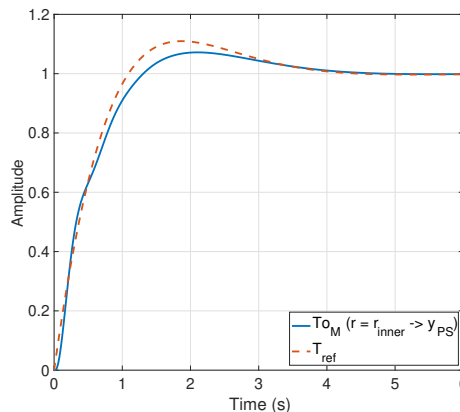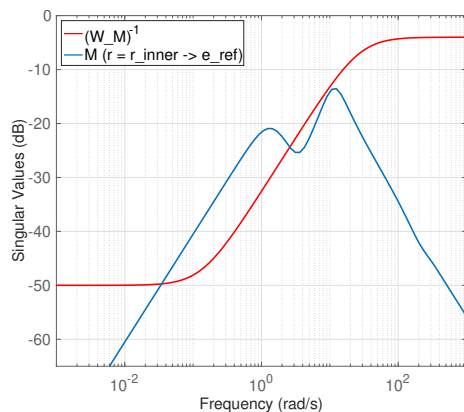
Figure 6.41: Model matching M and its filter inverse W_M^{-1} obtained from the structured modified CT design, when $C_{FF} = 1$.

Figure 6.42: Step response of the T_{ref} and of the CL TF T_{oM} obtained from the structured modified CT design, when $C_{FF} = 1$.
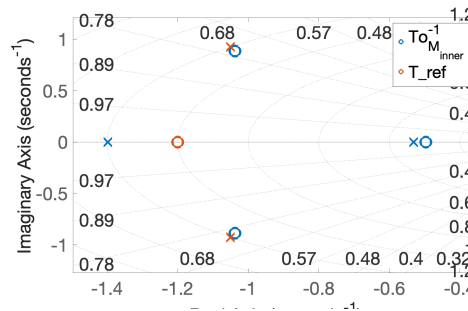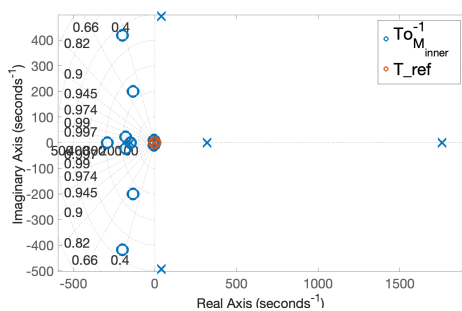
Figure 6.43: Pzmap of $T_{o_{M_{inner}}}^{-1}$ and of T_{ref}. Structured modified CT design.

Figure 6.44: Zoomed in portion of Figure 6.43.

6.5. MULTI-MODELING MODIFIED CT DESIGN

An extension to the previous modified CT controller is conducted which consists of the multi-modeling design. This approach involves the development of a single controller that performs effectively across a grid of flight conditions. Moreover, the methodology for the controller design is similar to the one conducted previously, where the setup is the same as the one portrayed in Figure 6.32. Nonetheless, for the current approach, a model array of state space models, which are obtained for the different flight conditions is substituted into the G and G_d models. Therefore, these models, whose conditions are detailed in Table 6.7, are used to collectively design a controller that guarantees acceptable robustness and performance over the entire set of conditions and that meets the requirements set in Section 6.2. The same input and output channels are used as before in order to impose the Go6 and model matching hard constraints. Thus, multi-modeling poses as an alternative option to gain-scheduling the entire flight envelope. Moreover, by accounting for variations in the system dynamics, this approach ensures that the controller is robust to changes in the nominal operating conditions, allowing for uncertainty in the altitude and speed of the aircraft.

Table 6.7: Flight conditions used for the multi-modeling modified CT controller design.

Model Name	Mach (-)	Altitude (m)
Ma06_h3250	0.6	3250
Ma06_h5450	0.6	5450
Ma06_h7650	0.6	7650
Ma05_h3250	0.5	3250
Ma05_h5450	0.5	5450
Ma05_h7650	0.5	7650
Ma04_h3250	0.4	3250
Ma04_h5450	0.4	5450

Thus, the WF need to be selected for the seven hard constraints. Furthermore, the necessity of imposing more flexible limits is expected, given that guaranteeing the achievement of the FCS requirements for the flight envelope with a single controller is more challenging than for the nominal case. The WFs inverse follow the same tendency as before, although, in general, slightly worsened in terms of crossover frequencies and HF gain limits. The selected values for the creation of the filters are summarized in Table 6.8 [1].

Table 6.8: WF characteristics for the multi-modeling modified CT structured controller design.

	$W_{S_o}^{-1}$	$W_{S_i}^{-1}$	$W_{T_i}^{-1}$	$W_{T_o}^{-1}$	$W_{KS_o}^{-1}$	$W_{S_oG}^{-1}$	W_M^{-1}
$\underline{k}$ (dB)	-50	-50	12.04	12.04	30	-50	-40
$\overline{\omega}$ (rad/s)	0.19	3.7	25.88	8.84	$2 \cdot 10^2$	10^{-2}	14.9
$\overline{\overline{k}}$ (dB)	0	0	0	0	-28.5	-29.7	0
$\overline{\overline{k}}$ (dB)	20	14.81	-80	-80	-100	30	12.04
Order	1	1	3	3	3	1	1

Moreover, with the filters imposed, the performance levels are obtained for each hard requirement. These are summarized in Table 6.9.

Table 6.9: Performance levels for each constraint for the multi-modeling modified CT structured controller design.

	S_o	S_i	T_i	T_o	KS_o	S_oG	M
γ	0.9987	0.9993	0.9992	0.9969	0.9969	0.9878	0.9992

Additionally, the controllers retrieved are represented in Equation (6.28), while the corresponding frequency response is shown in Figure 6.45. The feedback and pitch rate controller structures are the same

as the ones imposed on the modified CT controller design. However, to be able to meet the performance requirement in terms of model matching, the order of the feedforward controller was increased by a pole and a zero, becoming a second order structure. In case the same order structure were to be maintained the model matching bandwidth would have to be significantly reduced, which contributed to an oscillatory behavior of the reference tracking signal.

$$C_{FF}(s) = \frac{0.69923(s^2 + 2.698s + 2.72)}{s^2 + 1.928s + 1.921} \qquad C_{FB}(s) = \frac{-0.35899}{s} \qquad C_q(s) = -2.2247 \qquad (6.28)$$
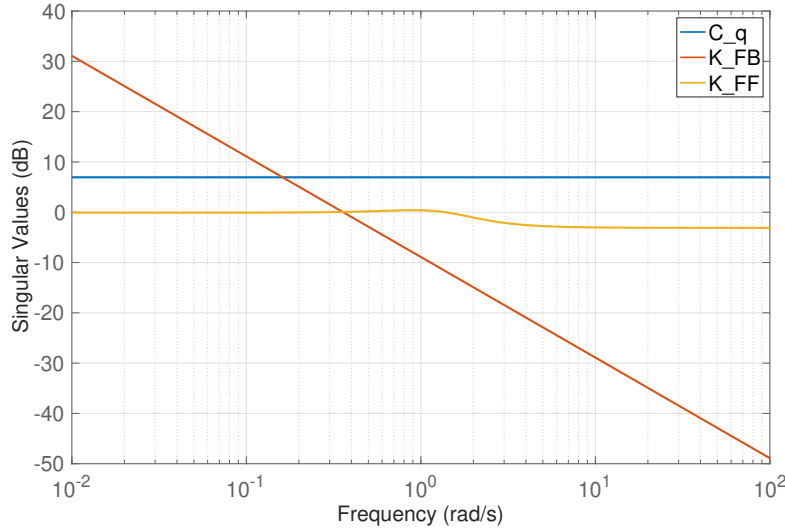
Figure 6.45: Singular Values of the controllers obtained for the multi-modeling modified CT FCS design.

As previously discussed, the controllers also need to be discretized because the FCS works with a fixed sampling rate. Thus, the controllers were discretized using the same method as for the modified CT design of the nominal condition, with the Tustin approximation. The DT controllers obtained with sampling time Ts = 0.0125 seconds, are shown in Equation (6.29).

$$C_{FF}(z) = \frac{0.70258(1 - 1.966z^{-1} + 0.9668z^{-2})}{1 - 1.976z^{-1} + 0.9762z^{-2}} \qquad C_{FB}(z) = \frac{-0.0022437 - 0.0022437z^{-1}}{1 - z^{-1}} \qquad C_q(z) = -2.2247$$
$$(6.29)$$

The open loops were computed with the digital implementation, whose results for all of the broken loop locations and flight conditions are shown in Figure 6.46. The behavior witnessed in similar to the previous ones, where large gains at LF are only observed at the plant input and at the virtual plant output C* where integral action is applied. At HF, it can be observed in all of the open loops that the gain decreases considerably, which is only observed until the Nyquist frequency.

Additionally, the Go6 closed loops TFs that were shaped in order to impose system robustness are shown in Figure 6.47. The WFs inverse are also portrayed in the figure. From the performance levels, which are all below unity, and from observing that all of the TFs are below the WFs inverse, it is verified that all of the filters are satisfied. It should be noted that the Go6 was computed in the simulations with the modified CT setup and, thus, information beyond ω_N is still observable. Moreover, it can be observed that these closed loops are very similar to the ones obtained in Figure 6.22 and Figure 6.36.

Furthermore, the model matching constraint and the corresponding TF are shown in Figure 6.48a, while Figure 6.48b portrays the step response of the signal to be tracked superimposed with the ideal reference model. Thus, it is verified that the performance requirements imposed in terms of reference tracking are accomplished.

(a) Open loop at the plant input, L_i.

(b) Open loop at the virtual plant output, $L_{o_{C*}}$.

(c) Open loop at the plant output, $L_{o_{nz(IMU)}}$.

(d) Open loop at the plant output, $L_{o_{nz(CoG)}}$.

(e) Open loop at the plant output, L_{o_q}.
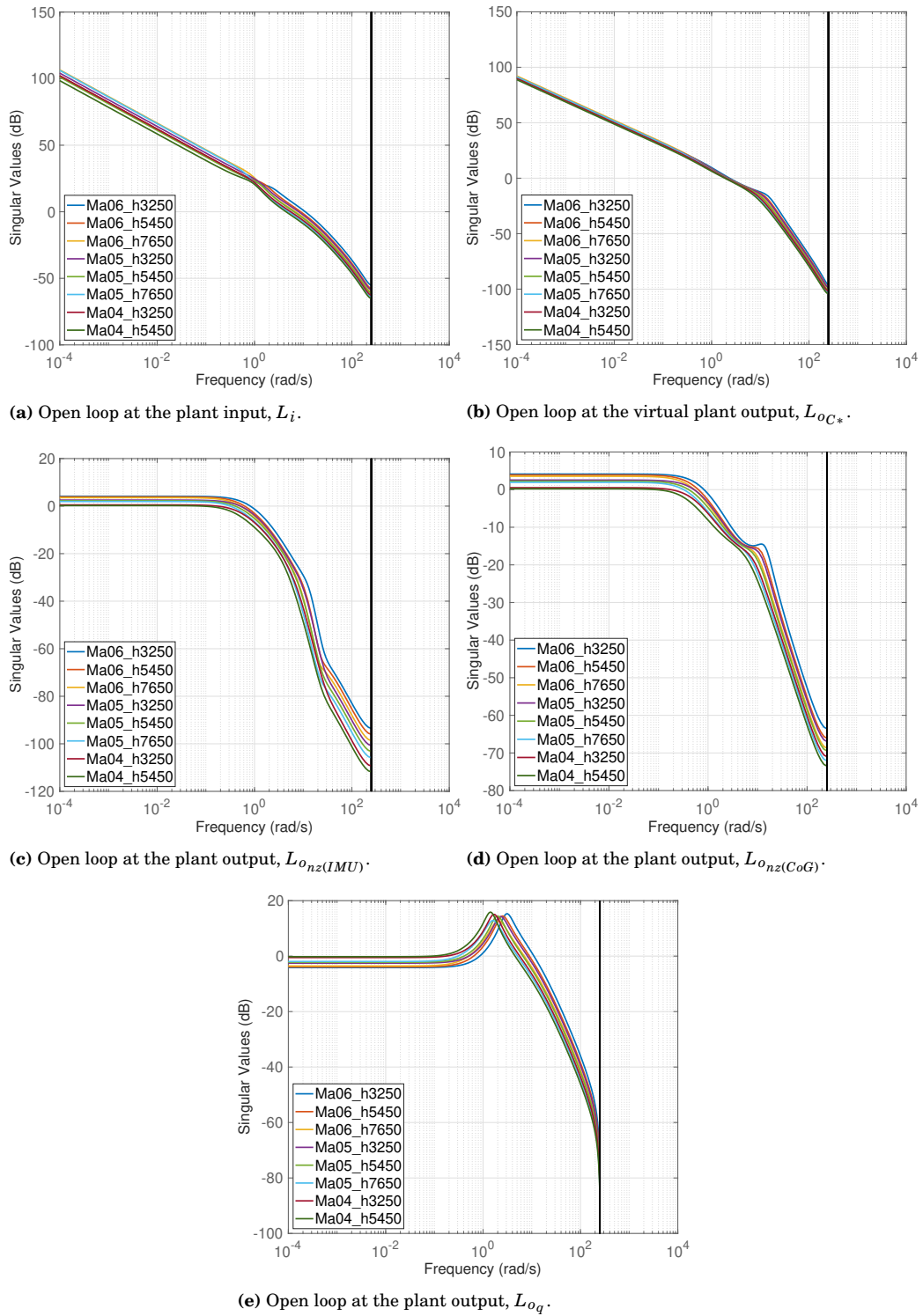
Figure 6.46: Open loop singular values open at the plant input (6.46a), virtual plant output C* (6.46b), and at the plant outputs nz measured in the IMU (6.46c), n_z measured at the CoG (6.46d), and at q (6.46e). Obtained from the multi-modeling structured modified CT design.
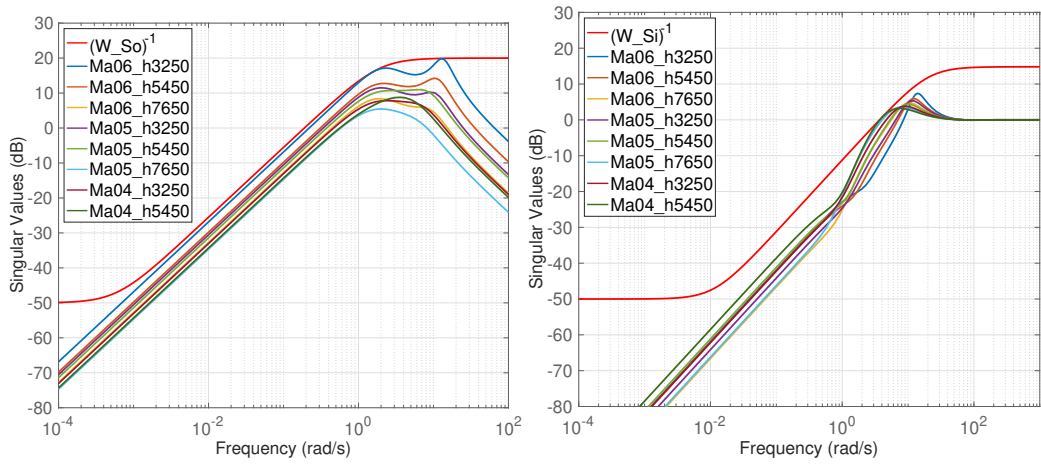
(a) Sensitivity S_o, and its filter inverse, W_{So}^{-1}.

(b) Sensitivity S_i, and its filter inverse, W_{Si}^{-1}.

(c) Complementary sensitivity T_o, and its filter inverse, W_{To}^{-1}.
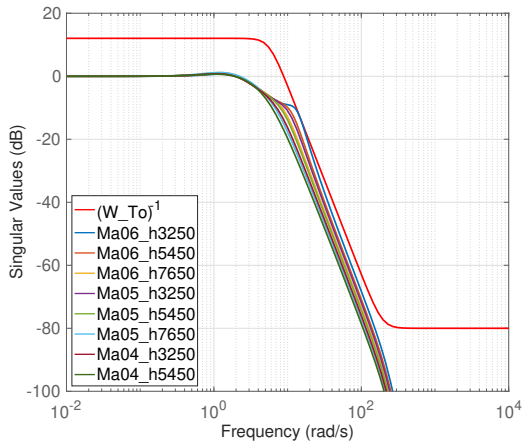
(d) Complementary sensitivity T_i, and its filter inverse, W_{Ti}^{-1}.
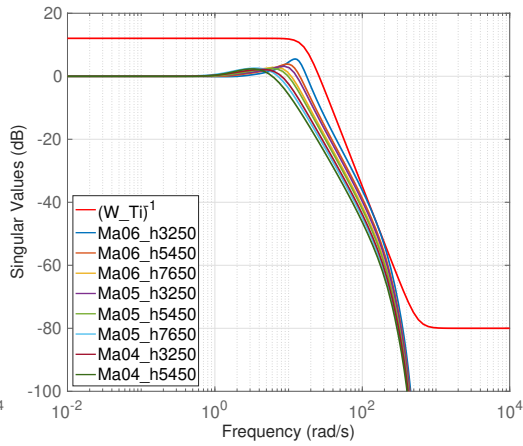
(e) Control sensitivity KS_o, KS_o scaled with $\underline{\sigma}(G)$ at LF, and its filter inverse, W_{KSo}^{-1}.
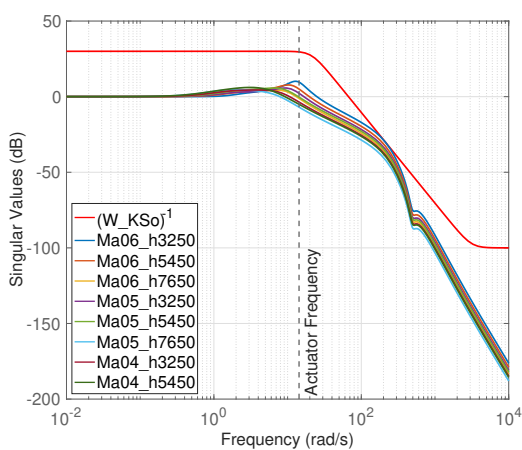
(f) S_oG, and its filter inverse.
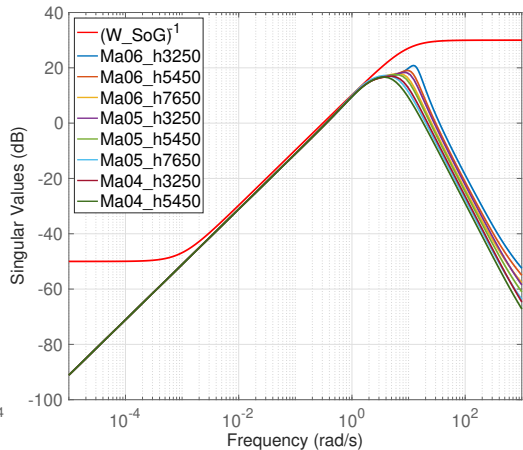
Figure 6.47: Singular Values of the Go6 closed loop TFs, namely of S_o (6.47a), S_i (6.47b), T_o (6.47c), T_i (6.47d), KS_o (6.47e), and S_oG (6.47f), with the associated WF inverse. Obtained from the multi-modeling structured modified CT design.

(a) Model matching M and its filter inverse W_M^{-1}.

(b) Step response of the T_{ref} and of the CL TF T_{oM}.
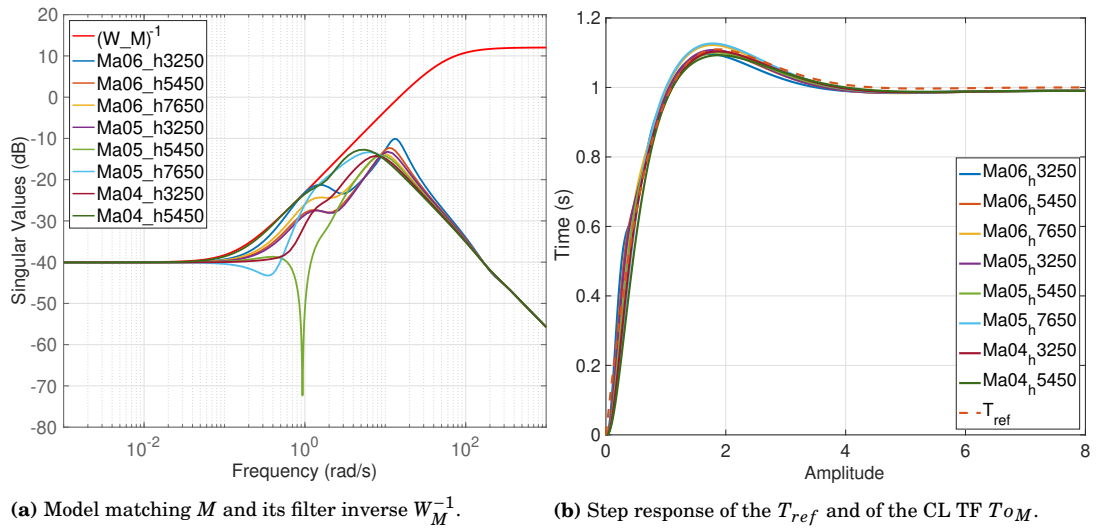
Figure 6.48: Performance of the reference tracking, in terms of model matching frequency 6.48a and time 6.48b responses, obtained from the multi-modeling structured modified CT controller design.

7

FLIGHT CONTROL SYSTEM ANALYSIS

In the previous chapter, three controllers were synthesized. Thus, the current chapter will focus on their analysis. Thus, to begin with, the digital implementation is first introduced in Section 7.1. Secondly, in Section 7.2, the stability margins are discussed. Additionally, three HQ criteria are examined for these controllers in Section 7.3, whereas the time domain simulations results and discussion are addressed in Section 7.4. Lastly, the robustness and performance analysis when uncertainty is applied to the system is examined in Section 7.5.

7.1. DIGITAL IMPLEMENTATION

The designs were conducted in CT using the Padé approximations of the discrete effects, as detailed in Section 6.4. However, the controllers obtained must be discretized for the implementation in the digital computer. For the FCS to become completely discrete, the digital configuration used for the modified CT design represented in Figure 7.1 is implemented digitally by using a ZOH Simulink® block for the ZOH, a delay block with sample time T_s for the computational delay, and a ZOH block to behave as the A/D converter right after the anti-alias filter, as depicted in Figure 7.2.

Furthermore, the Simulink® simulation is run with a fixed time step to simulate the discretization effects. For that reason, besides all of the discrete elements with their own sampling time, the solver details were changed and a fundamental step size of 1/30 of the computer sample time was defined. Thus, the CT elements of the simulation run at a $(1/80)/30 = 4.1667 \cdot 10^{-4}$ seconds.
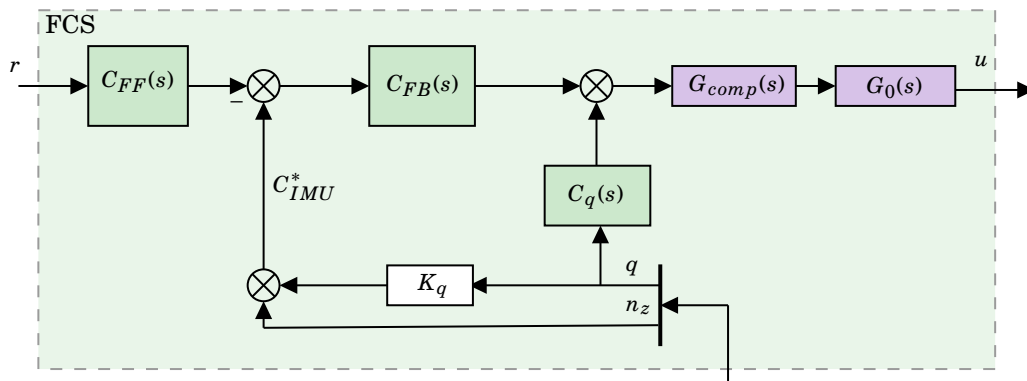
Figure 7.1: Simulink® representation used for the design of the modified CT FCS.
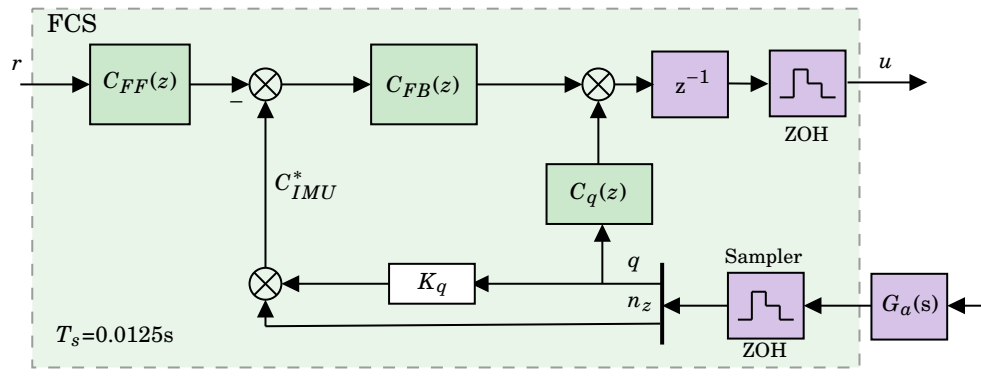
Figure 7.2: Simulink® representation used for the analysis of the digital FCS.

7.2. Stability Margins

To begin the analysis, the stability margins of the three controllers are computed. These will be discussed not only in terms of the disk margins, which are more realistic, but also in terms of classical stability margins in order to verify the FCS requirements satisfaction. Thus, at first, the robustness analysis is conducted for the CT and DT controllers in the nominal flight condition in Section 7.2.1, whereas the motivation behind the modified design is addressed in Section 7.2.2. Secondly, the multi-modeling robustness analysis is performed in Section 7.2.3.

7.2.1. Continuous Time and Digital Controllers Robustness Analysis

The CT and modified CT controllers were implemented in the CT and DT systems, respectively. The stability margins of these controllers are analyzed simultaneously for the several locations of the system.

Disk margins are a comprehensive measure of the robustness of the system due to the fact that these consider concurrent perturbations in the phase and gain of the system and, thus, extend the concept of classical gain and phase margins. Moreover, to complement the numerical evaluation of the disk margins, the system's open loops are visualized on Nichols charts, which are shown in Figure 7.3. In fact, a Nichols chart is a graphical representation that plots the open loops as a function of open loop gain and phase, in logarithmic and linear scales, respectively. Thus, this analysis provides a clear and intuitive view and provides insights into the robustness of the system to simultaneous gain and phase variations. For a more comprehensive analysis, the numerical disk margins were used to compute the disk margin regions and these were superimposed in the Nichols chart. Additionally, as previously discussed in Section 6.2, one of the FCS requirements is to have ideally 6dB and 45° of gain and phase margins, respectively, in terms of classical margins. In case the system does not violate this region using disk margins, then these will also be satisfied in the classical margins analysis.

As observed in Figure 7.3, most open loops satisfy the soft FCS requirement of R4 in terms of disk margins. The two exceptions involve the PM of the loops opened at the plant input and at the pitch rate output channel. Moreover, the SM for the DT controller are worse in two of the broken loop locations, namely at the plant outputs $n_{z_{IMU}}$ and q. Moreover, the design imposed for the modified CT controller was more flexible in terms of the WF when compared to the CT design, especially regarding the limits associated with the peaks of sensitivity functions. Although these are related to the SM, there is no pattern that proves that the modeified CT design was worse in terms of robustness. The margins associated with the peaks are the worst-case scenario and the maximum degradation that might be achieved. Nonetheless, only by computing the SM, conclusions on this robustness guarantees can be drawn. Furthermore, the stability margins associated with the load factor measured at the IMU are significantly larger than the ones for the load factor measured at the CoG. One possible explanation for this occurrence might be because of the extra computation needed to obtain $n_{z_{CoG}}$, which is dependent on the pitch acceleration. However, no information is available on how this might negatively affect the SM.
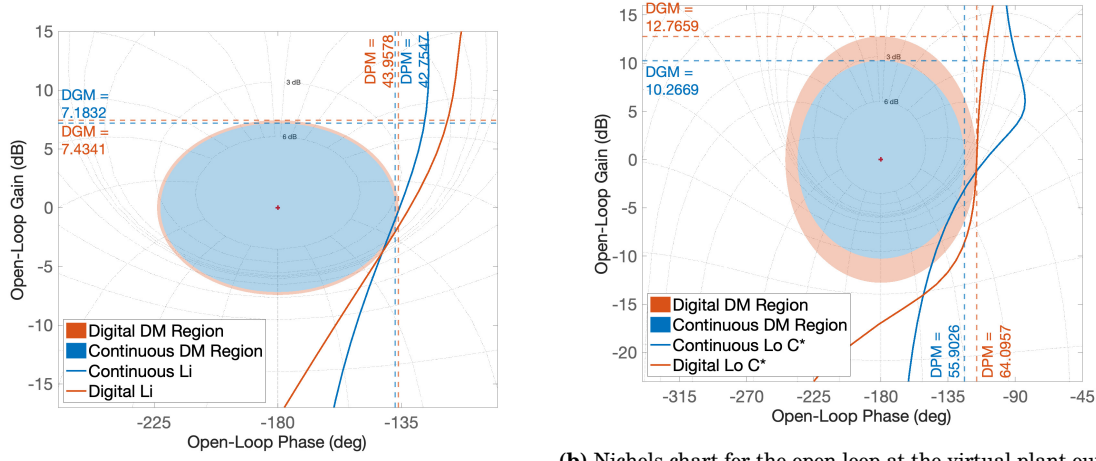
(a) Nichols chart for the open loop at the plant input, $\delta_{e_{cmd}}$.

(b) Nichols chart for the open loop at the virtual plant output, C^*_{IMU}.
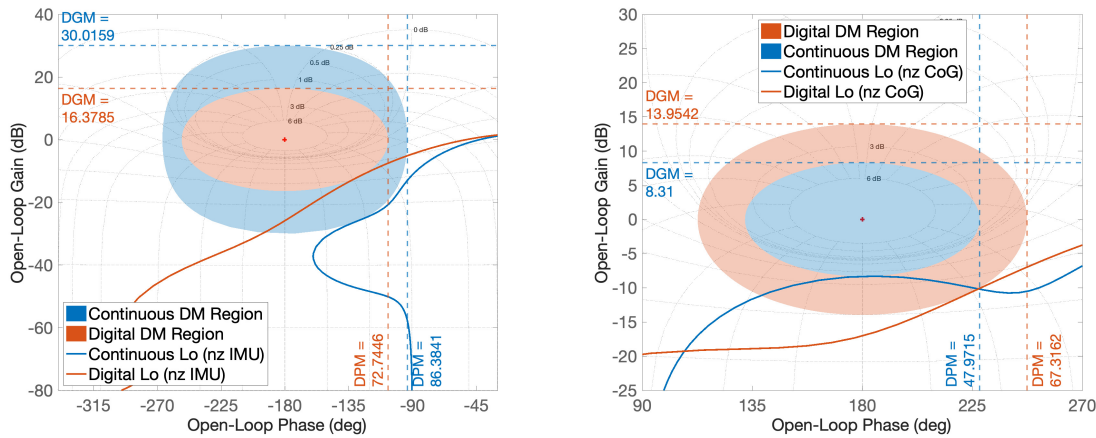
(c) Nichols chart for the open loop at the plant output, $n_{z_{IMU}}$.

(d) Nichols chart for the open loop at the plant output, $n_{z_{CoG}}$.
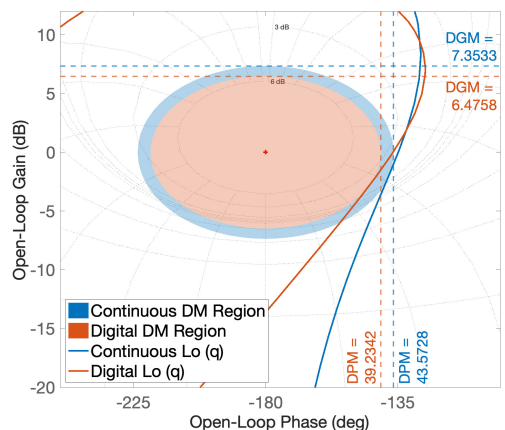
(e) Nichols chart for the open loop at the plant output, q.

Figure 7.3: Nichols charts of the CT and DT controllers superimposed with the corresponding disk margin regions and with the FCS exclusion requirements. Shown for all broken loops locations, including at the plant input (7.3a), at the virtual plant ouput (7.3b), and at the plant outputs n_z at the IMU (7.3c), n_z at the CoG (7.3d), and q (7.3e).

Furthermore, the information presented in Figure 7.3 regarding the disk margins is presented in Table 7.1 and in Table 7.2 for the CT and DT systems, respectively. Additionally, in these tables the classical GM and PM are also presented. Moreover, as expected, all of the values that concern the classical margins are higher than the more realistic method, the disk margins. Regarding the soft FCS stability margins requirement, it is verified that for the plant input and plant output q, the phase margins might be limited at certain frequencies. For the CT design, the classical PM fall short by $0.62°$ at the plant input, whereas, for the modified CT design, it falls short by $1.58°$ at the pitch rate outplut channel. Regarding the classical gain margins, all of the broken open loops for both controller satisfy the 6 dB requirement.

Table 7.1: Balanced disk and classical loop-at-a-time gain and phase margins for the CT controller.

Broken Loop	Disk Margins		Classical Margins	
	DGM (dB)	DPM (°)	GM (dB)	PM (°)
Plant input	± 7.18	± 42.75	∞	44.38
Virtual plant output (C*)	± 10.27	± 55.90	∞	70.03
Plant output (nz @ IMU)	± 30.02	± 86.38	∞	137.26
Plant output (nz @ CoG)	± 8.31	± 47.97	8.32	133.81
Plant output (q)	± 7.35	± 43.57	-22.85	45.19

Table 7.2: Balanced disk and classical loop-at-a-time gain and phase margins for the DT controller.

Broken Loop	Disk Margins		Classical Margins	
	DGM (dB)	DPM (°)	GM (dB)	PM (°)
Plant input	± 7.43	± 43.96	17.92	48.03
Virtual plant output (C*)	± 12.77	± 64.10	16.93	64.20
Plant output (nz @ IMU)	± 16.38	± 72.74	25.87	127.76
Plant output (nz @ CoG)	± 13.95	± 67.32	17.04	125.07
Plant output (q)	± 6.48	± 39.23	13.62	43.42

Furthermore, the disk margins were plotted as a function of frequency for all of the open loop systems for the CT controller in Figure 7.4a and for the DT controller in Figure 7.4b. It is possible to conclude that the DGM and DPM presented previously correspond to the minimum values obtained over the frequency
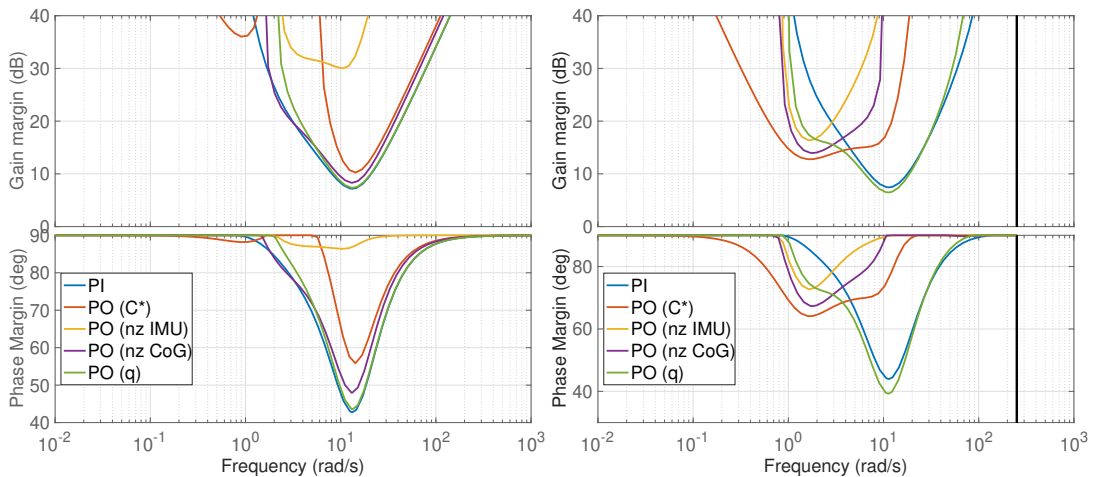
(a) Disk gain and phase margins for all broken loops as a function of frequency with the CT controller.

(b) Disk gain and phase margins for all broken loops as a function of frequency with the digital controller.

Figure 7.4: Disk gain and phase margins for all broken loops as a function of frequency with the CT 7.4a and DT 7.4b controllers.

range and it corresponds to the frequencies between 10^1 and $2 \cdot 10^1$. This frequency is exactly the one where the highest peak of the sensitivity functions occurs for the CT and modified CT designs, which can be observed in Figure 6.22 and Figure 6.36, respectively.

Additionally, a multi-loop analysis was also conducted on top of the loop-at-a-time stability margins. This entails introducing perturbations on the $\delta_{e_{cmd}}$ input signal and on the outputs $n_{z_{IMU}}$ and q. The results obtained are shown in Table 7.3. Naturally, lower SM margins are obtained in this situation because the multi-loop analysis mimics the system robustness more realistically, rather than an isolated view of each loop independently. Thus, as simultaneous perturbations are introduced in different channels, the DGM and DPM values in the multi-loop analysis are expected.

Table 7.3: Multiloop DGM and DPM for the CT and digital controllers.

	Disk Margins	
	DGM (dB)	DPM (º)
CT	± 2.61	± 16.94
Digital	± 3.06	± 19.81

7.2.2. MOTIVATION FOR MODIFIED CONTINUOUS CONTROL DESIGN

As previously discussed, the first controller consists of a CT design, which was consequently simulated in the CT configuration and does not take into consideration the discretization effects. The second is the modified CT controller design which, in the design phase, already includes the digital computer elements. The latter is, therefore, implemented in the digital configuration and analyzed in this scenario in the current chapter. Nonetheless, no major benefits have yet been discussed that support the need to include the extra complexity in the design phase with the discrete elements.

All of the controllers are, in the end, implemented in a digital computer. Thus, it is important to verify the characteristics of all controllers in this configuration and examine what are the consequences of not considering the discretization effects in the design. For that reason, the CT controller was implemented in the Simulink® file with the discrete elements and the stability margins in this context were computed. The resulting disk and classical SM values are shown in Table 7.4.

Table 7.4: Balanced disk and classical loop-at-a-time gain and phase margins for the CT controller implemented in the digital configuration.

Broken Loop	Disk Margins		Classical Margins	
	DGM (dB)	DPM (°)	GM (dB)	PM (°)
Plant Input	± 4.70	± 29.60	11.17	32.16
Virtual plant output (C*)	± 6.58	± 39.77	11.97	54.13
plant output (nz @ IMU)	± 25.63	± 84.00	27.69	136.99
plant output (nz @ CoG)	± 6.69	± 40.31	6.82	133.52
plant output (q)	± 3.80	± 24.32	8.01	26.85

All of these values decreased significantly, not only in terms of the disk margins but also regarding the classical ones when compared to the values in Table 7.1. Thus, the benefit of performing the modified CT controller design is clear. By implementing the CT controller in the digital frameworks, several effects might appear which may yield in negative effects. Additionally, for a straightforward comparison the DGM and DPM are plotted in Figure 7.5 for the CT design implemented in the CT configuration, for the modified CT design implemented in the DT configurations, and for the CT design implemented in the DT configuration. It can be clearly concluded that, in most cases, the region corresponding to the CT controller implemented in the digital file is considerably reduced.

(a) DGM and DPM at the plant input.

(b) DGM and DPM at the plant output (C^*).

(c) DGM and DPM at the plant output ($n_{z_{IMU}}$).

(d) DGM and DPM at the plant output ($n_{z_{CoG}}$).

(e) DGM and DPM at the plant output (q).
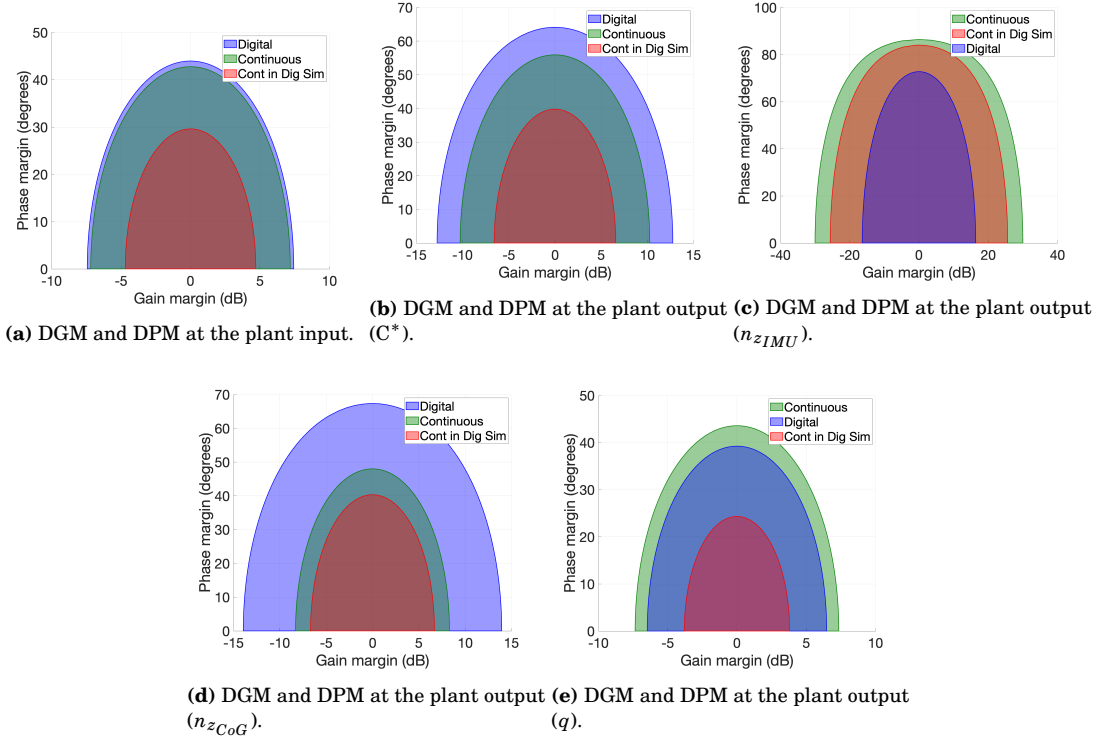
Figure 7.5: Comparison of the DGM and DPM at all of the open loop locations for the three controller configurations.

7.2.3. MULTI-MODELING ROBUSTNESS ANALYSIS

Additionally, the stability margins of the system in the flight envelope conditions are also analyzed when the multi-modeling controller is implemented. Thus, Figure 7.6 shows the disk-based stability margins for all broken loops locations and for all flight conditions. There are two frequencies ranges where the disk margins are significantly lower and, in fact, as expected, these correspond to the location of the two peaks of the output sensitivity function, portrayed in Figure 6.47a. In order to have a more comprehensive understanding of the margins computed, the worst case disk and classical stability margins are summarized in Table 7.5, where the respective flight condition is also described.

For almost all conditions, the flight condition with the worst case margins corresponds to the one with the highest velocity and the lowest altitude. A possible explanation for this occurrence might be linked with the dynamic pressure, which is higher both for decreasing altitudes and increasing velocities. Thus, in this flight point all of the effects in terms of elevator deflections or aerodynamics will generally be more pronounced. Therefore, perturbations induced in the system either at the plant input or output will also be translated into higher deviations, which decrease the stability margins. Regarding the WC classical stability margins, two of the loops do not satisfy the soft SM requirements, namely at the plant input, regarding both GM and PM, and at the pitch rate output, in terms of PM.

Table 7.5: Worst case disk and classical loop-at-a-time stability margins for the multi-modeling controller implemented in the digital configuration.

Broke Loop	WC Model Name	WC Disk Margins		WC Classical Margins	
		WC DGM (dB)	WC DPM (°)	WC GM (dB)	WC PM (°)
Plant input	Ma06_h3250	± 6.09	± 37.25	5.82	40.62
Plant output (C*)	Ma05_h7650	± 9.23	± 51.89	13.91	55.00
Plant output (nz IMU)	Ma06_h3250	± 14.56	± 68.81	22.29	109.72
Plant output (nz CoG)	Ma06_h3250	± 11.87	± 61.40	14.00	105.15
Plant output (q)	Ma06_h3250	± 5.03	± 31.45	10.96	34.67
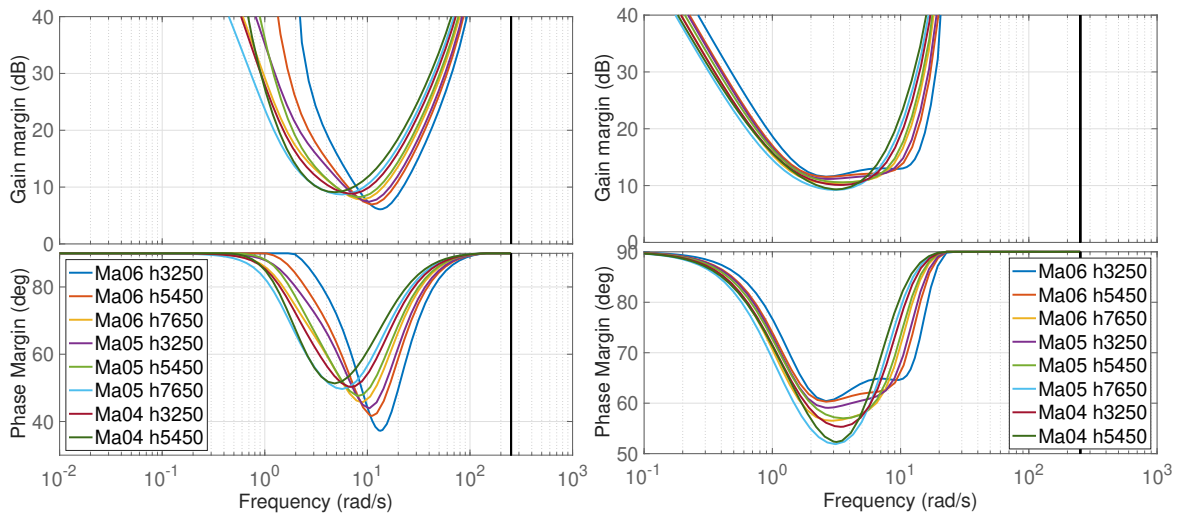
(a) Disk-Based Stability Margins at the plant input.

(b) Disk-Based Stability Margins at the plant output, C^*_{IMU}.
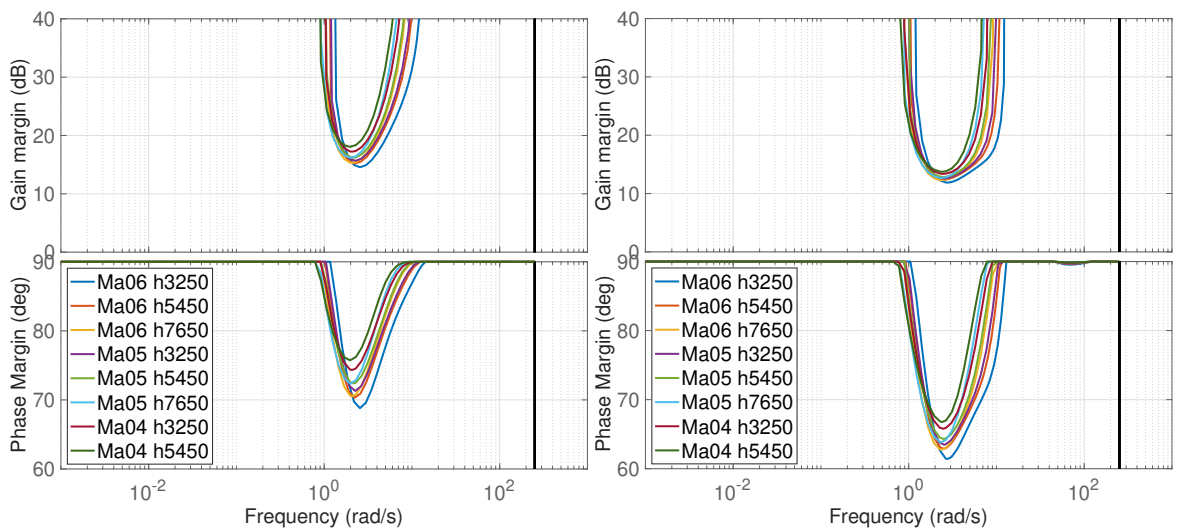
(c) Disk-Based Stability Margins at the plant output, $n_{z_{IMU}}$.

(d) Disk-Based Stability Margins at the plant output, $n_{z_{CoG}}$.
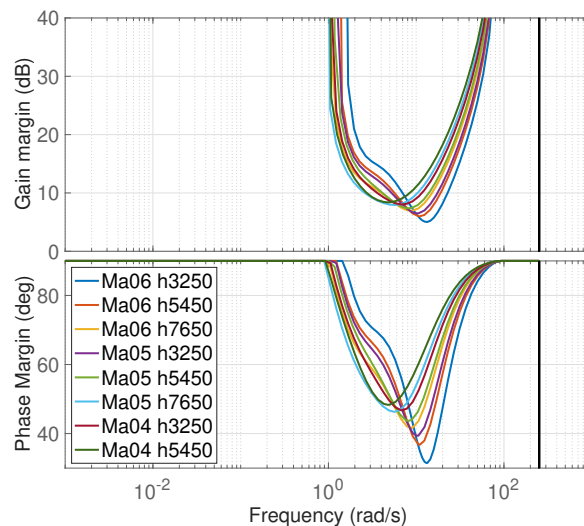
(e) Disk-Based Stability Margins at the plant output, q.

Figure 7.6: Disk-Based Stability Margins shown for all broken loops locations, namely at the plant input (7.6a), at the virtual plant ouput (7.6b), and at the plant outputs n_z at the IMU (7.6c), n_z at the CoG (7.6d), and q (7.6e), with the multi-modeling modified CT structured controller.

7.3. HANDLING QUALITIES

Handling qualities represent the dynamic characteristics of an aircraft as perceived by the pilot during control inputs, which influences the safety, performance, and pilot workload. Thus, analyzing HQ criteria is crucial to ensure that the aircraft responds predictably and effectively in the flight envelope. Moreover, as discussed in Section 4.4, the three main criteria which are used in the current research for HQ analysis are the attitude bandwidth, the flight path bandwidth, and the pitch rate overshoot & pitch attitude dropback, which are discussed in Section 7.3.1, Section 7.3.2, and Section 7.3.3, respectively.

7.3.1. ATTITUDE BANDWIDTH

Anonymous [1997] states that a measure of the handling qualities of an aircraft is its stability margin when operated in a CL compensatory task. Therefore, the bandwidth frequency, ω_{BW_θ} is referred to as the maximum frequency at which such CL tracking can take place without threatening stability. Thus, it is defined as the highest frequency at which the PM is at least 45° and the GM is at least 6 dB. In order to apply the criteria, the neutral stability frequency is determined, ω_{180}, followed by the computation of the $\omega_{BW_{gain}}$ and $\omega_{BW_{phase}}$ which correspond to the frequency where the GM is 6 dB and the PM is 45°, respectively. The bandwidth, ω_{BW_θ}, is the lesser of $\omega_{BW_{gain}}$ and $\omega_{BW_{phase}}$. Moreover, the shape of the phase curve at frequencies above ω_{BW_θ} is also relevant to evaluate the CL tracking. Phase roll-off can be represented by a time delay, whose parameter, τ_p, can be obtained by the relation of Equation (7.1) [Mitchell et al., 1994].

$$\tau_p = \frac{\Delta\Phi 2\omega_{180}}{57.3(2\omega_{180})} \tag{7.1}$$

Moreover, the limits for Category B, Class III are shown in Mitchell et al. [1994], although not represented in Anonymous [1997]. These are shown in Figure 7.7, with the results obtained with the controllers superimposed. In fact, Figure 7.7a shows the criteria limits and the results for the CT and DT controllers, whereas Figure 7.7b shows the results with the multi-modeling design for all of the flight conditions. It is concluded that for the three controller configurations, the system is within Level 1, as desired except for just one of the conditions in the multi-modeling design.
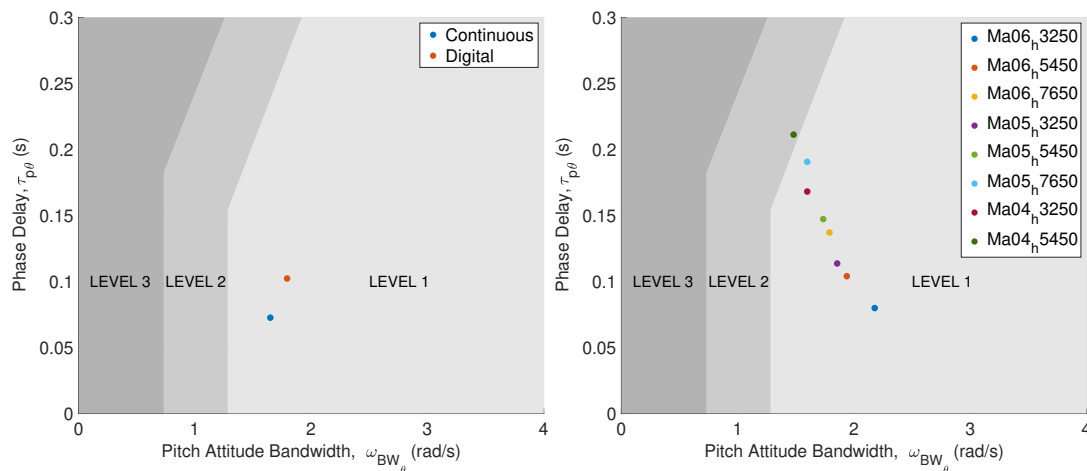
(a) Attitude bandwidth criteria, superimposed with the CT and DT results.

(b) Attitude bandwidth criteria, superimposed with the multi-modeling results.

Figure 7.7: Attitude bandwidth criteria limits, superimposed with the CT and digital results in 7.7a and with the multi-modeling results for all flight conditions in 7.7b.

7.3.2. FLIGHT PATH BANDWIDTH

The flight path response to pitch attitude change, for pilot control inputs, is also evaluated. The flight path bandwidth, ω_{BW_γ}, is defined as the frequency at which the response of γ lags the cockpit control input by 135°. The criteria is a function of this frequency and of the pitch attitude bandwidth, ω_{BW_θ}, and shall meet the requirements portrayed in Figure 7.8. Nonetheless, given that the primary means of controlling the flight path is not the attitude, the flight path bandwidth can degrade to Level 2. [Mitchell et al., 1994]

The results obtained with the three different controllers are shown in Figure 7.8. In fact, Figure 7.8a shows the criteria limits and the results for the CT and DT controllers, whereas Figure 7.8b shows the results with the multi-modeling design for all of the flight conditions. It is concluded that for the three controller configurations, the system is within Level 1, as desired, except for one of the flight envelope conditions (Ma = 0.4, h = 5450 m). Nonetheless, as previously mentioned, degrading to level 2 in this criteria is acceptable as the C^* parameter is the primary means of controlling γ [Mitchell et al., 1994].
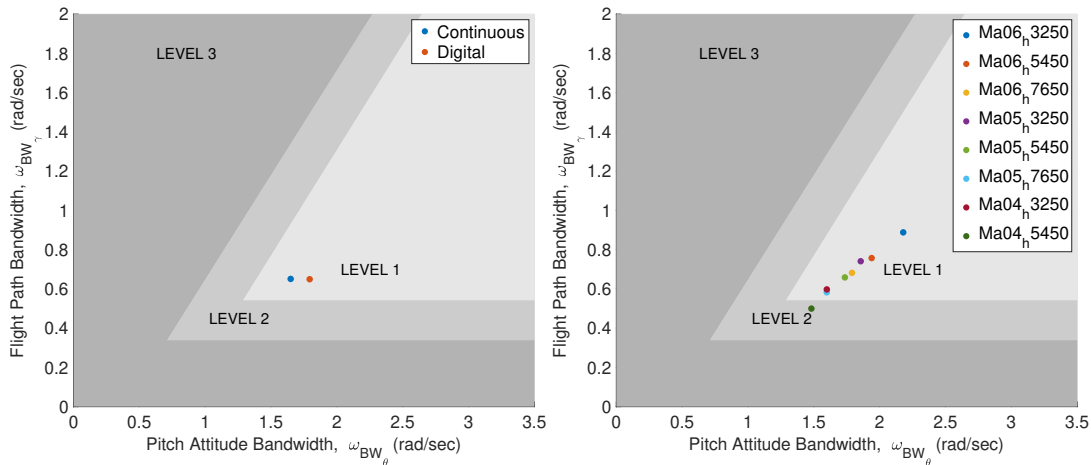
(a) Flight path bandwidth criteria limits, superimposed with the CT and digital results.

(b) Flight path bandwidth criteria limits, superimposed with the multi-modeling results.

Figure 7.8: Flight path bandwidth criteria limits, superimposed with the CT and DT results in 7.8a and with the multi-modeling results for all flight conditions in 7.8b.

7.3.3. PITCH RATE OVERSHOOT & PITCH ATTITUDE DROPBACK

The Dropback criterion was further developed by Gibson [1999], whose original definition was adopted in MIL-STD-1797A, dated from 1990. Although this documentation was canceled, its technical information was preserved in Anonymous [1997]. The criterion was later revised in Mitchell et al. [1994]. In fact, Dropback is a measure of the mid-frequency response to attitude changes which, in excessive values, yields in pilot complaints of abruptness and lack of precision in pitch control. Additionally, while the original definition is strongly influenced by time delay, the new proposed definition is unaffected by it. Since the Dropback is hypothesized as a limit in excessive mid-frequencies abruptness, it is desirable to use a parameter which is not highly influenced by time delay. This parameter is already accounted for separately in the pitch attitude bandwidth criterion, as discussed in Section 7.3.1. [Mitchell et al., 1994]

Furthermore, the criterion is evaluated based on the time-response plot of the pitch attitude dropback and pitch rate overshoot. Thus, for a better comprehension of the parameters used, the responses of the attitude, flight path and pitch rate, given a unit pilot step input from t = 1 s to t = 10 s, are shown in Figure 7.9 and Figure 7.10. These figures are plotted for the CT controller case for exemplification purposes. Nonetheless, the other two controller configurations yield similar responses .

Thus, based on these parameters, the values to be plotted in the criterion requirements can be computed. These are shown in Figure 7.11a for the CT and DT controllers and in Figure 7.11b for the multi-modeling design. As it can be observed, all of the results are within Level 1 HQ, as desired.
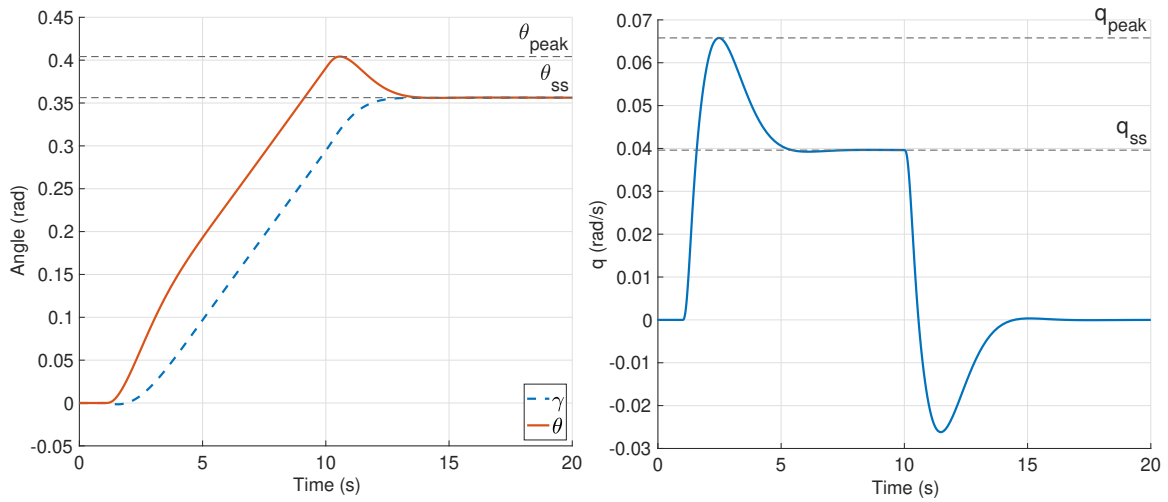
Figure 7.9: Attitude and flight path relationship, given a unit pilot step input from t = 1 s to t = 10 s.

Figure 7.10: Pitch rate response, given a unit pilot step input from t = 1 s to t = 10 s.
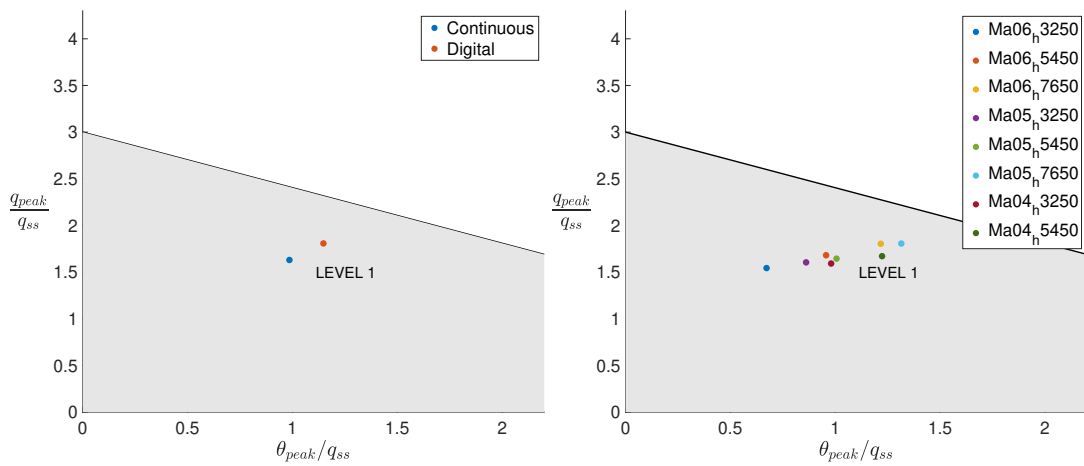
(a) Pitch rate overshoot & pitch attitude dropback criterion limits, superimposed with the CT and digital results.

(b) Pitch rate overshoot & pitch attitude dropback criterion limits, superimposed with the multi-modeling results.

Figure 7.11: Pitch rate overshoot & pitch attitude dropback criterion with results superimposed.

7.4. TIME DOMAIN SIMULATION

Testing the controllers in the linear domain is conducted by using the same closed loop system layout as it was represented in Figure 6.15 and Figure 6.32 for the structured controller design, respectively in CT and DT. The nonlinear implementation has different aspects to deal with and, thus, it is discussed in more detail in Section 7.4.1. Additionally, the CT and digital controllers are simulated in the linear and nonlinear models, whose results are shown in Section 7.4.2. Moreover, the validity of the multi-modeling design is examined in Section 7.4.3.

7.4.1. NONLINEAR IMPLEMENTATION

Firstly, to conduct the simulations in the 6 DoF Flying-V model, the FCS block is introduced. Similarly to the structures where the controllers were synthesized, the subsystem receives the reference and the sensor measurements as inputs and outputs the elevator deflection command and receives the data from the sensor measurements. The remaining control surfaces and thrust are kept in the trimmed value. Additionally, the input disturbances are added in the actuators' block, before the signal goes through the dynamics. The output disturbances, as previously stated, are introduced as α gusts. Hence, these are included in the Aerodynamics subsystem, right before the computation of the aerodynamic forces and
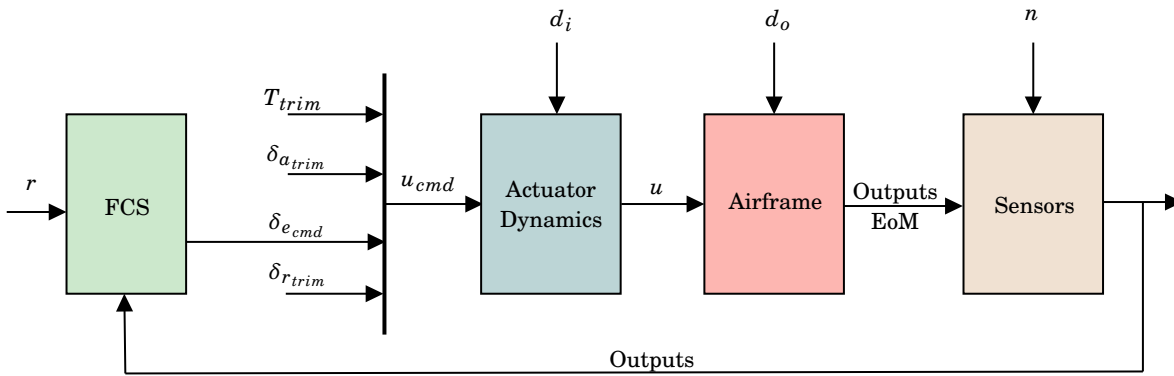
Figure 7.12: General configuration of the nonlinear Flying-V model with integrated FCS.

moments coefficients by adding the value to the α state. The noise is introduced in n_z and q, which are fedback to the FCS. Figure 7.12 portrays this general implementation of the FCS in the 6 DoF model.

Although the FCS is very similar to the previous structures mentioned, additional elements had to be included. Thus, the Digital FCS subsystem is shown in Figure 7.13. Firstly, the blocks in green correspond to the controllers, which are displayed as before. Secondly, the blocks in purple are the digital computer elements which, contrarily to the modified CT design, these consist of discrete Simulink® blocks, except for the anti-aliasing filter. Additionally, it should be mentioned that the sampler and ZOH blocks are introduced in the file. Nonetheless, these are only applied for conceptual accuracy reasons since Simulink® performs the digital to analog and vice-versa transformations automatically. Lastly, the velocity-based algorithm was introduced in order to tackle the initial undesired deviations. These consisted of the signal deviating from the initial trimmed value, even when no reference inputs were given for the system to follow. After a few seconds, the signal would behave as expected since the controller would impose the closed loop system to satisfactorily track any command. The unwelcomed phenomenon is addressed by the blocks in yellow, which are the discrete-time integrator and derivatives. The former is applied in the signal that goes to the plant input, whereas the latter blocks are introduced in the feedback paths. The proposed velocity-based method was introduced in Kaminer et al. [1995] as a systematic procedure to implement gain-scheduled controllers on the nonlinear plants. Its necessity follows from the fact that some gain-scheduled systems do not satisfy the linearization property. The property states that the same internal and input-output properties should hold in the feedback interconnection of the linearized plant and respective linear controller as well as in the feedback system consisting of the gain-scheduled controller and the nonlinear plant. In case this is not verified, loss of performance and instability may occur. Therefore, the idea is to provide integral action at the inputs to the plant. The feedback signals are differentiated so that all closed loop TFs are preserved.

Moreover, the integrator is initialized with the trimmed elevator deflection command. The CT controller implementation is very similar to the structure shown, except for the purple blocks which are not needed and the yellow ones that correspond to the CT integrator and derivatives.
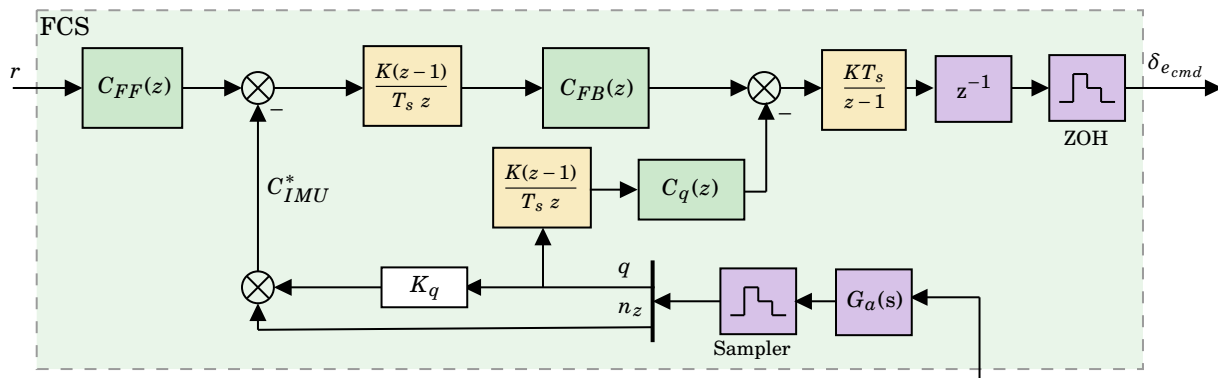
Figure 7.13: Digital FCS subsystem of the nonlinear model

7.4.2. Continuous Time & Digital Controllers Simulations

To begin the time domain simulations analysis, the CT and DT controllers will be tested both in the linear and nonlinear models. In a first instance, these 4 situations will be tested for the case of reference following, where the time evolution of the most relevant states and signals are shown. Secondly, noise and input and output disturbances are introduced with null reference signal, in order to evaluate the capacity of rejection and attenuation of these signals.

Reference Following - Linear & Nonlinear Simulations

Regarding the reference following, the relevant signal to consider is the C* parameter with the n_z measured at the PS. Thus, in Figure 7.14, this parameter time evolution is shown for the four configurations, which consist of the CT and DT controllers applied on the respective linear and nonlinear models. The step command inputs and the reference model to follow are also represented.

It is concluded that all of the simulations behave similarly until around $t = 26$ seconds. Beyond this instant, the linear models still closely match the reference model, whereas the nonlinear simulations start deviating from the desired value. Moreover, the reasoning behind this occurrence is the fact that the controller was designed for a linear and single flight condition. Since the C* commands resulted in the Mach and altitude values to diverge from this condition, unexpected behavior that was not accounted for during the controller design emerges. Moreover, for better analysis of the results the evolution of the flight condition are plotted in Figure 7.15 for the two nonlinear simulations, where the aerodynamic data points
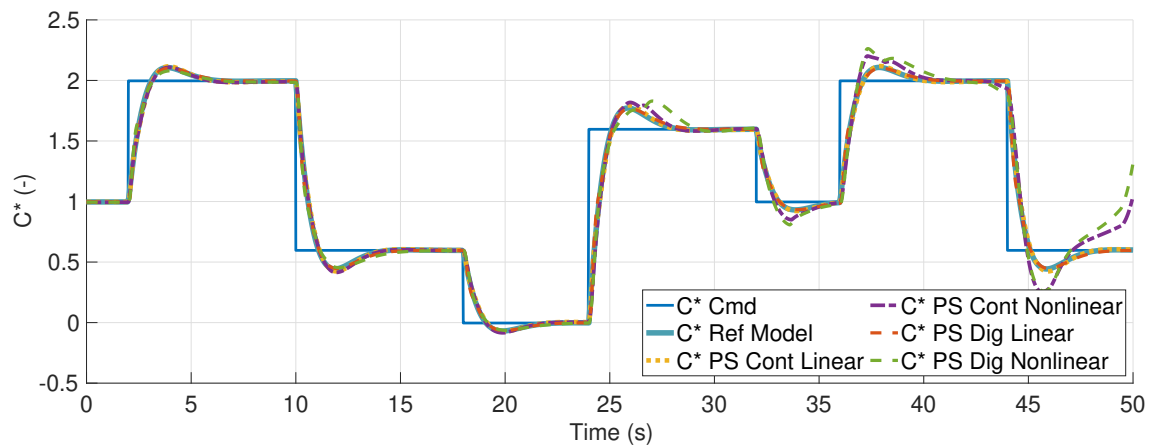
Figure 7.14: C* parameter time evolution for the 4 simulations, given a step reference command input.
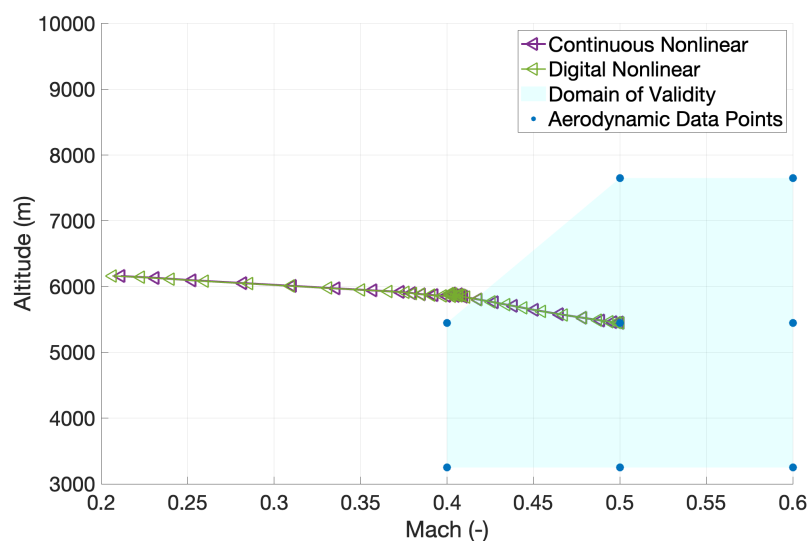
Figure 7.15: Flight condition evolution for the nonlinear time simulations with the CT and DT controllers.

are also shown. It is clear that although the Flying-V started in the nominal condition (Ma = 0.5 and h = 5450m), it rapidly diverged from this point. The response accuracy decrease is mainly due to the fact that the flight conditions reached have no valid information. In fact, the aerodynamic data of the region where the aircraft ended up in is computed as extrapolations from the bordering data points at Ma = 0.4.

Furthermore, the control surface deflections are also shown in Figure 7.16 and Figure 7.17, for the linear and nonlinear simulations, respectively. The different parameters for the control surfaces entail the elevator deflection at the controller output, $\delta_{e_{cmd}}$, after the input disturbance is introduced, $\delta_{e_{cmd plant}}$, and after the actuator dynamics, δ_e. Provided that d_i is null, the first two signals have the same time responses. During the first 35 seconds, the linear and nonlinear results are similar. Nonetheless, given that the aircraft experienced unexpected behavior, the deflections values also started deviating from acceptable ranges. Nevertheless, it is observed that the position is saturated in 14°, at the end of the simulation. Additionally, especially in Figure 7.16, it is noted that for the digital simulations, the overshoot of the deflections is higher and that these also experience more oscillations in comparison with the CT ones. This is probably caused due to the computational delay and discretization effects that do not allow to compute at every continuous time instant the best deflection angle.

Furthermore, the time evolution of the outputs n_z measured at the IMU and q are also represented in Figure 7.18 and Figure 7.19, respectively. Although, in the beginning, the linear and nonlinear simulation results are similar, these diverge after a while as expected given the reasoning already explained. Additionally, the angle of attack is also plotted in Figure 7.20, where it is noticeable that for the nonlinear simulations the values are rising significantly. These values might be a leading cause of aircraft instability. It should be noted again that these values are due to the fact the aircraft is leaving the acceptable region of the flight envelope, given the data points available.
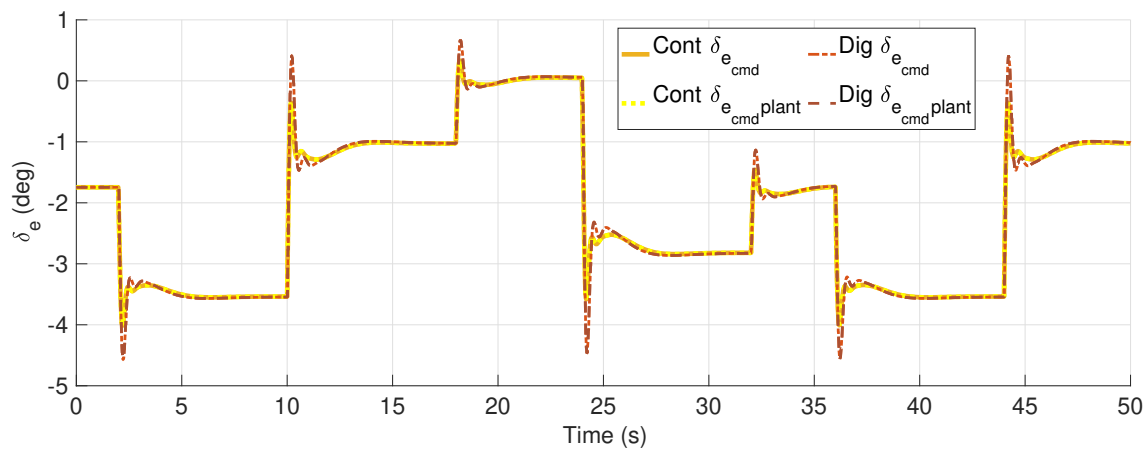
Figure 7.16: Control surface deflections for the linear simulations with the CT and digital controllers.
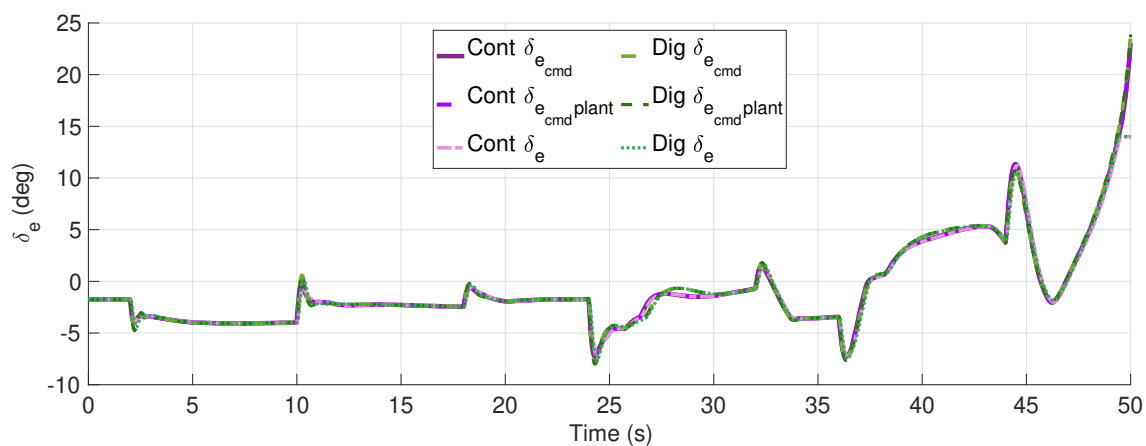
Figure 7.17: Control surface deflections for the nonlinear simulations with the CT and digital controllers.
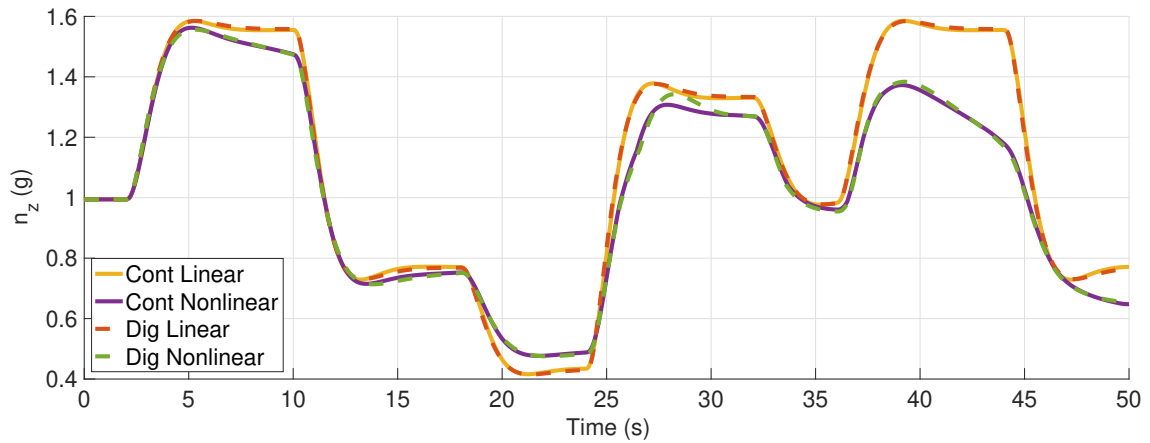
Figure 7.18: Load factor measured at the IMU time evolution for the four simulations, given the C^* step inputs.
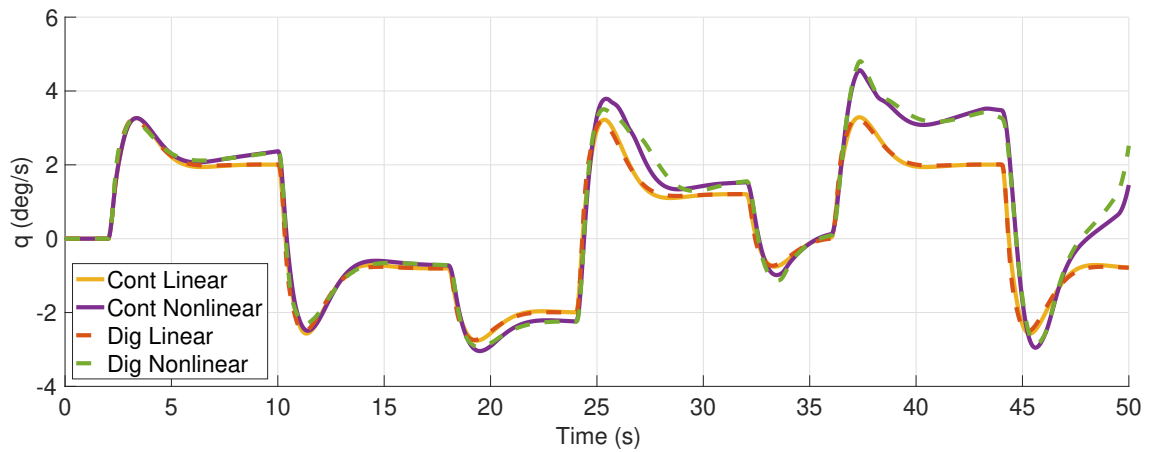
Figure 7.19: Pitch rate time evolution for the four simulations, given the C^* step inputs.
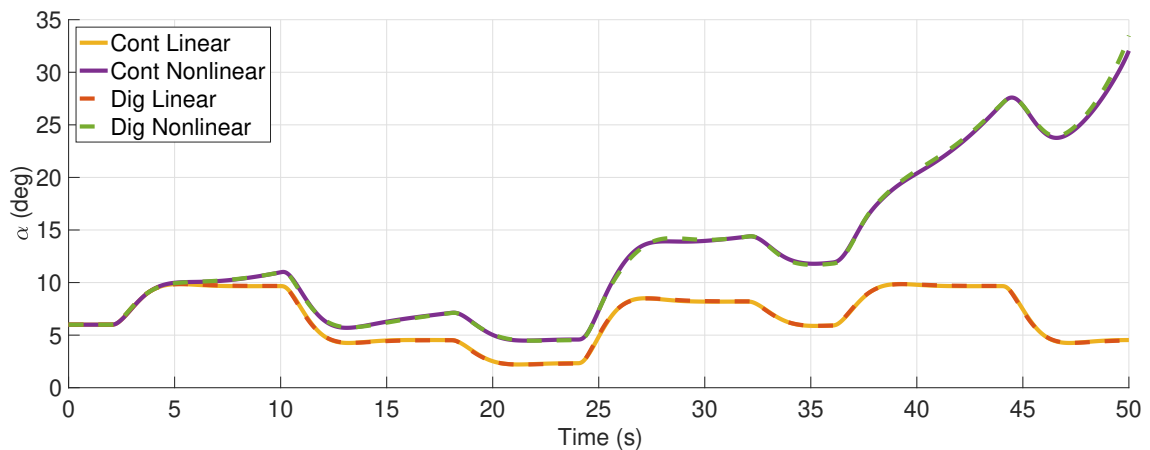
Figure 7.20: Angle of attack time evolution for the four simulations, given the C^* step inputs.

DISTURBANCE REJECTION & NOISE ATTENUATION - LINEAR & NONLINEAR SIMULATIONS
Given that the reference following has already been tested, it is also fundamental to analyze how well the input and output disturbances are rejected, as well as how satisfactorily the noise is rejected. Therefore, the values used for each of these signals are going to be detailed.

Firstly, regarding the output disturbance, which is modeled as an angle of attack gust is introduced as $1-\cos\alpha$, with a period of six seconds. The amplitude of the signal was chosen based on the previous simulation runs. In the linear domain, where the aircraft remains within the flight envelope, the maximum deviation of α from the trimmed condition was approximately $4°$. Thus, the value chosen should not be considerably higher than this one. In order to verify the extent to which the d_o attenuation is satisfactory, two gust were introduced in two different periods. The first is in $t \in [12, 18]s$ and the second in $t \in [30, 36]s$, where the amplitudes of the signals are, respectively, $3°$ and $7°$.

Secondly, the input disturbance is introduced as a step input, with an amplitude of $+2°$ at $t = 6s$ and of $-3°$ at $t = 22s$. The inputs chosen were provided based on previous simulations for the reference tracking, where the deviation from the trimmed position for δ_e was not higher than $3°$.

Lastly, the noise was implemented as white noise with a high pass filter, whose values were retrieved from Grondman et al. [2018]. Thus, the variance for the angular rates were defined as $\sigma^2 = 4 \cdot 10^{-7}$ and for the specific force measurements, considered to be the same as for the load factor, were defined as $\sigma^2 = 1.5 \cdot 10^{-5}$. In terms of the bias, which corresponds to the mean of the noise signal, these are defined as $3 \cdot 10^{-5}$ for p, q, r and as $2.5 \cdot 10^{-3}$ for n_x, n_y, n_z. In order to verify the contribution of noise independently, this signal was only introduced at $t = 40s$.

To begin with, Figure 7.21 shows the α parameter evolution when perturbed with the input disturbances but most importantly, when affected by the α gusts. This parameter is clearly significantly affected. Thus, this consequence on the remaining signals will be analyzed.

Moreover, the C^* parameter evolution measured at the IMU and PS for the four simulations are shown in Figure 7.22 and Figure 7.23, respectively. It can be concluded that the disturbances and noise are well attenuated. In fact, although the disturbances clearly affect the signals, these rapidly return to the trimmed value, given the null command for the reference.

Furthermore, it is noticed that, for the CT controller simulations, the input disturbances are attenuated faster and the overshoots are reduced. This is due to the higher attenuation of the CL TF S_oG for the CT design. In fact, as stated in Table 6.2 and Table 6.5, the difference in the weighting filters lies on an 5.7 dB of attenuation difference at 10^{-2}rad/s. Moreover, it is also observed that the output disturbances affect more the digital simulations than the CT ones when considering the IMU signal that is used for feedback. This is also due to the more relaxed filter of S_o for the modified CT design.
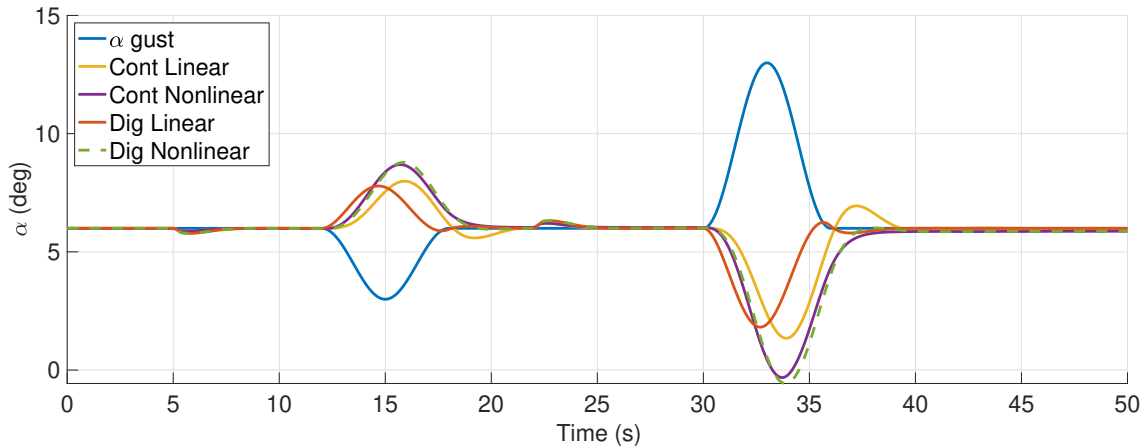
Figure 7.21: Angle of attack time evolution for the four simulations, with disturbances and noise introduced.
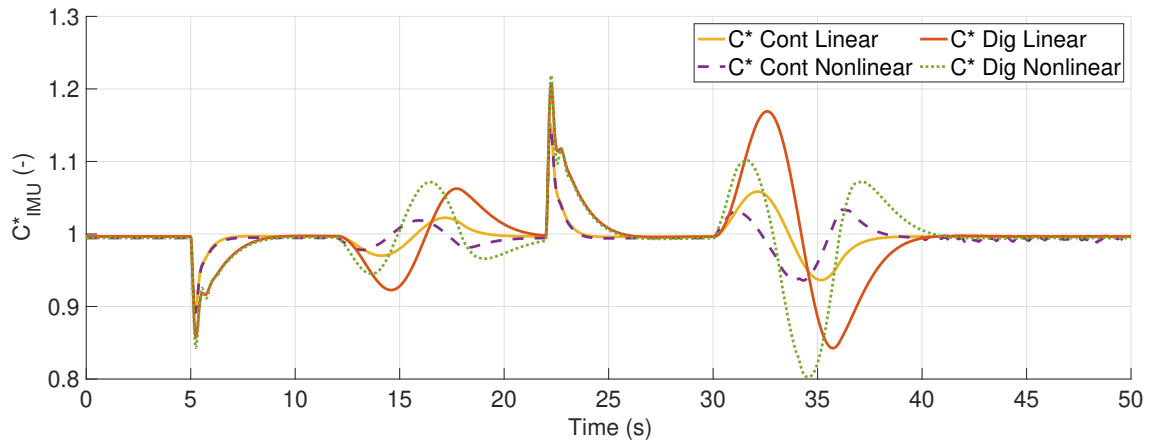
Figure 7.22: C^*_{IMU} parameter time evolution for the 4 simulations, with disturbances and noise introduced.
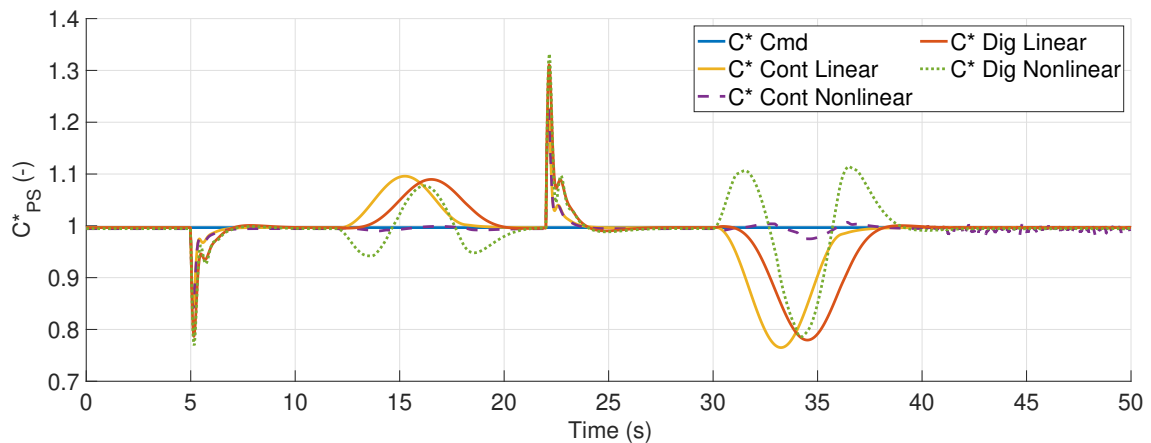
Figure 7.23: C^*_{PS} parameter time evolution for the 4 simulations, with disturbances and noise introduced.

Furthermore, given that the signal measured in the IMU is used for feedback, the peak values corresponding to d_i for this signal are significantly lower than the ones for the PS. This difference is also noticeable in the n_z time responses where, in the IMU (see Figure 7.24), the input disturbance has a very low impact when compared to the one measured at the PS (see Figure 7.25). Nevertheless, although this peak is higher, a common trend witnessed by observing Figure 7.22 and Figure 7.23 is that, in the PS, the error between the signal and the command input is reduced as much as possible. Thus, this yields a faster attenuation of the input disturbances and lower deviation magnitudes that arise due to the output disturbances. This phenomenon makes sense given that the PS signal is the one used for the reference tracking. Additionally, the time evolution of the pitch rate is also shown in Figure 7.26. Given that this signal is not being directly treated in the design, its behavior is mostly dependent on the outcomes of the C^* parameter. One thing that can be pointed out on this matter is that the sign of the magnitude of the n_z and q are opposed. Hence, the magnitude of the C^* parameter also decreases.

Additionally, it is also important to mention that the PS signals are more prone to noise than the ones in the IMU. This is clearly witnessed in Figure 7.24 and Figure 7.25. This is due to the fact that the PS parameters are dependent on the $\dot{q}$ parameter, which is a sensor property and, thus, more susceptible to the HF noise signal.
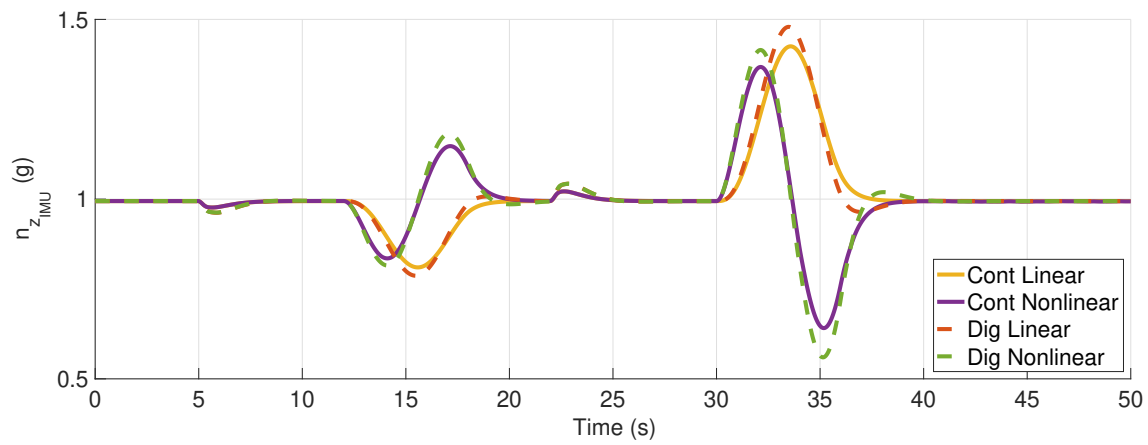
Figure 7.24: $n_{z_{IMU}}$ time evolution for the 4 simulations, with disturbances and noise introduced.
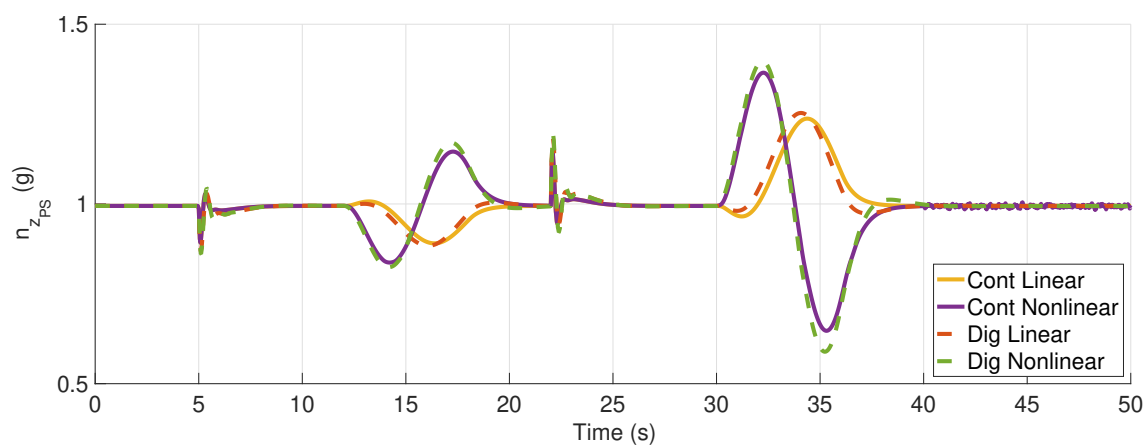
Figure 7.25: $n_{z_{IMU}}$ time evolution for the 4 simulations, with disturbances and noise introduced.
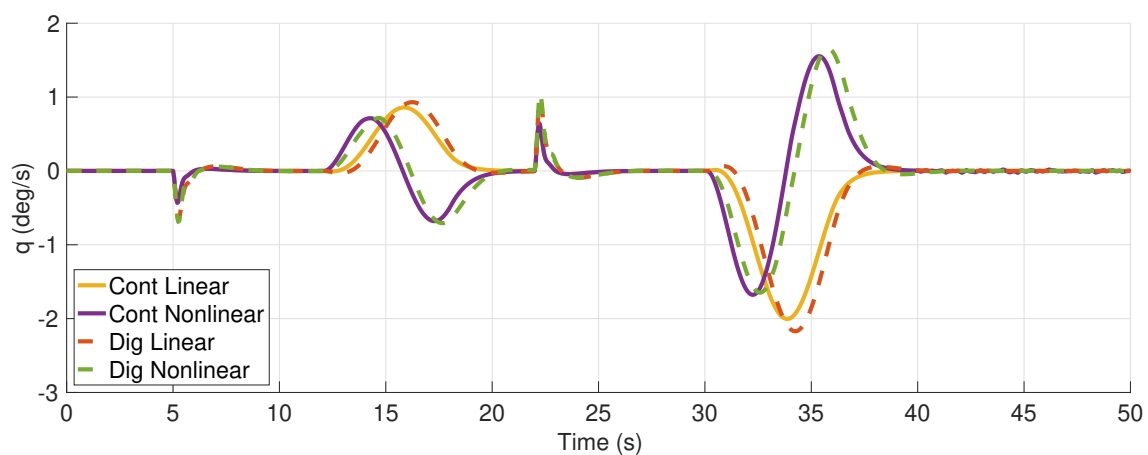
Figure 7.26: q time evolution for the 4 simulations, with disturbances and noise introduced.
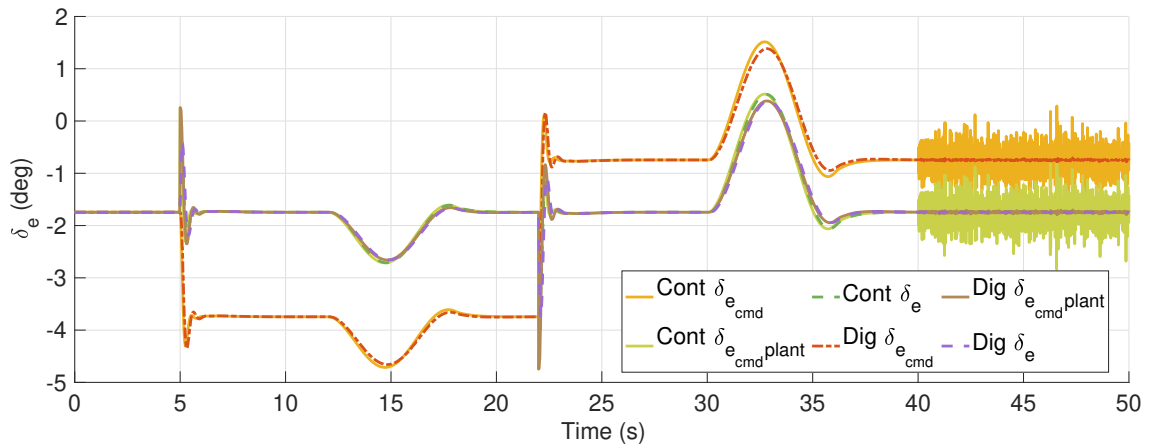
Figure 7.27: Control surface deflections for the linear simulations with the CT and digital controllers, with disturbances and noise introduced.
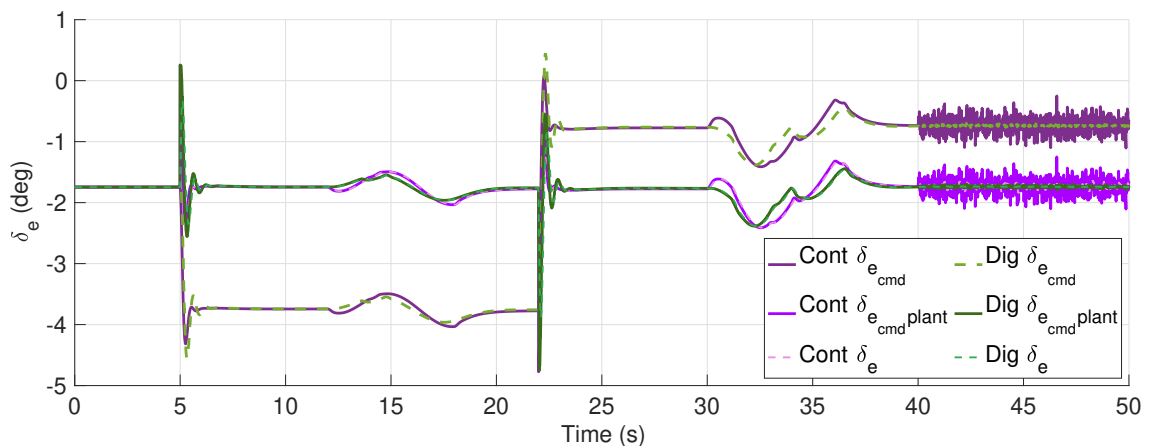
Figure 7.28: Control surface deflections for the nonlinear simulations with the CT and digital controllers, with disturbances and noise introduced.

Input disturbance rejection can also be observed in Figure 7.27 and Figure 7.28, where the control surface deflections over time are shown for the linear and nonlinear simulations, respectively. In fact, it is verified that the controller output is shifted in magnitude so that, when the disturbance is introduced, the commanded deflection that is given to the plant is the adequate value.

Another crucial aspect concerns the noise. As extensively discussed in Section 6.3.2, in the CT design, the noise is actually not attenuated. This occurrence is due to the lack of gain roll off in the feedback controller. This controller was kept with characteristic because it serves as a good analysis of the intricacies of the control design. In fact, this aspect is accounted for in the DT design, which is the final and most important controller. This point as addressed in the modified CT design not only because of the feedback controller roll-off at HF (given the integrator-like structure) but also because if the anti-aliasing low pass filter. Hence, all in all, it was concluded that in the CT design, low gain at HF for C_{FB} is needed whereas for the digital controller, such imposition is not necessary although recommended. For further context, consider Figure 6.23 and Figure 6.37. These phenomenons related to noise attenuation are observed in Figure 7.27 and Figure 7.28, where the noise in the controller output is only significant in the CT design.

It was consequently concluded that, even though noise could not be attenuated in the controller output, as verified in Figure 7.27 and Figure 7.28, measurement noise is attenuated in the plant output (refer to Figure 6.24b and Figure 6.38b). This is clearly observed in the the C^*, n_z. and q signals shown in Figure 7.22-7.26. Nonetheless, in order to further corroborate the statement, in the CT design, the signals y_{IMU} and y_{noise} (see Figure 6.15) were retrieved and plotted in Figure 7.29. These are the C^* parameter computed at the plant output and after the noise is introduced, respectively. It can be clearly concluded that the controller can almost reject completely the noise.
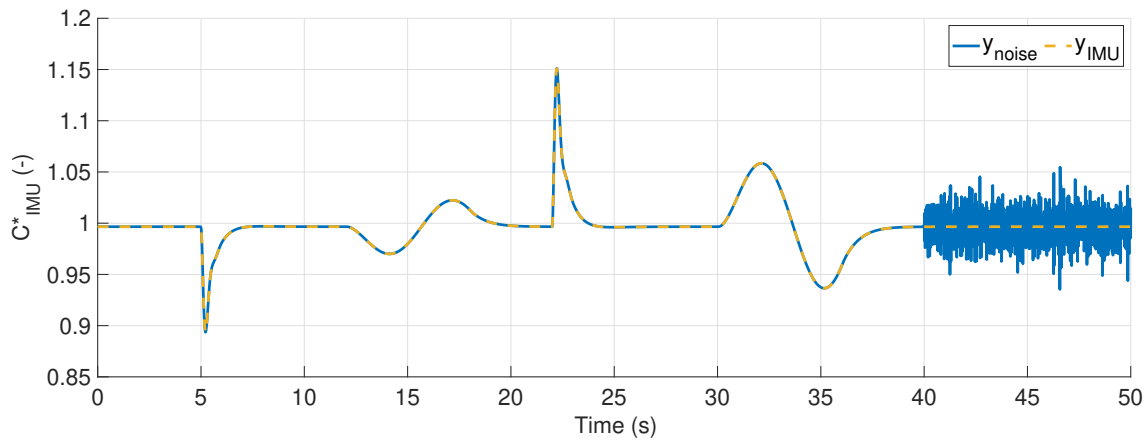
Figure 7.29: C^* parameter in the linear CT simulation retrieved at the plant output and after the noise introduction.

7.4.3. MULTI-MODELING DESIGN VALIDATION

A similar analysis to the one conducted for the CT and DT controllers in Section 7.4.2 could be performed for the multi-modeling design. This could be performed for the eight flight conditions where aerodynamic data is provided. However, given that the results would be very similar, it was decided to validate the design in a different format.

Hence, the idea is to verify that the controlled system behaves as desired over the entire flight envelope, when applied on the 6 DoF nonlinear model, which takes the discretization effects into account. It is important to highlight that the flight envelope is referred here to the region where valid data exists. Nonetheless, the flight envelope of the Flying-V will be extended. Moreover, to accomplish this validation, the system is tested over 82 runs. Figure 7.30 shows the Mach-altitude trajectories for each of these runs. The simulations start at conditions on the edge of the flight envelope, which are marked with red crosses.
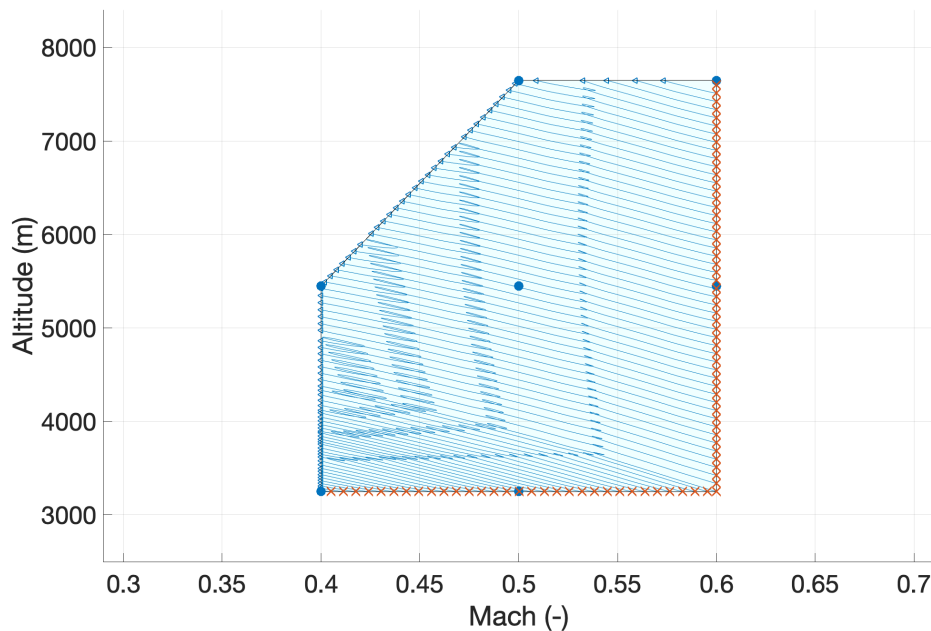
Figure 7.30: Flight envelope and the Mach-altitude trajectory of 82 simulation runs on the 6 DoF model. The red crosses indicate the beginning condition of the simulations and the blue arrows the trajectory followed over time.

Additionally, by commanding a repetitive reference signal, the flight envelope is spanned. In fact, the blue lines indicate the evolution of each flight condition and it can be seen that all of the region is covered. Moreover, a stopping command is activated when the trajectory leaves the intended region. The blue arrows indicate the end of each simulation run.

Hence, Figure 7.31 shows the C^* parameter in the PS evolution over time for the 82 runs, given a repetitive step input commands. It is clearly verified that for all of the flight conditions the behavior is very similar, which is desired given that a single reference model is used for the entire multi-modeling design points. However, it should be noted that the dynamics of each flight condition are quite different, as verified in Figure 5.6. All of the reference commands are satisfactorily followed. Additionally, Figure 7.32 shows a zoomed in portion of Figure 7.31, in order to be clear that all of the 82 runs are plotted.

Moreover, Figure 7.33, Figure 7.34, Figure 7.35, and Figure 7.36 show, respectively, the elevator deflections, the load factor measured at the IMU, the pitch rate, and the angle of attack time responses.
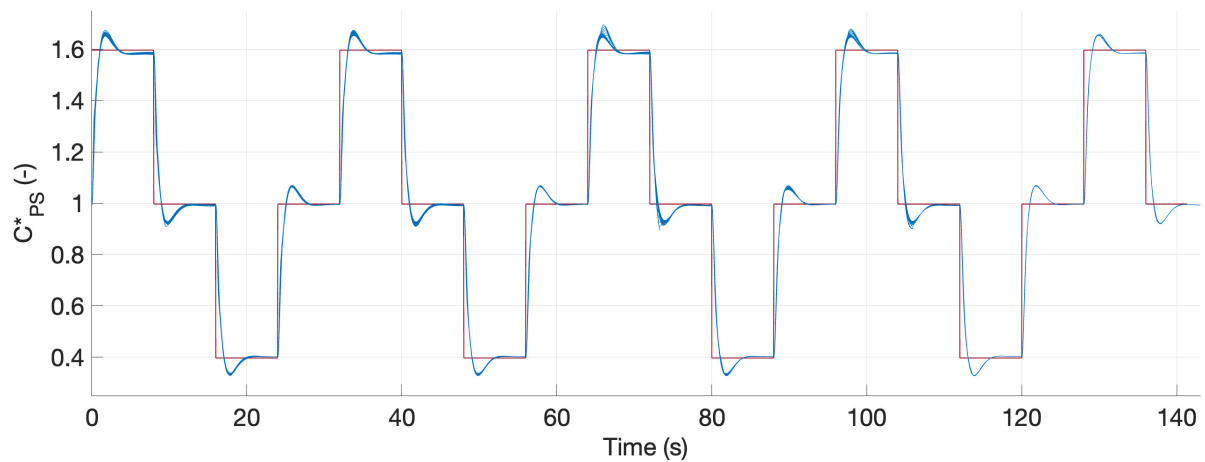
Figure 7.31: C^*_{PS} parameter response for the 82 simulation runs on the 6DoF, given a repetitive reference signal.
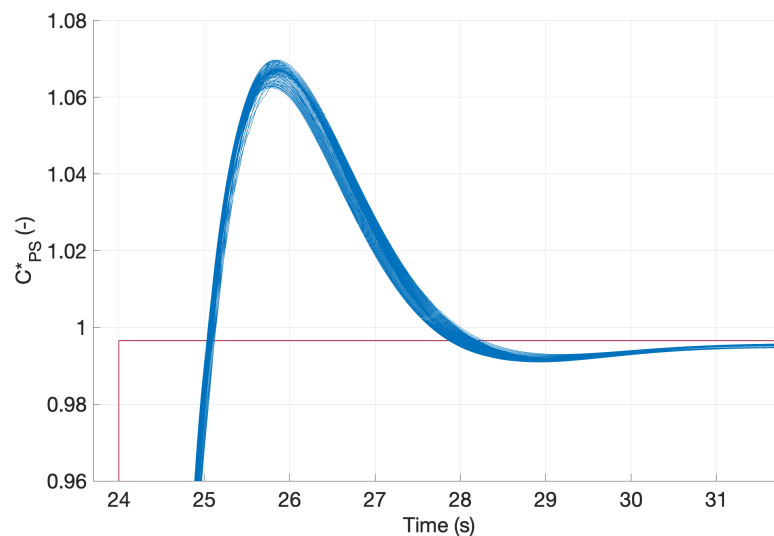
Figure 7.32: C^*_{PS} parameter response for the 82 simulation runs on the 6DoF, given a repetitive reference signal. Zoomed in portion of Figure 7.31.
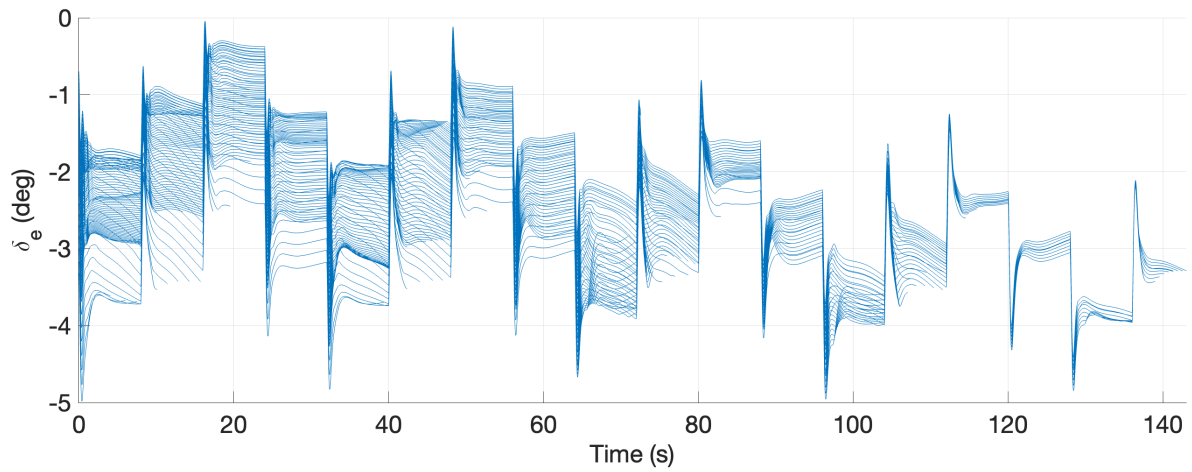
Figure 7.33: Elevator deflections for the 82 simulation runs on the 6DoF, given a repetitive reference signal.
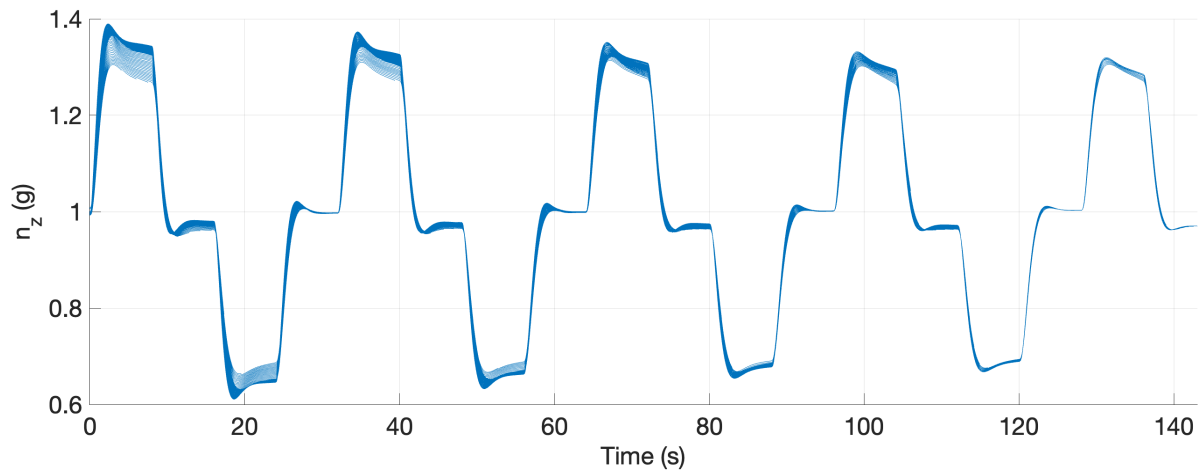
Figure 7.34: $n_{z_{IMU}}$ response for the 82 simulation runs on the 6DoF, given a repetitive reference signal.
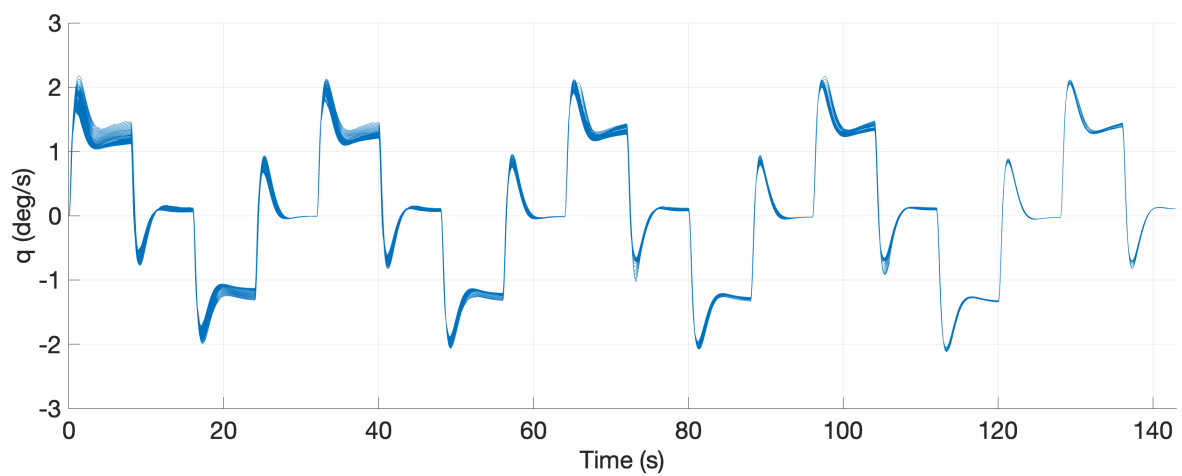
Figure 7.35: q response for the 82 simulation runs on the 6DoF, given a repetitive reference signal.
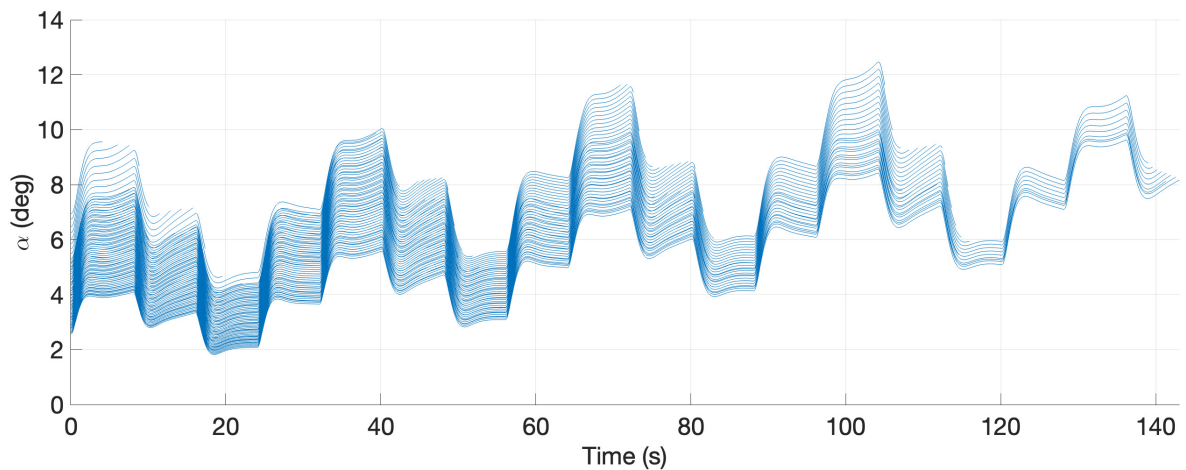
Figure 7.36: α response for the 82 simulation runs on the 6DoF, given a repetitive reference signal.

7.5. Uncertainty

The control system is robust if it is insensitive to mismatches between the actual aircraft and the model of the system that is used to design the system. Thus, it is important to check robust stability by verifying if the system remains stable for all plants in the uncertainty set. Additionally, it is also crucial to check robust performance, which determines whether the performance specifications are met for all these plants. Therefore, Section 7.5.1 focuses on describing the uncertainty formulation and how it is implemented, whereas Section 7.5.2 show the results obtained in terms of Go6, stability margins, and handling qualities.

7.5.1. Uncertainty Formulation & Implementation

In the current analysis, parametric uncertainty will be considered, which can arise due to several sources. Some are perfectly known and neglected on purpose for simplicity purposes. Others are undesired and the system should be robust against them. These include unknown variations in the mass, inertia, and aerodynamic stability and control coefficients. [Pollack, 2024] [Skogestad and Postlethwaite, 2005]

Moreover, although all of these parameters should be considered for the most accurate analysis, the uncertainty is just going to be tested in the aerodynamic coefficients. For the Flying-V, Stougie et al. [2024] implemented uncertainties on these parameters below 20%, Völker et al. [2023] introduced 25% aerodynamic variation. Lastly, Shahin [2024] introduced 75% in C_{m_α} and 25% in C_{m_q} and $C_{m_{\delta_e}}$. The uncertainty bounds have not yet been established for the Flying-V. However, these values were taken into consideration as well as the requirements listed in MIL-HDBK-516C [Anonymous, 2014], where it is stated that stability derivatives must be varied by 25% in the most adverse direction. Anonymous [2008] also states that 20% uncertainty should be applied in key stability derivatives and that the required SM shall not degrade by more than 50% in the presence of that uncertainty, at nominal flight conditions and at frequencies below the structural modes. Hence, it was decided to introduce up to 30% uncertainty in the stability and control derivatives that affect the SP SS the most, which consist of C_{z_α}, C_{m_α}, C_{m_q}, and $C_{m_{\delta_e}}$.

Furthermore, it was decided to only show the results of the uncertainty for the modified CT design (digital) for brevity reasons and given that this controller is the most representative. Moreover, the multi-modeling design already takes into account some aspects of the uncertainty, given that the controller is synthesized for variations in the Mach and altitude, which change the dynamics considerable. Hence, it is more relevant to test the robustness of a controller which was only designed for a single flight condition.

MATLAB & Simulink Uncertainty Implementation

Moreover, in terms of implementation, the uncertainty was integrated into the nonlinear 6 DoF model. This integration allows for the direct derivation of a CT state-space model of the system in question, already accounting for the uncertain elements. While the nominal values of the system's parameters remain unchanged, this approach enables the generation of as many uncertain state-space systems as desired, with varying parameters. A major advantage of implementing this approach within the nonlinear framework is that these systems can be retrieved directly and automatically, with parameters clearly defined from the outset.

To achieve that, in the path of the aerodynamic coefficients in Simulink®, an uncertain state space (uss) block in added. The prompt in this block consists of the uncertain system variable which is produced with the MATLAB® function `ureal()`. This function takes the mean value and the uncertainty range ($\pm 30\%$) as inputs.

7.5.2. UNCERTAINTY SIMULATION RESULTS

Thus, the robustness analysis with uncertainty will be conducted, namely by considering the Go6 and model matching CL constraints, the open loops, the stability margins, and handling qualities. Moreover, as previously stated, the uncertainties considered are taken from the range $[-30, 30]\%$. For each coefficient, 5 samples are taken and all of the combinations are tested, yielding in $5^4 = 625$ combinations.

GO6 CLOSED LOOP TFs

To begin the analysis, the Go6 closed loop transfer functions are shown for all the uncertain systems as well as for the nominal case in Figure 7.37. It is observed that for the sensitivity functions there is a significant increase in the dispersion of the results (see Figure 7.37a-7.37b). However, the desired behaviour at LF and HF is verified in all of the functions, although the filters are violated for some conditions. Thus, the results are satisfactory.

MODEL MATCHING

Besides the Go6, the model matching constraint should also be analyzed, as the reference tracking is one of the key specification requirements for the design. This is shown in Figure 7.38a, while the corresponding time step response is shown in Figure 7.38b. At LF, small gain is still observed. Nonetheless, the decrease observed in teh bandwidth frequency translates into performance degradation. However, as it is verified in Figure 7.38b, the reference tracking is still satisfactory, with negligible steady state error. In order to further analyze this model matching constraint, the HQ should be tested.

HANDLING QUALITIES

Hence, Figure 7.39a, Figure 7.39b, and Figure 7.11 depict the results for the attitude bandwidth, flight path bandwidth, and pitch rate overshoot and pitch attitude dropback HQ criteria results, respectively. It is observed that even in the face of uncertainty, the system is mostly within Level 1 HQ. For the pitch attitude bandwidth and the pitch rate overshoot and pitch attitude dropback criteria, all of the results are contained in the desired level. For the flight path criteria, there are some outliers that go into Level 2. However, these results are acceptable for the uncertainty applied and since the C* parameter is the primary means of controlling γ [Anonymous, 2014] Mitchell et al. [1994].

OPEN LOOPS & STABILITY MARGINS

Finally, the open loops and stability margins are analyzed by breaking the loops in the same locations as before, namely at the plant input (see Figure 7.40), at the virtual plant output (see Figure 7.41), at the output n_z measured at the IMU location (see Figure 7.42), at the output n_z measured at the CoG (see Figure 7.43), and at the output q (see Figure 7.44). For each of these open loop locations, the frequency response of the open loops are shown as well as the Nichols charts for the all the uncertain systems as well as for the nominal one. Additionally, the worst case scenario is highlighted and the respective worst case disk gain and phase margins are highlighted by the exclusion region in these charts.

Furthermore, the worst case classical and balanced disk margins are summarized in Table 7.6. As expected all of these margins are reduced when compared to the nominal case, whose values are presented in Table 7.2. Nonetheless, Anonymous [2008] states that stability margins can degrade up to 50% the required nominal values if faced by $\pm 20°$ uncertainty. Although reducing the stability requirements half (i.e. to GM of 3 dB and phase margins of 22.5 °) is conservative given that the uncertainty applied is greater than the $\pm 20°$, these references are still used. However, it is verified that the worst case value obtained for the classical margins is 11.10 dB, whereas for the phase margins is 35.63 °. Both values correspond to the loop open at the pitch rate signal and are significantly above these conservative requirements. Thus, it is concluded that the system is robust to uncertainties in the aerodynamic coefficients, given its low sensitivity to the change in the parameters.
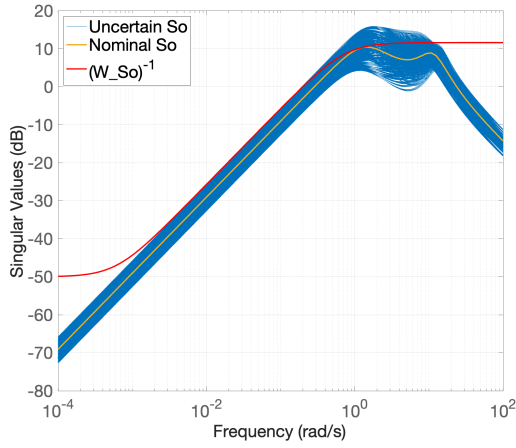
(a) Sensitivity S_o for the uncertain and nominal models, and its filter inverse, W_{So}^{-1}.
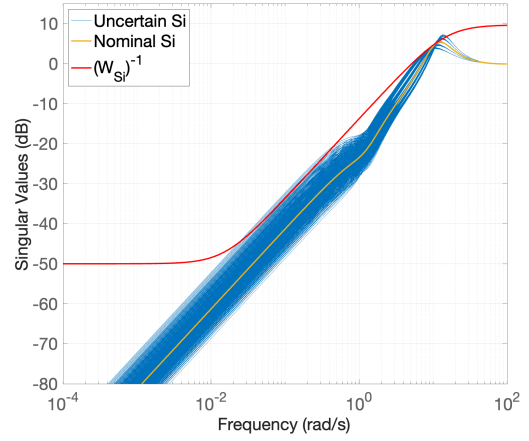
(b) Sensitivity S_i for the uncertain and nominal models, and its filter inverse, W_{Si}^{-1}.
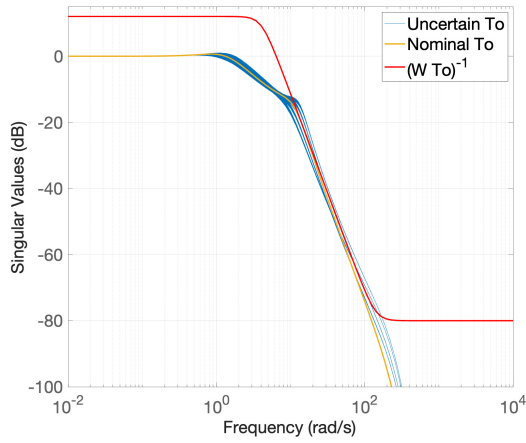
(c) Complementary sensitivity T_o for the uncertain and nominal models, and its filter inverse, W_{To}^{-1}.
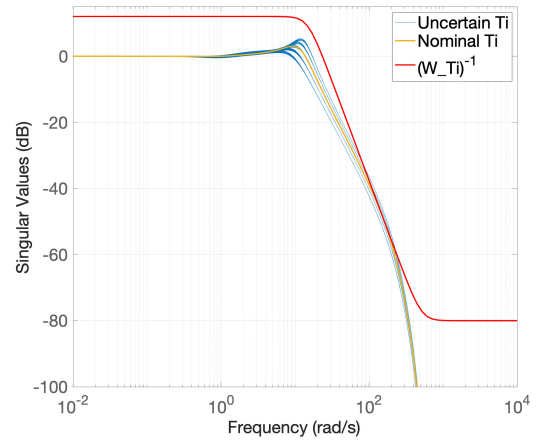
(d) Complementary sensitivity T_i for the uncertain and nominal models, and its filter inverse, W_{Ti}^{-1}.
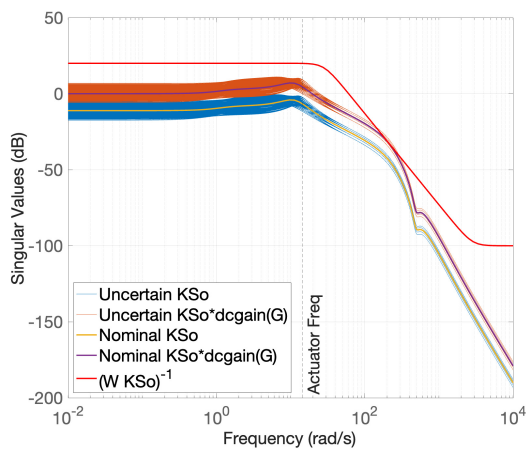
(e) Control sensitivity KS_o, KS_o scaled with $\underline{\sigma}(G)$ at LF, and its filter inverse, W_{KSo}^{-1}, for the uncertain and nominal models.
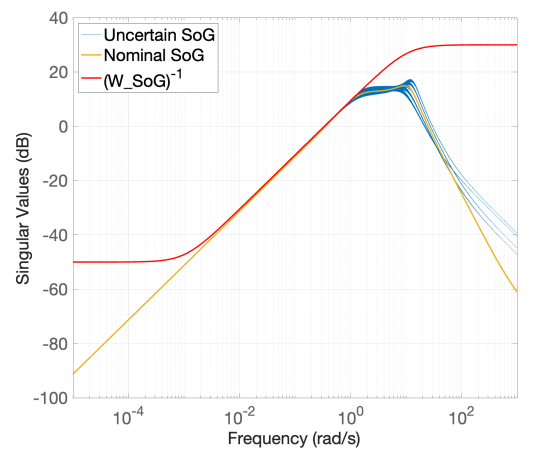
(f) S_oG for the uncertain and nominal models, and its filter inverse.
.

Figure 7.37: Singular Values of the Go6 closed loop TFs, namely of S_o (7.37a), S_i (7.37b), T_o (7.37c), T_i (7.37d), KS_o (7.37e), and S_oG (7.37f), with the associated weighting filters' inverse for the uncertain and nominal models. These concern the modified CT structured controller.
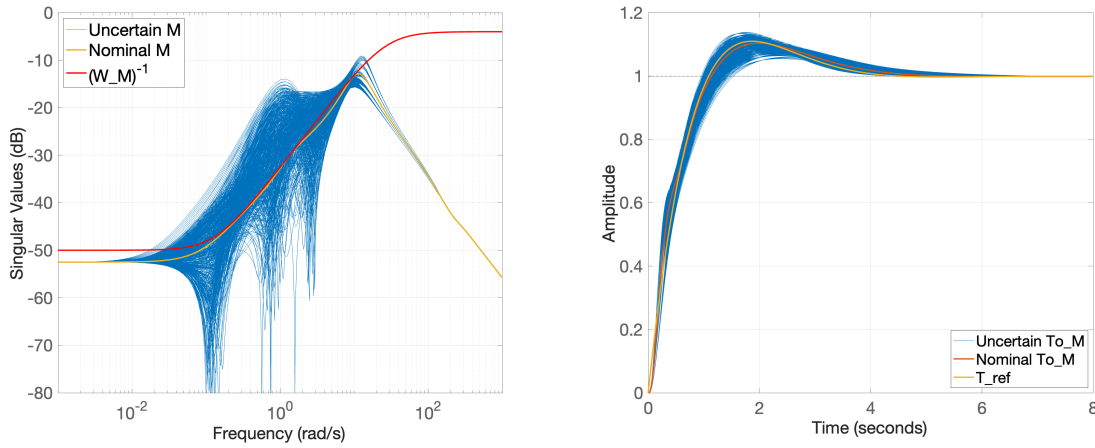
(a) Model matching M for the uncertain and nominal models, and its filter inverse.

(b) Step response of the T_{ref} and of the CL TF T_oM for the uncertain and nominal models.

Figure 7.38: Performance of the reference tracking, in terms of model matching frequency 7.38a and time 7.38b responses for the uncertain and nominal models, with the modified CT structured controller.
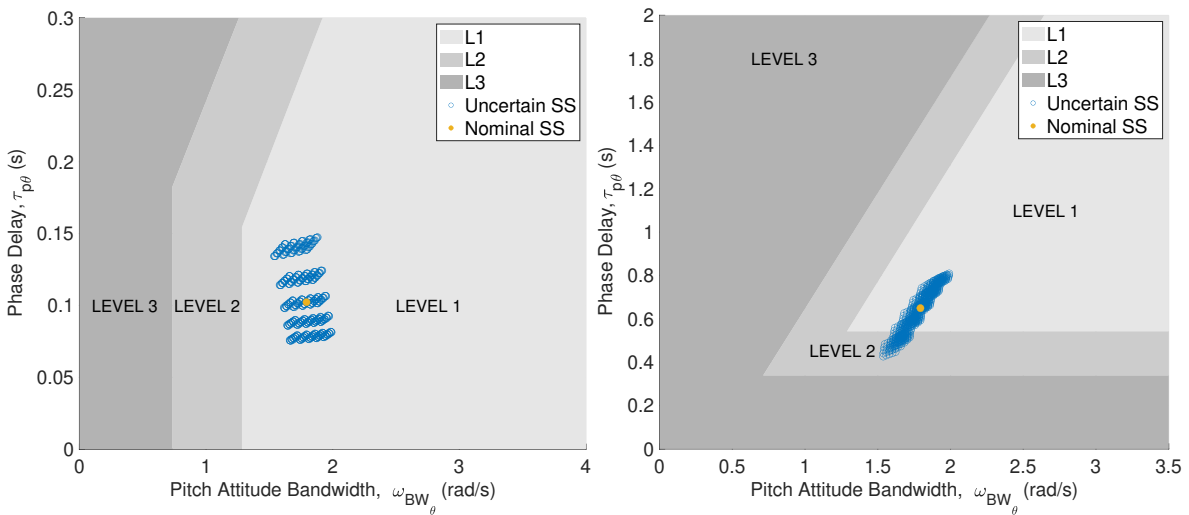
(a) Attitude bandwidth HQ criterion.

(b) Flight path bandwidth HQ criterion.
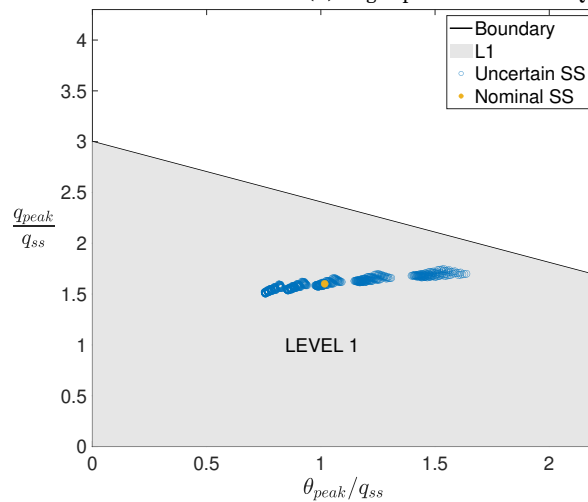
(c) Pitch rate overshoot & pitch attitude dropback HQ criterion.

Figure 7.39: HQ criteria for the uncertain and nominal models, with the modified CT structured controller.
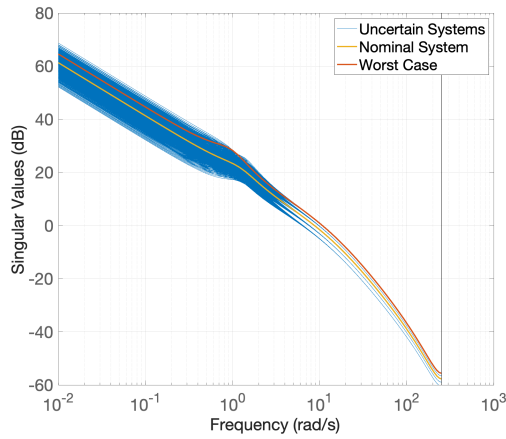
(a) Open loop frequency response.
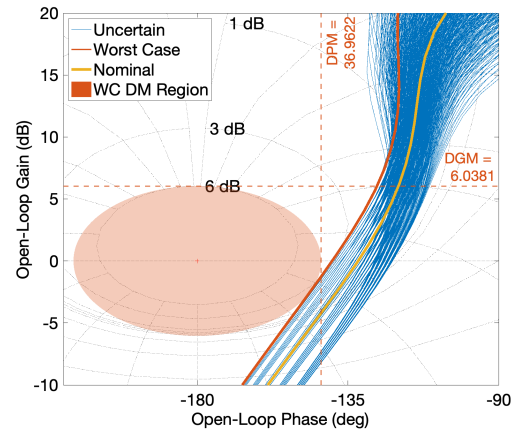
(b) Nichols chart and worst case disk gain and phase region.

Figure 7.40: Open loops (7.40a) frequency response and Nichols chart (7.40b) for the uncertain and nominal models, at the loops open at the plant input. These concern the modified CT structured controller.
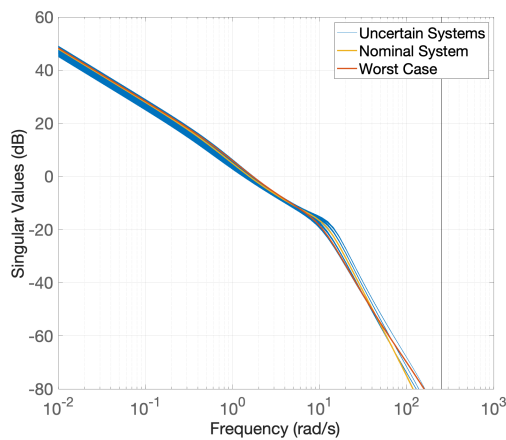
(a) Open loop frequency response.
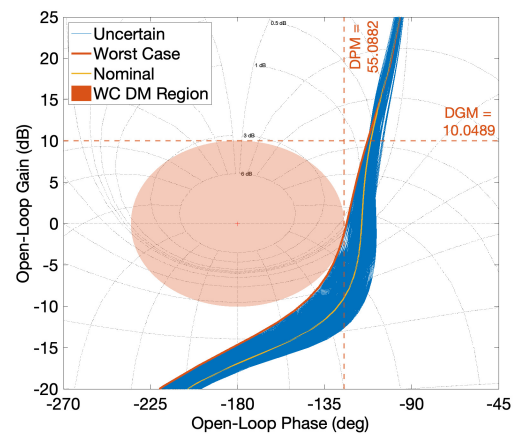
(b) Nichols chart and worst case disk gain and phase region.

Figure 7.41: Open loops (7.41a) frequency response and Nichols chart (7.41b) for the uncertain and nominal models, at the loops open at the virtual plant output, C^*. These concern the modified CT structured controller.
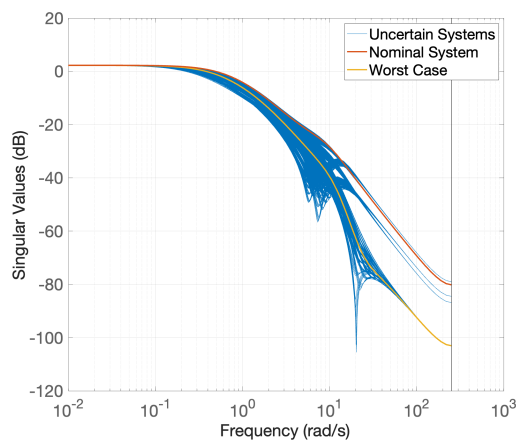
(a) Open loop frequency response.
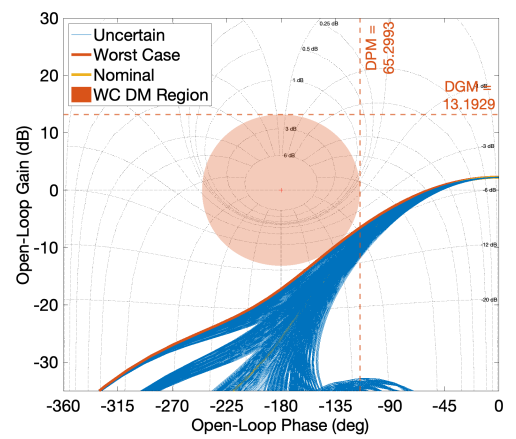
(b) Nichols chart and worst case disk gain and phase region.

Figure 7.42: Open loops (7.42a) frequency response and Nichols chart (7.42b) for the uncertain and nominal models, at the loops open at the plant output, $n_{z_{IMU}}$. These concern the modified CT structured controller.
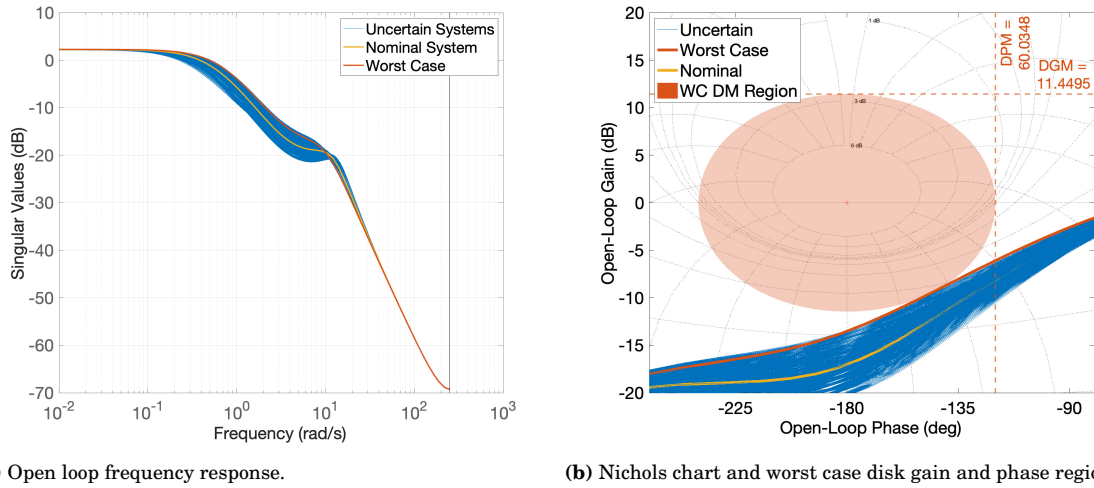
(a) Open loop frequency response.

(b) Nichols chart and worst case disk gain and phase region.

Figure 7.43: Open loops (7.43a) frequency response and Nichols chart (7.43b) for the uncertain and nominal models, at the loops open at the plant output, $n_{z_{CoG}}$. These concern the modified CT structured controller.
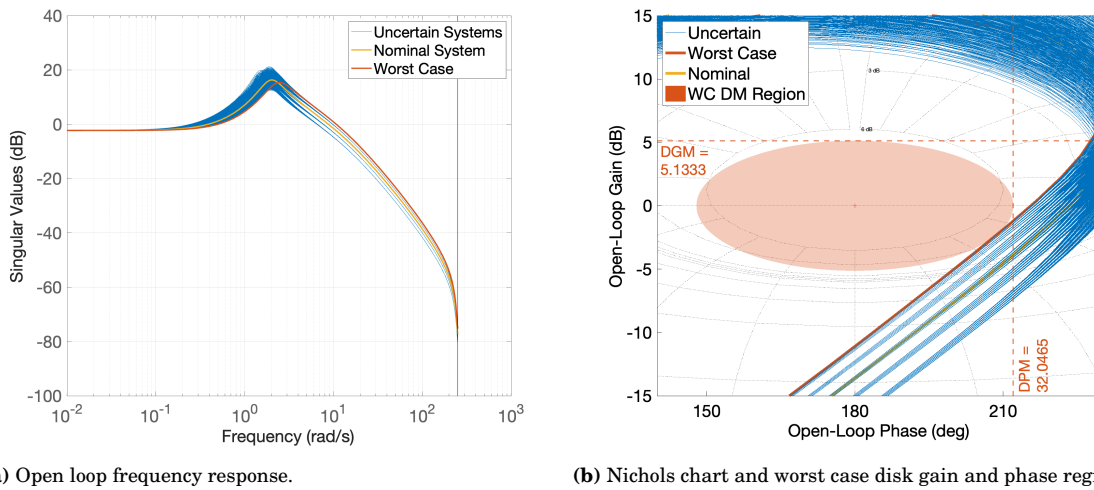
(a) Open loop frequency response.

(b) Nichols chart and worst case disk gain and phase region.

Figure 7.44: Open loops (7.44a) frequency response and Nichols chart (7.44b) for the uncertain and nominal models, at the loops open at the plant output, q. These concern the modified CT structured controller.

Table 7.6: Worst case disk and classical loop-at-a-time gain and phase margins of the uncertain models. These concern the modified CT structured controller.

Broken Loop	WC Disk Margins		WC Classical Margins	
	DGM (dB)	DPM (°)	GM (dB)	PM (°)
Plant Input	± 6.04	± 36.96	15.11	40.26
Virtual plant output (C*)	± 10.05	± 55.09	14.66	56.36
Plant output (nz @ IMU)	± 13.19	± 65.30	17.25	122.10
Plant output (nz @ CoG)	± 11.45	± 60.03	13.53	118.98
Plant output (q)	± 5.13	± 32.05	11.10	35.63

8

CONCLUSIONS

This research was conducted in the context of the Flying-V project, which, within the control and stability domain, aims for compliance with Level 1 HQ for certification. In this study, the Flying-V simulation model was successfully implemented, which served as the foundation for the subsequent controller designs. These designs entail a continuous controller and a modified continuous controller for a nominal flight condition, and a multi-modeling modified continuous controller design which is valid for the defined flight envelope. These were developed under the $\mathcal{H}_\infty$ optimization scheme with robust control methods, taking into consideration performance and robustness specifications in the synthesis phase. The controllers were examined in terms of stability margins, handling qualities, linear and nonlinear time domain simulations, and under the influence of parametric uncertainty. In Section 8.1, the research questions are revisited and answered based on the results shown in the previous chapters. Finally, Section 8.2 addresses the research objective and reflects on the extent to which the objective has been met.

8.1. REVISITING THE RESEARCH QUESTIONS

1. **How can the challenges and limitations of Flying-V's current nonlinear model be addressed, thereby facilitating the development of a robust and effective FCS design?**

   - **What are the main challenges of the previous modeling approach, and how can these limitations be improved?**

     The model originally provided in MATLAB® and Simulink® has several shortcomings, which could compromise the validity of results. This was highlighted by Traas [2024], who identified and rectified errors in the model. Additionally, in the initial phase of the current research, the trimming and linearization methods did not function well. Although this is less critical for the nonlinear methods applied so far, linearized systems are crucial for robust controller synthesis, necessitating immediate attention. The model's lack of organization complicates tracing the root of the problems encountered. Consequently, to achieve a valid and well-structured FCS synthesis, especially within a robust control framework, redesigning the model became imperative.

     To address these limitations, the Flying-V model was developed in MATLAB® and Simulink® using a tensor-based formulation, as detailed in Chapter 5. The model is subdivided into three main systems (see Figure 8.1) and subsequent subsystems. All values and variables used in the system are defined in a MATLAB® script and are introduced in Simulink® primarily through masked systems, ensuring an organized and systematic implementation.

Figure 8.1: Overview of the Flying-V model implemented in Simulink®.

- **How does the trimming and linearization of the Flying-V model facilitate the development of robust control systems, and what are the key considerations in this process?**

  Trimming and linearization procedures are pivotal in robust controller design as these transform complex nonlinear systems into linear models around steady-state operating points. For each operating point, the linearized system must accurately capture the key system dynamics to ensure that controllers perform as intended within a range around the specified flight condition when applied in the nonlinear framework.

  A key consideration in the trimming procedure involves the definition of the variables that must be adjusted by the algorithm. It was concluded that the system inputs, θ, α, and β must be adjusted by the coding script. The remaining variables are either known and, therefore, their values can be fixed, or they are interrelated with other states. Another category entails the states that can be specified freely. The reasoning behind these considerations is explained in Section 5.2. Moreover, in the linearization, it is important to define the states that excite the most important eigenmotions, which depend on the design. For the current research the SP mode is chosen and, thus the states α and q are selected.

- **What main aspects should be considered to ensure a successful implementation when translating the nonlinear model insights into a linear system?**

  To begin with, the model intricacies as well as the functions used must be dealt with precaution and must be well understood. On the one hand, once the trimming procedure is complete, a key aspect involves conducting time domain simulations in the 6 DoF model. When the states and inputs are initialized with the trimmed values, these must remain in steady state, except for the position on the x-axis. The physical properties of the trimmed values should be carefully examined over the flight envelope, as conducted in Section 5.2.2. For instance, analyzing the effect of variations in air dynamic pressure, wind, and altitude. On the other hand, it is crucial to verify the system's validity after the linearization procedure is conducted. This entails evaluating the parameters in the state space representation, in terms of magnitudes, signs, and conventions.

2. **How can the maturity of the Flying-V FCS be enhanced through the implementation of a $\mathcal{H}_\infty$ signal-based Mixed Sensitivity C^* controller?**

   - **What are the critical design alternatives for the longitudinal FCS, and how do these affect the systems' robustness and performance?**

     Three design alternatives were considered and discussed in Section 6.1, regarding the feedback signals, the measurement location of the C^* signals, and the output disturbance modeling.

     Firstly, it was concluded that using the combined demand approach for the feedback signal, by using the C^* parameter, is the preferred approach. It allows good disturbance rejection in this signal and a balanced rejection at LF in the signals q and n_z. Moreover, none of the basic maneuver demand systems which include feedbacking n_z and q have all the favorable qualities on their own, building an even stronger case for the combined commanded signal.

     Secondly, for reference tracking purposes the C^* signal is measured in the PS, given the intimate relation to the pilot cues. However, it was decided to measure the feedback signal at the IMU location, which was assumed to be near the ICR. The main reason is that open loop roll-off is desired at HF, which is achieved by not having a large derivative term in the n_z measurements that arise due to $\dot{q}$.

     Lastly, the output disturbance was introduced in the system by being added directly to the output signal and by modeling it as an α gust and introducing it as part of the SS system. The disturbance rejection is extremely improved on the C^* channel with the second approach. Although it takes more time to stabilize, the response is smoother and, in terms of magnitude, its response deviation is reduced by approximately 41%, in comparison with the first approach. Thus, it was decided to model the disturbance and consider it in the design phase.

- **How are the design requirements translated into the constraints imposed on the system?**

  The first design requirement entails disturbance rejection at the plant input and outputs. This specification is important at LF and it is achieved by shaping the closed-loop TF from d_o to y_{IMU} (S_o), from d_i to u_p (S_i), and from d_i to y_{IMU} (S_oG). Thus, all of these TF are constrained with low gain at LF. Secondly, sensor noise attenuation at the plant input and outputs is an HF problem and it is met by constraining the TF from r_{inner} to y_{IMU} (T_o) and from d_o to $u_{c,weighted}$ (KS_o) at HF with low gain. Moreover, control effort reduction is not dependent on the designer at LF. To achieve this specification in this frequency range, sufficient plant (control) authority is needed. The classical margin requirements are imposed by limiting the peak of the sensitivity function from d_o to y_{IMU} at medium frequencies. Moreover, unstructured input and output multiplicative uncertainty is addressed by T_i and T_o. Thus, limiting the gain of the TFs from d_i to u_c and from r_{inner} to C^*_{IMU} allows robustness guarantees against the independent parametric uncertainties introduced in the aerodynamic coefficients. Lastly, HQ compliance is achieved by defining a model matching constraint, M, defined from r to e_{ref}, which imposes the system to follow the defined reference model, T_{ref}. The constraints are imposed via weighting filters, whose inverses are defined as the desired frequency responses of the previously mentioned CL TFs, as represented in Figure 8.2.
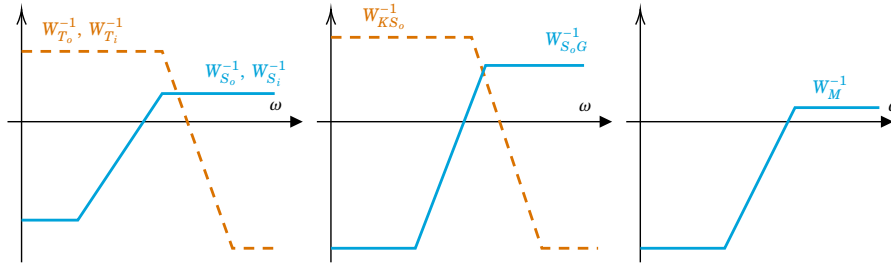
Figure 8.2: Singular Value shape for the desired CL TFs.

- **To what extent does the structure of the feedback controller influence the robustness of the system and how can it be determined?**

  At LF, the main specification is in terms of disturbance rejection. Imposing small gain on the sensitivity functions S_o and S_i in this frequency range, translates into high gain at LF in the open loops. This gain for the open loops is achieved by either having a high plant gain at LF, high controller gains, or both. However, if input disturbances are rejected at the plant output, then large control gains are a must since $\bar{\sigma}(S_oG) \approx 1/\underline{\sigma}(K)$.

  At HF, both noise and control signal attenuation are important, which are mainly affected by T_i, T_o, and KS_o. The first two TFs impose roll-off at the open loops. Moreover, given that, in this frequency range, the sensitivity function S_o stabilizes at 0dB, then $\bar{\sigma}(KS_o) \approx \bar{\sigma}(K)$. Hence, controller gains need to be small. This aspect was extensively discussed in Section 6.3.2, where a controller without roll-off was implemented, which led to a degraded control signal and noise attenuation, as verified in Section 7.4.2. Although this controller served as a good analysis of control design intricacies, a digital design was synthesized in Section 6.4.3, where roll-off was implemented in the feedback controller. Both this aspect and the anti-aliasing filter contribute to the desired disturbance and noise attenuation. The open loop considerations in terms of the design requirements are summarized in Figure 8.3.

  Moreover, the higher the order of the controller is, the higher the flexibility of the controller to respond to certain effects of the system over the frequency range. Thus, the robustness of the system may be amplified. However, the extra complexity associated with it usually does not balance the advantages that arise out of it. As performed in Section 6.3.1 and in Section 6.4.2, unstructured controllers can be synthesized as preliminary results. The designs obtained can be reduced and the most adequate structure can be identified from here.
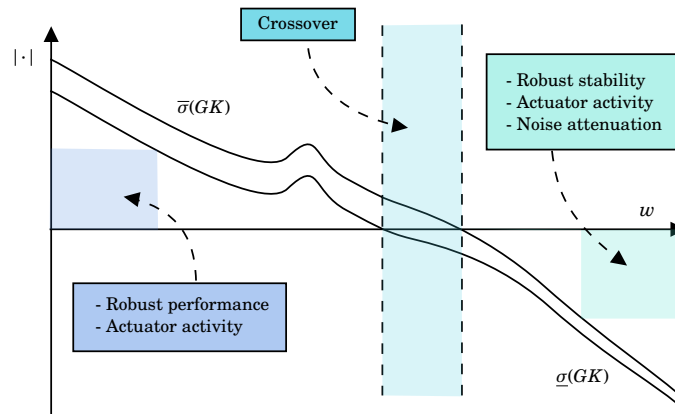
Figure 8.3: Design specifications of the open loop singular values. Based on [Pollack, 2024] and [Bates and Postlethwaite, 2002].

- **To what extent is the system influenced by the discretization effects of the flight computer and how can this potential challenge be addressed?**

    Control laws are implemented in a digital format in modern aircraft. Hence, the implementation involves D/A and A/D converters which, alongside the computations inherent to the FCS, take time. Thus, computation delays occur. One option to implement the digital controller in this flight computer formulation is to discretize the continuous controller synthesized. The stability margins were assessed both when the CT controller was implemented in a CT simulation and when the CT controller was discretized and consequently implemented in a DT simulation. From the analysis performed in Section 7.2.2, it was concluded that both classical and disk SM for the latter scenario were significantly reduced (see Table 7.1 and Table 7.4).

    For that reason, a modified CT controller was designed by including the discretization effects in the synthesis process. These consist of modeling an anti-alias filter as well as the ZOH and computational delay with Padé approximations to mimic the discrete behavior. Thus, the controller obtained is a clear improvement to the first option discussed since the stability margins are considerably less affected (see Figure 7.5).

3. **To what extent does the signal-based $\mathcal{H}_\infty$ Mixed Sensitivity C* controller meet the specified performance and robustness requirements across a range of flight conditions?**

    - **To what extent does the linear control system comply with the requirements imposed a priori?**

        The CT and DT controllers were extensively examined in Chapter 7 in terms of time domain simulations, stability margins, uncertainty, and handling qualities. To begin with and considering the requirements R1, R2, and R3, it was verified that the disturbances and noise are well attenuated in the input and virtual output, C* (see Section 7.4). It is observed that the input and output disturbances are attenuated faster and produce less overshoot for the CT design than for the DT one. Control effort attenuation was successfully achieved as the commanded elevator deflections remained moderate and within the specified limits. There is the exception for the CT controller, where there is no noise attenuation at the plant input (see Figure 7.16) given the lack of feedback controller roll-off at HF. However, such aspect is considered for the final design, the DT controller. Moreover, there is no disturbance rejection if disturbances are applied directly on the signals n_z and q, which is expected due to the open loops low gain at LF. Moreover, the SM are also satisfactory, since there is only a slight violation of the soft requirement in terms of PM for the loops opened at the plant input for the CT controller and at q for the DT controller (see Section 7.2). The predicted HQ for the two controllers are within Level 1 for the three criteria tested (see Section 7.3). Lastly, R5 specifies robustness guarantees in the presence of independent parametric uncertainties in the aerodynamic coefficients. These were varied across the range of ± 30 ° and it was verified that the stability margins were kept above the limits imposed by Anonymous [2008], the Go6 and the model matching constraints

also maintained the desired behavior, and that the HQ remained mostly within Level 1, with some conditions going into Level 2 (see Section 7.5).

- **How does the linear control system design behave in the nonlinear 6 DoF model?**
  The linear controller design is implemented in the 6 DoF nonlinear model and time domain simulations were conducted (see Section 7.4.2). It is verified that the reference tracking is satisfactory as well as the disturbance and noise attenuation, having similar results to the ones obtained in the linear simulations. However, due to the commanded signals, the flight condition achieved was out of the range of the valid data and, thus, unexpected behavior is noticeable.

- **How can the robustness and performance specifications be guaranteed across the flight envelope and to what extent are these met with the proposed design?**
  A multi-modeling approach was followed to ensure that the specifications defined a priori were met for all of the conditions within the flight envelope. It is important to highlight that the flight envelope discussed is defined based on the current version of the aerodynamic data provided and that the actual flight envelope of the Flying-V aircraft will be extended. A controller was synthesized by considering several plants in the design (see Section 6.5). The analysis of this controller is performed in Chapter 7. The worst case stability margins obtained from several flight conditions were shown (see Table 7.5), where the loops opened at the plant input and at q did not comply with the gain margin requirements. Regarding the HQ, all of the conditions are within Level 1 requirements except for one specific flight condition in two of the criteria. Furthermore, the validity of the multi-modeling design was verified by spanning the flight envelope by simulating the controller in the 6 DoF nonlinear model for 82 simulations that started at the edges of the flight envelope. It was verified that the obtained reference tracking results were very similar between flight conditions and that these were satisfactory.

8.2. Concluding Remarks

The answers provided to the research questions logically prompt a reflection on the extent to which the research objective has been met. Specifically, the objective reads:

The research objective is to increase the maturity of the FCS of the Flying-V by implementing a C* controller within the Signal-Based Mixed Sensitivity $\mathcal{H}_\infty$ framework, while guaranteeing robustness stability and performance against uncertainty, adequate performance in the presence of disturbances and measurement noise, and compliance with Level 1 HQ.

With the signal-based $\mathcal{H}_\infty$ mixed sensitivity approach, three FCS were successfully designed. These are based on the C* longitudinal law and were synthesized taking into consideration the robustness and performance requirements defined a priori. No similar designs applied on the Flying-V had been recorded in the literature. The proposed controllers addressed the main limitations highlighted for the nonlinear approaches previously suggested, regarding sensitivity to sensor measurement time delays by the modified CT controller alternative. Additionally, a main issue observed in past studies includes the lack of robustness in the presence of uncertainties, which is successfully tackled in the current project. Finally, this thesis confirmed with detailed analysis that the digital and multi-modeling digital controllers are promising structures to be applied on the FCS, with guaranteed noise attenuation, input and output disturbance rejection, robustness against uncertainties, as well as compliance with Level 1 HQ.

In essence, the research objective has been accomplished. The findings of this study hopefully contribute to ongoing efforts towards a more sustainable aviation industry and towards improved and alternative control system design choices for the Flying-V. Key recommendations for future research are outlined in the next chapter.

RECOMMENDATIONS

Several recommendations for future work follow naturally from the current research. Some of these recommendations are outlined below.

- **Simulation model:** The simulation model provides a solid foundation. Nevertheless, there are opportunities for further enhancements. To begin with, a more realistic engine model should be implemented as in the current state it is defined as a simple first order model. Additionally, the aerodynamic data should be implemented taking into consideration more than one control surface in each wing, which would motivate the need for control allocation. Depending on the flight condition, mass and CoG variations should also be imposed on the system. Furthermore, although sensor noise is added for analysis, the sensor dynamics are not modeled and, thus, it should be addressed. A rigid body assumption is used in the model. Nonetheless, aero elasticity and bending moments should be also considered. Lastly, from literature, it was decided to place the IMU sensor slightly in front of the ICR. Nonetheless, a more detailed analysis for the Flying-V should be conducted.

- **Aerodynamic data:** The aerodynamic data should be matured. Firstly, the flight envelope of the Flying-V should be defined, as the current points used in this research were specifically asked by the author of the thesis and not by a member of the flight performance group. Moreover, some aerodynamic points provided demonstrated unexpected characteristics, namely static instability after $2.5°$ of AoA for certain conditions in higher velocities. For this reason, these points were not considered for the multi-modeling design.

- **C^*U variation:** A drawback of the C^* control law pointed out in literature is the loss of airspeed stability. The C^*U approach is proposed, which consists of adding an airspeed feedback loop to the controller integrator. This artificially restores the stability and, thus, causes the aircraft to return to the commanded trim speed [Niedermeier and Lambregts, 2012]. Hence, this variation should be an interesting addition to the current design.

- **Lateral-direction control law:** In the current research, only the longitudinal dynamics were controlled. Thus, a lateral-directional controller should also be developed.

- **Gain-scheduling:** A multi-modeling controller was designed which achieved most of the desired characteristics. However, the accuracy of the robustness and performance guarantees of the system would be improved for each point in case a linear controller was synthesized for each specified flight condition and consequently gain-scheduled across the flight envelope. This would entail interpolating the gains wrt the scheduled parameters creating a nonlinear representation. This would allow tighter control in each operating point, where the gains adequately address the specific dynamics.

- **Linear Parameter-Varying (LPV) control:** An alternative approach to the scheduling problem previously mentioned is the LPV control technique. The main idea is to model the nonlinear dynamics of the plant over the flight envelope as a LPV system. The subsequent LPV controller computation relies on the solution of a set of LMI. The main advantage of the approach is that a self-scheduled full-envelope controller is computed in a single step.

- **Flight Envelope Protections:** As stated in the literature, the Flying-V presents unstable dutch roll and pitch break-up tendencies. Thus, as already included in other past studies [Stougie et al., 2024] [Traas, 2024], a FEP should be added to enhance safety by preventing aircraft from entering potentially unstable flight conditions.

- **Mass, MOI, and CoG uncertainties:** Although uncertainties were included in the system within the aerodynamic coefficients, other parameters should also be varied for a more comprehensive analysis. These include the mass, moments of inertia, the CoG position, and actuator and sensor dynamics.

- **Piloted assessment of HQ:** The handling qualities can be distinguished into predicted and assigned levels. The former was conducted in this research, which is based on a set of quantitative parameters that, together, are expected to accurately reflect HQ, whereas the former is based on piloted assessments during flight test maneuvers [Mitchell et al., 1994]. Nevertheless, there may be conflicts between the two since the the predicted levels may not capture accurately the characteristics experienced by the pilot. Thus, for an accurate assessment of the HQ levels, pilot assessments should also be conducted. These can be carried out in the SIMONA Research Simulator at TU Delft.

BIBLIOGRAPHY

Adams, R. and Banda, S. (1993). Robust flight control design using dynamic inversion and structured singular value synthesis. *IEEE Transactions on Control Systems Technology*, 1(2):80–92, DOI: 10.1109/87.238401.

Anderson, B. and Liu, Y. (1989). Controller Reduction: Concepts and Approaches. *IEEE Transactions on Automatic Control*, 34(8):802–812, DOI: 10.1109/9.29422.

Ankith John Santosh, A. (2020). Numerical Investigation of the Influence of Ground Effect on the FV Aircraft: Influence of Ground Effect on the Flying V Aircraft. MSc Thesis. URL: http://resolver.tudelft.nl/uuid:d34e14b2-fed5-4e4f-a448-aa0fb92e0331.

Anonymous (1997). Flying Qualities of Piloted Aircraft. MIL-HDBK-1797A. Technical report, U.S. Department of Defense (DoD).

Anonymous (2000). RTO-TR-029: Flight Control Design - Best Practices. Technical report, NATO Research and Technology Organization (RTO).

Anonymous (2008). Aerospace - Flight Control Systems - General Specification for Design, Installation, and Test of Piloted Military Aircraft. SAE-AS94900. Technical report, SAE International.

Anonymous (2014). Airworthiness Certification Criteria. MIL-HDBK-516C. Technical report, U.S. Department of Defense (DoD).

Apkarian, P., Dao, M. N., and Noll, D. (2015). Parametric Robust Structured Control Design. *IEEE Transactions on Automatic Control*, 60(7):1857–1869, DOI: 10.1109/TAC.2015.2396644.

Apkarian, P., Gahinet, P., and Buhr, C. (2014). Multi-Model, Multi-Objective Tuning of Fixed-Structure Controllers. In *2014 European Control Conference (ECC). Strasbourg, France*, pages 856–861. DOI: 10.1109/ECC.2014.6862200.

Apkarian, P. and Noll, D. (2006a). Nonsmooth $\mathcal{H}_\infty$ Synthesis. *IEEE Transactions on Automatic Control*, 51(1):71–86, DOI: 10.1109/TAC.2005.860290.

Apkarian, P. and Noll, D. (2006b). Nonsmooth Optimization for Multidisk $\mathcal{H}_\infty$ Synthesis. *European Journal of Control*, 12(3):229–244, DOI: 10.3166/ejc.12.229-244.

Apkarian, P. and Noll, D. (2007). Nonsmooth Optimization for Multiband Frequency Domain Control Design. *Automatica*, 43(4):724–731, ISSN: 0005-1098, DOI: 10.1016/j.automatica.2006.08.031.

Apkarian, P. and Noll, D. (2017). The $\mathcal{H}_\infty$ Control Problem is Solved. *Aerospace Lab 13*, pages 1–11, DOI: 10.12762/2017.AL13-01.

Apkarian, P., Noll, D., and Rondepierre, A. (2008). Mixed $\mathcal{H}_2/\mathcal{H}_\infty$ Control via Nonsmooth Optimization. *SIAM Journal on Control and Optimization*, 47(3):1516–1546, DOI: 10.1137/070685026.

Arent, L. and Falatko, J. (1992). 757 Fly-by-Wire Demonstrator Flight Test. In *The Boeing Company. 6th AIAA Biennial Flight Test Conference. Hilton Head, SC*, page 4099. DOI: 10.2514/6.1992-4099.

Åström, K. J. and Wittenmark, B. (1997). *Computer-Controlled Systems: Theory and Design*. Prentice Hall, 3 edition, ISBN: 7-302-05008-2.

Atmaca, D. and Kampen, E.-J. V. (2025). Fault Tolerant Control for the Flying-V Using Adaptive Incremental Nonlinear Dynamic Inversion. In *AIAA SCITECH 2025 Forum. AIAA 2025-0081. American Institute of Aeronautics and Astronautics. Orlando, FL*. DOI: 10.2514/6.2025-0081.

Balas, G. J. (2003). Flight Control Law Design: An Industry Perspective. *European Journal of Control*, 9(2):207–226, ISSN: 0947-3580, DOI: 10.3166/ejc.9.207-226, URL: https://www.sciencedirect.com/science/article/pii/S0947358003702763.

Bates, D. and Postlethwaite, I. (2002). *Robust Multivariable Control of Aerospace Systems*. Control and Simulation. Delft University Press. DUP Science, Delft, NL, ISBN: 90-407-2317-6.

Benad, J. (2015). The Flying V - A New Aircraft Configuration for Commercial Passenger Transport. pages 1–8. Deutscher Luft- und Raumfahrtkongress 2015, Rostock, DOI: 10.25967/370094.

Benad, J. and Vos, R. (2022). Design of a Flying V Subsonic Transport. In *33rd Congress of the International Council of the Aeronautical Sciences, ICAS 2022, Stockholm, Sweden*. URL: https://resolver.tudelft.nl/uuid:95ea413d-d5b1-4cb2-a650-828cb106dbbd.

Bennani, S. and Looye, G. (1998). Design of Flight Control Laws for a Civil Aircraft using μ-synthesis. AIAA-98-4133. In *AIAA Guidance, Navigation, and Control Conference and Exhibit. Boston,MA,U.S.A.* DOI: 10.2514/6.1998-4133.

Biertümpfel, F., Pfifer, H., and Theis, J. (2024). Robust Space Launcher Control with Time-Varying Objectives. *Journal of Guidance, Control, and Dynamics*, 0(0):1–11, ISSN: 1533-3884, DOI: 10.2514/1.G007632.

Bourget, G. (2020). The effect of landing gear implementation on Flying V aerodynamics, stability and controllability. MSc Thesis. URL: http://resolver.tudelft.nl/uuid:599eca91-6200-4d29-8dd7-e4e7060703e1.

Burke, J. V., Henrion, D., Lewis, A. S., and Overton, M. L. (2006). Stabilization via Nonsmooth, Nonconvex Optimization. *IEEE Transactions on Automatic Control*, 51(11):1760–1769, ISSN: 0018-9286, DOI: 10.1109/TAC.2006.884944.

Bérard, C., Biannic, J.-M., and Saussie, D. (2012). *La Commande Multivariable-Application au Pilotage d'un Avion*. L'Usine Nouvelle, Dunod, ISBN: 9782100585465.

Caldwell, B., Pratt, R., Taylor, R., and Felton, R. (2000). *Aeroservoelasticity*, pages 225–300. ISBN: 9780852967669, DOI: 10.1049/PBCE057E_ch7.

Cao, L. and Hori, Y. (1997). Mixed Sensitivity Optimization to Avoid Pole/Zero Cancellation. *Automatica*, 33(7):1379–1385, ISSN: 0005-1098, DOI: 10.1016/S0005-1098(97)00029-0.

Cappuyns, T. (2019). Handling Qualities of a Flying V Configuration. MSc Thesis. URL: http://resolver.tudelft.nl/uuid:69b56494-0731-487a-8e57-cec397452002.

Chen, S. Y., Waerdt, W. v. d., and Castro, S. G. (2023). Design for Bird Strike Crashworthiness Using a Building Block Approach applied to the Flying-V Aircraft. *Heliyon*, 9, ISSN: 2405-8440, DOI: 10.1016/j.heliyon.2023.e14723.

Chung, I. (2018). Cabin Interior Design of the Flying V. MSc Thesis. URL: http://resolver.tudelft.nl/uuid:44843121-ece2-4394-a94d-03da5bc563b3.

Cook, M. V. (2013). Chapter 10 - Flying and Handling Qualities. In Cook, M. V., editor, *Flight Dynamics Principles (Third Edition)*, pages 259–291. Butterworth-Heinemann, ISBN: 978-0-08-098242-7, DOI: 10.1016/C2010-0-65889-5.

Dahleh, M. and Díaz-Bobillo, I. (1995). *Control of Uncertain Systems: a Linear Programming Approach*. Prentice Hall, ISBN: 978-0-13-280645-9, URL: https://dahleh.lids.mit.edu/books/control-of-uncertain-systems-a-linear-programming-approach/.

De Paula, J. V. D. and Paglione, P. (2007). Longitudinal Control Laws Based on C* Criterion. In *Proceedings of COBEM 2007. 19th International Congress of Mechanical Engineering, Brasilia, DF, Brazil*, pages 5–8. URL: https://abcm.org.br/app/webroot/anais/cobem/2007/pdf/COBEM2007-1596.pdf.

de Ruiter, L. (2020). Weight Balance Estimation with Automated Structural Analysis for Subscale Flight Models. MSc Thesis. URL: http://resolver.tudelft.nl/uuid:57064c65-03d1-4c42-953d-a6d59f2a34c6.

Delannoy, S. and Oudin, S. (2013). Longitudinal Control Law for Modern Long Range Civil Aircraft. *Proceedings of the 2013 CEAS EuroGNC conference. Delft, The Netherlands.*

Dobos-Bubno, S. and Hartsook, L. B. (1977). AFFDL-TR-77-7: Validation of MIL-F-9490D - General Specification for Flight Control System for Piloted Military Aircraft. Technical report.

Dotman, T. (2021). A Structural Sizing Methodology for the Wing-Fuselage of the Flying-V. MSc Thesis. URL: http://resolver.tudelft.nl/uuid:69e21e65-7168-4f83-abf5-b646bb4c7fe5.

Doyle, J. (1996). Robust and Optimal Control. In *Proceedings of 35th IEEE Conference on Decision and Control. Kobe, Japan*, volume 2, pages 1595–1598 vol.2. ISBN: 0-7803-3590-2, ISSN: 0191-2216, DOI: 10.1109/CDC.1996.572756.

Doyle, J., Glover, K., Khargonekar, P., and Francis, B. (1988). State-Space Solutions to Standard $\mathcal{H}_2$ and $\mathcal{H}_\infty$ Control Problems. In *1988 American Control Conference. Atlanta, GA, USA*, pages 1691–1696. DOI: 10.23919/ACC.1988.4789992.

Doyle, J., Zhou, K., and Bodenheimer, B. (1989). Optimal Control with Mixed $\mathcal{H}_2$ and $\mathcal{H}_\infty$ Performance Objectives. In *1989 American Control Conference. Pittsburgh, PA, USA*, pages 2065–2070. DOI: 10.23919/ACC.1989.4790529.

Doyle, J. C., Wall, J. E., and Stein, G. (1982). Performance and Robustness Analysis for Structured Uncertainty. In *21st IEEE Conference on Decision and Control. Orlando, FL, USA*, pages 629–636. DOI: 10.1109/CDC.1982.268218.

Droste, C. and Walker, J. (1980). *A Case Study on the F-16 Fly-by-wire Flight Control System*. AIAA Professional Study Series. American Institute of Aeronautics and Astronautics, ISBN: 9781563473074, URL: https://books.google.pt/books?id=wzonPQAACAAJ.

Eftekhar, S. (2024). High Lift Split Flaps for the Flying-V. MSc Thesis. URL: http://resolver.tudelft.nl/uuid:0ad3c088-b6a6-472b-b60b-4b424a08e15c.

Elliott, J. (1977). Nasa's advanced control law program for the f-8 digital fly-by-wire aircraft. *IEEE Transactions on Automatic Control*, 22(5):753–757, ISSN: 0018-9286, DOI: 10.1109/TAC.1977.1101608.

Enns, D. F. (1984). Model Reduction with Balanced Realizations: An Error Bound and a Frequency Weighted Generalization. In *The 23rd IEEE Conference on Decision and Control. Las Vegas, NV, USA*, pages 127–132. DOI: 10.1109/CDC.1984.272286.

Erdinçler, O. (2021). Aerodynamic and Performance Analysis of Ground Spoilers on the Flying-V. MSc Thesis. URL: http://resolver.tudelft.nl/uuid:d8176c14-f3e1-4a6a-99b0-55c7251f9762.

Faggiano, F., Vos, R., Baan, M., and Dijk, R. v. (2017). Aerodynamic Design of a Flying-V Aircraft. *17th AIAA Aviation Technology, Integration, and Operations Conference. Denver, Colorado. AIAA 2017-3589. American Institute of Aeronautics and Astronautics*, DOI: 10.2514/6.2017-3589.

Favre, C. (1994). Fly-by-Wire for Commercial Aircraft: the Airbus Experience. *International Journal of Control*, 59(1):139–157, DOI: 10.1080/00207179408923072.

Field, E. (1993). *The Application of a C* Flight Control Law to Large Civil Transport Aircraft. Technical Report*. Cranfield, England : College of Aeronautics, Cranfield Institute of Technology.

Gahinet, P. and Apkarian, P. (1994). A Linear Matrix Inequality Approach to $\mathcal{H}_\infty$ Control. *International Journal of Robust Nonlinear Control*, 4(4):421–448, DOI: 10.1002/rnc.4590040403.

Gahinet, P. and Apkarian, P. (2011). Structured $\mathcal{H}_\infty$ Synthesis in MATLAB. *IFAC Proceedings Volumes. 18th IFAC World Congress*, 44(1):1435–1440, ISSN: 1474-6670, DOI: 10.3182/20110828-6-IT-1002.00708.

Gahinet, P. and Apkarian, P. (2013). Automated Tuning of Gain-scheduled Control Systems. In *52nd IEEE Conference on Decision and Control. IEEE. Firenze, Italy*, pages 2740–2745. IEEE, DOI: 10.1109/CDC.2013.6760297.

García, A. R. (2020). Aerodynamic model identification of the flying-v from wind tunnel data. *AIAA Aviation 2020 Forum. AIAA 2020-2739. American Institute of Aeronautics and Astronautics*, DOI: 10.2514/6.2020-2739.

Gibson, J. C. (1999). *Development of a Methodology for Excellence in Handling Qualities Design for Fly-by-Wire Aircraft*. Dissertation (TU Delft), Delft University Press, ISBN: 90-407-1842-3, URL: http://resolver.tudelft.nl/uuid:6b564b35-cb74-436c-8c47-845bfbbb8b4d.

Glover, K. (1984). All optimal Hankel-Norm Approximations of Linear Multivariable Systems and their L^∞ Error Bounds. *International Journal of Control*, 39(6):1115–1193, DOI: 10.1080/00207178408933239.

Goz, E. and Theodoulis, S. (2025). *Robust Multi-Objective $\mathcal{H}_\infty$ Control of GHAME Hypersonic Vehicle in Subsonic Flight*. AIAA SciTech 2025 Forum. AIAA 2025-2266. American Institute of Aeronautics and Astronautics. Orlando, FL, DOI: 10.2514/6.2025-2266.

Granata, F. (2023). Aerodynamic Optimization of a Flying V Aircraft using a Vortex Lattice Method. MSc Thesis. URL: http://resolver.tudelft.nl/uuid:35d70826-c242-4eb1-a10a-2a61955b7182.

Grondman, F., Looye, G., Kuchar, R. O., Chu, Q. P., and Van Kampen, E.-J. (2018). Design and Flight Testing of Incremental Nonlinear Dynamic Inversion-Based Control Laws for a Passenger Aircraft. In *2018 AIAA Guidance, Navigation, and Control Conference. AIAA-2018-0385. American Institute of Aeronautics and Astronautics. Kissimmee, FL, USA*, page 0385. DOI: 10.2514/6.2018-0385.

Guilhem, P. and Jean-Marc, B. (2013). Application of Robust Anti-Windup Design to the Longitudinal Aircraft Control to Cover Actuator Loss. *19th IFAC Symposium on Automatic Control in Aerospace. International Federation of Automatic Control Proceedings Volumes*, 46(19):506–511, DOI: 10.3182/20130902-5-DE-2040.00131.

Hamza, A., Mohamed, A. H., and El-Badawy, A. (2022). Robust $\mathcal{H}_\infty$ Control for a Quadrotor UAV. In *AIAA SCITECH 2022 Forum. AIAA 2022-2033. American Institute of Aeronautics and Astronautics. San Diego, CA Virtual*. DOI: 10.2514/6.2022-2033.

Hillen, M. (2020). Parametrisation of the Flying-V Outer Mould Line. MSc Thesis. URL: http://resolver.tudelft.nl/uuid:f4863ae4-2792-4335-b929-ff9dfdb6fed5.

Honeywell Technology Center, Lockheed Martin Skunk Works and Lockheed Martin Tactical Aircraft Systems (1996). Application of Multivariable Control Theory to Aircraft Control Laws, Final Report: Multivariable Control Design Guidelines. Tech. rep. WL-TR-96-3099. Technical report, Wright-Patterson AFB, OH, USA: Wright Laboratory.

Horwitz, J. (2021). Parametric Design of the Flying-V Winglets for Improved Lateral-Directional Stability and Control. MSc Thesis. URL: http://resolver.tudelft.nl/uuid:d7513b36-b9fd-4f8a-8726-f5c7ee7f3a6b.

Huang, Y., Pe, T., Popov, A. P., Werner, H., and Thielecke, F. (2010). Control of a two-load-path Trimmable Horizontal Stabilizer Actuator of an aircraft - Comparison of $\mathcal{H}_\infty$ design approaches. In *49th IEEE Conference on Decision and Control (CDC). Institute of Electrical and Electronics Engineers. Atlanta, GA, USA*, pages 4863–4868. ISBN: 978-1-4244-7745-6, ISSN: 0191-2216, DOI: 10.1109/CDC.2010.5716948.

Javed, S. B., Uppal, A. A., Samar, R., and Bhatti, A. I. (2021). Design and Implementation of Multi-Variable $\mathcal{H}_\infty$ Robust Control for the Underground Coal Gasification Project Thar. *Energy*, 216:119000, ISSN: 0360-5442, DOI: 10.1016/j.energy.2020.119000.

Ji, S. and Wu, A. (2011). Study on Dual-Loop Controller of Helicopter Based on the Robust $\mathcal{H}_\infty$ Loop Shaping and Mixed Sensitivity. In *2011 International Conference on Electrical and Control Engineering. Yichang, China*, pages 1291–1294. ISBN: 978-1-4244-8162-0, DOI: 10.1109/ICECENG.2011.6057783.

Johnson, N. (2021). Effect of Winglet Integration and Rudder Deflection on Flying-V Aerodynamic Characteristics. MSc Thesis. URL: http://resolver.tudelft.nl/uuid:b664ae03-846f-4ad3-849a-c081a32260ad.

Joosten, S., Stroosma, O., Vos, R., and Mulder, M. (2023). Simulator Assessment of the Lateral-Directional Handling Qualities of the Flying-V. In *AIAA SciTech 2023 Forum. AIAA 2023-0906. American Institute of Aeronautics and Astronautics*, page 0906. DOI: 10.2514/6.2023-0906.

Jorge, A. (2023). Quantifying Wind Tunnel Effects on the Flying-V. MSc Thesis. URL: http://resolver.tudelft.nl/uuid:b9076ade-2d6e-4faf-882c-1f6115a1317a.

Jr, W. (1999). F-22 Structural Coupling Lessons Learned. *RTO MP-36. RTO AVT Specialists' Meeting on "Structural Aspects of Flexible Aircraft Control". Ottawa, Canada. Lockheed Martin Tactical Aircraft Systems*.

Kaminer, I., Pascoal, A. M., Khargonekar, P. P., and Coleman, E. E. (1995). A Velocity Algorithm for the Implementation of Gain-Scheduled Controllers. *Automatica*, 31(8):1185–1191, ISSN: 0005-1098, DOI: 10.1016/0005-1098(95)00026-S.

Kim, C., Ji, C., Bang, J., Koh, G., and Choi, N. (2024). A Survey on Structural Coupling Design and Testing of the Flexible Military Aircraft. *International Journal of Aeronautical and Space Sciences*, 25(1):122–145, DOI: 10.1007/s42405-023-00643-y.

Kim, J.-H. and Whang, I. H. (2018). Augmented Three-Loop Autopilot Structure Based on Mixed-Sensitivity $\mathcal{H}_\infty$ Optimization. *Journal of Guidance, Control, and Dynamics*, 41(3):751–756, DOI: 10.2514/1.G003119.

Koenderink, R. (2024). Design Methodology for Unconventional Engine Mounting Structures, Including Crashworthiness Assessment. MSc Thesis. URL: http://resolver.tudelft.nl/uuid:2a250390-05c0-4f71-bf73-a21e4cf6567d.

Kwakernaak, H. (1993). Robust Control and $\mathcal{H}_\infty$ Optimization Tutorial Paper. *Automatica*, 29(2):255–273, ISSN: 0005-1098, DOI: 10.1016/0005-1098(93)90122-A.

Laar, Y., Atherstone, D., Benad, J., and Vos, R. (2024). Aerodynamic Design of a Flying V Aircraft in Transonic Conditions. In *AIAA SCITECH 2024 Forumm. AIAA 2024-2669. American Institute of Aeronautics and Astronautics. Orlando, FL*, page 2669. DOI: 10.2514/6.2024-2669.

Lawrence, D. A. and Rugh, W. J. (1995). Gain Scheduling Dynamic Linear Controllers for a Nonlinear Plant. *Automatica*, 31(3):381–390, DOI: 10.1016/0005-1098(94)00113-W.

Lhachemi, H., Saussie, D., and Zhu, G. (2014). A Robust and Self-Scheduled Longitudinal Flight Control System: a Multi-Model and Structured $\mathcal{H}_\infty$ Approach. In *AIAA guidance, navigation, and control conference. AIAA 2014-0601. American Institute of Aeronautics and Astronautics. National Harbor, Maryland*. DOI: 10.2514/6.2014-0601.

Lhachemi, H., Saussié, D., and Zhu, G. (2016). Gain-Scheduling Control Design in the Presence of Hidden Coupling Terms via Eigenstructure Assignment: Application to a Pitch-Axis Missile Autopilot. In *American Control Conference (ACC). Boston, MA, USA*, pages 4041–4046. ISBN: 978-1-4673-8683-8, ISSN: 2378-5861, DOI: 10.1109/ACC.2016.7525556.

Lombaerts, T., Looye, G., Ellerbroek, J., and Martin, M. (2017). Design and Piloted Simulator Evaluation of Adaptive Safe Flight Envelope Protection Algorithm. *Journal of Guidance Control and Dynamics*, 40:1902–19024, DOI: 10.2514/1.G002525.

Luckner, R. (2002). *Considerations for Clearance of Civil Transport Aircraft*, pages 447–456. Springer Berlin Heidelberg, Berlin, Heidelberg, ISBN: 978-3-540-45864-7, DOI: 10.1007/3-540-45864-6_24.

Malcom, L. G. and Tobie, H. N. (1965). New Short Period Handling Quality Criterion for Fighter Aircraft.

Marcos, A. (2017). Revisiting the Aircraft C* Control Law: A Comparison Between Classical and Structured designs. In *2017 IEEE Conference on Control Technology and Applications (CCTA). Maui, HI, USA*, pages 2114–2119. ISBN: 978-1-5090-2183-3, DOI: 10.1109/CCTA.2017.8062765.

Martinez-Val, R. (2007). Flying Wings. A New Paradigm for Civil Aviation? *Acta Polytechnica*, 47(1), DOI: 10.14311/914.

McFarlane, D. and Glover, K. (1992). A Loop-Shaping Design Procedure Using $\mathcal{H}_\infty$ Synthesis. *IEEE Transactions on Automatic Control*, 37(6):759–769, ISSN: 0018-9286, DOI: 10.1109/9.256330.

McFarlane, D. C. and Glover, K. (1990). *Robust Controller Design using Normalized Coprime Factor Plant Descriptions*, volume 138. Lecture notes in control and information sciences, Berlin, Heidelberg : Springer-Verlag Berlin Heidelberg GmbH, 1990, ISSN: 0170-8643.

McRuer, D., Ashkenas, I., and Graham, D. (1973). *Aircraft Dynamics and Automatic Control*. Princeton University Press, URL: http://www.jstor.org/stable/j.ctt7ztqhj.

Mitchell, D. G., Hoh, R. H., Aponso, B. L., and Klyde, D. H. (1994). Proposed Incorporation of Mission-Oriented Flying Qualities into MIL-STD-1797A. WL-TR-94-3162. Technical report, Wright-Patterson AFB, OH, USA: Wright Laboratory.

Muir, E. (1997). The HIRM Design Challenge Problem Description. Ed. by J.-F. Magni, S. Bennani, and J. Terlouw. Berlin, Heidelberg: Springer Berlin Heidelberg. In Magni, J.-F., Bennani, S., and Terlouw, J., editors, *Robust Flight Control*, pages 419–443. ISBN: 978-3-540-40941-0.

Mulder, J., van Staveren, W., van der Vaart, J., de Weerdt, E., de Visser, C., in 't Veld, A., and Mooij, E. (2013). Lecture Notes: Flight Dynamics. Deft University of Technology.

Nanninga, M. (2023). High-Fidelity Structural Sizing Method for Weight Estimation of a Flying-V. MSc Thesis. URL: http://resolver.tudelft.nl/uuid:2efac46a-1328-49af-bbd8-685512c3eff3.

Naäman, Y. (2024). Robustness Measures in the Nonlinear Domain: Investigating Frozen-Time Robustness of Structured $\mathcal{H}_\infty$ Controllers in Nonlinear Realizations. MSc Thesis. URL: https://resolver.tudelft.nl/uuid:28ef6742-832a-4e39-aa6b-e9e368c498f4.

Neal, T. and Smith, R. (1970). *An In-Flight Investigation to Develop Control System Design Criteria for Fighter Airplanes*. Defense Technical Information Center. Cornell Aeronautical Lab Inc Buffalo NY.

Niedermeier, D. and Lambregts, A. (2012). Fly-by-Wire Augmented Manual Control - Basic Design Considerations. *ICAS 2012-5.4.1. 28th Congress of the International Council of the Aeronautical Sciences 2012, ICAS 2012. Brisbane, Australia*, 4:3073–3086.

Nieto-Wire, C. and Sobel, K. (2011). Flight Control Design for a Tailless Aircraft using Eigenstructure Assignment. *International Journal of Aerospace Engineering*, 2011(1):549131, DOI: 10.1155/2011/549131.

Nolet, S. (2022). Improving the Flying V Directional Control Power by the Implementation of Split Flaps. MSc Thesis. URL: http://resolver.tudelft.nl/uuid:18847b0d-597d-4539-968f-ebc8a14c905e.

Oloomi, H. and Shafai, B. (2003). Weight Selection in Mixed Sensitivity Robust Control for Improving the Sinusoidal Tracking Performance. In *42nd IEEE International Conference on Decision and Control (IEEE Cat. No.03CH37475). Maui, HI, USA*, volume 1, pages 300–305 Vol.1. ISBN: 0-7803-7924-1, ISSN: 0191-2216, DOI: 10.1109/CDC.2003.1272577.

Oosterom, W. and Vos, R. (2022). Conceptual Design of a Flying-V Aircraft Family. In *AIAA Aviation 2022 Forum. AIAA 2022-3200. American Institute of Aeronautics and Astronautics. Chicago, IL Virtual*, page 3200. DOI: 10.2514/6.2022-3200.

Palermo, M. and Vos, R. (2020). Experimental Aerodynamic Analysis of a 4.6%-Scale Flying-V Subsonic Transport. In *AIAA Scitech 2020 Forum. AIAA 2020-2228. American Institute of Aeronautics and Astronautics. Orlando, FL*, page 2228. DOI: 10.2514/6.2020-2228.

Papageorgiou, G. and Hyde, R. A. (2001). Analysing the stability of NDI-based flight controllers with LPV methods. *AIAA Guidance, Navigation, and Control Conference and Exhibit. AIAA 2001-4039. American Institute of Aeronautics and Astronautics. Montreal, Canada*, DOI: 10.2514/6.2001-4039.

Papageorgiou, G. and Polansky, M. (2009). Tuning a Dynamic Inversion Pitch Axis Autopilot using McFarlane-Glover Loop Shaping. *Optimal Control Applications and Methods*, 30(3):287–308, DOI: 10.1002/oca.864.

Pirat, C., Ankersen, F., Walker, R., and Gass, V. (2020). $\mathcal{H}_\infty$ and μ -synthesis for nanosatellites rendezvous and docking. *IEEE Transactions on Control Systems Technology*, 28(3):1050–1057, ISSN: 1063–6536, DOI: 10.1109/TCST.2019.2892923.

Pollack, T. (2024). *Advances in Dynamic Inversion-based Flight Control Law Design: Multivariable Analysis and Synthesis of Robust and Multi-Objective Design Solutions*. Dissertation (TU Delft), Delft University of Technology, ISBN: 978-94-6384-643-1, DOI: 10.4233/uuid:28617ba0-461d-48ef-8437-de2aa41034ea.

Pollack, T., Theodoulis, S., and van Kampen, E. (2024). Commonalities beBtween Robust Hybrid Incremental Nonlinear Dynamic Inversion and Proportional-Integral-Derivative Flight Control Law Design. *Aerospace Science and Technology*, 152, ISSN: 1270–9638, DOI: 10.1016/j.ast.2024.109377.

Pollack, T. and van Kampen, E. (2023). Robust Stability and Performance Analysis of Incremental Dynamic-Inversion-Based Flight Control Laws. *Journal of Guidance, Control, and Dynamics*, 46(9):1785–1798, ISSN: 0731–5090, DOI: 10.2514/1.G006576.

Pratt, R. W. (2000). Flight Control Systems - Practical Issues in Design and Implementation. Chapter 1.5.2 Civil Aircraft Benefits. ISBN: 978-0-85296-766-9.

Reekers, M. (2021). Climate Effects of the Flying V. MSc Thesis. URL: http://resolver.tudelft.nl/uuid:27a0ae7a-75e4-42df-950e-1be79eacfce9.

Reiner, J., Balas, G. J., and Garrard, W. L. (1996). Flight control design using robust dynamic inversion and time-scale separation. *Automatica*, 32(11):1493–1504, ISSN: 0005-1098, DOI: 10.1016/S0005-1098(96)00101-X.

Rubio Pascual, B. (2018). Engine-Airframe Integration for the Flying-V. MSc Thesis. URL: http://resolver.tudelft.nl/uuid:75be27a7-6fd4-4112-a600-45df2999758f.

Rugh, W. J. (1990). Analytical Framework for Gain Scheduling. In *1990 American Control Conference. San Diego, CA, USA*, pages 1688–1694. DOI: 10.23919/ACC.1990.4791022.

Rugh, W. J. and Shamma, J. S. (2000). Research on Gain Scheduling. *Automatica*, 36(10):1401–1425, DOI: 10.1016/S0005-1098(00)00058-3.

Ruiz Garcia, A. (2019). Aerodynamic Model Identification of the Flying-V using Wind Tunnel Data. MSc Thesis. URL: http://resolver.tudelft.nl/uuid:79e01f29-1789-4501-8556-ca2bcf06f3ab.

Safonov, M. G., Chiang, R. Y., and Flashner, H. (1991). H (infinity) robust control synthesis for a large space structure. *Journal of guidance, control, and dynamics*, 14(3):513–520, DOI: 10.2514/3.20670.

Saripudin, Asali, M. O., Indriyanto, T., and Trilaksono, B. R. (2019). Visual Servoing using Mixed Sensitivity $\mathcal{H}_\infty$ Control for Yaw-Pitch Camera Platform. In *2019 International Conference of Artificial Intelligence and Information Technology (ICAIIT). Yogyakarta, Indonesia*, pages 48–53. ISBN: 978-1-5386-8449-8, DOI: 10.1109/ICAIIT.2019.8834610.

Seiler, P., Packard, A., and Gahinet, P. (2020). An Introduction To Disk Margins. *IEEE Control Systems Magazine*, 40(5), ISSN: 1066–033X, DOI: 10.1109/MCS.2020.3005277.

Sève, F., Theodoulis, S., Wernert, P., Zasadzinski, M., and Boutayeb, M. (2014). Pitch/Yaw Channels Control Design for a 155mm Projectile with Rotating Canards, using a $\mathcal{H}_\infty$ Loop-Shaping Design Procedure. In *AIAA Guidance, Navigation, and Control Conference. AIAA 2014-1474. American Institute of Aeronautics and Astronautics*, National Harbor, United States. DOI: 10.2514/6.2014-1474.

Shahin, R. (2024). Robust Flight Control for the Flying-V:Mixed μ-optimal Incremental Dynamic Inversion-based Flight Control. MSc Thesis. URL: https://resolver.tudelft.nl/uuid:5e0f45c7-4e3c-4648-9d72-4486af410cf4.

Shamma, J. S., Athans, M., et al. (1988). Analysis of Gain Scheduled Control for Linear Parameter-Varying Plants. *PhD thesis. Massachusetts Institute of Technology*.

Sieberling, S., Chu, Q., and Mulder, J. (2010). Robust Flight Control Using Incremental Nonlinear Dynamic Inversion and Angular Acceleration Prediction. *Journal of guidance, control, and dynamics*, 33(6):1732–1742, DOI: 10.2514/1.49978.

Siemonsma, K. (2022). Aerodynamic Model Identification of the Flying-V using Flight Data. MSc Thesis. URL: http://resolver.tudelft.nl/uuid:3cf35fb2-4fe7-49d7-9076-068c44fb2016.

Simões, A. M. and Cavalcanti, V. M. G. B. (2023). Missile Autopilot Design via Structured Robust Linear Parameter-Varying Synthesis. *Journal of Guidance, Control, and Dynamics*, 46(8):1649–1656, DOI: 10.2514/1.G007580.

Skogestad, S. and Postlethwaite, I. (2005). *Multivariable Feedback Control: Analysis and Design.* . John Wiley and Sons LTd., 2nd edition, ISBN: 978-0470011683.

Stein, G. (2003). Respect the Unstable. *IEEE Control Systems Magazine*, 23(4):12–25, DOI: 10.1109/MCS.2003.1213600.

Stevens, B. L., Lewis, F. L., and Johnson, E. N. (2015). *Aircraft Control and Simulation: Dynamics, Controls Design, and Autonomous Systems*. John Wiley & Sons, ISBN: 978-1118870976, DOI: 10.1002/9781119174882.

Stougie, J., Pollack, T., and Van Kampen, E.-J. (2024). Incremental Nonlinear Dynamic Inversion control with Flight Envelope Protection for the Flying-V. In *AIAA SCITECH 2024 Forum. AIAA 2024-2565. American Institute of Aeronautics and Astronautics. Orlando, FL*, page 2565. DOI: 10.2514/6.2024-2565.

Sève, F., Theodoulis, S., Wernert, P., Zasadzinski, M., and Boutayeb, M. (2017). Gain-Scheduled $\mathcal{H}_\infty$ Loop-Shaping Autopilot Design for Spin-Stabilized Canard-Guided Projectiles. In *Aerospace Lab, 13*, pages 1–24. DOI: 10.12762/2017.AL13-03.

Theis, J., Pfifer, H., and Seiler, P. (2016). Robust Control Design for Active Flutter Suppression. In *AIAA Atmospheric Flight Mechanics Conference. AIAA 2016-1751. American Institute of Aeronautics and Astronautics. San Diego, California, USA*. DOI: 10.2514/6.2016-1751.

Theodoulis, S. and Proff, M. (2021). *Robust Flight Control Tuning for Highly Agile Missiles*. AIAA Scitech 2021 Forum. AIAA 2021-1568. American Institute of Aeronautics and Astronautics. Virtual Event, DOI: 10.2514/6.2021-1568.

Theodoulis, S., Proff, M., and Marchand, C. (2020). Robust Design for Highly Agile Missile Autopilots. In *2020 28th Mediterranean Conference on Control and Automation (MED). Saint-Raphaël, France*, pages 67–72. ISBN: 978-1-7281-5743-6, ISSN: 2473-3504, DOI: 10.1109/MED48518.2020.9183304.

Torelli, R., Stroosma, O., Vos, R., and Mulder, M. (2023). Piloted Simulator Evaluation of Low-Speed Handling Qualities of the Flying-V. In *AIAA SciTech 2023 Forum. AIAA 2023-0907.American Institute of Aeronautics and Astronautics. National Harbor, MD Online*, page 0907. DOI: 10.2514/6.2023-0907.

Traas, T. (2024). Hybrid INDI with enhanced FEP for the Flying-V. MSc Thesis.

Tsai, M., Geddes, E., and Postlethwaite, I. (1990). Pole-Zero Cancellations and Closed-Loop Properties of an $\mathcal{H}_\infty$ Mixed Sensitivity Design Problem. In *29th IEEE Conference on Decision and Control. Honolulu, HI, USA*, pages 1028–1029 vol.2. DOI: 10.1109/CDC.1990.203754.

van der Pluijm, R. (2021). Cockpit Design and Integration into the Flying V. MSc Thesis. URL: http://resolver.tudelft.nl/uuid:da4a8d74-32fa-45f1-9f92-d01d45fdea01.

van Ieperen, M. (2021). Noise Prediction of the Flying V. MSc Thesis. URL: http://resolver.tudelft.nl/uuid:1697f11f-4b01-49d2-9cf8-9006dfdd4b579.

van Luijk, N. and Vos, R. (2023). Constrained Aerodynamic Shape Optimisation of the Flying V Outer Wing. In *AIAA Aviation 2023 Forum. AIAA 2023-3250. American Institute of Aeronautics and Astronautics. San Diego, CA and Online*, page 3250. DOI: 10.2514/6.2023-3250.

van Overeem, S. (2022). Modelling, Control, and Handling Quality Analysis of the Flying-V. MSc Thesis. URL: http://resolver.tudelft.nl/uuid:7fd04eec-41d4-4967-b246-89fdfac2446e.

van Overeem, S., Wang, X., and Van Kampen, E.-J. (2022). Modelling and Handling Quality Assessment of the Flying-V Aircraft. In *AIAA Scitech 2022 Forum. AIAA 2022-1429. American Institute of Aeronautics and Astronautics. San Diego, CA Virtual*, page 1429. DOI: 10.2514/6.2022-1429.

van Overeem, S., Wang, X., and Van Kampen, E.-J. (2023). Handling Quality Improvements for the Flying-V Aircraft using Incremental Nonlinear Dynamic Inversion. In *AIAA SCITECH 2023 Forum. AIAA 2023-0105. American Institute of Aeronautics and Astronautics. National Harbor, MD Online*, page 0105. DOI: 10.2514/6.2023-0105.

van Uitert, J. (2023). Experimental Investigation into the Effect of Aerodynamic Add-ons on the Aerodynamic Characteristics of the Flying-V. MSc Thesis. URL: http://resolver.tudelft.nl/uuid:fdfff622-792c-4d54-a048-b59abf477a11.

van Woensel, C. (2021). Integration of a Liquid Hydrogen Fuel Tank into the Concept of the Flying-V. MSc Thesis. URL: http://resolver.tudelft.nl/uuid:e45d2acb-2c85-4543-9160-536fb5195bc6.

Viet, R. (2019). Analysis of the Flight Characteristics of a Highly Swept Cranked Flying Wing by means of an Experimental Test. MSc Thesis. URL: http://resolver.tudelft.nl/uuid:90de4d9e-70ae-4efc-bd0a-7426a0a669c3.

Vigano, L., Riccardi, F., and Leonello, D. (2017). Development of Augmented Control Laws for a Tiltrotor in Low and High Speed Flight Modes. In *43rd European Rotorcraft Forum. Milan, Italy*. URL: http://hdl.handle.net/20.500.11881/3877.

Voeten, R. (2022). A Design Methodology for Unconventional Engine Mounting Structures Applied to the Flying-V. MSc Thesis. URL: http://resolver.tudelft.nl/uuid:8ae4ad77-43d6-44d4-ae34-bb3b118587dd.

Völker, W., Li, Y., and Van Kampen, E.-J. (2023). Twin-Delayed Deep Deterministic Policy Gradient for Altitude Control of a Flying-Wing Aircraft with an Uncertain Aerodynamic Model. In *AIAA Scitech 2023 Forum. AIAA 2023-2678. American Institute of Aeronautics. National Harbor, MD Online*, page 2678. DOI: 10.2514/6.2023-2678.

Vugts, G., Stroosma, O., Vos, R., and Mulder, M. (2023). Simulator Evaluation of Flightpath-Oriented Control Allocation for the Flying-V. In *AIAA Scitech 2023 Forum. AIAA 2023-2508. American Institute of Aeronautics and Astronautics. National Harbor, MD Online*, page 2508. DOI: 10.2514/6.2023-2508.

Wood, R. and Bauer, S. (2001). Flying Wings/Flying Fuselages. *39th Aerospace Sciences Meeting and Exhibit. AIAA 2001-0311 Reno, NV, U.S.A.*, DOI: 10.2514/6.2001-311.

Wu, M. (1974). A Note on Stability of Linear Time-Varying Systems. *IEEE transactions on Automatic Control*, 19(2):162–162, ISSN: 0018-9286, DOI: 10.1109/TAC.1974.1100529.

Zames, G. (1981). Feedback and Optimal Sensitivity: Model Reference Transformations, Multiplicative Seminorms, and Approximate Inverses. *IEEE Transactions on Automatic Control*, 26(2):301–320, ISSN: 0018-9286, DOI: 10.1109/TAC.1981.1102603.

Zhang, M., Gou, L., Jiang, Z., and Sun, C. (2021). Optimization of Aero-engine $\mathcal{H}_\infty$ Robust Controller Based on Quantum Genetic Algorithm. In *2021 12th International Conference on Mechanical and Aerospace Engineering (ICMAE). Athens, Greece*, pages 225–231. ISBN: 978-1-6654-3322-8, DOI: 10.1109/ICMAE52228.2021.9522430.

Zhao, X., Yuan, M.-n., Cheng, P., Le, X., and Yao, L. (2019). Robust $\mathcal{H}_\infty$/S-plane Controller of Longitudinal Control for UAVs. *IEEE Access*, PP:1–1, ISSN: 2169-3536, DOI: 10.1109/ACCESS.2019.2927000.

Zipfel, P. H. (2007). *Modeling and Simulation of Aerospace Vehicle Dynamics*. AIAA: American Institute of Aeronautics and Astronautics, Inc., 2nd edition, ISBN: 978-1-56347-875-8, DOI: 10.2514/4.862182.

A

PROJECT PLAN

From the research proposal detailed in Chapter 3, the research plan was outlined and it is presented in the current appendix. The research plan is divided into four different phases. The first encompasses the elaboration of the literature study and definition of research goals and objectives. The second phase focuses on the redesign of the Flying-V model and on the synthesis and analysis of preliminary controllers with $\mathcal{H}_\infty$ MS. The following research phase includes the exploration of alternative designs for the FCS configuration, the transition to digital design, and the multi-modeling approach. The research culminates in the dissemination, in which the report is submitted and the defense is prepared

Gantt chart — Project schedule

Phase	Literature Study	Research Phase I		Research Phase II	Dissemination

PROJECT WEEK:	1 2 3 4 5 6 7	8 9 10 11 12 13 14 15 16 17 18 19 20	21 22 23 24 25	26 27 28 29 30 31 32 33 34 35 36 37 38 39 40 41 42 43 44 45	46 47 48 49 50 51 52
	MAR	APR MAY JUN JUL	AUG	SEP OCT NOV DEZ	JAN FEB
DAY	4 11 18 25	1 8 15 22 29 6 13 20 27 3 10 17 24 1 8 15 22 29	5 12 19 26	2 9 16 23 30 7 14 21 28 4 11 18 25 2 9 16 23 30	6 13 20 27 3 10 17 24

1. Literature Study
- 1. Topic Definition
- 2. Flying V Research Overview
- 3. Hinf Mixed Sensitivity
- 4. Model Uncertainty & Robustness Analysis
- 6. Handling Qualities Analysis
- 7. Model Reduction Techniques
- 8. Gain Scheduling
- 9. C* Control Law
- 10. Review + Research Proposal
- 11. Reporting

2. Flying-V Model Redesign
- 12. Previous model Understanding
- 13. New Nonlinear Model Design
  - 13.1 Aerodynamic Model implementation
  - 13.2 EOM
  - 13.3 Actuator Dynamics
  - 13.4 Gradual Improvements
- 14. Trimming Procedure
- 15. Linearisation
- 16. Bare Airframe Analysis

3. Continuous Mixed Sensitivity Controller Design
- 17. Controller Objectives Outline
- 19. MS Design - standard C* approach
  - 19.1 Preliminary Unstructured Controllers
    - 19.1.1 2-, 3-, 4-Block
    - 19.1.2 Model Reduction
  - 19.2 Structured Controller Design
    - 19.2.1 Objectives to Constraints
    - 19.2.1 Weighting Filters
  - 19.3 Performance & Robustness Analysis
    - 19.3.1 Stability Margins
    - 19.3.2 Time Domain Sim
    - 19.3.3 Handling Qualities
- 20. Alternative Design Approaches
  - 20.1 Alternative Approaches
  - 20.2 New Controllers Design
  - 20.3 Performance & Robustness Analysis

4. Digital Design
- 21. Introduction to Digital Design
- 22. Unstructured Controller Synthesis & Reduction
- 23. Structured Controller Synthesis
- 24. Structured Controller Analysis
- 25. Motivation for Digital Design

5. Multi Modeling
- 26. Flight Envelope Definition
- 27. Modified Continuous Design
- 28. Performance Robustness Analysis
- 29. Multi-Modeling Validation

6. Project End
- 30. Code Clean-Up and Read Me file
- 32. Report Writing
- 33. Defense Preparation & Submission
- 34. Preparation Scientific Paper
- 35. Defense

Milestones: MID-TERM REVIEW · SUMMER BREAK · BREAK · DRAFT THESIS SUBMISSION · GREENLIGHT · PROJECT END

1

B

ROCOND 2025 PAPER SUBMISSION

This paper presents a longitudinal robust control law that ensures stability and compliance with Handling Quality standards. The design is similar to the one shown in Section 6.3. However, the output disturbance is not modeled. Thus, it offers an additional comparison to the previously designed controller.

Signal-Based Mixed-Sensitivity $\mathcal{H}_\infty$ Longitudinal Controller Design for the Flying-V

Beatriz Pedroso [*] **Tijmen Pollack** [*] **Spilios Theodoulis** [*]

[*] *Faculty of Aerospace Engineering, Delft University of Technology, Delft, 2629HS, The Netherlands*

Abstract:
This study details the design of a longitudinal robust control law for the Flying-V concept aircraft. The trimming procedure used to obtain operating points and linearized flight dynamics is explained, followed by a description of the design requirements which are systematically converted into hard constraints. These are employed in the structured controller synthesis, conducted within the signal-based $\mathcal{H}_\infty$ Mixed Sensitivity (MS) framework. The system's performance and robustness are evaluated in linear and nonlinear settings. Results indicate effective disturbance and noise rejection, stability under parametric uncertainties, Level 1 Handling Qualities predictions, and adequate performance. These results validate the C* control law effectiveness, paving the way for future enhancements in gain-scheduled robust controllers for the Flying-V and for the extension to lateral-directional controllers.

Keywords: Robust control, Mixed sensitivity synthesis, Flight control, $\mathcal{H}_\infty$ Optimization, Reduced-order models, Robust stability, Sustainable aviation, Flying wings.

1. INTRODUCTION

Commercial aviation has experienced a rising demand in recent years. The Flying-V aircraft is introduced as a promising concept that seeks to mitigate the industry's environmental impact. Preliminary assessments by Benad and Vos (2022) suggest that the Flying-V could achieve a 20% lower fuel burn when compared to the state-of-the-art reference aircraft performing the same mission. However, its unconventional shape and layout pose unique challenges in terms of stability and control, necessitating the development of advanced control systems.

This study focuses on the development of a robust flight control system tailored for the Flying-V aircraft. The proposed solution revolves around guaranteeing robustness against disturbances, measurement noise, and uncertainties in the model while ensuring performance and compliance with Level 1 Handling Qualities (HQ). To achieve this, a C* longitudinal control law is suggested, for which robust control methodologies such as the signal-based $\mathcal{H}_\infty$ MS framework are followed. Commercially available nonsmooth optimization tools are used. These result from the work developed by Apkarian and Noll (2006) that allows structured controller synthesis and elevates the potential of the robust control theory.

This paper is structured as follows: Section 2 presents the linearized dynamics as well as model intricacies, Section 3 discusses the C* parameter and the controller design requirements, structure, synthesis methodology and results, and lastly, Section 4 examines the flight control performance and robustness for the nominal and uncertain scenarios in linear and nonlinear settings.

2. FLYING-V MODEL DESCRIPTIONS

A 6 Degrees of Freedom (DoF) Flying-V model is implemented in MATLAB ®/Simulink ® in a tensor-based formulation. Tensors hold the physical characteristics regardless of the coordinate system. This generalizes the Equations of Motion (EoM), allowing for subsequent projection into any coordinate system (Zipfel, 2007).

The trimming procedure is the first step towards linearization of the flight dynamics. It involves a (usually numerical) method which calculates the equilibrium points around an imposed condition $\boldsymbol{\rho}(t) = \bar{\boldsymbol{\rho}} = [\bar{M}_a \ \bar{h}]^T$ so as to zero out the forces and moments contribution of the body and control surfaces. The EoM can be represented in a general parameter-dependent form as:

$$\begin{cases} \dot{\mathbf{x}}(t) = \mathbf{f}_x[\mathbf{x}(t), \mathbf{u}(t), \boldsymbol{\rho}(t)], \ t \in \Re_+ \\ \mathbf{y}(t) = \mathbf{f}_y[\mathbf{x}(t), \mathbf{u}(t), \boldsymbol{\rho}(t)] \end{cases} \quad (1)$$

where $\mathbf{x} = [p \, q \, r \, \phi \, \theta \, \psi \, V \, \alpha \, \beta \, x_L \, y_L \, z_L]^T$ represents the state vector, $\mathbf{u} = [T \, \delta_a \, \delta_e \, \delta_r]^T$ is the control input vector, and $\mathbf{y} = [n_x \, n_y \, n_z \, p \, q \, r]^T$ is the output vector. The aircraft is in equilibrium if $\dot{\mathbf{x}}(t) \triangleq 0$. Solving this condition assumes that there are as many algebraic equations as unknown variables, which is not the case. To overcome this, some of the unknown states need to be imposed. Assuming a steady wings-level flight, ϕ, p, q, and r are considered null and x_L, y_L, and ψ are specified freely. V is defined as known given its correlation with α through lift (Stevens et al., 2015). Null flight path angle is imposed as an additional constraint, assuming equal values for α and θ.

In the present study, the flight control system targets a single condition: Mach 0.5 at 5400 meters altitude,

where only the longitudinal motion is relevant. Thus, from the complete linearized dynamics, the appropriate states, inputs, and outputs are selected so as to form a linear-time-invariant system with phugoid and short period (SP) eigenmotions. The pilots can easily manage the low frequency (LF) phugoid, although it still needs to meet certain damping requirements (Stevens et al., 2015). Nonetheless, the SP is pivotal for controller design and for HQ satisfaction. Thus, the following SP approximation of the Flying-V will be considered:

$$\begin{bmatrix} \dot{\alpha} \\ \dot{q} \end{bmatrix} = \begin{bmatrix} -0.601 & 0.974 \\ -1.154 & -0.748 \end{bmatrix} \begin{bmatrix} \alpha \\ q \end{bmatrix} + \begin{bmatrix} -0.141 \\ -3.198 \end{bmatrix} \delta_e$$
$$\begin{bmatrix} n_{z_{CoG}} \\ q \end{bmatrix} = \begin{bmatrix} 9.655 & 0.4222 \\ 0 & 1 \end{bmatrix} \begin{bmatrix} \alpha \\ q \end{bmatrix} + \begin{bmatrix} 2.3 \\ 0 \end{bmatrix} \delta_e \quad (2)$$

3. FLIGHT CONTROL SYSTEM DESIGN

3.1 C* Longitudinal Control Law

The C* originated from a HQ criterion, which led to the creation of a response type. Variations of the C* control law became standard in the commercial aviation industry (Arent and Falatko, 1992) (Favre, 1994). The parameter is defined as a normalized sum of the pitch rate and normal acceleration at the Pilot Station (PS), as described in (3):

$$C^* = n_{z_{PS}} + \frac{V_{CO}}{g} q, \quad (3)$$

where g is the standard gravity and V_{CO} corresponds to the crossover velocity, where both cues translate into equal pilot sensation. It is asserted that pilots respond to a combination of these two signals, where the control priority shifts naturally from q to n_z as airspeed increases (Niedermeier and Lambregts, 2012).

3.2 Design Requirements

For controller design, the requirements considered are:

(R1) Disturbance rejection at plant input and outputs.
(R2) Sensor noise attenuation at plant input and outputs.
(R3) Control effort reduction.
(R4) Minimum allowable limit for the classical stability gain (GM) and phase (PM) margins of 6 dB and 45°, respectively, at plant input and outputs.
(R5) Robustness guarantees in the presence of independent parametric uncertainties in the aerodynamic coefficients, varied across the range of ±30%.
(R6) Predicted HQ within Level 1.

To achieve requirement R6, a reference model is necessary for model matching design. The following second-order reference model was iteratively tuned to achieve the desired dynamics for the short-term pitch response specifications (Anonymous, 2004) (Mitchell et al., 1994):

$$T_{ref}(s) = \frac{C^*_{ref}(s)}{r(s)} = \frac{K_{num}(s + z_{ref})}{s^2 + 2\xi_{ref}\omega_{ref}s + \omega_{ref}^2}, \quad (4)$$

where r corresponds to the pilot stick input signal. To minimize control surface activity (Favre, 1994), the desired natural frequency is set to $\omega_{ref} = 1.4$ rad/s, which is similar to the nominal bare airframe value ($\omega_{SP} = 1.25$ rad/s) for the chosen flight condition. Additionally, defining the desired damping ratio as $\xi_{ref} = 0.75$ and the numerator

$z_{ref} = 1.2$ yields Level 1 performance in the selected HQ criteria. $K_{num} = 1.6333$ was defined so that T_{ref} has unitary static gain.

3.3 Controller Structure

The flight control law is expressed as the transfer function (TF) in (5) (see Figure 1), inspired by Niedermeier and Lambregts (2012)'s work. The standard C* parameter is defined at the PS, due to its strong alignment with pilot cues, making it the preferred signal for reference tracking. However, the feedback signal is based on C* calculated with n_z measured at the Inertial Measurement Unit (IMU), which is positioned to reduced sensitivity to structural and other sources of high frequency (HF) dynamics. The IMU position is assumed to be near the aircraft's Instantaneous Center of Rotation (ICR), although a more in-depth analysis must be conducted on this matter. Besides the feedback controller K_{FB}, K_{FF} introduces a 2 DoF structure which enhances reference tracking capabilities. The controller on the pitch rate channel, K_q, is a gain and improves the SP damping.

$$\delta_{e,c} = K_{FB}(K_{FF}r - C^*_{IMU}) - K_q q \quad (5)$$
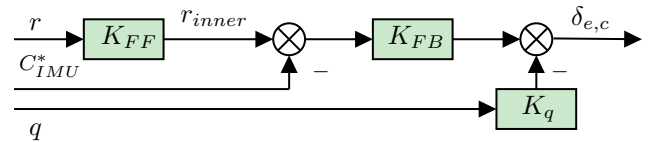
Fig. 1. Flying-V C* longitudinal controller configuration.

3.4 Mixed Sensitivity $\mathcal{H}_\infty$ Preliminary Design

To identify the optimal structure for K_{FB} in the final design, an unstructured controller was initially developed and a model order reduction was subsequently employed on it. The standard $\mathcal{H}_\infty$ MS four-block method design is used, since it effectively addresses both input and output disturbance rejection (Huang et al., 2010).

The initial structure of K_{FB} is determined. To achieve that, the plant output (PO), y (i.e. C*$_{IMU}$), and the controller output, u_c, are chosen as the output signals whereas the input and output disturbances, d_i and d_o, are chosen as the input signals (see Figure 2). Therefore, the weighted closed loop matrix TF $T_{wz}(s)$ is given as described in (6), where S_o, KS_o, S_oG, and T_i correspond to the respective individual TFs from the inputs to the output signals. K_q is defined a priori so that the typical value of $\xi_{SP} = 0.707$ is achieved for the SP damping, using root locus techniques.
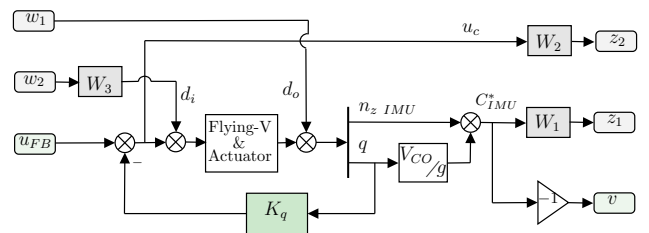
Fig. 2. Configuration for the full order design.

$$\begin{bmatrix} y \\ u_c \end{bmatrix} = \begin{bmatrix} S_o & S_o G \\ -K S_o & -T_i \end{bmatrix} \begin{bmatrix} d_o \\ d_i \end{bmatrix}$$
$$\implies T_{wz} = \begin{bmatrix} W_1 S_o & W_1 S_o G W_3 \\ -W_2 K S_o & -W_2 T_i W_3 \end{bmatrix} \quad (6)$$

Here, W_1, W_2, and W_3 are the weighting filters (WF) that are used to shape the closed loop TFs. Although W_1 and W_2 would allow a satisfactory design, the low-pass W_3 is a complement that allows a tighter shaping at $S_o G$ Medium Frequencies (MF) and of T_i roll-off. Given that disturbances are dominant at LF, S_o and $S_o G$ must have low gain in this range. Control signal attenuation can only be imposed in MF and HF since the controller designer does not have any influence at LF. This is due to the fact that $\underline{\sigma}(K S_o) \approx 1/\underline{\sigma}(G)$ and that $\underline{\sigma}(T_i) \approx 1$ from the duality with the sensitivity function. Hence, $K S_o$ and T_i must have low gain at HF. Moreover, a peak in the sensitivity and complementary sensitivity functions is unavoidable and it is related to the closest distance to the critical point -1 in the complex plane, which affects the stability margins, as described by (Seiler et al., 2020):

$$\alpha_{max} = \frac{1}{\|S + \frac{\sigma-1}{2}\|_\infty}, \quad (7)$$

where α_{max} represents the smallest of all the frequency-dependent Disk Margins (DM) and σ represents the skew. At MF, the peak should be attenuated. The low pass filter $W_1^{-1}(s)$ and the high pass filter $W_2^{-1}(s)$ are defined as:

$$W_1^{-1}(s) = \frac{s + \underline{k}_{W_1} \overline{k}_{W_1}}{\overline{k}_{W_1}^{-1} s + \overline{k}_{W_1}}, \; W_2^{-1}(s) = \frac{\overline{k}_{W_2} s + \overline{k}_{W_2}}{s + \overline{k}_{W_2} \underline{k}_{W_2}^{-1}}, \quad (8)$$

where $\underline{k}_{W_1} = -50$ dB and $\overline{k}_{W_1} = 6.02$ dB are the desired LF and HF attenuation of S_o, and $\overline{k}_{W_1} = 0$ dB is the desired gain at the frequency $\overline{\omega}_{W_1} = 1.1$ rad/s [1]. Similarly, for W_2^{-1}, $\underline{k}_{W_2} = 50$ dB, $\overline{k}_{W_2} = -50$ dB, $\overline{k}_{W_2} = -23.5$ dB, and $\overline{\omega}_{W_2} = 14.3$ rad/s [1]. Lastly, W_3 is a high-pass filter with steady state gain $k = 0.1$, the zero $z_3 = 10$ rad/s, and the pole $p_3 = 10^4$ rad/s.

The $\mathcal{H}_\infty$ optimal controller is obtained by solving:

$$\min_K \|T_{wz}\|_\infty, \quad (9)$$

where K is a stabilizing controller. Assuming that the optimal $\mathcal{H}_\infty$ norm is $\gamma = \min_K \|T_{wz}\|_\infty$, the resulting TFs from a solution to (9) are close to γ times the bounds selected by the designer via the WF. Nevertheless, the unstructured controller is computed as a result of the optimization of a stacking procedure, which is selected for mathematical purposes and does not enable individual bound specifications. Thus, for each, there is a possible resulting error of at most $\sqrt{n}$, where $n = 4$ corresponds to the number of stacked requirements. (Skogestad and Postlethwaite, 2005)

The goal is to ensure $\|T_{wz}\|_\infty < \gamma < 1$. A $\gamma = 0.9814$ was achieved and the obtained full-order (FO) controller is detailed in (10). Model order reduction was applied to the FO controller [2] and the frequency responses of both reduced and FO controllers are shown in Figure 3. From

---

[1] makeweight() MATLAB[®] function is used to obtain the WF.
[2] getrom() MATLAB[®] function is used to obtain the reduced-order models using balanced truncation.

---

the FO TF, it is evident that the zeros s = -8829 rad/s and s = -278.9 rad/s and the poles s = -2.3 · 10⁶ rad/s and s = -1.3 · 10⁴ rad/s are very HF and, hence, can be discarded. The zero s = -14.5 rad/s and the pole s = -17.3 rad/s can be reduced, as well as the pole s = -1.4 rad/s and one of the zeros from the complex conjugate, whose frequency is $\omega = 1.38$ rad/s. Only the integrator-like pole (s = -0.003 rad/s), the pole s = -5.7 rad/s, and the second complex conjugate zero remain, justifying the second order solution (see (11)). Choosing the controller structure balances complexity and effectiveness, with a low-order controller preferred for real implementation. As expected, the second and third order controllers are very similar (see Figure 3). While the second order result (PI with a low pass) closely matches the FO controller until 10^3 rad/s, the first order controller is a satisfactory approximation until $2 \cdot 10^0$ rad/s. The second-order structure appears to be the most adequate choice to impose on the final design.

$$K_{FB_{FO}}(s) = \frac{-6187.8(s + 8829)(s + 278.9)(s + 14.5)}{(s + 2.3 \cdot 10^6)(s + 1.3 \cdot 10^4)(s + 17.2)}$$
$$\frac{(s^2 + 2.4s + 1.9)}{(s + 5.7)(s + 1.4)(s + 0.003)} \quad (10)$$

$$K_{FB_{O2}}(s) = \frac{-0.53(s + 1.73)}{s(s + 8.90)} \quad (11)$$
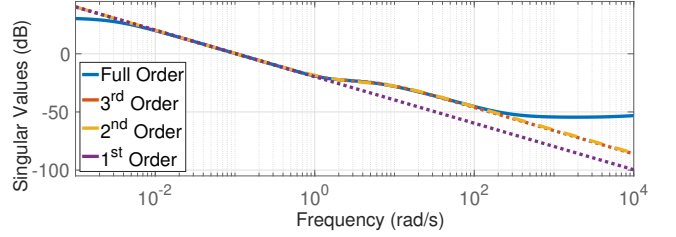
Fig. 3. Unstructured controller model order reduction.

3.5 Signal-Based Mixed Sensitivity $\mathcal{H}_\infty$ Optimization

The final design configuration is inspired from robust control theory (Skogestad and Postlethwaite, 2005) and it is represented in Figure 4. The bare airframe dynamics represented in (2) correspond to the Flying-V block in the figure, which was augmented to contain the output $\dot{q}$. This parameter is used for the computation of the C^*_{PS} signal that is crucial for the reference tracking. Additional inputs include the disturbances d_i and d_o and the sensor noise n.
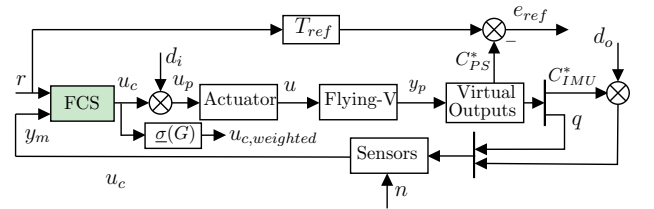
Fig. 4. Configuration for the structured controller design.

The requirements outlined in 3.2 are achieved by shaping the following seven individual TFs, $C(s)$, which are consequently treated as hard constraints, via WF:

(C1) $S_o(s)$ ($d_o \rightarrow C^*_{IMU}$) involves output disturbance rejection at the virtual PO. The TF LF gain must be reduced to enhance the rejection properties.

(C2) $S_i(s)$ $(d_i \rightarrow u_p)$ rejects input disturbances at the plant input (PI). Similarly to S_o, small gain at LF is necessary.

(C3) $T_i(s)$ $(d_i \rightarrow u_c)$ rejects input disturbances at the controller output by the TF low gain at HF. It also contributes to control signal attenuation.

(C4) $T_o(s)$ $(r_{inner} \rightarrow C_{IMU}^*)$ attenuates sensors noise. Thus, the TF from n to C_{IMU}^* could also be selected for the same purpose. Since noise is a HF signal, the TF must have low gain in this range.

(C5) $KS_o(s)$ $(d_o \rightarrow u_{c,weighted})$ reduces control effort and provides noise attenuation at HF by its low gain. The TF LF gain is approximately equal to the plant gain inverse. For better interpretation of the attenuation level at MF and HF, the scaling $\underline{\sigma}(G)$ is multiplied with the u, originating the signal $u_{c,weighted}$ (see Figure 4), before applying the WF.

(C6) $S_oG(s)$ $(d_i \rightarrow C_{IMU}^*)$ constrains the input disturbances at the PO. Small LF gain is mandatory.

(C7) $M(s)$ $(r \rightarrow e_{ref})$ is the model matching constraint that imposes the T_{ref} behavior on the signal C_{PS}^* response. The TF must have low gain at LF and MF.

Hence, the disturbance rejection requirement R1 is ensured by C1, C2, C3, and C6. The noise attenuation specification R2 is achieved by imposing C4 and C5, while R3, the control effort reduction, is guaranteed by C5. The stability margins, R4, result from MF peak limitation in C1. Moreover, unstructured input and output multiplicative uncertainty is addressed by T_i and T_o. Thus, C3 and C4 contribute to R5. Lastly, C7 yields HQ compliance (R6).

The WFs $W_C(s) = [W_{S_o} W_{S_i} W_{T_i} W_{T_o} W_{KS_o} W_{S_oG} W_M]^T$ allow the constraints to be written as $\|W_{C_i}(s)C_i(s)\|_\infty$, where i is the index of the vector. Hence, the expression

$$\|W_{C_i}(s)C_i(s)\|_\infty < \gamma \iff \forall \omega \in \Re, |C_i(j\omega)| < \frac{\gamma}{|W_{C_i}(j\omega)|} \quad (12)$$

is verified, which concludes that defining the WF as the inverse of the desired shapes for each TF of $C(s)$ and having a performance level, γ, lower or equal to unity, results in the satisfaction of the gain limitations imposed.

As determined in Section 3.4, K_q and K_{FB} correspond to, respectively, a gain and a PI plus low-pass structures. Initially, K_{FF} is not synthesized to evaluate its necessity. A few trials were conducted by shaping the gain limits on the constraints. It is concluded that the pole and zero of the resulting K_{FB} were very close in terms of frequency (see (13)). Thus, its order could be further simplified.

$$K_{FB} = \frac{-0.20884(s + 13.38)}{s(s + 13.52)} \quad (13)$$

Provided that the obtained Stability Margins (SM) were very optimistic, it was decided to reduce the complexity of the controller and define its structure as a simple integrator and a static gain. This controller structure was also obtained in the model reduction shown in Figure 3. A potential advantage of the PI with low pass would be the open loop slope decrease around crossover, possibly yielding ameliorated stability margins. Nonetheless, if the simpler controller meets all of the requirements, it is the best solution. The WF inverse characteristics are presented

in Table 1. The tendency of the filters inverse for the TFs in C1, C2, C6, and C7 follow a similar tendency to W_1^{-1}, whereas C3, C4, and C5 are similar to W_2^{-1} (see (8)).

Table 1. Weighting filters characteristics [1].

	$W_{S_o}^{-1}$	$W_{S_i}^{-1}$	$W_{T_i}^{-1}$	$W_{T_o}^{-1}$	$W_{KS_o}^{-1}$	$W_{S_oG}^{-1}$	W_M^{-1}
$\underline{k}$ (dB)	-50	-50	12.04	12.04	50	-50	-50
$\overline{\omega}$ (rad/s)	1.70	4.60	7.96	3.08	14.30	10^{-2}	1
$\underline{k}$ (dB)	0	0	0	0	-4.80	-25.30	-20.9
$\overline{k}$ (dB)	5.58	5.58	-80	-80	-50	30	-10
Order	1	1	2	2	1	1	1

These design specifications are defined via `sltuner()` [3] which interfaces with a Simulink® file similar to the configuration in Figure 4. For each constraint, the obtained γ, is displayed in Table 2. The controllers retrieved are:

$$K_{FB} = \frac{-0.20696}{s} \qquad K_q = -1.43320 \quad (14)$$

Table 2. γ values obtained for each constraint.

	S_o	S_i	T_i	T_o	KS_o	S_oG	M
γ	0.9996	0.9998	0.9998	0.9587	0.9968	0.9935	0.9965

The frequency responses of the closed loops TFs S_o and T_o, S_i and T_i, KS_o, S_oG, and M are shown in Figures 5, 6, 7, 8, and 9, respectively, as well as the WF inverse imposed for each. It is verified that with unitary K_{FF}, the model matching constraint is not violated. The lack of necessity of this controller is explained by Figure 10. In fact, $C_{FF_{ideal}} = T_{o_M}^{-1} \cdot T_{ref}$, where T_{o_M} is the TF from r to C_{PS}^*. It is observed that the most dominant pole and zeros of $T_{o_M}^{-1}$ have frequencies of $\omega_p = 1.4$ rad/s and $\omega_z = 1.82$ rad/s, respectively, while T_{ref} has poles and a zero with frequencies of $\omega_p = 1.4$ rad/s and $\omega_z = 1.2$ rad/, respectively. The frequencies proximity suggests that the inner closed loop TF has an approximate behavior to the desired T_{ref}, highlighting the feedforward controller as noncompulsory. This statement is to be corroborated by the HQ and nonlinear simulations assessments.

The singular values of the open loops at the PI, Li, and at the PO at n_z in the center of gravity and q, respectively Lo_{n_z} and Lo_q, and at the virtual output C_{IMU}^*, $Lo_{C_{IMU}^*}$, are shown in Figure 11. On the one hand, the small gain at LF in the sensitivity functions are translated into large gains in the open loops at the PI and virtual output. On the other hand, T_o and T_i impose roll off in the open loops at HF. Nevertheless, it is noticeable that there is no disturbance rejection on n_z and q, given the small gain at LF. Such outcome is expected since that no integral action is applied on these signals. This is due to the single-input multiple-output formulation. The plant only contains a single singular value. Therefore, with one input, it is not possible to control more than one output. Thus, it is concluded that to have a balanced disturbance rejection at LF on the signals n_z and q, the pure C* configuration should be followed, which also yields good disturbance rejection in this signal. If integral action is applied on the n_z (or q) signal, the q (or n_z) disturbance rejection is aggravated, with smaller gain observed at LF.

---

[3] The `TuningGoal.Gain` class is used to impose the gain limits from a specified input to a specified output over the frequency range.
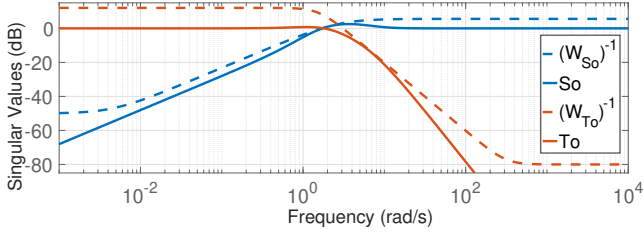
Fig. 5. Frequency responses of $S_o(s)$ and $T_o(s)$.
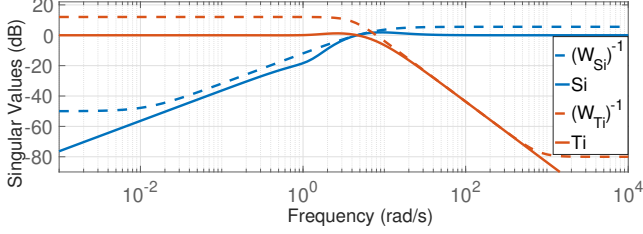
Fig. 6. Frequency responses of $S_i(s)$ and $T_i(s)$.
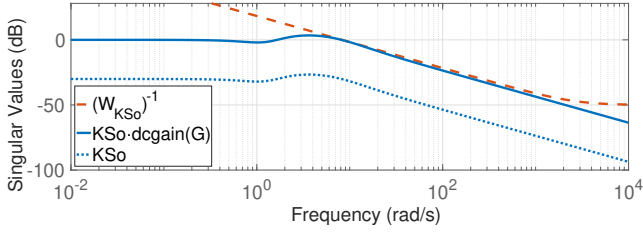
Fig. 7. Frequency response of $KS_o(s)$.
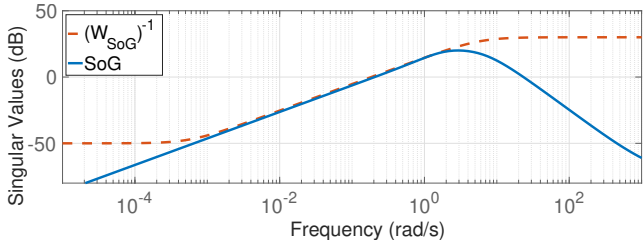
Fig. 8. Frequency response of $S_oG(s)$.
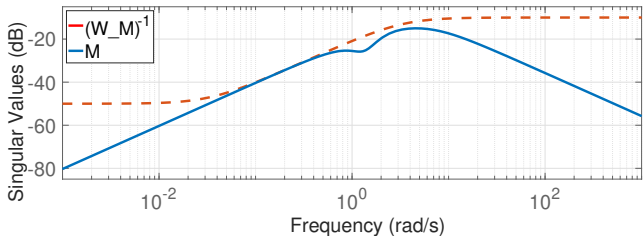
Fig. 9. Frequency response of $M(s)$.

4. FLIGHT CONTROL SYSTEM ANALYSIS

4.1 Stability Margins

SM assessment is a key specification, as highlighted by R4, which is also crucial when uncertainty is applied to the system (R5). Anonymous (2008) states that in the latter scenario, the requested SM are reduced, highlighting an allowable degradation up to 50% the desired nominal values if faced by $\pm20\%$ uncertainty. In this study, parametric uncertainty bounded by $\pm30°$ is applied to the stability
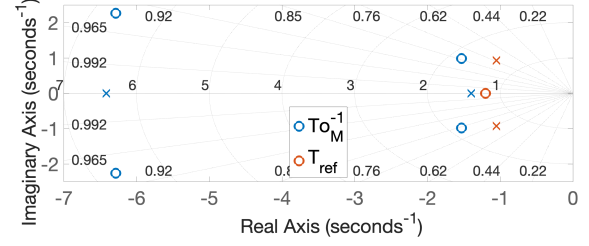
Fig. 10. Pole-zero map of the inner closed loop TF and T_{ref}.
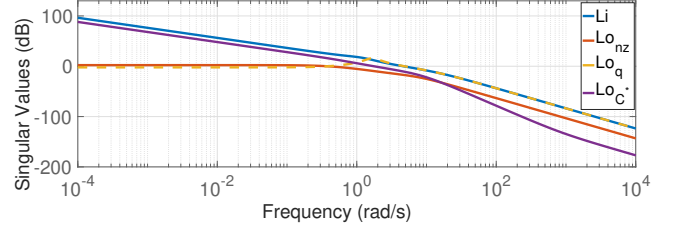
Fig. 11. Open loops frequency response at the PI and PO.

and control derivatives that affect the SP the most (i.e. C_{z_α}, C_{m_α}, C_{m_q}, and $C_{m_{\delta_e}}$). Five uniformly distributed samples were taken in this range for each coefficient, yielding 625 uncertain conditions. Therefore, the classical loop-at-a-time SM are computed, as well as the balanced (S-T) Disk Gain and Phase Margins (DGM and DPM, respectively). Table 3 presents these values for the nominal scenario, whereas Table 4 shows the Worst Case (WC) results for the uncertainty simulations. It is verified that the minimum values of 6 dB and 45° are guaranteed for the nominal system and uncertainty scenarios.

Table 3. Disk (S-T) and classical loop-at-a-time GM and PM, for the nominal scenario.

Broken Loop	Disk Margins DGM (dB)	Disk Margins DPM (°)	Classical Margins GM (dB)	Classical Margins PM (°)
Plant Input	$\pm$ 11.19	$\pm$ 59.16	∞	59.65
PO (nz @ CoG)	$\pm$ 12.84	$\pm$ 64.31	14.54	127.02
PO (q)	$\pm$ 10.94	$\pm$ 58.32	-15.40	58.36
Virtual PO (C*)	$\pm$ 10.38	$\pm$ 56.32	18.63	59.02

Table 4. WC disk (S-T) and classical loop-at-a-time GM and PM, subject to uncertainty.

Broken Loop	Disk Margins DGM (dB)	Disk Margins DPM (°)	Classical Margins GM (dB)	Classical Margins PM (°)
Plant Input	$\pm$ 9.00	$\pm$ 50.92	∞	55.69
PO (nz @ CoG)	$\pm$ 9.60	$\pm$ 53.36	10.77	119.59
PO (q)	$\pm$ 8.31	$\pm$ 47.99	-28.47	51.27
Virtual PO (C*)	$\pm$ 7.14	$\pm$ 42.55	14.59	45.98

4.2 Handling Qualities

Handling qualities represent the dynamic characteristics of an aircraft as perceived by the pilot, which intimately influences the safety, performance, and pilot workload. Thus, analyzing HQ criteria is crucial to ensure the aircraft responds predictably and effectively. Three main criteria are used, namely the attitude bandwidth (BW), the flight path BW, and the pitch rate overshoot & pitch attitude dropback, as proposed by Mitchell et al. (1994). The results are shown in Figures 12, 13, and 14, respectively. The BW is calculated as the highest frequency at which

the PM is at least $45°$ and the GM is at least 6 dB. Considering w_{180} as the frequency at which the phase crosses $-180°$, the phase delay parameter τ_p is computed by dividing the difference in phase from ω_{180} to $2\omega_{180}$ with the frequency $2\omega_{180}$, with appropriate scaling with units. Lastly, the subscript in q_{ss} signifies steady state. Besides the nominal values, the ones retrieved from the 625 uncertain conditions are also shown. As desired, the nominal case is within Level 1 and the uncertain points are also mostly within this level, except for some outliers.
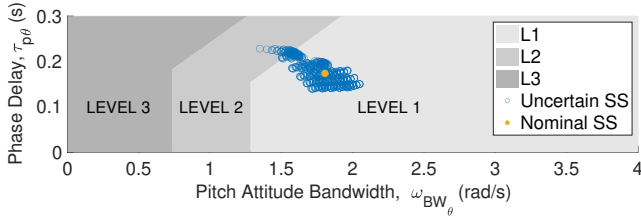
Fig. 12. Pitch attitude BW HQ criteria.
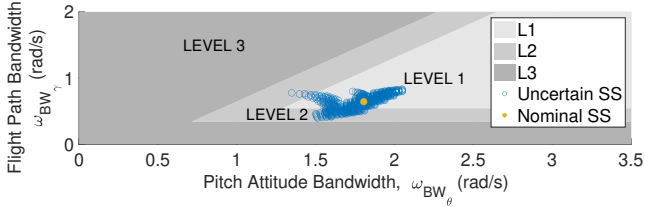
Fig. 13. Flight path BW HQ criteria.
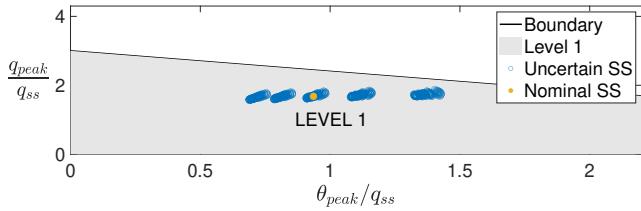
Fig. 14. Pitch rate overshoot & attitude dropback HQ criteria.

4.3 Nonlinear Time Domain Simulations
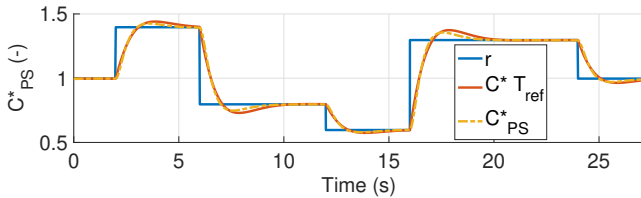
Fig. 15. Reference tracking C^*_{PS} response in the NL model.

The linear controller is implemented in the nonlinear 6 DoF model. Due to lack of space, only the reference tracking signal (see Figure 15) is shown. It is verified that the system behaves similarly to the linear case and identically to the reference model imposed by the constraint $M(s)$.

5. CONCLUSION

This study presented a longitudinal control law design for the Flying-V aircraft. The controller synthesized respected all of the requirements and constraints imposed. It demonstrated satisfactory stability margins, compliance with Level 1 Handling Qualities, and solid performance in the nonlinear model. Future work should address the discretization effects of the flight computer, expansion to lateral-directional design, and gain-scheduling to cover a larger flight envelope.

REFERENCES

Anonymous (2004). Flying Qualities of Piloted Aircraft. MIL-STD-1797A. Notice 3. Technical report, U.S. DoD.

Anonymous (2008). *Aerospace - Flight Control Systems - General Specification for Design, Installation, and Test of Piloted Military Aircraft*. SAE-AS94900.

Apkarian, P. and Noll, D. (2006). Nonsmooth $\mathcal{H}_\infty$ Synthesis. *IEEE Transactions on Automatic Control*, 51(1), 71–86.

Arent, L. and Falatko, J. (1992). *757 fly-by-wire demonstrator flight test*. 6th American Institute of Aeronautics and Astronautics, AIAA.

Benad, J. and Vos, R. (2022). Design of a Flying-V subsonic transport. In *33rd Congress of the International Council of the Aeronautical Sciences, ICAS 2022*, volume 2.

Favre, C. (1994). Fly-by-wire for commercial aircraft: the Airbus experience. *International Journal of Control*, 59(1), 139–157.

Huang, Y., Pe, T., Popov, A.P., Werner, H., and Thielecke, F. (2010). Control of a two-load-path Trimmable Horizontal Stabilizer Actuator of an aircraft - Comparison of $\mathcal{H}_\infty$ design approaches. In *49th IEEE Conference on Decision and Control (CDC)*, 4863–4868.

Mitchell, D.G., Hoh, R.H., Aponso, B.L., and Klyde, D.H. (1994). Proposed Incorporation of Mission-Oriented Flying Qualities into MIL-STD-1797A. WL-TR-94-3162. *Wright-Patterson AFB, USA*.

Niedermeier, D. and Lambregts, A. (2012). Fly-by-wire Augmented Manual Control - Basic Design Considerations. *28th Congress of the International Council of the Aeronautical Sciences 2012, ICAS 2012*, 4, 3073–3086.

Seiler, P., Packard, A., and Gahinet, P. (2020). An Introduction To Disk Margins. *IEEE Control Systems Magazine*, 40.

Skogestad, S. and Postlethwaite, I. (2005). *Multivariable Feedback Control: Analysis and Design*, volume 2. John Wiley and sons.

Stevens, B.L., Lewis, F.L., and Johnson, E.N. (2015). *Aircraft control and simulation: dynamics, controls design, and autonomous systems*. John Wiley & Sons.

Zipfel, P.H. (2007). *Modeling and Simulation of Aerospace Vehicle Dynamics*. AIAA: American Institute of Aeronautics and Astronautics, Inc., 2nd edition.